UNIVERSITÀ DEGLI STUDI
DI GENOVA

ISTITUTO ITALIANO
DI TECNOLOGIA

**Università degli Studi di Genova**

**Corso di Dottorato in Neuroscienze**

**Coordinatore Prof. Angelo Schenone**

**Curriculum Neuroscienze e Neurotecnologie**

**Ciclo XXXII (A.A. 2019/2020)**

# Closed-loop approaches for innovative neuroprostheses

**Author: Stefano Buccelli**

**Supervisor: Dr. Michela Chiappalone**

# Table of contents

*Introduction* 6

*Chapter 1: State of the art of Neurotechnologies and applications* 8

**Overview** 8

**Techniques to interact with the brain** 9

Reading the neural code 9

Writing the neural code 17

Radically Innovative techniques 22

**Neurotechnology applications** 26

Rectify 26

Replace 31

Retrain 38

**Ethical issues** 44

**References** 46

*Chapter 2: Replace: in vitro neuroprosthesis* 54

**Overview** 54

***In vitro* cultures** 56

In vitro development 56

Modular cultures 60

**Introduction to the BrainBow project** 62

**Methods** 65

Experimental methods 66

Online processing 70

Spiking neural network 73

SNN implementation on FPGA 79

Offline data analysis 82

**Results** 85

Neuroprosthetic architecture 85

Control experiments 87

Bidirectional Bridging (BB) 94

Hybrid bidirectional bridging (HBB) 97

**Discussion** 102

**Personal contribution** 105

**Conclusions** 106

**References** 107

***Chapter 3: Rectify: ex vivo neuroprosthesis*** ***114***

**Overview** 114

**Introduction** 114

**Materials and Methods** 117

Dissection procedure 117

Custom chamber and perfusion control system for brain slices 118

**Results** 118

**Conclusion** 126

**References** 128

***Chapter 4: Retrain: in vivo neuroprosthesis*** ***130***

**Overview** 130

**Introduction** 133

**Methods** 135

Hardware architecture 135

Software interface 137

Spike detection state machine 138

Surgical implant and recording for in vivo testing 139

Offline performance testing 142

**Results** 144

Ability to detect waveforms of interest 144

Performance in awake ambulatory rats 147

Mean latency from spike peak to stimulus delivery 150

Discussion 151

**References** 155

***Chapter 5: Perspective on humans*** ***158***

**References** 163

***Conclusions*** ***164***

***List of related publications*** ***166***

***Appendix*** ***168***

**Chapter 4 Appendix** **168**

Simulink testbench 169

MATLAB testbench 169

Validation 169

Code Availability 170

***Acknowledgements*** ***171***

# Introduction

When Neuroscience meets Engineering, the Neurotechnology field starts to grow. In the last decades, various neurotechnologies are closing the gap between the nervous system and artificial devices. The classification and terminology of all the different applications in the field of Neurotechnology can vary depending on the authors. For this thesis, I will use the following classification for neurotechnologies based on their final goal:

- **Rectify**. In this category we will include all the systems aimed at stopping a pathological activity (e.g. tremor in motor disorders and epileptic seizures in epileptic patients)
- **Replace**. In this class, we will include all the devices that aim to substitute or bypass a non-functional circuit or part of the body.
- **Retrain**. Here we will include all the systems aimed at "helping the brain" to help itself taking advantage of neuroplasticity.

It worth noticing that the borderline among these classes is not always clear-cut. For instance, the replacing and retraining goals can overlap in many cases thanks to the incredible adaptability of the neural circuits to different environments and neural interfaces.

Many pathologies can benefit from electrical stimulation of the brain. Some of them, such as Parkinson's disease and epilepsy are currently the most studied but usually implement open-loop stimulation (i.e. independent from the current activity) to perturb brain activity. Open-loop stimulation can have several drawbacks and therefore the so-called closed-loop approach can be a more natural way of delivering stimulation with less side effects. The term closed-loop, commonly used in neuroscience, can be controversial when compared to closed-loop systems in the field of control engineering. In Neuroscience, we usually call closed-loop systems all those systems that record activity from the brain, process and deliver stimulation back to the brain in real-time. In the last years, the interest towards the closed-loop paradigms has grown exponentially. The main advantages of using a closed-loop stimulation include: the reduced number of stimuli when compared to the open-loop ones and the close relationship of the stimulation with the current "state" of the brain.

In this context, the goal of this thesis is to study new ways to interact with the nervous system in case of damage or pathology. In particular, I focused my effort towards the development of innovative, closed-loop stimulation protocols in various scenarios, covering all the three kinds of applications mentioned above.

In order to describe the work that I performed during my PhD, I organized this Thesis in five chapters.

The first one gives an overview of the state of the art of Neurotechnologies for reading and writing the neural code; it also contains several innovative applications of these techniques, with a particular attention to closed-loop applications, with a final paragraph concerning possible ethical issues (Chapter 1). The second chapter describes a neuroprosthetic device applied to an *in vitro* model of focal brain lesion. In that project, I used different stimulation protocols aimed at reconnecting or **replacing** (by means of an artificial neural network) parts of a damaged neuronal network (Chapter 2). Using cell cultures plated over Micro Electrode Arrays (MEAs) can be useful in many scenarios given the high controllability of the entire neural network. The main limitation of this model is that it lacks some of the relevant features of brain circuits. Therefore, in (Chapter 3), I describe the development of a setup for real-time acquisition, processing and stimulation on *ex vivo* brain slices recorded through MEAs. The goal of this stimulation protocol was aimed at reducing the occurrence of epileptic seizures (**rectify**) thanks to the real-time activity dependent stimulation. *In vitro* and *ex vivo* models have both many advantages but lack the behavioral outcome that is needed to assess the quality of the neuroprosthetic approach. To overcome this limitation, in (Chapter 4) I describe the development of a reliable spike detection on a commercial, fully open-source system to perform activity dependent stimulation on behaving rodents or non-human primates. The main application of this activity dependent stimulation is to **retrain** the brain after a lesion. The reduced quality of the signals while the animal is moving or chewing are peculiar of these studies and are totally absent in the context of *in vitro* and *ex vivo* recordings. Therefore, increasing the specificity in the detection is crucial to improve the effectiveness of these kind of studies. Chapter 5 gives a perspective, related to human recordings by means of non-invasive techniques that we recently started in our lab. The last chapter provides a brief recap and the conclusion for this thesis (Conclusions).

# Chapter 1: State of the art of Neurotechnologies and applications

## Overview

Understanding how the brain works is probably the most exciting challenge of the XXI century. Uncovering the underlying mechanisms of the brain is so complex because of the interactions between elements at various spatial (from molecular to system level), temporal (from hundreds of µs of the molecular scale to days and years for development studies) and topological scales (from single node to the network as a whole (Figure 1.1).

To deal with this complexity, researchers are now using a multilevel approach involving many different branches of biology (molecular and cellular biology, genetics, biochemistry, etc.) but also physics, mathematics, engineering and related fields.

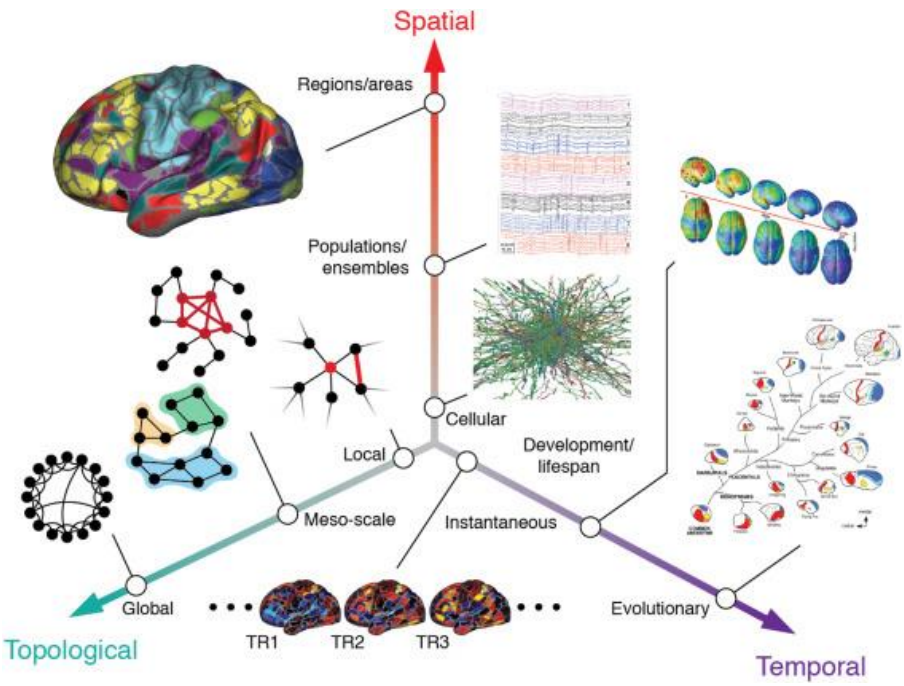


*Figure 1.1: The multi-scale brain in terms of Spatial, Temporal and Topological scales. From (Betzel and Bassett 2017)*

Indeed, advancing our understanding of brain function involves innovations in both the experimental methods, used to observe and perturb brain activity, but also in the computational tools used to analyze the recorded data. Nowadays many recording and perturbation techniques of the human brain are available. Depending on the research question, they differ in terms of temporal and spatial resolution, the invasiveness, the risk and the feasibility of human application.

Here we will give an overview of the most widely used and promising methods, highlighting pros and cons of each technique with respect to the others. First, we will list the main “reading” and “writing”

techniques with a small paragraph dedicated to the most innovative techniques. Then, we will present some of the main applications currently available both in clinical and preclinical practice. The last paragraph will focus on the main ethical issues related to the misuse of neurotechnologies.

## Techniques to interact with the brain

### *Reading the neural code*

First, we will give a brief historical overview of recording techniques. Then, we will divide the paragraph in terms of recording locations. We will list some of the main recording techniques from outside the skull (non-invasive techniques) and from inside the skull (invasive techniques, Figure 1.2). Within the invasive techniques paragraph, we will also include devices for *in vivo* recordings (in animal models) and *in vitro* recordings (considering extracellular recordings as part of the invasive techniques category).

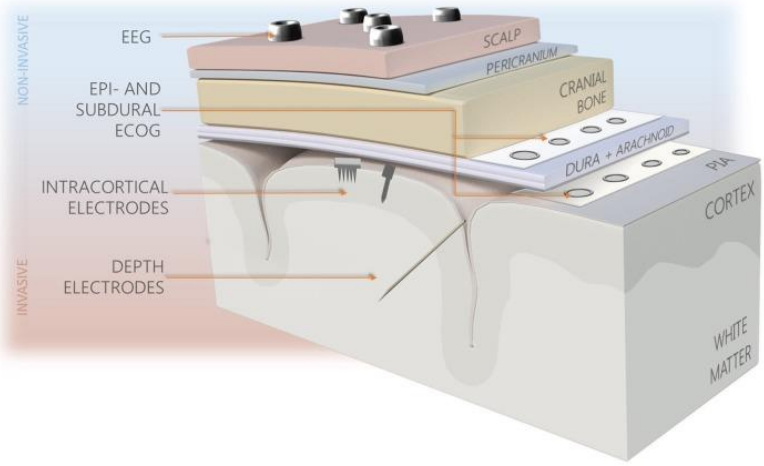


*Figure 1.2: Types of brain interfacing electrodes and their location in the reference to the brain. Less invasive systems (blue background) provide recordings of lower resolution in comparison to intracortically-implanted electrodes. from (Szostak et al. 2017).*

#### *Brief historical overview on brain recordings*

After the first intuitions attributed to the work of the Italian physician Luigi Aloisio Galvani (1737–1798), it took more than a century to have the first recording (Berger 1929) of electrical activity from the brain performed by a German psychiatrist: Hans Berger (1873-1941). Berger was inspired by the work done by Richard Caton (1842–1926) in England with animals like rabbits, dogs and monkeys. He performed the first encephalogram (EEG) recording on human brain and identified different oscillations present in both healthy and pathological (e.g. epileptic) brains. The number of electrodes for these pioneering works was limited to two and therefore the spatial resolution and the quality of recordings was low. Today commercial EEG systems can have up to 256 electrodes and many techniques have been developed to increase the spatial resolution of such method but the basic

principle of EEG is still the same. More than forty years after Berger's work, a new technique based on the magnetic fields was developed: magnetoencephalography (MEG) (Cohen 1972). Using MEG have different pros and cons when compared to EEG as we will discuss in the next paragraph. Both EEG and MEG are non-invasive techniques but different electrodes can be placed inside the skull to get signals closer to the neuronal sources. Electrocorticography (ECoG) and intracortical recordings are two ways of "reading" the neural code with higher signal to noise ratio and higher spatial resolution that non-invasive techniques. It is worth noticing that several techniques for functional brain imaging currently used in clinical practice like positron emission tomography (PET) and functional magnetic resonance imaging (fMRI) do not use electrical or magnetic fields to infer the brain activity (Raichle 2009).

The list of neurotechnologies to "read" the neural code is growing exponentially and many of them can be used not only to understand but also to interact in useful ways with the nervous system. Here we divided the list of reading neurotechnologies in devices that record from outside and from inside the skull (including extracellular recordings).

***Recording from outside the skull***

EEG (Electroencephalography)

EEG is a non-invasive, electrophysiological monitoring method to record electrical activity of the brain. Electrodes placed along the scalp allow to measure voltage fluctuation resulting from ionic current within the brain. To pick up electric fields from outside the skull, the activity needs to be coordinated in time and spatially organized. In particular, pyramidal neurons of the cortex are arranged in a parallel way and when active, intra- and extracellular currents flow; the longitudinal components of these currents add, whereas their transverse components cancel (da Silva 2013). The number of sources (generators of EEG activity) outnumbers the available sensors by several orders of magnitude and therefore the source reconstruction is an ill-posed inverse problem where a unique solution can only be obtained by making additional assumptions (Castaño-Candamil et al. 2015). EEG is probably the most widespread technique to record electrical activity in a non-invasive way and therefore many products are available on the market (Figure 1.3). Depending on the application, one can choose low-cost, low spatial resolution products like Neurosky (http://neurosky.com/biosensors/eeg-sensor/), Emotiv (https://www.emotiv.com/) and OpenBCI (https://openbci.com/) up to 16 electrodes as well as middle-price solutions (up to 64 channels) and high-price, high-density products (up to 256 channels, https://neurosoft.com/en/catalog/view/id/2623/sid/1).

*Figure 1.3: Representative EEG systems with a different number of electrodes. A, EMOTIV EPOC+ 14-Channel Wireless EEG Headset; B, R-net is available with 32, 64, 96 or 128 channels (brainproducts.com) C, 256-channels Quik-Cap Neo Net – SynAmps 2/RT and Neuvo (compumedicsneuroscan.com).*

MEG (Magnetoencephalography)

MEG is a non-invasive method to record magnetic field produced by electrical currents in the brain. To detect the weak magnetic fields induced by synchronized neuronal currents, arrays of SQUIDs (superconducting quantum interference devices) are currently used. The brain's magnetic field is 8-10 orders of magnitude smaller than the ambient magnetic noise in an urban environment, which is on the order of $10^{-4}$ T (Braeutigam 2013). The distortion due to the different electrical properties and complex geometry of the layers of tissue between neurons and electrodes has a stronger influence on the EEG than on MEG. Moreover, MEG is more sensitive to the primary intracellular currents while EEG reflects mainly extracellular currents (da Silva 2013). The main drawback of MEG when compared to EEG is related to the portability of the system. So far to get meaningful magnetic fields reflecting brain activity you needed a huge setup, where head movements can have devastating effects on the quality of data (Gross et al. 2013). A MEG system that can be worn on the head during movement was recently published (Boto et al. 2018) and can have disruptive effects on both research and clinical practice.

*Figure 1.4: Comparison between conventional and innovative MEG systems. Left: a conventional 275-channel cryogenic MEG system. Weighing ~450 kg the system is fixed and cumbersome and subjects must remain still relative to the fixed sensor array. Right, the portable MEG system helmet. The helmet weighs 905 g and is*

*customized such that the sensors (which in this prototype only cover right sensorimotor cortex) are directly adjacent to the scalp surface. The subject is free to move their head. adapted from (Boto et al. 2018)*

fMRI (functional Magnetic Resonance Imaging)

fMRI is an indirect way of measuring brain activity by detecting changes in blood flow. This technology was built on the earlier structural MRI brain scans after the discovery of the blood oxygenation level-dependent (BOLD) contrast in 1990 (Kim and Ogawa 2012). BOLD-contrast imaging, is based on the differences in magnetic properties of arterial (oxygen-rich) and venous (oxygen-poor, with deoxygenated hemoglobin that is paramagnetic) blood. A variety of studies ranging from task to resting state protocols and including memory, language, pain, learning and emotion take advantage of fMRI. Multimodal brain imaging such as EEG-fMRI aiming to achieve both high temporal and spatial resolution are rapidly evolving and are promising ways to get a complete picture of the human brain (Huster et al. 2012). The main drawback of fMRI is the huge and expensive scanner that limits its application to clinical environments. Moreover, is susceptible to movement artefacts (e.g., requires rigorous head stabilization) and it has a low temporal resolution (in the order of 0.5 Hz).

fNIRS (functional Near-Infrared Spectroscopy)

fNIRS has emerged as an alternative hemodynamic-based approach that possesses a number of strengths where fMRI is limited, most notably in portability and low-cost (Irani et al. 2007, Scarapicchia et al. 2017). It detects neural activity by measuring blood flow patterns revealed by changes in near-infrared light. Twenty devices are currently commercially available, with different numbers of channels (from 1 to 496) and sampling frequencies (1–100 Hz). The majority of them implement wireless data transmission and allow the synchronization of multiple devices (Pinti et al. 2018).

*Figure 1.5: a wearable fNIRS device equipped with fibers (LIGHTNIRS, Shimadzu, Japan) measuring over the motor cortices, where wires are connected to the control unit carried through a backpack (Photo courtesy of Shimadzu, Japan) adapted from (Pinti et al. 2018).*

***Recording from inside the skull***

ECoG (Electrocorticography)

ECoG or intracranial electroencephalography (iEEG), uses electrodes placed outside the dura mater (epidural) or under the dura mater (subdural). Avoiding the low conductivity of bone, ECoG spatial resolution is much higher than EEG. The subdural ECoG technique has been applied in the majority of clinical applications, such as identification of seizure foci (Luther et al. 2011), but it is associated with significant complications especially for long-term recordings. Epidural recordings can provide a good signal to noise ratio (no significant reduction when compared to subdural recordings) and lower risks when compared to subdural ECoG (Martens et al. 2014) and therefore can be considered one of the best solutions for very specific applications.

Extracellular electrodes

When placed closer to the cortical neurons, electrodes can record spikes of activity (extracellular recordings of the action potentials) and local field potentials. Intracortical electrodes can be: bundles of wires and Micro Electro-Mechanical Systems (MEMS) devices. Bundles of wires involve forming individual electrode wires into structures for intracortical study. MEMS devices include two main devices: the Michigan probe and the Utah array (Henderson 2015). Michigan arrays allow a higher density of sensors for implantation. They record signals along the length of the shank, rather than just at the ends of the shanks. Utah arrays are 3-D, consisting of 100 conductive silicon needles but signals can be detected only from the tips of each electrode, which limits the amount of information that can be obtained. One of the most successful projects using intracortical electrodes on humans, is the BrainGate (https://www.braingate.org/about-braingate/). They used Utah arrays implanted in the cortex and used to decode the intention to move a limb. Such probes consist of 96 fine tipped micro-electrodes in a compact 4×4 mm array (Figure 1.6).

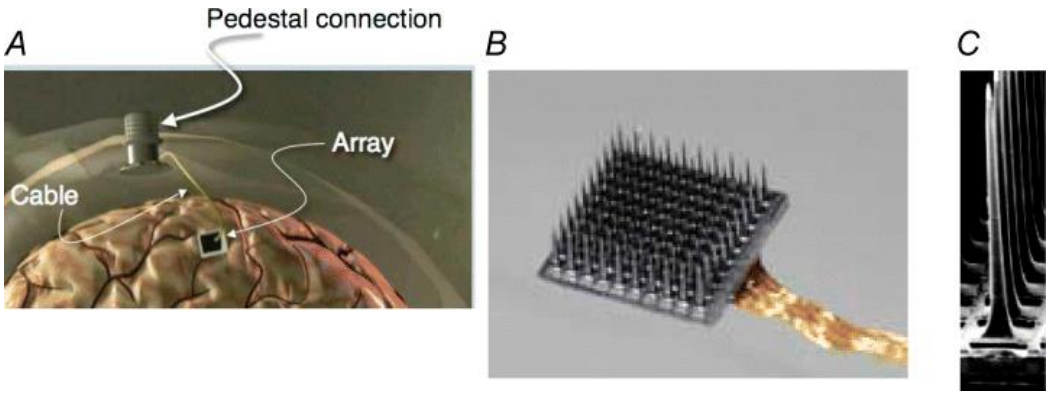


*Figure 1.6: A, parts of the implant include the array, skull mounted percutaneous pedestal, and a 96 wire cable that connects them. B, 10 × 10 array of electrodes, each separated by 400 µm. C, scanning electron micrograph one electrode showing its shape and pointed, platinum (Pt)-coated tip. from (Donoghue et al. 2007).*

The main problem related to intracortical electrode arrays regards their long-term viability. In some cases, implants seem to last for years, but in other cases, they become unusable after just a few months mainly because of immune responses (Henderson 2015). Researchers in the field of biocompatible materials are studying innovative solutions to prevent such immune responses thus allowing a larger use of such devices. Going deeper into the brain (usually in the sub thalamic nuclei) deep brain stimulation (DBS) is used to deliver electrical stimulation and reduce movement disorders.

In parallel with human studies, *in vivo* and *in vitro* studies can provide more freedom to the researchers working with neural interfaces.

*In vivo MEAs (Micro Electrode Arrays)*

Many electrodes are available with different layouts, different applications (Wise et al. 2008) and different features (e.g. capacitive interface (Schröder et al. 2015)), here we will focus on the novel high-density *in vivo* MEAs that were recently developed. Using CMOS technology (Gingerich et al. 2001), it is possible to achieve an incredible integration and thus allow to record from thousands of neurons at the same time. Nowadays, Neuropixels (Jun et al. 2017) is probably the most widespread fully-integrated silicon CMOS digital neural probe for research in small animals (usually rodents).

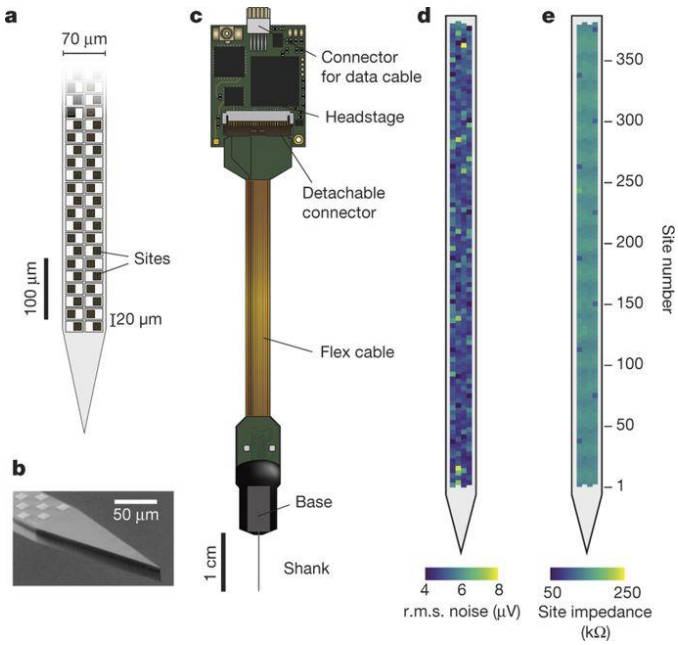


*Figure 1.7: a, Illustration of probe tip, showing checkerboard site layout (dark squares). b, Scanning electron microscope image of probe tip. c, Probe packaging, including flex cable and headstage for bidirectional data transmission. d, Example of r.m.s. noise levels of the AP band in saline, for 384 sites (switchable option). Mean ± s.d. = 5.1 ± 0.6 µV. e, Typical site impedance in saline, for 384 sites, measured for each site with sinusoidal 1 nA injected currents at 1 kHz (see Methods). Mean ± s.d. = 149 ± 6 kΩ. from (Jun et al. 2017).*

In a recent research (Stringer et al. 2018), eight Neuropixels probes where used to extract 2296, 2668, and 1462 units stable across ~1 hour of ongoing activity in three mice. They were able to

simultaneously record from frontal, sensorimotor, visual, and retrosplenial cortex, hippocampus, striatum, thalamus, and midbrain.

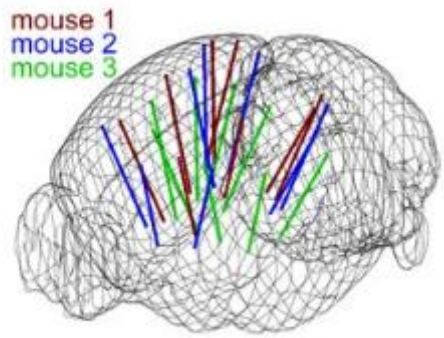


*Figure 1.8: Reconstructed probe locations of recordings in three mice from (Stringer et al. 2018).*

Other attempts to build high-density CMOS *in vivo* probes are the SiNAPS Active Pixel Sensor CMOS probe (Boi et al. 2019) and the NeuroSeeker project (Raducanu et al. 2016). All of these projects are investing in the creation of high-density technologies to better understand how the neural circuits work.

*In vitro MEAs (Micro Electrode Arrays)*

Non-implantable MEAs can be used to record and perturb neural networks *in vitro*. These arrays are usually coupled with cell cultures (from cortex, hippocampus, retina etc.) or acute brain slices (from mice or rats). In two of the projects described in this thesis, we used primary cell cultures and acute brain slices on MEAs to explore novel neuroprosthetic approaches (cf. Chapter 2 and Chapter 3).

The most used devices are MEA with 60 electrodes and many different layouts are available on the market depending on the application, with various electrode numbers and electrodes spacing (Figure 1.9).

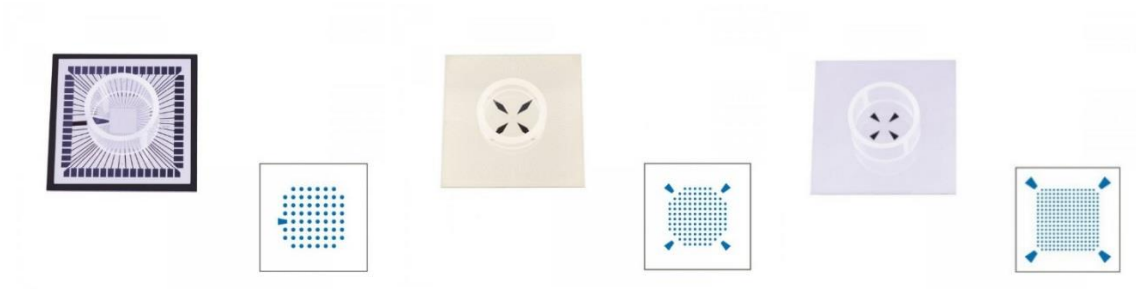

*Figure 1.9: different MEAs from left to right with 60, 120 and 256 respectively (Multichannel Systems Inc).*

In the last decade companies started to commercialize CMOS technology for *in vitro* application, similar to the one used for the *in vivo* application. With this technology, it is possible to simultaneously record from more than 4 thousands electrodes achieving single neuron precision which can be crucial

for understanding how the neural circuits work. Moreover, it is possible to deliver electrical stimulation and observe the propagation with a high spatial and temporal resolution.

*Figure 1.10: left CMOS-MEA (multichannelsystem.com), right HD-MEA Area (3brain.com)*

## *Writing the neural code*

### *Brief historical overview on brain stimulation*

Many researchers attribute to the roman physician Scribronius Largus the first hypothesis concerning the therapeutic power of electric stimulation (long before any knowledge of electricity existed) for alleviating headache and gout (Tsoucalas et al. 2014). He suggested that the live ray of an electric fish (*Torpedo nobiliana*) to the head of a patient suffering from a headache had a therapeutic effect (Schwalb and Hamani 2008). Many centuries had to pass before one could speak of a conscious use of electricity in medicine. The birth of modern electrophysiology is attributed to the work of the Italian physician Luigi Aloisio Galvani (1737–1798), a professor of medicine at the University of Bologna. His most famous observation was that the dissected leg of a dead frog kicked as if it were alive when touched with a metal scalpel bearing a charge (Guarnieri 2014). Such observation revealed the existence of a relationship between electricity and biological activity paving the way for all future electrophysiological studies.

In 1870 Gustav Fritsch and Edvard Hitzig showed that electrical stimulation of the cerebral cortex of a dog produced movements. As stated by Charles Gross in (Gross 2007): "*This was a crucial event in the development of modern neuroscience because it was the first good experimental evidence for a) cerebral cortex involvement in motor function, b) the electrical excitability of the cortex, c) topographic representation in the brain, and d) localization of function in different regions of the cerebral cortex*."

Four years later, Robert Bartholow published a work reporting the first experiment in which stimulating electrodes were used on a human cerebral cortex (Harris and Almerigi 2009). A fundamental contribution to this newborn research field was given by an American-Canadian neurosurgeon: Wilder Penfield (1891-1976). He invented a procedure (called "Montreal Procedure") in which he treated patients with severe epilepsy by destroying nerve cells in the seizure foci. Before operating, he observed the response of patients (under local anesthesia) when an electrical pulse was delivered to a particular location in the brain. In 1951 he published "Epilepsy and the Functional Anatomy of the Human Brain" (Penfield and Jasper 1954) where he described the discoveries he made with his colleague Herbert Jasper. He was the father of the cortical homunculus (Figure.11): a distorted representation of the human body, based on a neurological "map" of the areas and proportions of the human brain dedicated to processing motor and sensory functions, for different parts of the body.

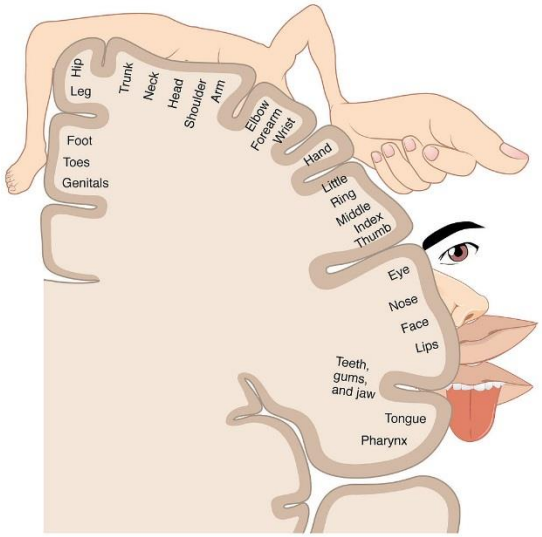


*Figure 1.11: A 2-D cortical sensory homunculus. From Wikipedia (en.wikipedia.org/wiki/Cortical_homunculus)*

From this landmark work, a huge series of experiments have been performed. Selimbeyoglu and Parvizi (Selimbeyoglu and Parvizi 2010) published a review of experiential phenomena and behavioral changes that are caused by electrical stimulation of the cerebral cortex (or subcortical nuclei) in awake and conscious human subjects in the last 100 years. They reported perceptual phenomena including: recall of past events, emotional feelings, sensory illusions, hallucinations, cessation of an ongoing behavior such as speech, spontaneous lip smacking and so on. Although giant steps have been made with respect to Penfield studies, there is still a multitude of scientific questions awaiting answers.

Here, similarly to the previous paragraph, we organized the list of stimulating techniques in: outside the skull (non-invasive) technologies and inside the skull (invasive) technologies.

***Stimulating from outside the skull***

The first successful transcranial electric stimulation (TES) was presented in (Merton and Morton 1980) by means of high-voltage electric stimuli through electrodes on the scalp. TES was a painful stimulation and was quickly replaced by painless techniques called Non-invasive Brain Stimulation (NIBS) (Bergmann et al. 2016). As reported in (Polania et al. 2018), the large variety of NIBS techniques cover a wide range of spatial and temporal resolution and the number of publications using NIBS is growing exponentially (Figure 1.12 panel B).

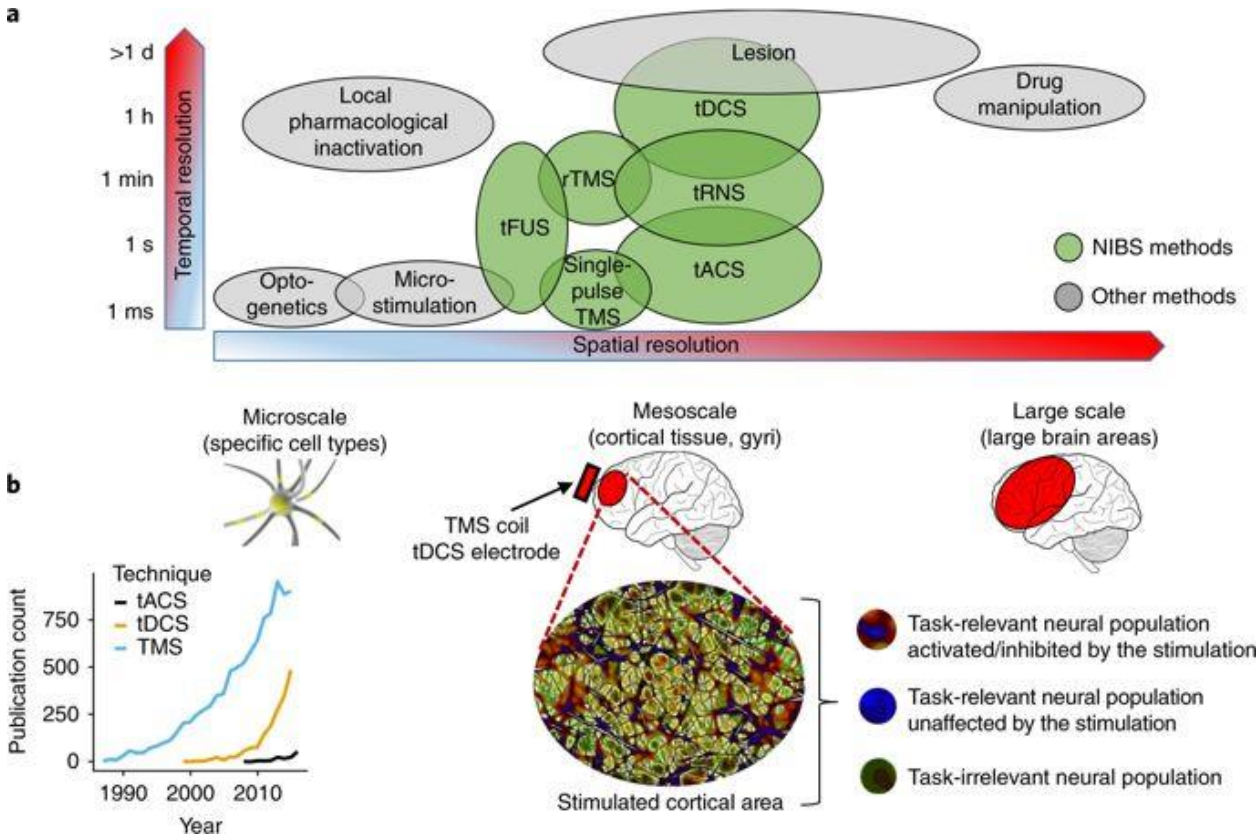


*Figure 1.12: a, The temporal and spatial resolution at which different causal brain interventions work. NIBS methods work at the mesoscale level, and the temporal resolution varies between high and low depending on the specific NIBS protocol. NIBS necessarily involves the relatively indiscriminate activation of large numbers of neurons; the apparent temporal and spatial specificity seen in NIBS studies is thus unlikely to reflect the anatomical and temporal specificity of the stimulation. Instead, it may indicate disruption of behaviorally relevant operations that are carried out by a relatively small number of cell groups within larger brain regions. b, The exponentially growing number of citations per year for TMS, tDCS and tACS (source: http://ncbi.nlm.nih.gov/pubmed/; search dates from 1980 to 2016). from (Polania et al. 2018).*

TMS (Transcranial Magnetic Stimulation)

In 1985 Barker and coworkers introduced TMS (Barker et al. 1985). TMS (supratreshold stimulation) can focally excite assemblies of neurons and thus is well suited to quantify excitability and connectivity, or to interfere with ongoing spontaneous or task-related neuronal activity (Siebner et al. 2009). TMS of the motor cortex leads to a twitch in the target muscle evoking motor-evoked potential (MEP) on electromyography and this is usually used to assess the corticospinal tract excitability (Klomjai et al. 2015). TMS can be applied as one stimulus at a time (single pulse), as trains of stimuli delivered at a fixed frequency (rTMS) or in combination with the actual brain state (Zrenner et al. 2018). Paired-pulse TMS consists of 2 successive pulses through the same coil, delivered with a short inter-stimulus interval (ISI) of a few milliseconds or a long ISI (from tens to hundreds of milliseconds) (Klomjai et al. 2015). Paired-pulse TMS can reveal inhibitory cortical networks more easily than excitatory networks, which are less investigated (Klomjai et al. 2015).

The effect of a repetitive TMS (rTMS) depends on stimulation frequency and duration of the stimulation period (Simonetta-Moreau 2014). It was reported that low-frequency stimulation (< 1 Hz) has inhibitory effects, whereas higher frequency stimulation (> 5 Hz) leads to excitatory effects in the brain (Klomjai et al. 2015). These protocols constitute the first step of non-invasive focal stimulation with possible potentiation effects on the human brain. An important improvement with respect to these studies consists in combining these protocols with the monitoring of the actual brain state which goes in the direction of personalized medicine (Zrenner et al. 2018).

tDCS (transcranial Direct Current Stimulation)

Fifteen years after the TMS, Nitsche and Paulus (Nitsche and Paulus 2000) introduced tDCS (subthreshold stimulation), the current flowing in the brain modulates the cellular excitability of resting neurons by changing the membrane voltage (transmembrane polarization) (Nitsche and Paulus 2000). Reported effects have been generally promising but heterogeneous (Reato et al. 2013). tDCS delivers low-amplitude direct currents to the brain via two surface sponge electrodes (anode and cathode) attached to distinct areas of the scalp with a rubber headband (Wagner et al. 2007). The temporal resolution of this technique is low: the neuromodulatory effects start to take place a few seconds after the start of the stimulation (Polania et al. 2018). Anodal and cathodal tDCS have been investigated in many studies with different results (Brückner and Kammer 2017), therefore further studies are needed to asses and understand the real efficacy of this devices.

tACS (transcranial Alternating Current Stimulation)

tACS (Antal et al. 2008) (subthreshold stimulation) induce alternated currents between the anode and the cathode (switching polarity) with a sinusoidal waveform. The predominant hypothesis of tACS action is that alternating fields can increase or decrease power of endogenous brain rhythms in the brain in a frequency-dependent manner by synchronizing or desynchronizing neuronal networks (Reato et al. 2013) and modulation of spike timing dependent plasticity (Vossen et al. 2015). For instance, tACS can be used to study the role of frontal gamma oscillations during logical reasoning (Santarnecchi et al. 2013), the role of beta and gamma frequencies in motor behavior (Joundi et al. 2012, Moisa et al. 2016) and many other roles of oscillations in the human brain. Despite these works, it is debated how tACS affects oscillatory activity in humans. One of the main limitations is due to technical complications with recording during the application of electrical field. Additional efforts need to be done in terms of artifact rejection methods in order to provide reliable recordings during tACS application (Noury and Siegel 2017).

tRNS (transcranial Random Noise Stimulation)

tRNS was introduced in 2008 (Terney et al. 2008) and consists in delivering a random electrical oscillation spectrum (instead of a sine wave as in tACS) over the motor cortex. It was reported an

enhancement of motor cortex excitability (lasting 60 minutes) after only 10 minutes of tRNS application (Terney et al. 2008). tRNS can be applied in the frequency range from 0.1 to 640 Hz offering a wide spectrum of investigation both in the low and high frequency ranges (Miniussi et al. 2013) but further studies need to be done.

As anticipated, the growing popularity of NIBS is accompanied by increasingly critical debates about their effective usefulness. A recent study (Vöröslakos et al. 2018) studied the real influence of transcranial electric stimulation on brain circuits. The authors reported that ~75% of scalp-applied currents are attenuated by soft tissue and skull and claimed that: "*neuronal circuits are instantaneously affected by intensity currents that are higher than those used in conventional protocols*". Indeed in clinical practice, currents larger than 2mA are avoided because higher intensities are associated with skin sensation, phosphenes, and other side effects (Nitsche and Bikson 2017). The same authors, in previous studies (Ozen et al. 2010, Berényi et al. 2012) showed that: "1 *mV/mm is needed to affect neuronal firing consistently and even larger strengths may be needed to phase-entrain brain rhythms to arbitrary stimulus frequencies*". In 2018 they demonstrated that scalp-applied currents should exceed 4–6 mA to achieve 1 mV/mm voltage gradient in brain tissue. They concluded that: "*behavioral and cognitive effects reported in previous tACS studies have likely been achieved by indirect mechanisms on brain activity, which needs to be explored in detail*". It is worth noting that different researches (Chhatbar et al. 2018, Ruhnau et al. 2018) showed an effect of tDCS detectable through DBS electrodes at the level of subthalamic nuclei. In (Chhatbar et al. 2018), the authors found that: "*the crude estimate of the generated electric field with 2 mA bitemporal tDCS was 0.12–0.13 mV/mm (and 0.19–0.26 mV/mm when 4mA were applied)";* these values are lower than 1 mV/mm as suggested by Buzsaki. Their criticism was related to the fact that the value of 1 mV/mm was based on rodent cortex patch clamp recordings *in vivo*, through a skull window, which may not be representative of human anatomy/physiology. Moreover, they claimed that there is a strong difference between pyramidal cells of the cortex (which typically remain silent) unlike neurons on subthalamic nuclei (which have a regular firing pattern irrespective of movements and can be more susceptible to even milder strengths of electric fields).

<u>tFUS (transcranial Focused Ultrasound Stimulation)</u>

tFUS was introduced in 2010 (Tufail et al. 2010) in a study on the mouse brain. It was reported a lateral spatial resolution of approximately 2 mm which is higher than the other transcranial electrical and magnetic stimulation methods. It was recently demonstrated on humans that tFUS targeted to the primary somatosensory cortex (S1) enhanced performance on sensory discrimination tasks without affecting task attention or response bias (Legon et al. 2014). This technique is growing in the last years and is one of the most promising techniques available now (Tyler et al. 2018).

***Stimulating from inside the skull***

DBS (Deep Brain Stimulation)

Nowadays DBS is the most widespread neuromodulation technique applied to drug-resistant patients with motor disorders (Parkinson's disease, dystonia and tremor) and it is tested and used in patients with obsessive-compulsive disorders, chronic pain, depression and epilepsy. To date, approximately 160,000 patients have been implanted at over 700 centers world-wide (Harmsen et al. 2018). However, the effect of DBS on brain networks remains unclear despite its use for almost 60 years. Moreover, specific features of the stimulus train (such as amplitude, frequency and temporal distribution) need to be tuned for a successful outcome. Optimal parameters often vary between patients and even for the same patient in time. Nowadays, research institutions and medical companies are attempting to create closed-loop adaptive DBS (cf. Neurotechnology applications, Rectify).

ICMS (Intra-Cortical Micro-Stimulation)

One of the first examples of ICMS dates back to 1972 in a work of Asanuma and Rosén (Asanuma and Rosen 1972). The authors inserted a microelectrode into the deep output layers and delivered low amplitude stimulation (activating excitatory pyramidal projection neurons in layer 5 of the motor cortex) producing contraction of contralateral distal forelimb muscles in a monkey. In contrast to surface stimulation, ICMS was confined to the hand area thus producing localized contractions. Starting from this work, ICMS became the gold standard to obtain motor maps. Recently ICMS was used in the framework of the development of neuroprosthesis used in the restoration of sensory and motor functions (Murphey et al. 2009, Guggenmos et al. 2013, Hussin et al. 2015).

## *Radically Innovative techniques*

Almost all the following techniques can be defined as innovative but all of them have pros and cons. In the last years, radically innovative techniques are trying to overcome some of the issues that limited the diffusion of neurotechnologies. Here we list some of the most promising.

***Endovascular recordings***

The main drawback related to ECoG or intracortical and deep brain recordings is related to the access to the brain, which requires invasive procedures, such as the removal of a portion of the skull or the drilling of a burr hole. To overcome these issues, one possible frontier is related to endovascular stents that can record cortical signals with a minimally-invasive interface (John et al. 2018). The endovascular neural interface, known as the StentrodeTM, was recently used to focally stimulate the sheep motor cortex in a minimally-invasive way (Opie et al. 2018) and is currently tested in an early feasibility study

in humans with loss of motor function due to paralysis from spinal cord injury, motor neuron disease, stroke, muscular dystrophy or loss of limbs (ClinicalTrials.gov Identifier: NCT03834857).

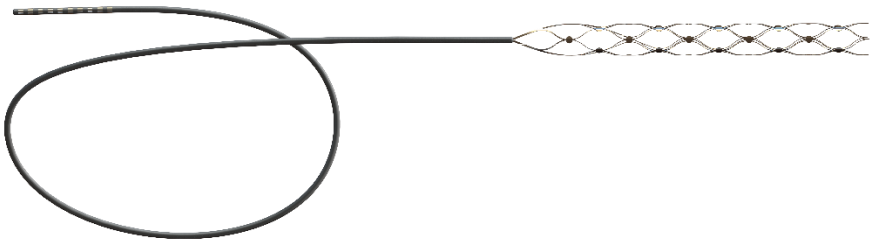

*Figure 1.13: StentrodeTM from (https://www.synchronmed.com/stentrode/)*

***Neural dust***

Among the most promising technologies for the future, the Neural dust is one of the most elegant. Neural dust is a wireless, battery-free, ultrasonic neural interface platform. Wireless power and communication are attractive features for next-generation neural interfaces. The technology was developed by scientists at the University of California, Berkeley and is now implemented by a start-up called Iota Biosciences (https://iota.bio/). Researchers validated the first version of a neural dust system *in vivo* in the rat peripheral nervous system (PNS) and skeletal muscle, reporting both electroneurogram (ENG) recordings from the sciatic nerve and electromyographic (EMG) recordings from the gastrocnemius muscle (Seo et al. 2016). Future developments seek to enable chronic recording, stimulation, and CNS delivery (Neely et al. 2018).

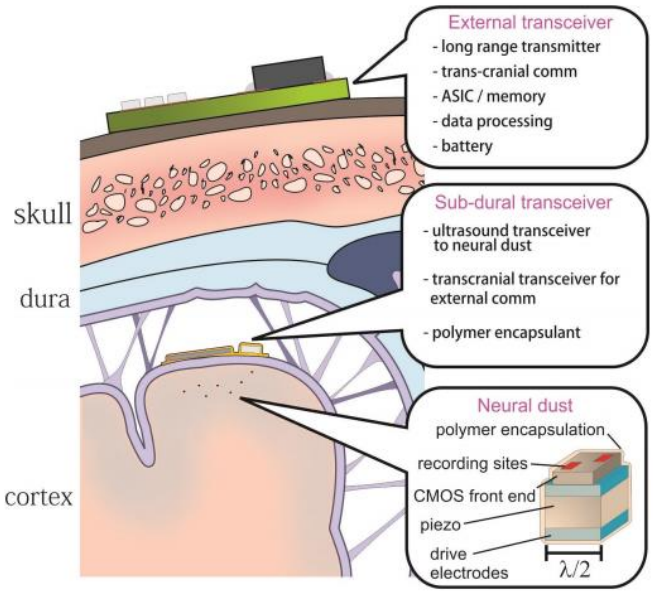


*Figure 1.14: Neural dust system diagram showing the placement of ultrasonic interrogator under the skull and the independent neural dust sensing nodes dispersed throughout the brain. From (Seo et al. 2013).*

***Neural lace***

Elon Musk recently founded Neuralink (https://www.neuralink.com/), a startup with ambitious goals related to Neurotechnology. In a white paper recently published by Musk and co-workers, they presented arrays of threads each much thinner than a hair, with as many as 3,072 electrodes per array distributed across 96 threads. Moreover, they presented a neurosurgical robot capable of inserting six threads together carrying 192 electrodes into a brain in one minute, avoiding blood vessels. Although less innovative than endovascular stents and neural dust, this project can have an immediate return of investment and will be tested soon on humans.

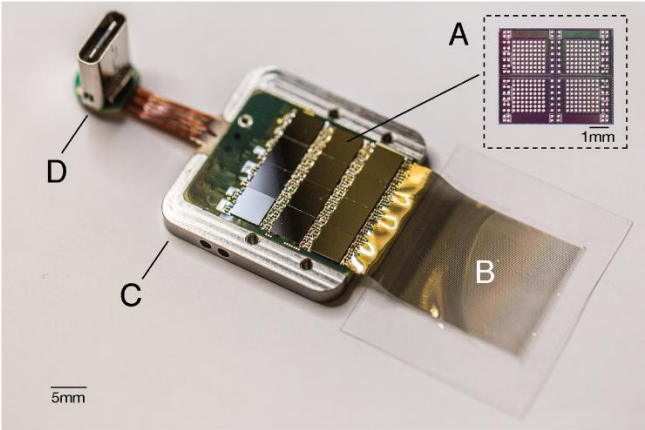


*Figure 1.15: A packaged sensor device. A. individual neural processing ASIC capable of processing 256 channels of data. This particular packaged device contains 12 of these chips for a total of 3,072 channels. B. Polymer threads on parylene-c substrate. C. Titanium enclosure (lid removed). D. Digital USB-C connector for power and data. from (Musk 2019).*

***Optogenetics***

Optogenetic technology combines optical technology for imaging and control living neural circuits that have been genetically modified to express light-sensitive ion channels (Deisseroth et al. 2006). Cells are injected with viruses containing microscopic opsin proteins that can be activated by light (Tye and Deisseroth 2012). The single cell resolution, high temporal precision and the possibility to excite or inhibit neuronal activity makes it one of the most promising tools to understand how the neural code works (Deisseroth 2015). Despite the obvious difficulties related to human applications, a small-scale, phase I/II clinical trial is currently underway (ClinicalTrials.gov NCT02556736). The goal is to render secondary and tertiary neurons of the retina light-sensitive in order to replace degenerate or dysfunctional photoreceptors in people with inherited retinal disease (Simunovic et al. 2019). Despite its presence since 2006, I decided to include this technique in this paragraph because I think that it can continue to grow in the coming years and can have (in the mid-term) disruptive effects on human applications.

***Sonogenetics***

One of the problems related to optogenetics is the current invasive surgical procedure to deliver light to target cells. An alternative solution, called Sonogenetics (Ibsen et al. 2015) can be a non-invasive way of manipulating vertebrate neurons. It uses ultrasound waves (range are above the normal threshold for human hearing but also that of bats and whales that use ultrasonic frequencies). The efficacy of sonogenetics was proved in (Ibsen et al. 2015), where it was applied in the nematode, *Caenorhabditis elegans* and was able to modify its locomotory behaviors.

Many other techniques, not listed here, are trying to conquer space in this field and they include but are not limited to: temporal interference of electric signals (Grossman et al. 2017), the use of magnetic nanoparticles excited through alternating magnetic fields (Chen et al. 2015), the use nanoparticles excited by near infrared stimulation (Chen et al. 2018).

## Neurotechnology applications

The classification of all the different applications in the field of Neurotechnology is complicated and the terminology can vary depending on the authors. Here I designed three mail classes based on the primary aim of each application:

- **Rectify**. In this category we will include all the systems aimed at stopping a pathological activity (e.g. tremor in motor disorders and epileptic seizures in epileptic patients)
- **Replace**. In this class we will include all the devices that aim to substitute or bypass a non functional circuit or part of the body.
- **Retrain**. Here we will include all the systems aimed at "helping the brain" to help itself taking advantage of the neuroplasticity.

In this paragraph, we will follow this classification but it worth noticing that the borderline among these classes is not always clear-cut. For instance, replacing and retraining the brain can overlap in many cases thanks to the incredible adaptability of the neural circuits to different environments and neural interfaces.

### *Rectify*

#### *Perturbing motor disorders*

As described in a previous paragraph, DBS provides symptomatic motor benefit for patients with essential tremor, dystonias and Parkinson's disease (Antonini et al. 2018). The common DBS operates in open-loop, delivering constant high-frequency stimulations with parameters that are manually set by a trained clinician. The main drawback of this approach is the delivery of a lot of energy not needed that can cause adverse effects such as dyskinesia (Habets et al. 2018). One possible solution is the so-called adaptive DBS (aDBS) in which the stimulation depends on the neural signals detected in real-time. In a recent work by Swann and co-workers (Habets et al. 2018), two patients with Parkinson's disease (PD) were implanted with a commercial system (Activa PC + S, Medtronic) an investigational implantable pulse generator (IPG) that allows chronic recording as well as stimulation. Reading the activity by means of ECoG over motor cortex in the gamma (60–90 Hz) range they were able to detect whether dyskinesia was likely. If the signal was high (suggesting dyskinesia was likely) stimulation in the ipsilateral subthalamic nucleus (STN) was reduced, and if it was low, stimulation was increased (Figure 1.16). In this way, they were able to reduce the adverse effect of DBS in STN.

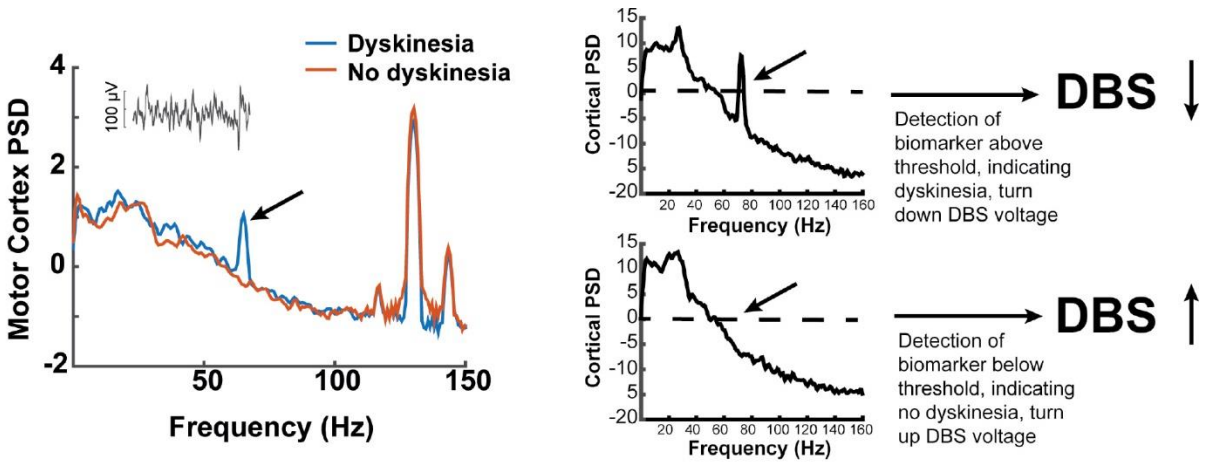


*Figure 1.16: Left, example of power spectral densities from motor cortex recorded with and without dyskinesia, both during DBS. Inset shows raw motor cortex signal when DBS was off. Black arrow indicates narrowband gamma signal used for feedback. Right, schematic of closed-loop algorithm. DBS voltage is decreased if narrowband gamma exceeds a threshold and increased when below the threshold. from (Habets et al. 2018)*

This is just one of the many papers in this field. There are various triggering options that are under investigation: subcortical recordings (STN Local Field Potentials) with repeated reports of correlation with rigidity and tremor and wearable sensors (accelerometer and gyroscope) correlated very well with tremor (Figure 1.17). For a complete overview refer to (Habets et al. 2018).

| Input signal vs. Parkinsonian symptoms | Correlation w/ tremor | Correlation w/ bradykinesia/ rigidity | Correlation w/ (freezing of) gait | Correlation w/ dyskinesia | Correlation w/ non-motor symptoms |
|---|---|---|---|---|---|
| Subcortical recordings (STN LFP) | repeated reports<br>small evidence<br>on debate<br>●●○ | repeated reports<br>reproduced evidence<br>starting consensus<br>●●● | first reports<br>small evidence<br>no consensus<br>●○○ | first reports<br>small evidence<br>no consensus<br>●○○ | first reports<br>no evidence<br>no consensus<br>◐○○ |
| Cortical recordings (ECoG) | first reports<br>no evidence<br>no consensus<br>◐○○ | repeated reports<br>reproduced evidence<br>starting consensus<br>●●● | not possible yet*<br>○○○ | first reports<br>small evidence<br>●○○ | not possible yet *<br>○○○ |
| Wearable sensors (accelerometer, gyroscope) | repeated reports<br>reproduced evidence<br>starting consensus<br>●●● | first reports<br>small evidence<br>no consensus<br>●○○ | first reports<br>small evidence<br>no consensus<br>●○○ | first reports<br>small evidence<br>no consensus<br>●○○ | not possible yet<br>○○○ |
| Mobile application | first reports<br>no evidence<br>no consensus<br>◐○○ | repeated reports<br>no evidence<br>no consensus<br>●○○ | first reports<br>no evidence<br>no consensus<br>◐○○ | first reports<br>no evidence<br>no consensus<br>◐○○ | repeated reports<br>small evidence<br>no consensus<br>●◐○ |

* In Parkinsonian patients, repeatedly reported with small evidence in other diseases.

*Figure 1.17: Overview of published evidence of the feasibility of different input signals regarding different parkinsonian symptoms for aDBS in PD. All input signals are scored on three categories per symptom. For each category 0, 0.5, or 1 bullet is given and the sum of them is visualized. The first line indicates the amount of publications: not possible yet (0), first reports (0.5), and repeated reports (1). The second line indicates the quality of reported evidence: no evidence (0), small evidence (0.5), and reproduced evidence (1). The third line indicates the amount of consensus on the use of an input signal for a symptom: no consensus (0), on debate (0.5), and starting consensus (1). from (Habets et al. 2018).*

All reported aDBS systems in PD until now are based on automatic amplitude modulation (AM) and can be summarized in three different ways (Habets et al. 2018) as depicted in figure 1.18:

- ON/OFF paradigm, that varies between periods during which stimulation is given with a predefined amplitude and a set frequency and pulse width, and periods during which stimulation is switched off
- Gradual paradigm, which increases or decreases stimulation amplitude stepwise when input signal exceeds or does not exceed a certain threshold respectively.
- Continuous paradigm, which modifies stimulation amplitude according to strength of input signal.

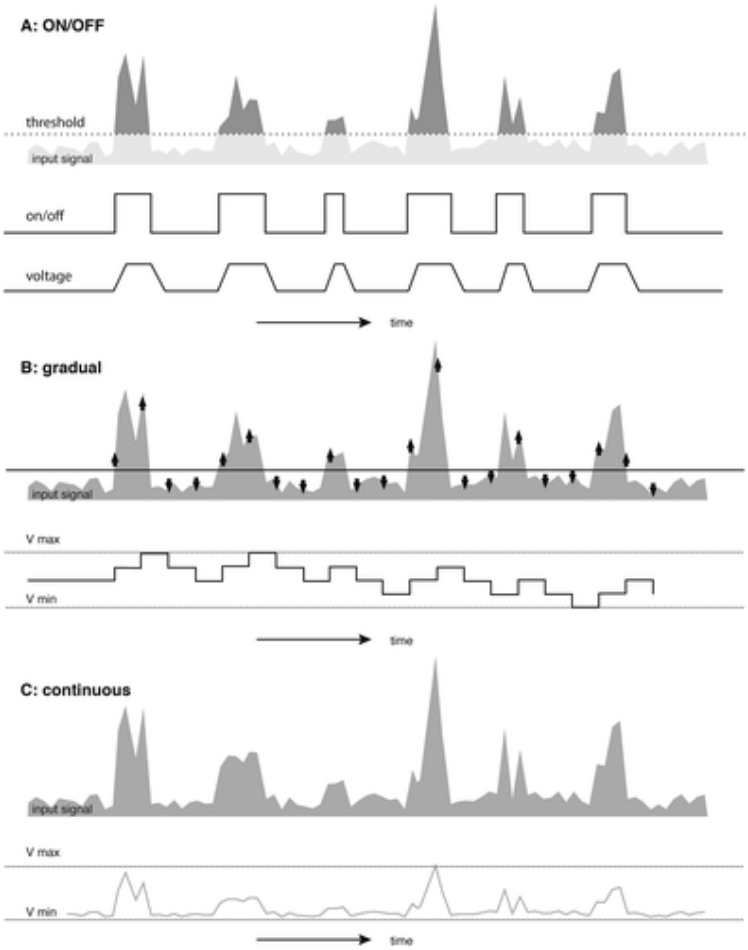


*Figure 1.18: Schematic overview of different amplitude modulation paradigms used in aDBS in PD. From (Habets et al. 2018).*

In a recent study (Arlotti et al. 2018), it was found that aDBS is technically feasible in everyday life and provides a safe, well-tolerated, and effective treatment in controlling PD motor symptoms.

***Perturbing epileptic seizures***

Epilepsy is a common neurologic disease, affecting 1,2% of the US population (Zack and Kobau 2017). It is characterized by abnormal synchronized firing of a large number of neurons, causing seizures or

periods of unusual behavior and sometimes loss of consciousness. Currently, anticonvulsant drug therapies are the most common approach to alleviate seizures, but unfortunately up to 30% of epilepsy patients do not respond to pharmacological treatment. Drug-resistant patients may be subjected to:

- resective surgery (if a seizure focus is localized).
- electrical stimulation (if there are multiple seizure foci, the focus cannot be localized, or when the seizure onset zone resides in a location that excludes a resective approach)

Responsive NeuroStimulation (RNS) system NeuroPace® was approved in the US for drug-resistant focal epilepsy in 2013. This system consists of an implanted stimulator connected to one or two subdural strips or depth leads, each containing four electrodes (Figure 1.19). These are placed at seizure foci and deliver a stimulation in response to detected ECoG patterns. The pattern recognition is programmed by the physician based on the patient's ictal ECoG patterns (Heck et al. 2014).

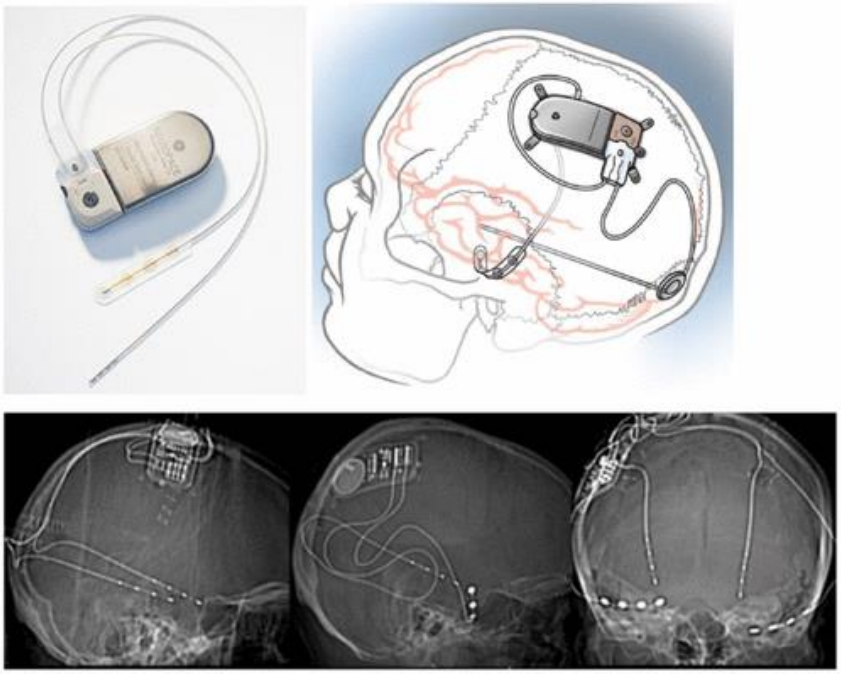

*Figure 1.19: Responsive neurostimulator (RNS): the top left image is the stimulator attached to subdural and depth electrodes; the top right diagram shows placement of the stimulator in the skull; the bottom three images are radiographic images of lead placement and wires. from (Hartshorn and Jobst 2018).*

To recognize an incoming seizure, different algorithms have been implemented in the RNS Neurostimulator. One of the simplest algorithms for the online detection of an ictal (or inter-ictal) event is the line-length algorithm based on the comparison between the short-term and long-term line length (Fitzpatrick 2014). The line-length is defined as the average of the absolute sample to sample difference within a time window. The area algorithm is similar to an energy or power measurement, comparing the area under curve in a short-term time window with a long-term time

window. The half-wave algorithm finds local minima and maxima and measures the distance between them and is thus representative of the frequency components of the signals (Luders 2008).

Another option available for epilepsy is the vagal nerve stimulator (VNS, LivaNova Inc., Houston, TX, USA), responsive to tachycardia. The rationale behind this input signal is the observation that both focal and generalized seizures are associated with tachycardia in up to 82% of patients (Eggleston et al. 2014).

## *Replace*

### *Hippocampal prosthesis*

Several diseases (e.g. Alzheimer's disease and age-related dementia), brain injuries and drugs can reduce memory in humans; therefore restoring memory function could have disruptive effects in the society. A group of researchers, led by Theodore W Berger (USC), is trying to solve the problem by means of neural electronics. The role of the human hippocampus in encoding and retrieval of retained information is known from more than 70 years (Scoville and Milner 1957). Many researchers studied the role of hippocampal CA1 and CA3 subfields but only few of them tried to restore memory by means of a bypass of the damage. In different studies that range from rodents (Berger et al. 2011), nonhuman primates (Hampson et al. 2013) and humans (Hampson et al. 2018), a prosthesis was used to facilitate memory encoding. In all these studies, a nonlinear multi-input, multi-output (MIMO) model (Song et al. 2015) of hippocampal CA3 and CA1 neural firing is computed. The model reads the activity of CA3 neurons and predicts activation patterns of CA1 neurons during a short-term memory task. Based on this prediction, electrical stimulation in different CA1 locations was proved to facilitate memory. These studies constitute the proof of principle that a memory prosthesis is feasible but much work needs to be done in order to see these procedure implanted in humans to have an effective memory restoration.

### *Cochlear implants*

Cochlear implants are surgically implanted devices that provide a sense of sound to people with a relevant hearing loss. They are the world's most widely used neuroprosthesis with more than 400k people using them (http://www.hearingreview.com). The implant consists of an external portion that sits behind the ear and a second portion that is surgically placed under the skin (Figure 1.20). An implant consists of:

- A microphone, which detects sound from the environment.
- A speech processor, which performs a signal processing.
- A transmitter and receiver/stimulator, which receive signals from the speech processor and convert them into electric impulses.
- An electrode array, which is a group of electrodes that collects the impulses from the stimulator and sends them to different regions of the auditory nerve.

It is worth noticing that an implant does not restore normal hearing but it can give a deaf person a useful representation of sounds in the environment (https://www.nidcd.nih.gov/health/cochlear-implants).

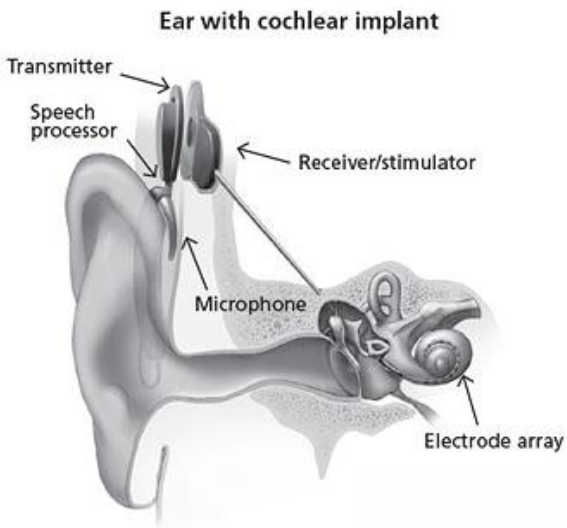


*Figure 1.20: Ear with cochlear implant Source: NIH/NIDCD from: [https://www.nidcd.nih.gov/health/cochlear-implants](https://www.nidcd.nih.gov/health/cochlear-implants)*

Different stimulating strategies are implemented in commercial cochlear implants but the main problem is related to the spatial resolution of the stimulation. The human ear has around 30,000 auditory nerve fibers, but only 16–22 electrodes can be implanted. This huge mismatch caused researchers to focus on innovative stimulation strategies to encode the spectrum of the sound with the highest resolution. For a complete review on monaural strategies, refer to (Wouters et al. 2015).

***Visual prosthesis***

Retinitis pigmentosa and age-related macular degeneration, can lead to loss of photoreceptor (PR) cells, while generally preserving the inner retinal neurons (Bloch et al. 2019). Recent advances in biotechnology have seen the first in-human trials, and in some cases market approval, of stem cell and gene therapies as well as retinal prostheses (Bloch et al. 2019).

The most widely used retinal prosthesis, with over 250 patients estimated to have undergone implantation to date (Bloch et al. 2019), is The Argus II prosthesis (Second Sight Medical Products Inc., Sylmar, CA, USA). The external components consists of a glasses-mounted camera linked to a portable visual processing unit, which processes the image for transmission to an external communication coil (also glasses mounted). The signal processing is crucial to reduce the complexity of the visual field to a set of features that are worth transmitting. This coil provides power induction and data transmission via wireless radiofrequency (RF) telemetry to an internal matching coil, which is fixed to the sclera with a silicone scleral buckle. Once received, the RF signal is decoded back to an electrical signal and an application-specific internal circuit (ASIC) sets the output command, which passes directly to the

intra-ocular retinal stimulator, comprising a 60-microelectrode array, each 200 µm in diameter, covering a 20° field of vision (Bloch et al. 2019).

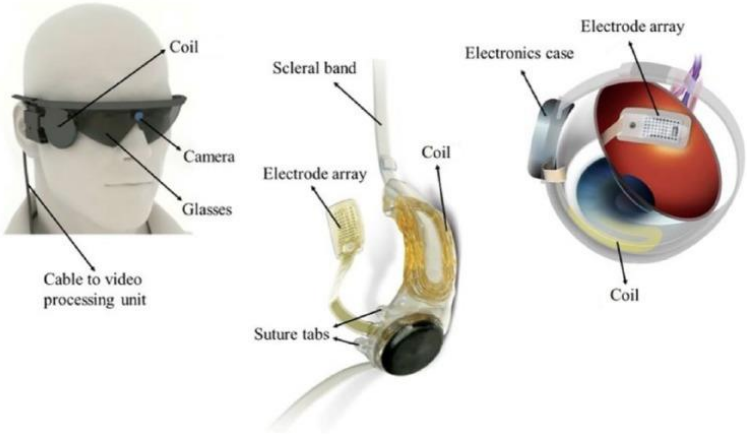


*Figure 1.21: The Argus II Retinal Prosthesis System. Adapted from Second Sight Medical Products, Inc., Sylmar, CA, USA from (Bloch et al. 2019).*

Other epiretinal prosthesis are: The Intelligent Retinal Implant System (IRIS) II and The EPI-RET3 Retinal Prosthesis System. For a complete review, refer to (Bloch et al. 2019).

A different class of devices, subretinal prosthesis are aimed at exploiting, the intrinsic signal processing capacity of the retinal interneurons with less demand for image processing. Examples of these innovative prosthesis are: The Boston Retinal Implant Project (BRIP), the artificial silicon retina by Optobionics (Glen Ellyn, IL, USA), The Alpha IMS, the photovoltaic Retinal Implant (PRIMA) Bionic Vision System. Some of these project are still active, some were acquired by medical companies but in general, the world of retinal prosthesis is very dynamic given that no single approach has yielded results that suggest a significant advantage over other systems (Bloch et al. 2019).

Recently, Second Sight Medical Products (the same company that developed the Argus II) announced the development and commercialization of its Orion Visual Cortical Prosthesis System. This prosthesis converts images captured by a similar setup with respect to the Argus II in electrical pulses delivered through an array of electrodes implanted on the surface of the brain's visual cortex. The goal in this case, is to provide the perception of patterns of light (https://eyewire.news/). Given the increasing electrode density, it is conceivable that this approach can have some mid-term success in many cases. For a complete list of visual prosthesis and clinical trials in which they are tested, refer to (Mirochnik and Pezaris 2019).

***Limb prosthesis***

Limb prostheses include both upper and lower-extremity prostheses. The upper limb prosthesis goal is to allow a fine control of the movements, usually by means of surface Electromyography (sEMG) that detects the intention to open and close, grasp objects etcetera (Cordella et al. 2016). On the other

side, a crucial aspect regarding limb prosthesis is the lack of sensory feedback. Many techniques have been developed so far: non-invasive sensory feedback systems such as mechanotactile (Schoepp et al. 2018), vibrotactile (Risi et al. 2019), electrotactile (Schweisfurth et al. 2016) and combinational systems but also invasive techniques both extraneural and intraneural electrodes (Svensson et al. 2017). In the last years, direct neural stimulation through transversal intrafascicular multichannel electrodes (Boretius et al. 2010) has enabled upper- and lower-limb amputees to feel touch sensations from the missing hand, knee motion and the sole of the foot touching the ground (Petrini et al. 2019). All these advancement require high performance signal processing, embedded on a device that needs to reliably work on the long-term to improve the quality of life of amputees.

***Extending the output capabilities of the nervous system, allowing it to control an external device***

In a complete review of control signals by Ramadan and Vasilakos (Ramadan and Vasilakos 2017) three different brain computer interfaces (BCI) definitions are listed:

- Donoghue (Donoghue 2002) defined the BCI as Brain Machine Interface (BMI) in which its major goal is to provide a command signal from the cortex that controls disabled body parts or physical devices, such as computers or robotic limbs.
- Wolpaw and co-workers (Wolpaw et al. 2002) defined the BCI as a device that provides the brain with a new, non-muscular communication and control channel.
- Schwartz and co-workers (Schwartz 2004) defined the BCI as "*Microelectrodes embedded chronically in the cerebral cortex hold promise for using neural activity to control devices with enough speed and agility to replace natural, animate movements in paralyzed individuals*."

Summing up, a Brain Computer Interface (BCI) can be defined as a communication device, which, by combining hardware and software, is capable of controlling an external agent such as a computer or robotic arm. Typical pathologies that can have a benefit from such an approach include amyotrophic lateral sclerosis (ALS), locked-in syndrome (LiS) and many others. In these cases, a direct reading of patient's intention to speak or move can be the key to improve their life and the communication with the external word.

In a recent paper (Anumanchipalli et al. 2019), ECoG signals were used to decode the kinematic and sound representations encoded in human cortical activity to synthesize audible speech. A bidirectional long short-term memory (bLSTM) recurrent neural network, decodes articulatory kinematic features from continuous neural activity (high-gamma amplitude envelope and low frequency component) recorded from ventral sensorimotor cortex, superior temporal gyrus and inferior frontal gyrus (Figure 1.22). A separate bLSTM, decodes acoustic features from the decoded articulatory features from the first stage. The decoded acoustic features are then used to synthesize the audio signal.

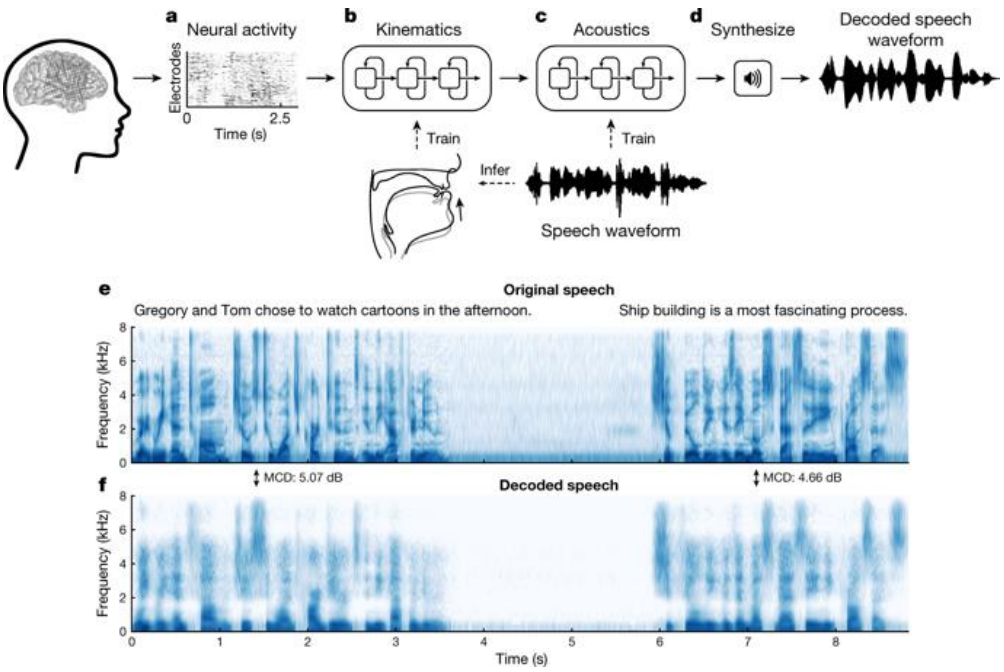


*Figure 1.22: a, The neural decoding process begins by extracting relevant signal features from high-density cortical activity. b, A bLSTM neural network decodes kinematic representations of articulation from ECoG signals. c, An additional bLSTM decodes acoustics from the previously decoded kinematics. Acoustics are spectral features extracted from the speech waveform. d, Decoded signals are synthesized into an acoustic waveform. e, Spectrogram shows the frequency content of two sentences spoken by a participant. f, Spectrogram of synthesized speech from brain signals recorded simultaneously with the speech in e (repeated five times with similar results). from (Anumanchipalli et al. 2019).*

This work advances the clinical viability of using speech neuroprosthetic technology to restore spoken communication for patients with paralysis and can be listed as one of the most promising speller BCI to date.

Controlling robots using signals acquired with intracortical implants is possible but is limited by the substantial amount of medical and surgical expertise required to correctly implant and operate these systems. A noninvasive approach (based on EEG recording, Figure 1.23) was recently able to control a 7-degree of freedom robotic arm for continuous random target tracking (Edelman et al. 2019). This work represents an example of the research interest towards the creation of non-invasive robotic arm control that can help patients with various types of paralysis.

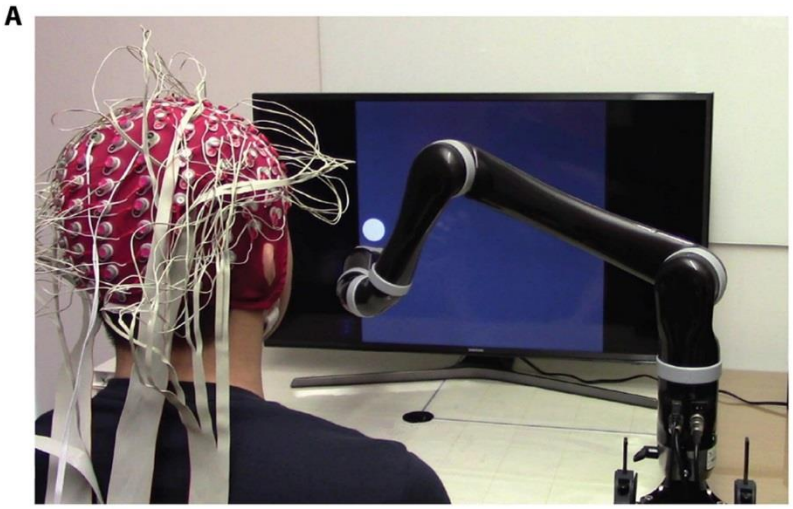


*Figure 1.23: Robotic arm CP BCI setup. Users controlled the 2D continuous movement of a 7–degree of freedom robotic arm to track a randomly moving target on a computer screen. from (Edelman et al. 2019).*

### *Retrain*

#### *Corticocortical prosthesis*

Taking advantage of neuroplasticity it is possible to imagine the use of neuroprosthesis aimed at retraining a damaged part of the brain (or spinal cord). Stroke and Traumatic brain injury are among the leading causes of disease (Peeters et al. 2015, Béjot et al. 2016) affecting the central nervous system. Here we list the few cases founded in literature that reported the efficacy of corticocortical stimulation to reconnect or retrain a part of the brain. All these studies, in accordance with Hebbian principles (Hebb 1949) regarding plasticity, can strengthen specific connections between neurons. The first report of long-term motor cortex plasticity induced by and electronic corticocortical prosthesis was presented by Jackson and coworkers (Jackson et al. 2006). In this work, they demonstrated that a stable reorganization of motor output could be induced by an artificial connection between two sites in the motor cortex of freely behaving primates. They developed an implantable electronic circuit (Neurochip) that detected action potentials on one site and delivered an intracortical microstimulation (ICMS) to another site (Figure 1.24). The implant was able to function continuously over days of unrestrained behavior.

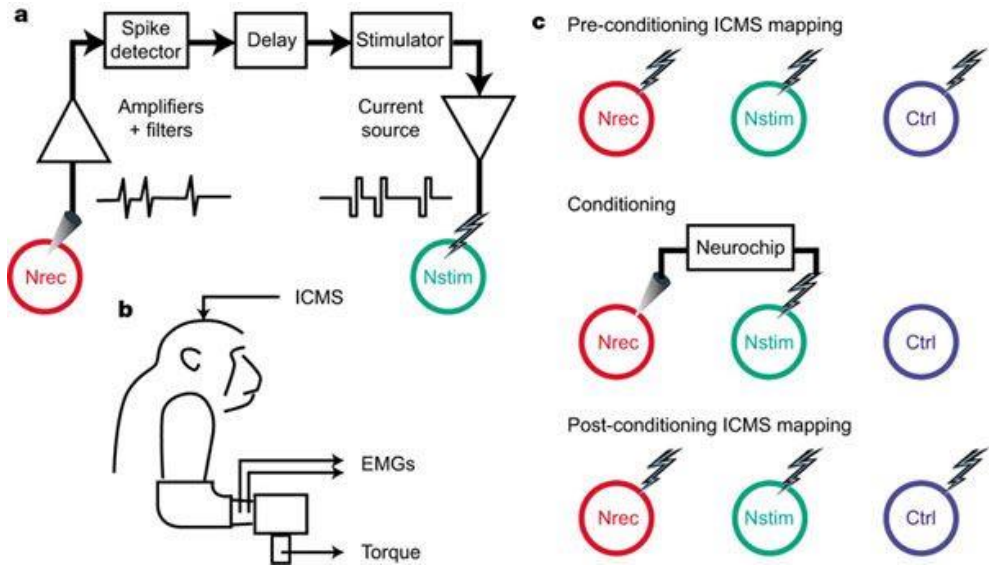


*Figure 1.24: a, Diagram of the artificial connection. Action potentials detected in the signal recorded from the Nrec (recording) electrode triggered electrical stimuli delivered to the Nstim (stimulating) electrode after a predefined delay. b, Experimental setup for testing output effects of ICMS on the right wrist. c, Experimental sequence of ICMS testing and conditioning with the Neurochip. from (Jackson et al. 2006).*

After one or more days of continuous operation, the output evoked from the recording site shifted to resemble the output from the corresponding stimulation site. Changes persisted in some cases for more than one week, whereas the output from sites not incorporated in the connection was unaffected (Jackson et al. 2006).

Starting from this work, many researchers tried to take advantage of synaptic plasticity at the cortical level by means of electrical stimulation. In 2013 Guggenmos and coworkers, used a similar strategy to speed-up the recovery in a rat model of traumatic brain injury (further details in Chapter 4).

In 2018, Zanos and coworkers (Zanos et al. 2018) demonstrated that electrical stimulation triggered from cortical beta oscillations induces synaptic plasticity. They also confirmed the importance of the oscillatory phase in determining the potentiation or depression effect of the stimulation. The effects of cycle-triggered stimulation in primate cortex were investigated under two conditions: intracellular recordings of evoked excitatory postsynaptic potentials (EPSPs) and epidural recordings of cortically evoked potentials (CEPs). For the latter, they used minimally invasive, epidural electrocorticography (ECoG) electrodes to record ECoG. The strength of their synaptic connections was measured by the size of the cortically evoked potentials (CEPs) evoked at the triggering site by test stimuli at the stimulated site. When closed-loop stimulation was triggered from a negative oscillatory potential at the triggering site (depolarizing-phase stimulation, DPS), the CEP responses to test stimuli following a conditioning burst were larger than those to test stimuli preceding the burst (Figure 1.25A, top). This occurred only for conditioning bursts with three or more consecutive cycle-triggered stimuli; bursts with two stimuli were typically not associated with significant changes in CEP amplitude. To control for the possibility that this potentiation could be due to the stimulation sequence itself they delivered an identical stimulation sequence in open-loop with no evidence for CEP amplitude potentiation (Figure 1.25A bottom). When triggering from the positive oscillatory potentials (hyperpolarizing phase stimulation, HPS), they observed depression of the CEP response following the conditioning burst (Figure 1.25B, top). This change was not present in open-loop control conditions (Figure 1.25B, bottom).

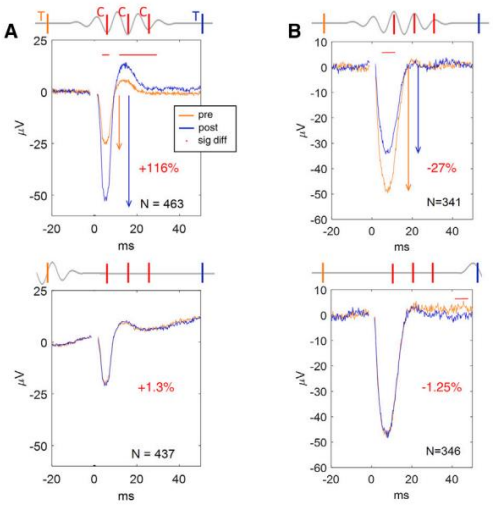


*Figure 1.25: (A) Depolarizing phase stimulation produces synaptic potentiation. Top: Conditioning stimulation was triggered from the negative (depolarizing) phase of oscillatory beta cycles (red vertical bars, C) and test stimuli (T) were delivered before (orange) and after (blue) conditioning episodes. Cortically evoked potentials*

*(CEPs) elicited by test stimuli were registered at the triggering site. Traces show the average CEP elicited by test stimuli preceding conditioning episodes with at least three cycle-triggered stimuli (orange) and the CEP elicited by test stimuli following the episodes (blue). The amplitude of the first component (downward arrows) of the post-conditioning CEP was 116% larger than that of the pre-conditioning CEP. See also Figure S3. Bottom: Delivering the same sequence of test and cycle-triggered stimuli at a later time in open-loop mode produced no significant changes in the CEP amplitude. (B) Hyperpolarizing phase stimulation produces synaptic depression. Top: Post-conditioning episode CEPs was 27% smaller than pre-conditioning episode CEPs. Bottom: No significant changes were seen in CEP amplitude in the control experiment. Red horizontal bars with asterisks indicate the portions of the CEP during which contiguous samples are significantly different in the pre- versus post-conditioning comparison (at the p = 0.001 confidence level). from (Zanos et al. 2018)*

Regarding the duration of the plasticity effect, they demonstrated that the potentiation effect (with DPS) lasted for up to 2 seconds after the end of conditioning, whereas the depression effect (after HPS) lasted up to 1.5 seconds. It is worth noticing that their results were limited to few seconds, meaning a short-term plasticity, and not long-term plasticity as in the works by Jackson and others (Kuba and Kumamoto 1990, Jackson et al. 2006) but are still relevant in the context of a possible rehabilitation paradigm.

Beyond work in animals, for applications such as stroke rehabilitation in humans, recent work has reported LTP-like motor plasticity using the negative μ-rhythm phase as trigger for a rTMS protocol (Zrenner et al. 2018). Zrenner and coworkers built a Simulink Real-Time model (Mathworks Ltd, USA, R2015a) to isolate the μ-oscillations (Figure 1.26). To overcome the algorithmic delays introduced by the FIR filters, they used and autoregressive model estimation to perform a 128 ms time-series forward-prediction in order to predict the actual phase of the signal (Zrenner et al. 2018). Based on this clever technique, they were able to deliver a stimulation based on an estimation of the actual brain state, providing a new way to control efficacy of plasticity induction in humans in a non-invasive way. The stimulation used was a 100 Hz TMS triplet triggered when a negative peak was estimated. It was delivered in M1 (orthogonal to the central sulcus) in a way that is considered highly effective in trans-synaptically activating the corticospinal neurons (Rossini et al. 2015).

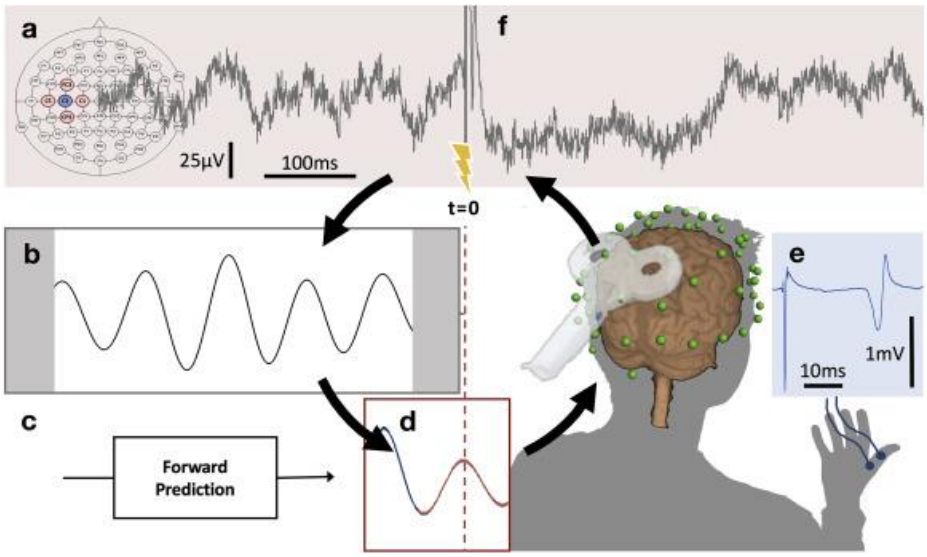


*Figure 1.26: µ-oscillation phase-triggered brain stimulation apparatus. (a) Scalp EEG raw data derived from a 5-point sum-of-difference operation centered on the C3 EEG electrode (Hjorth-C3) over left sensorimotor cortex is streamed to a real-time system with 3 ms latency where the processing algorithm is computed at a rate of 500 Hz. (b) A 500 ms sliding window of data is 8–12 Hz bandpass filtered forward and backward and edge artefacts (shaded) are removed. (c) Coefficients for an autoregressive model are calculated from the filtered data. (d) The signal is forward predicted (red trace), phase is estimated at time zero (t = 0) using a Hilbert transform and the TMS stimulator is triggered when a pre-set phase condition is met. (e) TMS of the hand area of left primary motor cortex produces a motor evoked potential (MEP) in right hand muscles recorded with surface EMG. (f) Recovery of the µ-oscillation ~300 ms after the TMS pulse. from (Zrenner et al. 2018)*

They reported an LTP-like increase in corticospinal excitability, while no change occurred if the same rTMS protocol was triggered at the low-excitability state, or at random µ-rhythm phase (Zrenner et al. 2018).

The rationale behind this study is the same of the studies on monkeys by Fets anz Zanos but, given its non-invasive approach, this can have a disruptive effect in clinical practice towards the development of a corticocortical prosthesis.

***Spinal cord injury prosthesis***

The World Health Organization (WHO) approximates that between 250,000 and 500,000 people suffer from a spinal cord injury (SCI) each year (Fehlings et al. 2017). As stated by Courtine (Courtine and Sofroniew 2019): "*a cure that could repair the injured spinal cord is unforeseeable, recent advances in biological and engineering strategies have opened promising avenues for improving function after SCI*". Starting from the observation that lateral hemisection of the spinal cord (Brown–Sequard syndrome) triggers reorganization of intraspinal (Takeoka et al. 2014), brainstem and corticospinal tract projection circuits (Hilton et al. 2016) that supports remarkable levels of spontaneous recovery (Friedli et al. 2015), researchers are trying to help such a spontaneous mechanism. This plasticity within the spinal cord leads to a remapping of motor cortex output to spinal circuits; therefore, motor cortex can play a crucial role after SCI. The research group led by Dr. Courtine is studying a strategy

that comprises both biological and technological approaches to improve functionality in people with SCI. On the biological side, to restore connectivity across spinal lesions researchers are focusing on stimulating endogenous axon regrowth through the lesions or grafting new neurons into lesions to re-establish communication through new relay circuits (Courtine and Sofroniew 2019). On the neurotechnological side, many options are available, each one with different pros and cons. After SCI, sensorimotor circuits embedded in the spinal cord lack the supraspinal sources of modulation and excitation essential for enabling their functionality. Starting from these observations, researchers implemented neuromodulation of circuits below and above the injury.

The figure below, from (Courtine and Sofroniew 2019), summarizes the main neurotechnological strategies related to SCI restoration therapies.

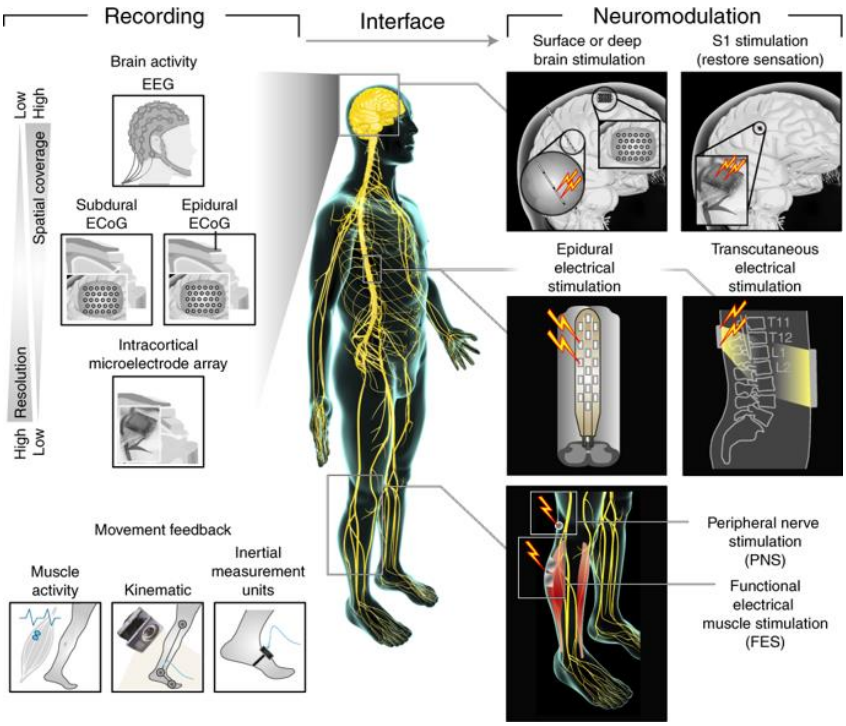


*Figure 1.27: Neurotechnological strategies related to SCI restoration therapies. From (Courtine and Sofroniew 2019).*

On the recording side, many options are available, such as:

- EEG, which is the less invasive but with the lower spatial resolution to record movement intention;
- ECoG (both Subdural and Epidural) with an higher spatial and temporal resolution but sometimes it is not enough to decode intention with high accuracy;
- intracortical microelectrode array, have the best spatio-temporal resolution (the easier decoding) accompanied by the highest risks (e.g. immune response);

On the neuromodulation side, other options with different aims are available such as:

- Surface or deep brain stimulation, which can help improving the functionality of the spinal cord after injury (Bachmann et al. 2013).
- Somatosensory cortex stimulation protocols, which allowed a paralyzed person to recognize pressure-like sensations in individual fingers of a robotic hand (Flesher et al. 2016).
- Epidural electrical stimulation over specific spinal cord locations with a precise timing (related to cortex activity), which was able to modulate the degree of leg extension and flexion in rats (Bonizzato et al. 2018) and non-human primate models of SCI (Capogrosso et al. 2016).
- Functional electrical muscle stimulation, which was used in a 24-year-old male with stable, non-spastic C5/C6 quadriplegia from cervical spinal cord injury (SCI) sustained in a diving accident 4 years previously conferring on him the critical abilities to grasp, manipulate, and release objects (Bouton et al. 2016). A similar proof-of-concept study was performed on a 53-year-old man with tetraplegia (cervical level 4) (Ajiboye et al. 2017).

Taken altogether, these evidences constitute the most promising applications of neuroprosthesis aimed at retraining the human body to bypass an injury and improve its functionality.

***Extending the input capabilities of the nervous system***

Few researchers so far presented augmentation studies where a sensory prosthesis was used to "*give the brain an additional sense*". In different works lead by the group of Nicolelis (Thomson et al. 2013, Hartmann et al. 2016) a microstimulation-based neuroprosthesis was used to discriminate among infrared (IR) light sources (Figure 1.28 A). They demonstrated that the adult mammalian neocortex can readily absorb completely new information sources into its representational repertoire, and use this information in the production of adaptive behaviors (Hartmann et al. 2016). Thirteen animals quickly learned to discriminate IR sources using the ICMS delivered to S1 in which the amplitude intensity of the IR signal was encoded in terms of stimulation frequency (Figure 1.28 C)

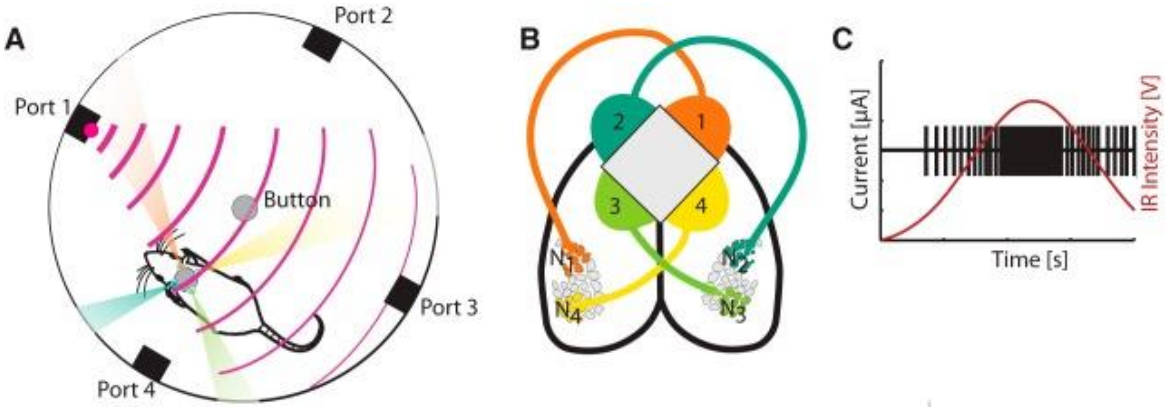


*Figure 1.28: Methods for rat IR discrimination training. A, Schematic of the behavioral chamber used for the task.B, Topographical organization of information from four IR detectors in rat S1. C, Stimulation frequency depended on IR intensity in each sensor. The intensity of each IR light was translated into different stimulation frequencies, in real time, in its corresponding stimulation channel. adapted from (Hartmann et al. 2016)*

These works can have important consequences both in basic neuroscience and in rehabilitation after a brain injury. It is worth noticing that so far, they used an invasive approach (ICMS) to convey precise spatio-temporal information to the brain but a non-invasive replication of these studies could open exciting avenues for the future.

## Ethical issues

In a recent Perspective, the Royal Society encouraged the development of a Neural Interface Ecosystem to accelerate the development of neural interfaces in the UK but also to use an "early and often" approach to address the ethical considerations in the field. It might take years of even decades until some of the Neurotechnologies presented here will be part of our daily lives but it is never too early to anticipate the possible ethical issues related to it. Possible futuristic misuse of neurotechnologies include:

- implanting fraudulent memories;
- control the behavior of a person;
- control the desires of a person;
- exacerbate social inequalities;
- reduce freedom;
- and many others

Excising ethics guidelines are insufficient (Yuste et al. 2017), given the exponential grow of neurotechnologies. Different documents deal with these issues, such as: the Declaration of Helsinki (Association 2014), the Belmont report (Health and Services 1979) and the Asilomar artificial intelligence statement of cautionary principles. The Morningside Group which included neuroscientists, neurotechnologists, clinicians, ethicists and machine-intelligence engineers, recently suggested four ethical priorities in this direction (Yuste et al. 2017). Regarding "privacy and consent", they suggested that citizens should have the ability to keep their neural data private and sale, commercial transfer and use of neural data should be strictly regulated. They also encouraged the use of blockchain techniques to avoid the need for a centralized authority and open-data formats to improve transparency (Yuste et al. 2017). Another critical point regards "identity". It was recently reported a case of a man treated with DBS for depression who said: "*It blurs to the point where I'm not sure ... frankly, who I am*". It is worth noting that DBS is still poorly understood and it may modulate aspects of personality and emotion (Klein et al. 2016). Therefore, protecting individual identity and the ability to choose our actions as basic human rights will be crucial in the near future. The authors of the declaration (Yuste et al. 2017) recommended adding clauses protecting such right (namely "neurorights") to international treaties, such as the Universal Declaration of Human Rights and others.

The “augmentation” is another point to study. Following what is happening for gene editing in humans (Scheufele et al. 2017), the authors (Yuste et al. 2017) recommended paying particular attention to the use of neurotechnologies for military purposes usually aimed at augmenting soldiers and analysts mental abilities for combat settings and data streams decoding. Regarding gender and racial bias, neurotechnologies, similarly to artificial intelligence can be prone to such discrimination and therefore it is crucial to pay particular attention to this problem for the near future.

Taken altogether, these considerations should be taken seriously by national and international associations but also by neuroscientist, in order to protect human rights.

## References


Ajiboye, A. B., F. R. Willett, D. R. Young, W. D. Memberg, B. A. Murphy, J. P. Miller, B. L. Walter, J. A. Sweet, H. A. Hoyen and M. W. Keith (2017). "Restoration of reaching and grasping movements through brain-controlled muscle stimulation in a person with tetraplegia: a proof-of-concept demonstration." The Lancet **389**(10081): 1821-1830.

Antal, A., K. Boros, C. Poreisz, L. Chaieb, D. Terney and W. Paulus (2008). "Comparatively weak after-effects of transcranial alternating current stimulation (tACS) on cortical excitability in humans." Brain stimulation **1**(2): 97-105.

Antonini, A., E. Moro, C. Godeiro and H. Reichmann (2018). "Medical and surgical management of advanced Parkinson's disease." Movement Disorders **33**(6): 900-908.

Anumanchipalli, G. K., J. Chartier and E. F. Chang (2019). "Speech synthesis from neural decoding of spoken sentences." Nature **568**(7753): 493.

Arlotti, M., S. Marceglia, G. Foffani, J. Volkmann, A. M. Lozano, E. Moro, F. Cogiamanian, M. Prenassi, T. Bocci and F. Cortese (2018). "Eight-hours adaptive deep brain stimulation in patients with Parkinson disease." Neurology **90**(11): e971-e976.

Asanuma, H. and I. Rosen (1972). "Topographical organization of cortical efferent zones projecting to distal forelimb muscles in the monkey." Experimental brain research **14**(3): 243-256.

Association, G. A. o. t. W. M. (2014). "World Medical Association Declaration of Helsinki: ethical principles for medical research involving human subjects." The Journal of the American College of Dentists **81**(3): 14.

Bachmann, L. C., A. Matis, N. T. Lindau, P. Felder, M. Gullo and M. E. Schwab (2013). "Deep brain stimulation of the midbrain locomotor region improves paretic hindlimb function after spinal cord injury in rats." Science translational medicine **5**(208): 208ra146-208ra146.

Barker, A. T., R. Jalinous and I. L. Freeston (1985). "Non-invasive magnetic stimulation of human motor cortex." The Lancet **325**(8437): 1106-1107.

Béjot, Y., H. Bailly, J. Durier and M. Giroud (2016). "Epidemiology of stroke in Europe and trends for the 21st century." La Presse Médicale **45**(12): e391-e398.

Berényi, A., M. Belluscio, D. Mao and G. Buzsáki (2012). "Closed-loop control of epilepsy by transcranial electrical stimulation." Science **337**(6095): 735-737.

Berger, H. (1929). "Über das elektrenkephalogramm des menschen." European archives of psychiatry and clinical neuroscience **87**(1): 527-570.

Berger, T. W., R. E. Hampson, D. Song, A. Goonawardena, V. Z. Marmarelis and S. A. Deadwyler (2011). "A cortical neural prosthesis for restoring and enhancing memory." Journal of neural engineering **8**(4): 046017.

Bergmann, T. O., A. Karabanov, G. Hartwigsen, A. Thielscher and H. R. Siebner (2016). "Combining non-invasive transcranial brain stimulation with neuroimaging and electrophysiology: current approaches and future perspectives." Neuroimage **140**: 4-19.

Betzel, R. F. and D. S. Bassett (2017). "Multi-scale brain networks." Neuroimage **160**: 73-83.

Bloch, E., Y. Luo and L. da Cruz (2019). "Advances in retinal prosthesis systems." Therapeutic advances in ophthalmology **11**: 2515841418817501.

Boi, F., N. Perentos, A. Lecomte, G. Schwesig, S. Zordan, A. Sirota, L. Berdondini and G. N. Angotzi (2019). "Multi-shanks SiNAPS Active Pixel Sensor CMOSprobe: 1024 simultaneously recording channels for high-density intracortical brain mapping." bioRxiv: 749911.

Bonizzato, M., G. Pidpruzhnykova, J. DiGiovanna, P. Shkorbatova, N. Pavlova, S. Micera and G. Courtine (2018). "Brain-controlled modulation of spinal circuits improves recovery from spinal cord injury." Nature communications **9**(1): 3015.

Boretius, T., J. Badia, A. Pascual-Font, M. Schuettler, X. Navarro, K. Yoshida and T. Stieglitz (2010). "A transverse intrafascicular multichannel electrode (TIME) to interface with the peripheral nerve." Biosensors and Bioelectronics **26**(1): 62-69.

Boto, E., N. Holmes, J. Leggett, G. Roberts, V. Shah, S. S. Meyer, L. D. Muñoz, K. J. Mullinger, T. M. Tierney and S. Bestmann (2018). "Moving magnetoencephalography towards real-world

applications with a wearable system." Nature **555**(7698): 657.
Bouton, C. E., A. Shaikhouni, N. V. Annetta, M. A. Bockbrader, D. A. Friedenberg, D. M. Nielson, G. Sharma, P. B. Sederberg, B. C. Glenn and W. J. Mysiw (2016). "Restoring cortical control of functional movement in a human with quadriplegia." Nature **533**(7602): 247.
Braeutigam, S. (2013). "Magnetoencephalography: fundamentals and established and emerging clinical applications in radiology." ISRN radiology **2013**.
Brückner, S. and T. Kammer (2017). "Both anodal and cathodal transcranial direct current stimulation improves semantic processing." Neuroscience **343**: 269-275.
Capogrosso, M., T. Milekovic, D. Borton, F. Wagner, E. M. Moraud, J.-B. Mignardot, N. Buse, J. Gandar, Q. Barraud and D. Xing (2016). "A brain–spine interface alleviating gait deficits after spinal cord injury in primates." Nature **539**(7628): 284.
Castaño-Candamil, S., J. Höhne, J.-D. Martínez-Vargas, X.-W. An, G. Castellanos-Domínguez and S. Haufe (2015). "Solving the EEG inverse problem based on space–time–frequency structured sparsity constraints." NeuroImage **118**: 598-612.
Chen, R., G. Romero, M. G. Christiansen, A. Mohr and P. Anikeeva (2015). "Wireless magnetothermal deep brain stimulation." Science **347**(6229): 1477-1480.
Chen, S., A. Z. Weitemier, X. Zeng, L. He, X. Wang, Y. Tao, A. J. Huang, Y. Hashimotodani, M. Kano and H. Iwasaki (2018). "Near-infrared deep brain stimulation via upconversion nanoparticle–mediated optogenetics." Science **359**(6376): 679-684.
Chhatbar, P. Y., S. A. Kautz, I. Takacs, N. C. Rowland, G. J. Revuelta, M. S. George, M. Bikson and W. Feng (2018). "Evidence of transcranial direct current stimulation-generated electric fields at subthalamic level in human brain in vivo." Brain stimulation **11**(4): 727-733.
Cohen, D. (1972). "Magnetoencephalography: detection of the brain's electrical activity with a superconducting magnetometer." Science **175**(4022): 664-666.
Cordella, F., A. L. Ciancio, R. Sacchetti, A. Davalli, A. G. Cutti, E. Guglielmelli and L. Zollo (2016). "Literature review on needs of upper limb prosthesis users." Frontiers in neuroscience **10**: 209.
Courtine, G. and M. V. Sofroniew (2019). "Spinal cord repair: advances in biology and technology." Nature medicine: 1.
da Silva, F. L. (2013). "EEG and MEG: relevance to neuroscience." Neuron **80**(5): 1112-1128.
Deisseroth, K. (2015). "Optogenetics: 10 years of microbial opsins in neuroscience." Nature neuroscience **18**(9): 1213.
Deisseroth, K., G. Feng, A. K. Majewska, G. Miesenböck, A. Ting and M. J. Schnitzer (2006). Next-generation optical technologies for illuminating genetically targeted brain circuits, Soc Neuroscience.
Donoghue, J. P. (2002). "Connecting cortex to machines: recent advances in brain interfaces." Nature neuroscience **5**(11s): 1085.
Donoghue, J. P., A. Nurmikko, M. Black and L. R. Hochberg (2007). "Assistive technology and robotic control using motor cortex ensemble-based neural interface systems in humans with tetraplegia." The Journal of physiology **579**(3): 603-611.
Edelman, B., J. Meng, D. Suma, C. Zurn, E. Nagarajan, B. Baxter, C. Cline and B. He (2019). "Noninvasive neuroimaging enhances continuous neural tracking for robotic device control." Science Robotics **4**(31): eaaw6844.
Eggleston, K. S., B. D. Olin and R. S. Fisher (2014). "Ictal tachycardia: the head–heart connection." Seizure **23**(7): 496-505.
Fehlings, M. G., L. A. Tetreault, J. R. Wilson, B. K. Kwon, A. S. Burns, A. R. Martin, G. Hawryluk and J. S. Harrop (2017). A clinical practice guideline for the management of acute spinal cord injury: introduction, rationale, and scope, SAGE Publications Sage CA: Los Angeles, CA.
Fitzpatrick, D. (2014). Implantable electronic medical devices, Elsevier.
Flesher, S. N., J. L. Collinger, S. T. Foldes, J. M. Weiss, J. E. Downey, E. C. Tyler-Kabara, S. J. Bensmaia, A. B. Schwartz, M. L. Boninger and R. A. Gaunt (2016). "Intracortical microstimulation of human somatosensory cortex." Science translational medicine: aaf8083.

Friedli, L., E. S. Rosenzweig, Q. Barraud, M. Schubert, N. Dominici, L. Awai, J. L. Nielson, P. Musienko, Y. Nout-Lomas and H. Zhong (2015). "Pronounced species divergence in corticospinal tract reorganization and functional recovery after lateralized spinal cord injury favors primates." Science translational medicine **7**(302): 302ra134-302ra134.

Gingerich, M. D., J. F. Hetke, D. J. Anderson and K. D. Wise (2001). A 256-site 3D CMOS microelectrode array for multipoint stimulation and recording in the central nervous system. Transducers' 01 Eurosensors XV, Springer**:** 416-419.

Gross, C. G. (2007). "The discovery of motor cortex and its background." Journal of the History of the Neurosciences **16**(3): 320-331.

Gross, J., S. Baillet, G. R. Barnes, R. N. Henson, A. Hillebrand, O. Jensen, K. Jerbi, V. Litvak, B. Maess and R. Oostenveld (2013). "Good practice for conducting and reporting MEG research." Neuroimage **65**: 349-363.

Grossman, N., D. Bono, N. Dedic, S. B. Kodandaramaiah, A. Rudenko, H.-J. Suk, A. M. Cassara, E. Neufeld, N. Kuster and L.-H. Tsai (2017). "Noninvasive deep brain stimulation via temporally interfering electric fields." Cell **169**(6): 1029-1041. e1016.

Guarnieri, M. (2014). "The Big Jump from the Legs of a Frog [Historical]." IEEE Industrial Electronics Magazine **8**(4): 59-61, 69.

Guggenmos, D. J., M. Azin, S. Barbay, J. D. Mahnken, C. Dunham, P. Mohseni and R. J. Nudo (2013). "Restoration of function after brain damage using a neural prosthesis." Proc Natl Acad Sci U S A **110**(52): 21177-21182.

Habets, J. G., M. Heijmans, M. L. Kuijf, M. L. Janssen, Y. Temel and P. L. Kubben (2018). "An update on adaptive deep brain stimulation in Parkinson's disease." Movement Disorders **33**(12): 1834-1843.

Hampson, R. E., D. Song, I. Opris, L. M. Santos, D. C. Shin, G. A. Gerhardt, V. Z. Marmarelis, T. W. Berger and S. A. Deadwyler (2013). "Facilitation of memory encoding in primate hippocampus by a neuroprosthesis that promotes task-specific neural firing." Journal of neural engineering **10**(6): 066013.

Hampson, R. E., D. Song, B. S. Robinson, D. Fetterhoff, A. S. Dakos, B. M. Roeder, X. She, R. T. Wicks, M. R. Witcher and D. E. Couture (2018). "Developing a hippocampal neural prosthetic to facilitate human memory encoding and recall." Journal of neural engineering **15**(3): 036014.

Harmsen, I. E., N. C. Rowland, R. A. Wennberg and A. M. Lozano (2018). "Characterizing the effects of deep brain stimulation with magnetoencephalography: a review." Brain stimulation **11**(3): 481-491.

Harris, L. J. and J. B. Almerigi (2009). "Probing the human brain with stimulating electrodes: the story of Roberts Bartholow's (1874) experiment on Mary Rafferty." Brain and cognition **70**(1): 92-115.

Hartmann, K., E. E. Thomson, I. Zea, R. Yun, P. Mullen, J. Canarick, A. Huh and M. A. Nicolelis (2016). "Embedding a panoramic representation of infrared light in the adult rat somatosensory cortex through a sensory neuroprosthesis." Journal of Neuroscience **36**(8): 2406-2424.

Hartshorn, A. and B. Jobst (2018). "Responsive brain stimulation in epilepsy." Therapeutic advances in chronic disease **9**(7): 135-142.

Health, U. D. o. and H. Services (1979). The belmont report.

Hebb, D. O. (1949). The organization of behavior: A neuropsychological approach, John Wiley & Sons.

Heck, C. N., D. King-Stephens, A. D. Massey, D. R. Nair, B. C. Jobst, G. L. Barkley, V. Salanova, A. J. Cole, M. C. Smith and R. P. Gwinn (2014). "Two-year seizure reduction in adults with medically intractable partial onset epilepsy treated with responsive neurostimulation: final results of the RNS System Pivotal trial." Epilepsia **55**(3): 432-441.

Henderson, P. (2015). Implanted intracortical electrodes as chronic neural interfaces to the central nervous system, PeerJ PrePrints.

Hilton, B. J., E. Anenberg, T. C. Harrison, J. D. Boyd, T. H. Murphy and W. Tetzlaff (2016). "Re-establishment of cortical motor output maps and spontaneous functional recovery via spared

dorsolaterally projecting corticospinal neurons after dorsal column spinal cord injury in adult mice." Journal of Neuroscience **36**(14): 4080-4092.

Hussin, A. T., J. A. Boychuk, A. R. Brown, Q. J. Pittman and G. C. Teskey (2015). "Intracortical microstimulation (ICMS) activates motor cortex layer 5 pyramidal neurons mainly transsynaptically." Brain stimulation **8**(4): 742-750.

Huster, R. J., S. Debener, T. Eichele and C. S. Herrmann (2012). "Methods for simultaneous EEG-fMRI: an introductory review." Journal of Neuroscience **32**(18): 6053-6060.

Ibsen, S., A. Tong, C. Schutt, S. Esener and S. H. Chalasani (2015). "Sonogenetics is a non-invasive approach to activating neurons in Caenorhabditis elegans." Nature communications **6**: 8264.

Irani, F., S. M. Platek, S. Bunce, A. C. Ruocco and D. Chute (2007). "Functional near infrared spectroscopy (fNIRS): an emerging neuroimaging technology with important applications for the study of brain disorders." The Clinical Neuropsychologist **21**(1): 9-37.

Jackson, A., J. Mavoori and E. E. Fetz (2006). "Long-term motor cortex plasticity induced by an electronic neural implant." Nature **444**: 56-60.

John, S. E., N. L. Opie, Y. T. Wong, G. S. Rind, S. M. Ronayne, G. Gerboni, S. H. Bauquier, T. J. O'Brien, C. N. May and D. B. Grayden (2018). "Signal quality of simultaneously recorded endovascular, subdural and epidural signals are comparable." Scientific reports **8**(1): 8427.

Joundi, R. A., N. Jenkinson, J.-S. Brittain, T. Z. Aziz and P. Brown (2012). "Driving oscillatory activity in the human cortex enhances motor performance." Current Biology **22**(5): 403-407.

Jun, J. J., N. A. Steinmetz, J. H. Siegle, D. J. Denman, M. Bauza, B. Barbarits, A. K. Lee, C. A. Anastassiou, A. Andrei, C. Aydin, M. Barbic, T. J. Blanche, V. Bonin, J. Couto, B. Dutta, S. L. Gratiy, D. A. Gutnisky, M. Hausser, B. Karsh, P. Ledochowitsch, C. M. Lopez, C. Mitelut, S. Musa, M. Okun, M. Pachitariu, J. Putzeys, P. D. Rich, C. Rossant, W. L. Sun, K. Svoboda, M. Carandini, K. D. Harris, C. Koch, J. O'Keefe and T. D. Harris (2017). "Fully integrated silicon probes for high-density recording of neural activity." Nature **551**(7679): 232-236.

Kim, S.-G. and S. Ogawa (2012). "Biophysical and physiological origins of blood oxygenation level-dependent fMRI signals." Journal of Cerebral Blood Flow & Metabolism **32**(7): 1188-1206.

Klein, E., S. Goering, J. Gagne, C. V. Shea, R. Franklin, S. Zorowitz, D. D. Dougherty and A. S. Widge (2016). "Brain-computer interface-based control of closed-loop brain stimulation: attitudes and ethical considerations." Brain-Computer Interfaces **3**(3): 140-148.

Klomjai, W., R. Katz and A. Lackmy-Vallée (2015). "Basic principles of transcranial magnetic stimulation (TMS) and repetitive TMS (rTMS)." Annals of physical and rehabilitation medicine **58**(4): 208-213.

Kuba, K. and E. Kumamoto (1990). "Long-term potentiations in vertebrate synapses: a variety of cascades with common subprocesses." Progress in neurobiology **34**(3): 197-269.

Legon, W., T. F. Sato, A. Opitz, J. Mueller, A. Barbour, A. Williams and W. J. Tyler (2014). "Transcranial focused ultrasound modulates the activity of primary somatosensory cortex in humans." Nature neuroscience **17**(2): 322.

Luders, H. O. (2008). Textbook of epilepsy surgery, CRC Press.

Luther, N., E. Rubens, N. Sethi, P. Kandula, D. R. Labar, C. Harden, K. Perrine, P. J. Christos, J. B. Iorgulescu and G. Lancman (2011). "The value of intraoperative electrocorticography in surgical decision making for temporal lobe epilepsy with normal MRI." Epilepsia **52**(5): 941-948.

Martens, S., M. Bensch, S. Halder, J. Hill, F. Nijboer, A. Ramos-Murguialday, B. Schoelkopf, N. Birbaumer and A. Gharabaghi (2014). "Epidural electrocorticography for monitoring of arousal in locked-in state." Frontiers in human neuroscience **8**: 861.

Merton, P. and H. Morton (1980). "Stimulation of the cerebral cortex in the intact human subject." Nature **285**(5762): 227.

Miniussi, C., J. A. Harris and M. Ruzzoli (2013). "Modelling non-invasive brain stimulation in cognitive neuroscience." Neuroscience & Biobehavioral Reviews **37**(8): 1702-1712.

Mirochnik, R. M. and J. S. Pezaris (2019). "Contemporary approaches to visual prostheses." Military Medical Research **6**(1): 1.

Moisa, M., R. Polania, M. Grueschow and C. C. Ruff (2016). "Brain network mechanisms underlying motor enhancement by transcranial entrainment of gamma oscillations." Journal of Neuroscience **36**(47): 12053-12065.

Murphey, D. K., J. H. Maunsell, M. S. Beauchamp and D. Yoshor (2009). "Perceiving electrical stimulation of identified human visual areas." Proceedings of the National Academy of Sciences **106**(13): 5389-5393.

Musk, E. (2019). "An integrated brain-machine interface platform with thousands of channels." BioRXiv: 703801.

Neely, R. M., D. K. Piech, S. R. Santacruz, M. M. Maharbiz and J. M. Carmena (2018). "Recent advances in neural dust: towards a neural interface platform." Current opinion in neurobiology **50**: 64-71.

Nitsche, M. A. and M. Bikson (2017). "Extending the parameter range for tDCS: safety and tolerability of 4 mA stimulation." Brain stimulation **10**(3): 541.

Nitsche, M. A. and W. Paulus (2000). "Excitability changes induced in the human motor cortex by weak transcranial direct current stimulation." The Journal of physiology **527**(3): 633-639.

Noury, N. and M. Siegel (2017). "Phase properties of transcranial electrical stimulation artifacts in electrophysiological recordings." Neuroimage **158**: 406-416.

Opie, N. L., S. E. John, G. S. Rind, S. M. Ronayne, Y. T. Wong, G. Gerboni, P. E. Yoo, T. J. Lovell, T. C. Scordas and S. L. Wilson (2018). "Focal stimulation of the sheep motor cortex with a chronically implanted minimally invasive electrode array mounted on an endovascular stent." Nature biomedical engineering **2**(12): 907.

Ozen, S., A. Sirota, M. A. Belluscio, C. A. Anastassiou, E. Stark, C. Koch and G. Buzsáki (2010). "Transcranial electric stimulation entrains cortical neuronal populations in rats." Journal of Neuroscience **30**(34): 11476-11485.

Peeters, W., R. van den Brande, S. Polinder, A. Brazinova, E. W. Steyerberg, H. F. Lingsma and A. I. Maas (2015). "Epidemiology of traumatic brain injury in Europe." Acta neurochirurgica **157**(10): 1683-1696.

Penfield, W. and H. Jasper (1954). "Epilepsy and the functional anatomy of the human brain."

Petrini, F. M., M. Bumbasirevic, G. Valle, V. Ilic, P. Mijović, P. Čvančara, F. Barberi, N. Katic, D. Bortolotti and D. Andreu (2019). "Sensory feedback restoration in leg amputees improves walking speed, metabolic cost and phantom pain." Nature medicine **25**(9): 1356-1363.

Pinti, P., C. Aichelburg, S. Gilbert, A. Hamilton, J. Hirsch, P. Burgess and I. Tachtsidis (2018). "A review on the use of wearable functional near-infrared spectroscopy in naturalistic environments." Japanese Psychological Research **60**(4): 347-373.

Polania, R., M. A. Nitsche and C. C. Ruff (2018). "Studying and modifying brain function with non-invasive brain stimulation." Nature neuroscience **21**(2): 174.

Raducanu, B. C., R. F. Yazicioglu, C. M. Lopez, M. Ballini, J. Putzeys, S. Wang, A. Andrei, M. Welkenhuysen, N. Van Helleputte and S. Musa (2016). Time multiplexed active neural probe with 678 parallel recording sites. 2016 46th European Solid-State Device Research Conference (ESSDERC), IEEE.

Raichle, M. E. (2009). "A brief history of human brain mapping." Trends in neurosciences **32**(2): 118-126.

Ramadan, R. A. and A. V. Vasilakos (2017). "Brain computer interface: control signals review." Neurocomputing **223**: 26-44.

Reato, D., A. Rahman, M. Bikson and L. C. Parra (2013). "Effects of weak transcranial alternating current stimulation on brain activity—a review of known mechanisms from animal studies." Frontiers in human neuroscience **7**: 687.

Risi, N., V. Shah, L. A. A. Mrotek, M. Casadio and R. A. Scheidt (2019). "Supplemental vibrotactile feedback of real-time limb position enhances precision of goal-directed reaching." Journal of neurophysiology.

Rossini, P. M., D. Burke, R. Chen, L. Cohen, Z. Daskalakis, R. Di Iorio, V. Di Lazzaro, F. Ferreri, P. Fitzgerald

and M. George (2015). "Non-invasive electrical and magnetic stimulation of the brain, spinal cord, roots and peripheral nerves: basic principles and procedures for routine clinical and research application. An updated report from an IFCN Committee." Clinical Neurophysiology **126**(6): 1071-1107.

Ruhnau, P., K. Rufener, H.-J. Heinze and T. Zaehle (2018). "Sailing in a sea of disbelief: in vivo measurements of transcranial electric stimulation in human subcortical structures." Brain Stimulation: Basic, Translational, and Clinical Research in Neuromodulation **11**(1): 241-243.

Santarnecchi, E., N. R. Polizzotto, M. Godone, F. Giovannelli, M. Feurra, L. Matzen, A. Rossi and S. Rossi (2013). "Frequency-dependent enhancement of fluid intelligence induced by transcranial oscillatory potentials." Current Biology **23**(15): 1449-1453.

Scarapicchia, V., C. Brown, C. Mayo and J. R. Gawryluk (2017). "Functional magnetic resonance imaging and functional near-infrared spectroscopy: insights from combined recording studies." Frontiers in human neuroscience **11**: 419.

Scheufele, D. A., M. A. Xenos, E. L. Howell, K. M. Rose, D. Brossard and B. W. Hardy (2017). "US attitudes on human genome editing." Science **357**(6351): 553-554.

Schoepp, K. R., M. R. Dawson, J. S. Schofield, J. P. Carey and J. S. Hebert (2018). "Design and integration of an inexpensive wearable mechanotactile feedback system for myoelectric prostheses." IEEE journal of translational engineering in health and medicine **6**: 1-11.

Schröder, S., C. Cecchetto, S. Keil, M. Mahmud, E. Brose, Ö. Dogan, G. Bertotti, D. Wolanski, B. Tillack and J. Schneidewind (2015). CMOS-compatible purely capacitive interfaces for high-density in-vivo recording from neural tissue. 2015 IEEE Biomedical Circuits and Systems Conference (BioCAS), IEEE.

Schwalb, J. M. and C. Hamani (2008). "The history and future of deep brain stimulation." Neurotherapeutics **5**(1): 3-13.

Schwartz, A. B. (2004). "Cortical neural prosthetics." Annu. Rev. Neurosci. **27**: 487-507.

Schweisfurth, M. A., M. Markovic, S. Dosen, F. Teich, B. Graimann and D. Farina (2016). "Electrotactile EMG feedback improves the control of prosthesis grasping force." Journal of neural engineering **13**(5): 056010.

Scoville, W. B. and B. Milner (1957). "Loss of recent memory after bilateral hippocampal lesions." Journal of neurology, neurosurgery, and psychiatry **20**(1): 11.

Selimbeyoglu, A. and J. Parvizi (2010). "Electrical stimulation of the human brain: perceptual and behavioral phenomena reported in the old and new literature." Frontiers in human neuroscience **4**: 46.

Seo, D., J. M. Carmena, J. M. Rabaey, E. Alon and M. M. Maharbiz (2013). "Neural dust: An ultrasonic, low power solution for chronic brain-machine interfaces." arXiv preprint arXiv:1307.2196.

Seo, D., R. M. Neely, K. Shen, U. Singhal, E. Alon, J. M. Rabaey, J. M. Carmena and M. M. Maharbiz (2016). "Wireless recording in the peripheral nervous system with ultrasonic neural dust." Neuron **91**(3): 529-539.

Siebner, H. R., G. Hartwigsen, T. Kassuba and J. C. Rothwell (2009). "How does transcranial magnetic stimulation modify neuronal activity in the brain? Implications for studies of cognition." Cortex **45**(9): 1035-1042.

Simonetta-Moreau, M. (2014). "Non-invasive brain stimulation (NIBS) and motor recovery after stroke." Annals of physical and rehabilitation medicine **57**(8): 530-542.

Simunovic, M., W. Shen, J. Lin, D. Protti, L. Lisowski and M. Gillies (2019). "Optogenetic approaches to vision restoration." Experimental eye research **178**: 15-26.

Song, D., B. S. Robinson, R. E. Hampson, V. Z. Marmarelis, S. A. Deadwyler and T. W. Berger (2015). Sparse generalized Volterra model of human hippocampal spike train transformation for memory prostheses. 2015 37th Annual International Conference of the IEEE Engineering in Medicine and Biology Society (EMBC), IEEE.

Stringer, C., M. Pachitariu, N. Steinmetz, C. B. Reddy, M. Carandini and K. D. Harris (2018). "Spontaneous behaviors drive multidimensional, brain-wide population activity." BioRxiv:

306019.
Svensson, P., U. Wijk, A. Björkman and C. Antfolk (2017). "A review of invasive and non-invasive sensory feedback in upper limb prostheses." Expert review of medical devices **14**(6): 439-447.
Szostak, K. M., L. Grand and T. G. Constandinou (2017). "Neural interfaces for intracortical recording: Requirements, fabrication methods, and characteristics." Frontiers in Neuroscience **11**: 665.
Takeoka, A., I. Vollenweider, G. Courtine and S. Arber (2014). "Muscle spindle feedback directs locomotor recovery and circuit reorganization after spinal cord injury." Cell **159**(7): 1626-1639.
Terney, D., L. Chaieb, V. Moliadze, A. Antal and W. Paulus (2008). "Increasing human brain excitability by transcranial high-frequency random noise stimulation." Journal of Neuroscience **28**(52): 14147-14155.
Thomson, E. E., R. Carra and M. A. Nicolelis (2013). "Perceiving invisible light through a somatosensory cortical prosthesis." Nature communications **4**: 1482.
Tsoucalas, G., M. Karamanou, M. Lymperi, V. Gennimata and G. Androutsos (2014). "The “torpedo” effect in medicine." International maritime health **65**(2): 65-67.
Tufail, Y., A. Matyushov, N. Baldwin, M. L. Tauchmann, J. Georges, A. Yoshihiro, S. I. H. Tillery and W. J. Tyler (2010). "Transcranial pulsed ultrasound stimulates intact brain circuits." Neuron **66**(5): 681-694.
Tye, K. M. and K. Deisseroth (2012). "Optogenetic investigation of neural circuits underlying brain disease in animal models." Nature Reviews Neuroscience **13**(4): 251.
Tyler, W. J., S. W. Lani and G. M. Hwang (2018). "Ultrasonic modulation of neural circuit activity." Current opinion in neurobiology **50**: 222-231.
Vöröslakos, M., Y. Takeuchi, K. Brinyiczki, T. Zombori, A. Oliva, A. Fernández-Ruiz, G. Kozák, Z. T. Kincses, B. Iványi and G. Buzsáki (2018). "Direct effects of transcranial electric stimulation on brain circuits in rats and humans." Nature communications **9**(1): 483.
Vossen, A., J. Gross and G. Thut (2015). "Alpha power increase after transcranial alternating current stimulation at alpha frequency (α-tACS) reflects plastic changes rather than entrainment." Brain stimulation **8**(3): 499-508.
Wagner, T., A. Valero-Cabre and A. Pascual-Leone (2007). "Noninvasive human brain stimulation." Annu. Rev. Biomed. Eng. **9**: 527-565.
Wise, K. D., A. M. Sodagar, Y. Yao, M. N. Gulari, G. E. Perlin and K. Najafi (2008). "Microelectrodes, microelectronics, and implantable neural microsystems." Proceedings of the IEEE **96**(7): 1184-1202.
Wolpaw, J. R., N. Birbaumer, D. J. McFarland, G. Pfurtscheller and T. M. Vaughan (2002). "Brain–computer interfaces for communication and control." Clinical neurophysiology **113**(6): 767-791.
Wouters, J., H. J. McDermott and T. Francart (2015). "Sound coding in cochlear implants: From electric pulses to hearing." IEEE Signal Processing Magazine **32**(2): 67-80.
Yuste, R., S. Goering, G. Bi, J. M. Carmena, A. Carter, J. J. Fins, P. Friesen, J. Gallant, J. E. Huggins and J. Illes (2017). "Four ethical priorities for neurotechnologies and AI." Nature News **551**(7679): 159.
Zack, M. M. and R. Kobau (2017). "National and state estimates of the numbers of adults and children with active epilepsy—United States, 2015." MMWR. Morbidity and mortality weekly report **66**(31): 821.
Zanos, S., I. Rembado, D. Chen and E. E. Fetz (2018). "Phase-locked stimulation during cortical beta oscillations produces bidirectional synaptic plasticity in awake monkeys." Current Biology **28**(16): 2515-2526. e2514.
Zrenner, C., D. Desideri, P. Belardinelli and U. Ziemann (2018). "Real-time EEG-defined excitability states determine efficacy of TMS-induced plasticity in human motor cortex." Brain stimulation **11**(2): 374-389.

# Chapter 2: Replace: *in vitro* neuroprosthesis

## Overview

One of the greatest challenges of modern neuroscience is to find reliable and sustainable treatments for the disabling effects caused by many chronic and incurable brain conditions. With the greatest impact carried by stroke (Feigin et al. 2017) and traumatic brain injury (Maas et al. 2017), brain disorders are among the leading causes of disabilities worldwide. One of the most peculiar properties of the brain is the capability to exploit plasticity to allow performing cognitive or motor task even when there is a damage. This is because the brain is redundant and intrinsically modular, being composed of local networks that are embedded in networks of networks (Meunier et al. 2009), sparsely connected to each other (Levy et al. 2012): the connections can reorganize bypassing the damage or reinforcing weak connections (Nudo 1999, Guggenmos et al. 2013).

Indeed, understanding the intricacy of brain signals, what is the effect of a damage on signal generation (Bassett and Bullmore 2009), and how this impacts on the electrophysiological behavior of brain networks and on their reorganization, has a twofold importance: from one side it is necessary in order to shape suitable intervention strategies (Kleim and Jones 2008) based on novel bioelectronic devices (Guggenmos et al. 2013); from the other side it will help in designing novel 'neurobiohybrid' technologies (Vassanelli and Mahmud 2016) which can exploit the brain self-repair capability in case of a damage. To reach the above goals it is fundamental to deeply characterize and understand how a damage affects the electrophysiological behavior of a network.

Within this framework, simplified *in vitro* models of cell assemblies can provide useful insights to investigate the interactions between networks of neurons, both in physiological and in pathological conditions. *In vitro* systems, by overcoming the limits of *in vivo* models imposed by the complexity of the surrounding networks and by the consequent low level of reproducibility, can thus serve as test bed for innovative solutions ranging from neuropharmacological to electroceutical applications (Tessadori et al. 2012, Bonifazi et al. 2013, Colombi et al. 2013). Moreover, in silico models, either software or hardware, of the electrophysiological behavior of such reduced networks can be used to replace neuronal functionalities in the framework of novel neuroprosthetic devices.

In this chapter, I will briefly introduce cell cultures with a particular focus on cell cultures plated over micro-electrode arrays (MEA). I will then introduce the BrainBow project, a European project aimed at creating an innovative neuroprosthesis to be tested on cell cultures over MEAs. I will describe the

methods used and the result obtained, together with a final discussion and conclusion. Large part of this chapter, related to the BrainBow project, is part of the following publications:

- Buccelli S, Bornat Y, Colombi I, Ambroise M, Martines L, Pasquale V, Bisio M, Tessadori J, Nowak P, Grassia F, Averna A, Tedesco M, Bonifazi P, Difato F, Massobrio P, Levi T, Chiappalone M. A neuroprosthetic system to restore neuronal communication in modular networks. iScience (2019). Vol 19, P402-414. Doi: https://doi.org/10.1016/j.isci.2019.07.046
- Averna A, Caré M, Buccelli S, Semprini M, Difato F and Chiappalone M. A multimodular system to study the impact of a focal lesion in neuronal cell cultures. Lecture Notes in Computer Science (2019), 11705, pp. 5--19, 2019. Doi: https://doi.org/10.1007/978-3-030-28042-0_1

## *In vitro* cultures

### *In vitro development*

In the early 1900s scientists explored the possibility, until then relegated to science fiction, of culturing and growing neural cells under controlled conditions (Carrel and T BURROWS 1910, Harrison 1912). These pioneering works have brought a growing interest in the study of cell cultures outside the body (Peterson and Murray 1955, Nakai and Kawasaki 1959).

We can divide *in vitro* cultures in two main categories: cell lines and primary cultures. Cell lines are mostly derived from tumor cells (Giard et al. 1973, Liu et al. 2017). These cells express a reasonably stable phenotype and can be sub-cultured repeatedly being highly proliferative. Primary cultures, on the other hand, derive from cells taken directly from the animal. Primary neuronal cell cultures can be an ideal model for investigating interconnected neurons for different purposes ranging from neuropharmacological tests to improvements in bioelectronics interfaces. These cultures retain some of the physiological characteristics of *in vivo* neurons in a highly controlled environment. Under favorable conditions, it is possible to maintain such cultures for months, thus making them an ideal tool for basic research. The most widespread protocol for culturing primary cultures of neurons involves the dissection of specific regions of the brain, such as the hippocampus or cortex, from young rats (or mice), either embryonic or neo–natal. The main drawback is that they have a limited expansion capacity, and thus for every preparation one animal has to be sacrificed.

In the last years, neurons derived from human induced Pluripotent Stem Cells (hiPSCs) have emerged as a promising tool (Zhang et al. 2001). The greatest advantage in using this new technique lies in the possible translation of results obtained *in vitro* to humans (Frega et al. 2017). Many protocols for differentiating hiPSCs into neurons have been developed (Frega et al. 2017), each one with different pros and cons. The main drawback of such cultures is that they require more time for differentiation with respect to rodent cell cultures. In the near future, it is easy to imagine that this type of preparation can replace animal cell cultures for many applications but currently, rodent cell cultures still have many advantages and therefore were used in the present work.

Despite their simplicity, neuronal networks represent an excellent *in vitro* model used in many fields of neuroscience. Potter and DeMarse (Potter and DeMarse 2001) demonstrated that cultures on MEAs can survive for over a year *in vitro* which makes these preparations ideal for a large number of applications. Several factors must be taken in account when studying cell cultures: i) the animal model (e.g. mouse, rat or even human-derived cells can be very different); ii) the brain region from which

you take neurons (e.g. hippocampus, cortex etc.); iii) the cell density (which affects the network connectivity); iv) the environment (e.g. the medium composition and temperature can affect the system). All of these characteristics are not static but evolve over time due to the maturation processes of neurons and networks (Chiappalone et al. 2006)

To characterize and understand changes in morphological and electrophysiological aspects of neuronal networks several techniques can be used: from immunostaining to calcium imaging, from single cell patch clamp to multisite multi-site electrophysiological techniques. All these techniques have different purposes and all of them are needed to understand the brain a step at the time.

As described in (Ben-Ari 2001), during different phases of development there is a sequence of events that are needed to form a functional network connectivity and thus a healthy electrical activity (Figure 2.1).

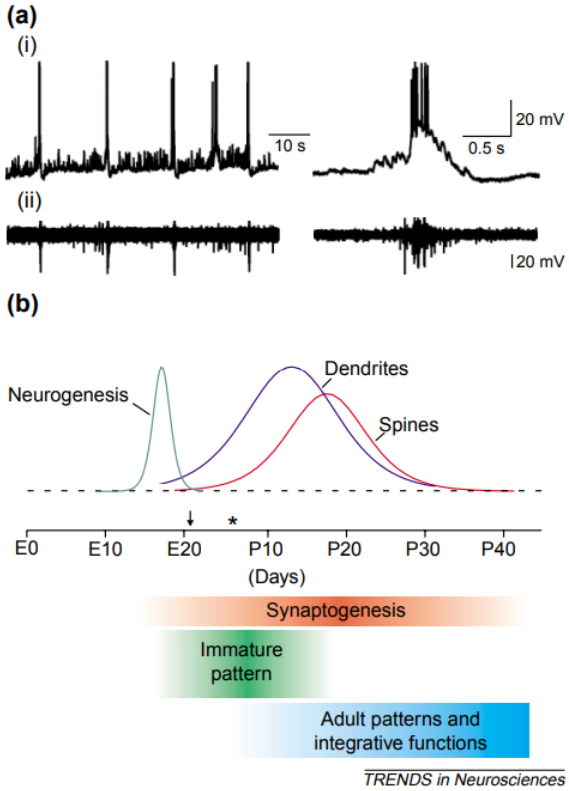


*Figure 2.1: Patterned spontaneous activity in the developing hippocampus. (a) In the neonatal rat hippocampus, neuronal activity is synchronized in spontaneous network discharges (GDPs). Simultaneous recordings of CA3 pyramidal cell (i) and extracellular field in CA3 pyramidal cells layer (ii) in postnatal day (P) 6 hippocampal slice. Single GDP is shown on the expanded time scale on the right. (b) Principal events in the development of the rat hippocampal network. Principal pyramidal cells are generated before birth and differentiate during the first postnatal month. Hippocampal neurons start to establish synaptic connections around birth [birth occurs at embryonic day (E) 21, indicated by arrow] and during the two postnatal weeks, most synaptic activity is synchronized in immature patterns – GDPs. Adult hippocampal patterns and hippocampal dependent integrative functions emerge later, during the second to third postnatal weeks. Asterisk indicates P6. From (Ben-Ari 2001)*

In the present work (and in almost every work involving neuronal cell cultures over MEA), dissociated neuronal cultures are prepared from the neocortex of 18-day-old (E18) embryonic rats. Once plated over MEA, neural networks start to grow creating connections and thus changing both the morphological and electrophysiological features of the network (Van Pelt et al. 2004, Chiappalone et al. 2006, Cotterill et al. 2016).

Chiappalone and co-workers (Chiappalone et al. 2006) clearly showed that between the second and the third week of culture, the network changed in terms of electrophysiological patterns (Figure 2.2).

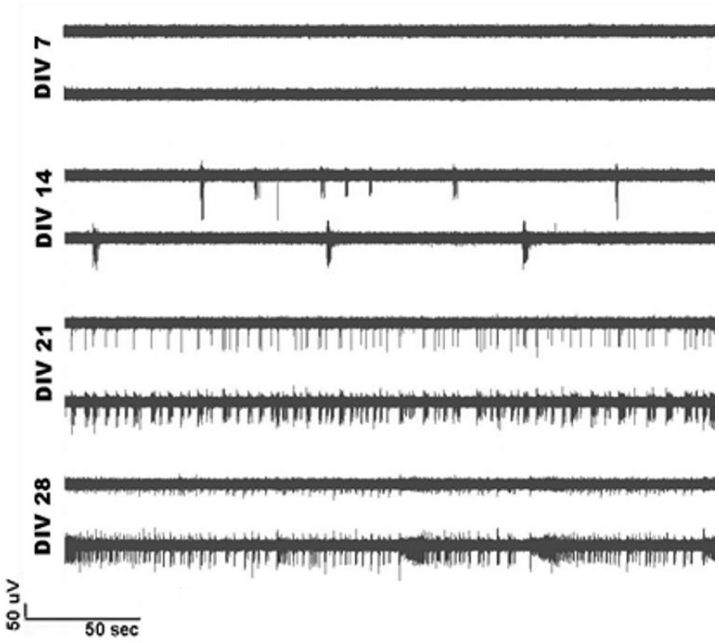


*Figure 2.2. Two representative traces of two channels from MEA at four developmental phases 7-14-21-28 DIV. from (Chiappalone et al. 2006)*

A more recent study by Cotterill and co-workers (Cotterill et al. 2016) used multiwell MEA plates over the first 12 days *in vitro* (DIV) to confirm previous results (Van Pelt et al. 2004, Chiappalone et al. 2006) by means of several parameters summarized in (Figure 2.3) focusing their attention to the very first 12 DIV. In particular they found that spiking activity was sporadic and unorganized at early DIV, becoming more and more organized over time in terms of bursting parameters (both at single channel and network levels). To characterize synchrony they used a feature called network spike (defined as short time intervals with a number of active channels above threshold). They found an increase in the frequency of network spikes and they confirmed this with a pairwise cross correlation measure (spike time tiling coefficient, described in (Cutts and Eglen 2014)).

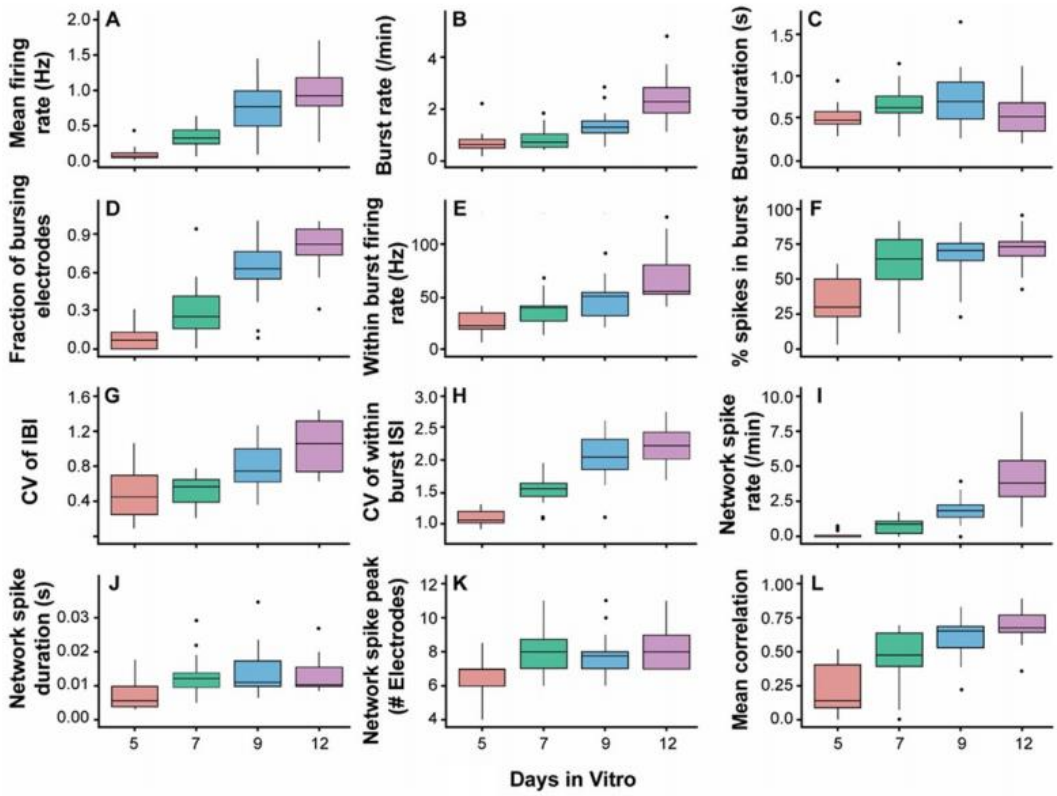


*Figure 2.3 Mean firing (A) and burst rates (B) increase with development. Box plots showing median and interquartile range are shown for n = 16 plates. (C) Burst duration. (D) Fraction of bursting electrodes. (E) Within-burst firing rate. (F) Percentage of spikes in bursts. (G) CV of IBI. (H) CV of within-burst ISI. (I) Network spike rate. (J) Network spike duration. (K) Network spike peak. (L) Mean pairwise correlation. From (Cotterill et al. 2016)*

Other works studied the neuronal network for longer periods (covering the usual DIV when cultures are recorded). In (Van Pelt et al. 2004) the authors studied network bursts with age-dependent firing rate profiles, and durations significantly increasing in the 3rd week *in vitro* and decreasing after about 1 month *in vitro*, when they evolved into short events (Figure 2.4).

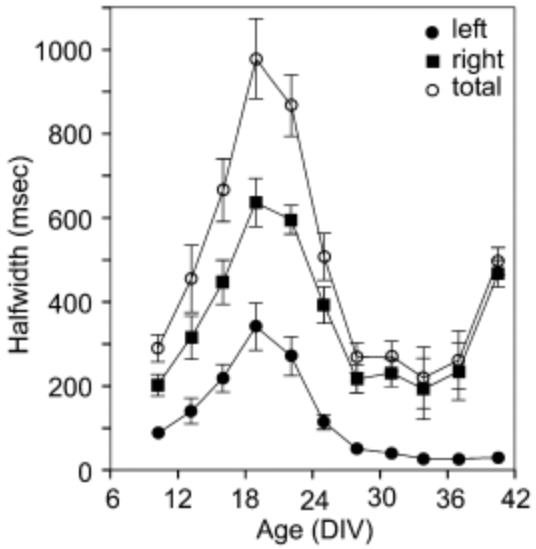


*Figure 2.4 Mean duration in milliseconds of network bursts at different ages in vitro, as calculated for five longitudinal experiments on the basis of half width values of the averaged amplitude/time profile, obtained by summation of all detected bursts on each day of recording. 'left' – rising phase to the 'center' of the burst 'right' – falling phase from the center; 'total' – total burst. From (Van Pelt et al. 2004)*

In (Wagenaar et al. 2006), the authors investigated the importance of different plating densities on development. They also showed that cortical cells exhibited a much richer repertoire of activity patterns than previously reported that changed over time. These results were confirmed by a more recent study (Biffi et al. 2013) where spiking and bursting activity were characterized by a functional peak during maturation, followed by a stable phase (for sparse and medium density cultures, i.e. 900 and 1800 cells/mm$^2$ respectively) or by a decrease phase (for high dense neuronal cultures, i.e. 3600 cells/mm$^2$).

Starting from these findings, for the experiments showed in the present work, we plated cell cultures with medium cell density and we focused our attention to periods of mature development, starting the recordings from the third week *in vitro*.

### *Modular cultures*

In the last decade, different groups have started to realize *in vitro* modular structures (Shein-Idelson et al. 2011, Bisio et al. 2014, Forro et al. 2018, Yamamoto et al. 2018). In particular, (multi) modular cell cultures plated over Micro Electrode Arrays (MEAs) represent an interesting bio-artificial experimental model for studying neuronal networks at the mesoscale level for different reasons. First, cell cultures on MEA can be manipulated in several ways (ranging from pharmacological to electrical, optical and other kinds of perturbations) and can survive longer with respect to other preparations

(Potter and DeMarse 2001). Second, recording from multiple sites is crucial for investigating neural information processing, in case of neural networks and in particular when dealing with multimodular cell assemblies. Third, the high temporal resolution of MEAs allow characterizing the neuronal activity at a time scale that is critical to understand neuronal dynamics.

In (Bisio et al. 2014), modular networks consisting of two confined active and inter-connected sub-populations of neurons were realized and recorded from three up to eight weeks after plating over MEA (Figure 2.5). Although globally less correlated than uniform cultures, modular networks exhibited higher intra-cluster than inter-cluster correlations, thus demonstrating that segregation and integration of activity coexisted in this simple yet powerful *in vitro* model.

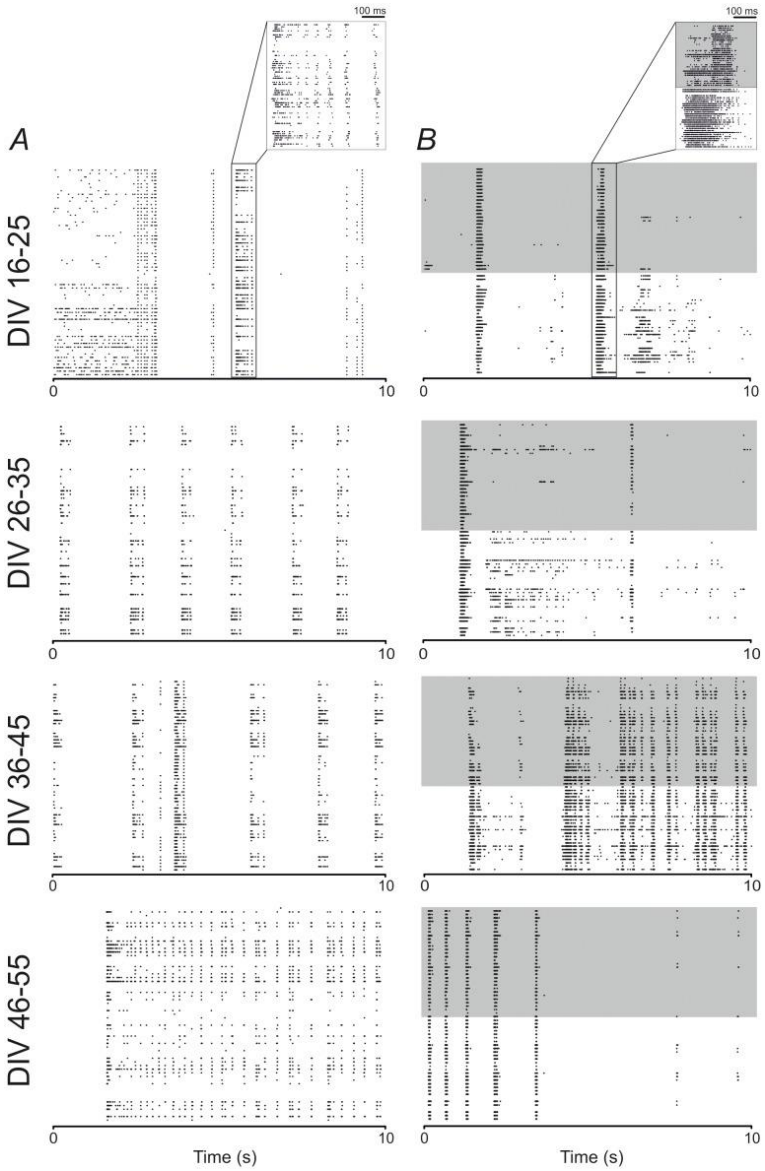


*Figure 2.5: A. 10-s raster plots of spontaneous activity of a representative uniform network, recorded by 60 electrodes at four different developmental phases: 16–25 DIV, 26–35 DIV, 36–45 DIV and 46–55 DIV, respectively*

*from top to bottom. Each black dot represents a detected spike. A zoomed network burst is reported above the raster plot at the first developmental period (DIV 16–25). B. 10-s raster plots of spontaneous activity of a representative modular network, recorded by 60 electrodes at four different developmental phases: 16–25 DIV, 26–35 DIV, 36–45 DIV and 46–55 DIV, respectively from top to bottom. Each black dot represents a detected spike, and the network confinement is highlighted by the grey shaded area, which corresponds to the top compartment. A zoomed network burst is reported above the raster plot at the first developmental period (DIV 16–25). from (Bisio et al. 2014).*

A recent paper by Yamamoto and co-workers (Yamamoto et al. 2018) investigated the impact of modular organization on dynamical richness. They used fluorescence calcium imaging to record the activity of single neurons in a modular configuration consisting of four spatially segregated areas (200 µm by 200 µm squares) connected either by zero, one, or three lines. By means of a graph theoretical analysis, they showed that modularity (the tendency to exhibit distinct communities or modules (Fortunato 2010), increased as connections between the four areas were reduced. They also used dynamical richness to measure the spatiotemporal variability in modular cultures (Zamora-López et al. 2016). This quantity, as well as similar ones termed "complexity", reflects the ability of a neuronal network to exhibit a broad range of dynamical states. They defined richness as the combination of two measures: 1) the variability among the activity patterns of firing neurons; 2) the variability among the size of global network activations (GNAs). Values close to zero are related to small variability among activity patterns, higher values are related to a larger variability (i.e. richness or complexity).

In a different work, Okujeni and coworkers (Okujeni et al. 2017) investigated the role of clustered connectivity for the generation, maintenance and variability of spontaneous activity dynamics in neuronal networks. Computational works already addressed this issue (Klinshov et al. 2014) but a detailed analysis at the biological level was needed.

Taken altogether, the results showed in Yamamoto and Okujeni suggest the usefulness of modular cultures as testbed for different applications ranging from neuropharmacology to network dynamics. Both these applications can be exploited *in silico*, taking advantage of the newest computational models, but testing the scientific hypotheses on a biological substratum is still indispensable.

## Introduction to the BrainBow project

The European Project BrainBow was a Future and Emerging Technologies (FET) project aimed at creating an innovative neuroprosthesis to be tested on cell cultures plated over MEAs. The project was coordinated by the Istituto Italiano di Tecnologia and involved the University of Genova, Tel Aviv University and Centre National de la Recherche Scientifique (CNRS, Bordeaux).

In this project, we first characterized the electrophysiological activity of both spontaneous and electrically evoked activity in the modular cell cultures confined in 2, 3 or 4 modules. Neuronal modules, during development, projected to each other and therefore self-organized themselves in a

network with intricate functional and anatomical connectivity to mimic at least a part of the modular properties of the neuronal tissue of origin. We then used a custom-made laser setup (Difato et al. 2011) able to produce a focal lesion between modules, thus affecting the anatomical connectivity among the neuronal modules. We thus observed the changes in connectivity between modules.

Starting from these results, we asked ourselves: *how can we help the brain help itself?*

Due to recent advances in bioelectronics and in neural and neuromorphic engineering, direct interfacing of artificial circuits with large neuronal networks is possible to develop novel 'neurobiohybrid' systems (such as neuroprostheses (Vassanelli and Mahmud 2016)), which are envisaged as potentially interesting clinical applications for brain lesions (Broccard et al. 2017).

Modern neural interfaces are mainly designed to restore lost motor functions in only one direction, i.e., from the brain to the body (Abdulkader et al. 2015) or from the body to the brain (Flesher et al. 2016). Additionally, recent neuroprosthetic developments have shown the enormous potential of neural interfaces to aid and accelerate functional recovery (Rosin et al. 2011, Bouton et al. 2016). However, a major obstacle in developing novel neuroprostheses for bidirectional communication with and within the brain is the complex nature of interactions among different brain areas, which in turn presents a challenge for the development of appropriate stimulation protocols as well as for testing such devices using *in vivo* models (Kohler et al. 2017).

Starting from the control experiments anticipated above, we interfaced the biological element (the bimodular culture) following the lesion with a neuroprosthetic prototype. Our hardware neuroprosthesis could perform low-power computations in hard real-time (Pirog et al. 2018), collecting the inputs coming from neural recordings, processing those signals and generating suitable electrical stimulation triggers as an output. With this experimental setup, we tested two specific applications, namely, *bidirectional bridging* (BB) to artificially reconnect two disconnected neuronal modules and *hybrid bidirectional bridging* in which a real-time spiking neural network (SNN) replaced the activity of one of the two modules in real-time while implementing bidirectional connectivity with the remaining neuronal module.

The motivation of our research is to provide a new technological instrument as a novel form of neuroprosthesis aimed at treating disabling brain pathologies. The hardware choice (field-programmable gate array, FPGA) maximize the real-time performances of the system and allows for a faster development of a future implantable device for biomedical applications. The adoption of bidirectional communication allows the development of a generalized non-specific approach that is applicable to the central nervous system (CNS) or peripheral nervous system. In particular, prostheses

for the CNS should restore the communication between two or more neuronal assemblies whose functional and anatomical path could be distributed and sparse and not necessarily known *a priori*.

Indeed, our idea to develop a generalized approach comes from the future perspective of creating a cerebral neuroprosthesis for direct implantation in the brain that could be used by patients affected by stroke or brain injury.

## Methods

The following schematic provides an overview of the main elements involved in the project that will be described in detail in this paragraph.

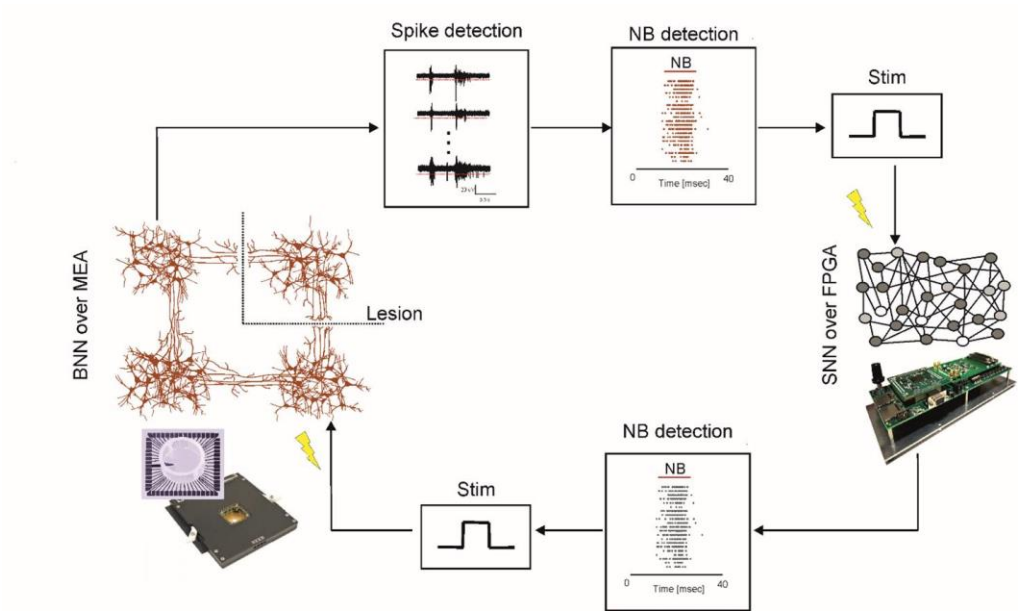


*Figure 2.6 Schematic of the BrainBow project interaction after lesion. On the left: a schematic representation of a patterned culture (with 4 modules) plated over a 60-electrodes MEA after a focal lesion aimed at isolating the top right module. Proceeding clockwise, a real-time spike detection (red lines representing thresholds) and a real-time Network Burst (NB) detection are applied to the recorded BNN. If a spike count in a time window exceeds a certain threshold a stim pulse is delivered to the SNN model implemented on the neuroprosthetic device. Another NB detector, applied to the SNN, triggers an electrical stimulation to the BNN thus closing the loop. The aim of the SNN is to interact with the rest of the BNN and behave like the isolated module.*

I will start describing the experimental methods needed to perform the experiments. Then, I will describe the neuroprosthesis in terms of online processing and Spiking Neural Network (SNN) and then I will describe the offline processing.

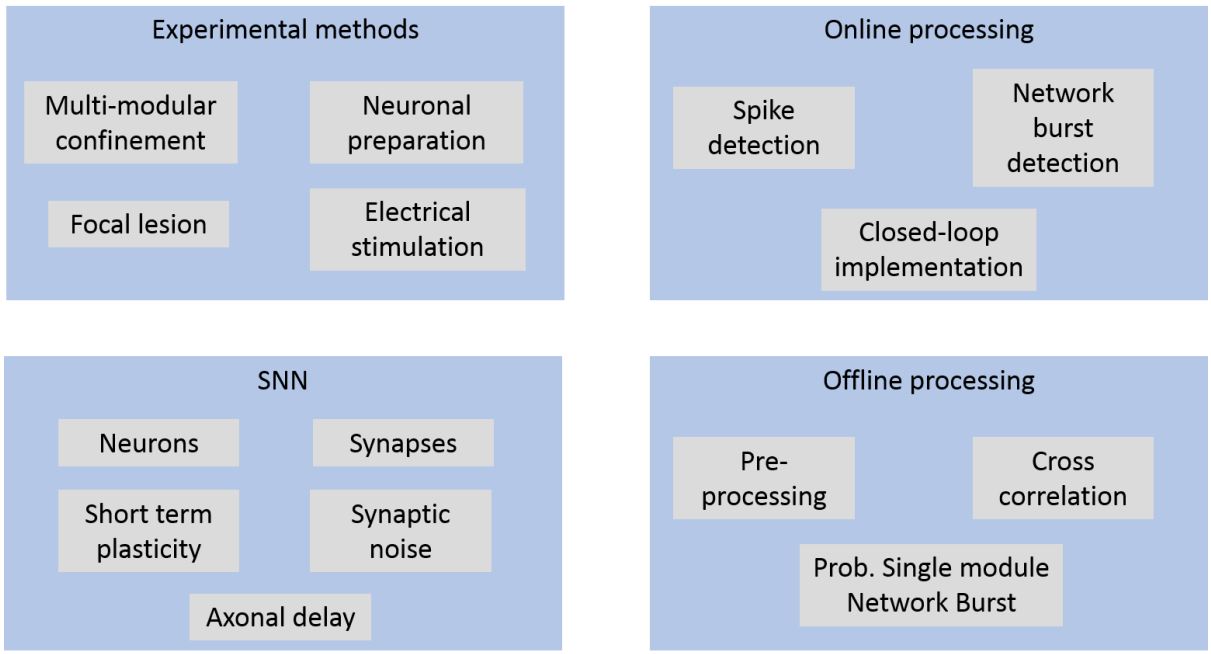


*Figure 2.7. Schematic of the Methods described in this paragraph.*

### *Experimental methods*

#### *Multi-modular confinement*

The polymeric structure for the physical confinement of neuronal cultures on conventional MEAs has been realized in polydimethylsiloxane (PDMS) by soft lithography and by using a photolithographically defined EPON SU-8 master on a silicon substrate. PDMS is an elastomer widely used for biomedical applications because of its high temperature, chemical and oxidation resistance; biocompatibility; transparency; and permeability to gases (Mata et al. 2005). These features also render PDMS particularly suited to the culture of primary neurons (Taylor and Jeon 2010). In addition, PDMS can be easily micro-structured by soft lithography, thus obtaining several low-cost replicas from a single master (Whitesides et al. 2001, Weibel et al. 2007, Habibey et al. 2015). In our case, replicas were produced for single use even if they could in principle be sterilized and re-used. In particular, PDMS stencil fabrication consisted of the following consecutive steps: i) structure design; ii) in silico wafer fabrication through a photolithographic technique; and iii) fabrication of PDMS replicas (for details, see (Bisio et al. 2014)). The developed bimodular neuronal networks were composed of two 3x2 mm modules that were interconnected by 25 channels 390 µm long and 10 µm wide with an inter-channel distance of 50 µm. The developed multi-modular neuronal networks were composed of 3 or 4 modules, 600 x 600 µm each. Once the PDMS masks were ready, they were positioned on the MEA substrates to include all the electrodes within the two modules. Next, the MEAs underwent the coating procedure for promoting cell adhesion, and the following day, the PDMS mask was removed

immediately before the plating procedure, thus allowing neurons to slowly move only towards the promoting adhesion areas.

***Neuronal preparation***

Dissociated neuronal cultures were prepared from the neocortex of 18-day-old embryonic rats (pregnant Sprague-Dawley female rats were obtained from Charles River Laboratories Italia, Milano, Italy). All experimental procedures and animal care were conducted in conformity with institutional guidelines in accordance with the European legislation (European Communities Directive of 24 November 1986, 86/609/EEC) and with the NIH Guide for the Care and Use of Laboratory Animals. Culture preparation was performed as in (Bisio et al. 2014, Colombi et al. 2016). First, we coated MEAs overnight with poly-D-lysine and laminin to promote cell adhesion (Figure 2.8 A1). We washed the MEA devices at least 3 times with sterilized water before plating (Figure 2.8 A2). The neocortex of 4–5 embryos was dissected from the brain and dissociated first by enzymatic digestion in trypsin solution 0.125% (25–30 minutes at 37°C) and subsequently by mechanical dissociation with a fire-polished pipette. The resulting tissue was resuspended in Neurobasal medium supplemented with 2% B-27, 1% Glutamax-I, 1% Pen-Strep solution and 10% Foetal Bovine Serum (Invitrogen, Carlsbad, CA) at a final concentration of 500 cells/ul (Figure 2.8 A3). Cells were then plated onto 60-channel MEAs and maintained with 1 ml nutrient medium (i.e., serum-free Neurobasal medium supplemented with B27 and Glutamax-I). Then, cells were placed in a humidified incubator with an atmosphere of 5% $CO_2$–95% air at 37°C. Half of the medium was changed weekly.

***Immunofluorescence staining and image analysis***

The cultures on coverslips were fixed with 4% paraformaldehyde in phosphate-buffered saline (PBS) for 30 minutes. After permeabilization with 0.1% Triton X-100 in PBS for 10 minutes four times, the cultures were incubated with PBS containing 5% goat serum and 0.1% Triton X-100 for 1 hour. The permeabilized cultures were incubated with primary antibodies (anti-microtubule associated protein 2 [MAP2] mouse IgG; 1:100; Sigma-Aldrich) in PBS containing 5% goat serum overnight at 4°C and were rinsed with PBS for 10 minutes four times. Then, the cultures were incubated with a secondary antibody (Alexa Fluor 488-labelled anti-mouse IgG; Molecular Probes) in PBS containing 5% goat serum, for 2 hours at room temperature and rinsed four times. The coverslips were removed from 12-well plates and mounted on glass slides with mounting media containing DAPI for nuclear staining. Fluorescence images (Figure 2.8 C) were captured using a fluorescence microscope (Nikon eclips80). More details on the procedure can be found in (Ito et al. 2010).

***Focal lesion procedure and laser setup***

The laser dissection system (Difato et al. 2011) allowed for focal ablation of the sample in a three-dimensional confined volume due to the sub-nanosecond pulsed UVA laser source, which required

delivering very low average power, thus confining the material breakdown to the focus spot. The setup was configured in an upright optical layout to allow optical surgery of neuronal networks plated on thick and non-transparent support such as the MEA chip. Therefore, simultaneously monitoring network activity using the MEA device and fluorescence calcium imaging during optical dissection of the connection of neuronal assembly was possible. The system was equipped with a custom micro-incubator (Aviv et al. 2013) maintaining the physiological parameters of the neuronal cultures (pH, osmolarity and temperature) to carry out long-term network activity recording before and after laser injury (Soloperto et al. 2016).

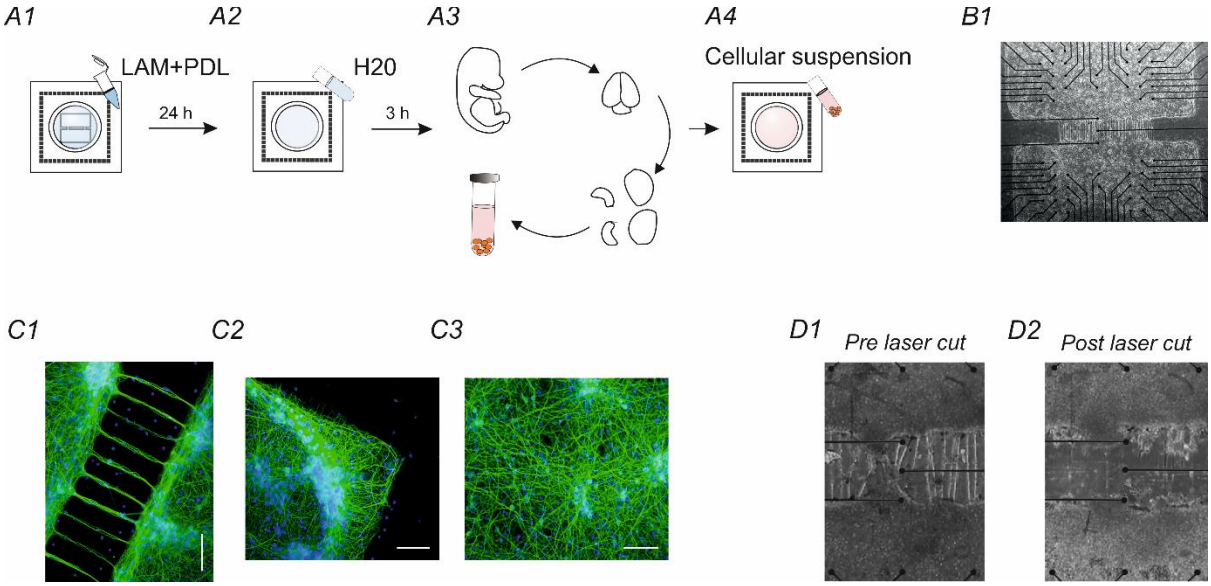


*Figure 2.8. Bimodular neuronal network preparation steps and morphological characterization. A1 MEA surface coating using poly-D-lysine (PDL) and laminin (LAM) to promote cell adhesion. A2 Three consecutive surface rinsing steps using sterilized water and 3 hours of waiting before plating cells. A3 Dissection and dissociation procedures of E18 rat neocortex followed by resuspension of the resulting tissue in Neurobasal medium (see 'Methods'). A4 Cellular solution plating onto a 60-channel MEA surface. B1 A 60-channel MEA (Multichannel Systems MCS, Reutlingen, Germany) with square layout (4Q) plated with a bimodular pattern. C1 Immunofluorescence micrograph of MAP2 of a representative bimodular culture on a coverslip at DIV 25 with magnification of the connections between modules. C2, C3 Immunofluorescence micrographs of MAP2 of a representative uniform culture and of one corner on a coverslip at DIV 25. Scale bar = 200 µm. D1 Magnification of the connections between the two modules before performing the laser cut. D2 Magnification of the cut connections between the two modules.*

***Micro-electrode array recordings***

MEAs (Multi Channel Systems, MCS, Reutlingen, Germany) consisted of 60 TiN/SiN planar round electrodes (electrode diameter: 30 µm; inter-electrode distance: 200–500 µm). One recording electrode was replaced by a larger ground electrode. Each electrode provided information on the activity of the neural network in its immediate area. A microwire connected each microelectrode of the MEA to a different channel of a dedicated amplifying system with a gain of 1100. The signals from the biological neural network (BNN) were amplified by a commercial system (MEA1060-Inv-BC amplification system, Multi Channel Systems, MCS, Reutlingen, Germany).

To reduce the thermal stress of the cells during the experiment, we maintained MEAs at 37°C with a controlled thermostat (MCS) and covered them with a custom PDMS cap to avoid evaporation and prevent changes in osmolarity (Blau et al. 2009). Additionally, we used a custom chamber to maintain a controlled atmosphere (i.e., gas flow of 5% $CO_2$ and 95% $O_2$ + $N_2$) during the entire recording time (Frega et al. 2012).

***Electrical stimulation***

All electrical stimuli were delivered by a commercial stimulator, STG 4002, Multi Channel Systems, MCS, Reutlingen, Germany. That system can be triggered by software (for regular stimulation) or by a TTL pulse (delivered by our neuroprosthetic device). The basic electrical stimulus was a biphasic voltage pulse, 300 µs in the half-length phase and 750 mV of half-amplitude (in accordance with the literature (Wagenaar et al. 2004)).

***Experimental protocols and databases***

The general protocol included at least 30 minutes of no recording immediately after the culture was moved from the incubator to the amplifier to ensure the stability of the network in recording conditions. For control experiments (on bimodular cultures) without lesions, the four hours were recorded continuously. In controls with lesions, after the first hour of recording, we took the culture from the amplifier system, and we moved it to a separate room for laser ablation. The entire procedure usually took 20 minutes. After the lesion, the culture was moved back to the amplifier system where we immediately started the recording. The total number of experiments performed with these protocols was 9 for controls without lesions (26.8 ± 0.8 days *in vitro*, DIV) and 4 for controls with lesions (26 ± 0.6 DIV). For the bidirectional bridging (BB) protocol and hybrid bidirectional bridging (HBB), we performed similar protocols. We recorded 20 minutes of spontaneous activity before the lesion. Next, we performed laser ablation as described above and then waited for two hours to achieve stable activity in both modules, as shown by the results of control experiments (Figure 2.13). Then, we recorded 20 minutes of spontaneous activity after the lesion. To choose the best parameters that allowed us to reliably detect NBs in both modules, we performed offline NB detection. Next, we set these detection parameters on the FPGA with a custom-made MATLAB code and performed a 20 minute session of BB or HBB. The final step consisted of recording 20 minutes of spontaneous activity. The total number of experiments performed with these protocols was 9 for BB (26 ± 0.8 Days *in vitro*, DIV) and 7 for HBB (26 ± 1.5 DIV). In one HBB experiment, we did not record the last spontaneous phase because of a technical problem. For control experiments (on multimodular cultures) we used 8 multimodular cultures with a reduced protocol as described in the dedicated paragraph.

### *Online processing*

#### *Real-time spike detection*

The custom experimental system retrieved analogue data from MEA1060-Inv-BC pre-amplifiers through a standard MCS connector. Analogue input signals were packed in subgroups of 8 signals. For each subgroup, the signals were connected to the input of an analogue multiplexer that switched from one signal to the next one at a frequency of 80 kHz (each 12.5 µs) as shown in Figure 2.9 A. Then, the output signals were amplified. The amplification gain ranged from 1 (no amplification) to 100. Multiplexed signals were finally converted to digital with 16-bit accuracy at a frequency of 80 kHz to provide one sample each time the multiplexer switched to a new input. Then, each of the 8 inputs of each multiplexer was sampled at a frequency of 10 kHz. The system relied on the antialiasing filters embedded in the pre-amplifier.

The spike detection module of the neuroprosthetic device was based on a threshold principle. A detection system was available for each input channel of the system. The first step of the detection was to increase the signal to noise ratio (SNR) of the input signal. The second step was to determine the appropriate threshold to perform the detection; this part of the processing is illustrated in Figure 2.9 B. To emphasize the amplitude of spike shapes and improve SNR, we used the wavelet decomposition technique – SWT (Quotb et al. 2012). This technique consisted of applying two orthogonal filters (one highpass and one lowpass) tailored to the characteristic shape of a spike.

Because of the impedance variation phenomenon, the input gain was expected to be different from one electrode to another and from one experiment to another. Therefore, we needed automatically set thresholds to avoid setting this parameter for each input channel individually. We determined these thresholds as a multiple of the standard deviation (σ) of the first detail level from the SWT outputs. The module that computed σ was referenced as an amplitude estimator (AE) in Figure 2.9. The correspondence factor to determine the threshold was set system-wide by the experimenter depending on the experimental conditions. To compute σ, we used a continuous evaluation to avoid characteristic steps that occurred when performing computation on windows. To reduce computation resources, we digitized a method from analogue computing (Harrison 2003). With the hypothesis that the signal distribution was constant, we knew the proportion of samples below and above the standard deviation, and the system used this property to determine σ with a regulation loop. The signal distribution may change from experiment to experiment, but the estimated σ will always be relevant to the signal amplitude. Then, variations are compensated by adjusting the multiplier that determines the final threshold. Harrison (Harrison 2003) showed that in addition to its computation

efficiency, this method was much more immune to accidental phenomena such as spike residues or stimulation artefacts.

As previously stated, the threshold was applied to the chosen output detail level of the SWT. The final step was to filter glitches that may come from noise around the threshold value and to change a spike-length pulse to a single event. This step was performed by a state machine that, as far as the threshold had been crossed, provided a detected spike event and remained silent during a user-configured refractory period. Then, the output event was available as a spike event for the remaining computation modules of the system.

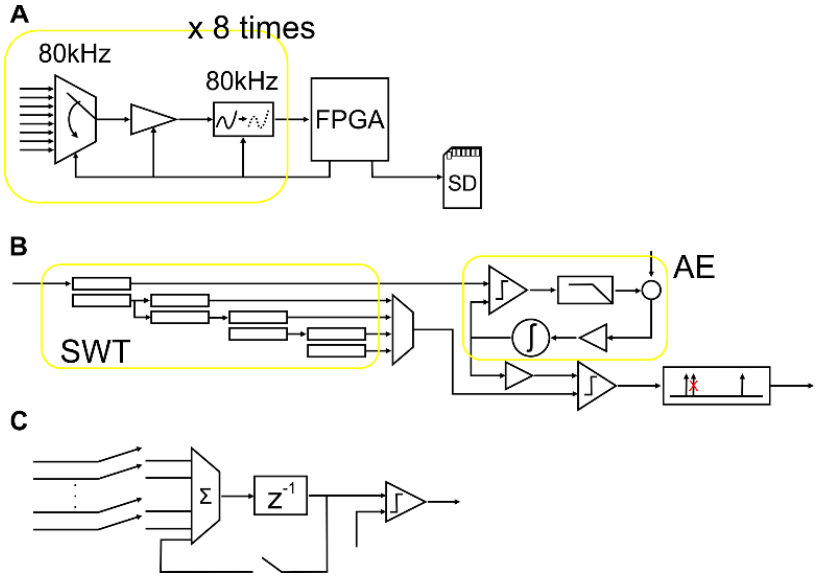


*Figure 2.9. Schematic view of the hardware computation architecture. A, Integrated circuit data flow on the device (Multiplexer: ADG1408, amplifier: LTC6912, analogue to digital converter: AD7686, FPGA: XC6SLX150). Each flow makes it possible to sample 8 channels at 10 kHz (80 kHz multiplexing), eight equivalent structures are connected to the FPGA to sample 64 inputs, and 60 of these inputs are connected to the MEA. B, Hardware spike detection architecture embedded in the FPGA. SWT represents the wavelet-based signal enhancement (stationary wavelet transform). The SWT consists of a series of FIR filters. The first two filters (on the left) are on the 8th order, and the following filters are on the 16th order with 8 null coefficients. AE represents the signal amplitude estimator used to set the final threshold. The loop estimates the standard deviation as the value above 15.9% of samples. The comparator and lowpass filter measure the ratio of samples above the estimated standard deviation; then, the target value is subtracted to identify the relative error. The regulator is composed of an amplifier and integrator to update the estimation of the standard deviation. After the final threshold, an event filter drops each second event too close to the previous one. C, Hardware network burst detector, incoming sources are events produced by the spike detector or the ISI-based burst detector, and the event count is stored in the accumulator (z^-1) and cleared according a timer (the accumulator is not actually cleared, but its value is updated without considering the number of accumulated events thus far, which results in data clearance). The number of events counted since the beginning of the time window is compared with the user-defined threshold to decide whether the network is in a burst state.*

***Addressing the signal to noise ratio (SNR) with the stationary wavelet transform (SWT)***

The Stationary Wavelet Transform (SWT) technique we used is composed of a set of orthogonal filters (one high-pass, one low-pass). The output of the high-pass filter (detail level) was used as an output of the decomposition. The output of the low-pass filter (approximation level) was downsampled, and

the filters were applied to provide the next detail and approximation outputs. The process is repeated as long as necessary. From the theoretical point of view, this method split the noise among the different detail outputs but restricted the spike contribution to one or two outputs, which improved the SNR for these specific outputs. The drawback is that the downsampling generated non-stationary behaviours and resulted in sub-optimal detection when the spike time corresponded to dropped samples. To avoid this phenomenon, we chose to replace signal downsampling by filter upscaling (transforming an $8^{th}$ order filter to a $16^{th}$ order filter containing 8 interleaved null coefficients). With the stationary wavelet transform (SWT) (Pesquet et al. 1996), we kept the best performance for all samples with a price of computational requirements twice as high, and memory requirements 4 times higher. This change in requirements was not an issue since we used hardware computing, and we added the computing resources according to our needs. Although our hardware was able to compute $8^{th}$ order mother wavelets (high-pass/low-pass filter couples), experience showed that the Haar mother wavelet ($2^{nd}$ order) was sufficient (Quotb et al. 2012). An empirical study showed that the third detail level provides the best performance for detection. As the first detailed output was expected to receive very few contributions from the spikes, it was used to determine the comparison threshold for spike detection.

***Real-time network burst detection***

The network burst detector (NBD) was based on the number of action potentials. Although this module was usable on a single channel, it was intended to gather events from multiple channels at the network scale as the preliminary experiments raised the necessity. Therefore, this module was not part of the computation flow build for each channel. There were 16 NBDs. Each NBD received events produced by all the incoming channels. Whether the input channels contributed to any of the 16 NBDs was user-defined. During a predefined time window, events on the selected channels were counted. At the end of the time window, the number of events was compared to a user-defined threshold to determine if an activity burst was occurring or not, and the counter was reset. The detector constantly kept track whether a burst was pending or not. Depending on user choice, each NBD could be independently configured to produce a single event when a burst started, a single event when a burst stopped, one event at each end of computing window detecting a burst, or continuously while the detector was in burst mode. The NBD could receive any event coming from the inputs on the system, including ISI-based burst detection events. It was possible to weight the event contributions such that an event coming from an ISI-based detected burst might have a much higher weight than an action potential on a single channel. The 16 NBDs worked on 1 kHz sampled signals because the application they fed was sampled at that frequency. Input events (10 kHz) were combined with a logical OR by group of 10 to produce the downsampling.

An offline version of the NBD module was written in MATLAB to expedite the choice of parameters for reliable NB detection during experiments. By running the offline NBD with a combination of different windows in the range 1-50 ms and different thresholds in the range 1-250, we looked for a combination of parameters that could reliably detect NBs.

***Closed-loop implementation***

To close the loop, we chose to deliver a stimulation either to the BNN or the spiking neural network (SNN) based on the detection of a network burst (NB). The time to propagate the NB event depended on the source on which it is computed (BNN or SNN) and the stimulation destination (BNN or SNN). To follow the computation rhythm of the SNN, all events were processed at a frequency of 1kHz (so an event might have to wait for 900 µs until the next step occurs).

NBs were computed within 37.4 µs (including spike detection) and were available for processing 1.3 µs later. Therefore, the BNN to SNN latency was 38.7 µs. After a computation step of the SNN, the stimulator was eventually activated after a delay of 3.9 µs. As we measured the stimulator delay to be 85 µs, the SNN to BNN latency was 88.9 µs.

The BNN to BNN latency was composed of the BNN to SNN latency, the time to wait for the next computation step (*Tw*), and the BNN to SNN latency. *Tw* was time dependent; values were equally distributed between 61.3 µs and 961.3 µs with a mean value of 511.3 µs.

The choice to use an FPGA allowed a fine closed-loop performance that can be defined as “hard real-time”. Having a control in the sub-millisecond timescale is crucial especially when the number of recording channels increase. In this scenario, a fine control of the computational time needed to perform a task is mandatory. Depending on the type of closed-loop and time constraints that one wants to achieve, even less advanced implementations (e.g. CPUs and real-time operating systems) can be a good choice. For instance, closing the loop based on the power of LFP signals (you can check it in time windows of hundreds of ms) have fewer constraints and can be implemented on CPUs. In our case, the closed-loop activity was based on spikes (events that last less than a ms) and network bursts (which lasts in tens of ms) and therefore the real-time performances were crucial.

### *Spiking neural network*

The biomimetic SNN is a neuromorphic system with a most detailed level of analogy with the nervous system. The SNN is a network of silicon neurons connected via excitatory and inhibitory silicon synapses and plasticity rules. The characteristics of the systems for bio-hybrid experiments are compatible with the time constants of the real biological systems, complex neuronal models and

plasticity that reproduce spatio-temporal patterns of activation. The hardware real-time implementation needs a low-resource neuron model.

***Neuron model***

The (Izhikevich 2003) IZH model is composed of two equations (1) and (2) in which the state variables '*v*' represents the membrane potential of a neuron and '*u*' represents the regeneration of the membrane potential, which takes into account the activation of ionic currents $K^+$ and the inactivation of ionic currents $Na^+$. $I_{Izh}$ describes the input current from other neurons. The integration time stamp *dt* of the IZH model is 1 ms.

$$\frac{dv}{dt} = 0.04v^2 + 5v + 140 - u + I_{Izh} \tag{1}$$

$$\frac{du}{dt} = a(bv - u) \tag{2}$$

with the after-spike resetting conditions:

$$if \quad v \geq 30mV \Rightarrow \begin{cases} v \leftarrow c \\ u \leftarrow u + d \end{cases} \tag{3}$$

In this model, parameter *a* describes the time scale of the regeneration variable *u(t)*. Lower values of *a* indicate slower regeneration. Parameter *b* describes the sensitivity of the regeneration variable influencing the under-threshold fluctuations of the membrane potential. Parameters *c* and *d* are the reset values of the membrane voltage and regeneration variable after an action potential, respectively. The IZH model can reproduce the behavior of all known cortical neurons by changing only 4 parameters (*a*, *b*, *c* and *d*).

The detailed model and its implementation in digital hardware (Ambroise et al. 2013) are described below (see SNN implementation on FPGA).

***Synapse***

Synaptic transmission includes both excitatory and inhibitory models. In particular, the proposed model takes into account AMPA (i.e., an excitatory neurotransmitter) and GABA (i.e., an inhibitory neurotransmitter). Depolarization or hyperpolarization are represented by a positive or negative contribution to synaptic currents $I_{syn}$. Following the effects of AMPA and GABA, all excitatory or inhibitory synaptic currents tend to zero out, exponentially decreasing (Ben-Ari et al. 1997). These two synaptic currents obey the same law of exponential decay $\tau_{syn}$ (3 ms for excitatory decay and 10 ms for inhibitory decay). According to the literature (Izhikevich 2004), whenever a pre-synaptic neuron emits a peak, a synaptic weight ($W_{syn}$) is added to the synaptic current of the post-synaptic neuron.

To connect the BNN to the SNN, we added external synapses to the SNN. Each neuron of the SNN was connected to one external synapse which can be tuned to be excitatory or inhibitory. Each event detected in the BNN could be used to stimulate the SNN through these external synapses. The SNN stimulation was performed through current stimulation via the external synapses. The stimulation duration depended on the type of synapses (excitatory or inhibitory) and the amplitude depended on the weight applied to the synapses. In our case study, excitatory synapses with 3ms exponential decay and with a weight of 9 are used for connection with BNN. We stimulated a maximum of 20 neurons to avoid over stimulation of the SNN.

***Short-term synaptic plasticity model***

To improve the biological behavior of the synaptic model, we added short-term synaptic plasticity, which modified the synaptic weight according to the activity of pre-synaptic neurons.

Short-term plasticity is a biological phenomenon that modifies and regulates connection weights as a function of network activity. The model used in this work was proposed by (Izhikevich and Edelman 2008). This model is called "short-term plasticity" because the facilitation as well as the depression of a synapse is reabsorbed when no action potential has been emitted during a time constant. The implementation of the short-term plasticity and synapses are described below (parameters: $x_{syn}$, $P$ and $t_{syn}$, see SNN implementation on FPGA).

***Synaptic noise and axonal delay***

To enable spontaneous activity and the activity of our network, we added stochasticity by a source of current noise for each neuron in the neuron model. We used the Ornstein-Uhlenbeck (OU) process (with parameters: mean value = 0; degree of volatility = 35; dissipation rate = 1), which is a suitable model for modelling synaptic noise in a neural network (Rudolph and Destexhe 2005). The OU process $X_t$ is a prototype of a noisy relaxation process and an example of a Gaussian process that has bounded variance and a stationary probability distribution. The process is stationary, Gaussian and Markovian. It satisfies the following stochastic differential equation:

$$dX_t = \theta(\mu - X_t)dt + \sigma dW_t \tag{4}$$

Where $\theta > 0$, $\mu$ and $\sigma > 0$ are the parameters, and $W_t$ is the Wiener process.

The parameter $\mu$ represents the equilibrium or the mean value of the process. The stationary variance is given by:

$$var(X_t) = \frac{\sigma^2}{2\theta} \tag{5}$$

This form of current may represent an approximation to that resulting from the random opening and closing of ion channels on a neuron's surface or to randomly occurring synaptic input currents with exponential decay (Tuckwell et al. 2002).

Figure 2.10 C represents the dynamic behavior of the neuron model (tonic bursting neuron) family in which the parameters are set for tonic bursting activity. This figure represents the same neuron in which we add the stochastic input currents. We noticed that the current noise source caused variability in the timing of action potentials. The digital implementation of this OU process is described in (Grassia et al. 2016) (see also SNN implementation on FPGA).

The synapse computation core also manages the axonal delay. The axonal delay is the phenomenon according to which an action potential emitted at time t arrives at time t + t1 to the post-synaptic neuron. In our implementation, the axonal delay was implemented by a 50-bit delay (shift register) vector, a D value and a multiplication factor. We stored the action potential (1 bit) in this vector delay at the position indicated by the value D. We can have a delay from 0 to 49 ms if the multiplication factor is equal to 1. We can increase this time by tuning this factor. The axonal delay makes it possible to describe a superposition of a network of neurons in 2D and consequently design pyramidal or 3D networks.

***Neural network architecture***

Our architecture of the neural network was based on blocks of RAM (storage of the parameters necessary for the definition of a network), two computing cores (a neuron and synapse), a block to manage the state machine and addresses and an "RS232 Communication" block (which will allow us to configure/modify the parameters of our system from a configuration file). Figure 2.10 A shows the interaction between these blocks. To simplify the figure, we did not represent the clock signal, but the entire architecture is synchronous. The limitation of the number of neurons is due to the following factors: 1) the clock frequency used to maximize the number of neurons in parallel and 2) the size of the RAM, which allows the storage of the parameters, especially the synapses. The resources used are presented in Table 2.2.

One of the advantages of our architecture was that each neuron and synapse were independent. A network configuration file was sent to the FPGA to select the connections and set the number of neurons, synapses, and used options. We could also define multiple networks with different connectivity between networks and within each network.

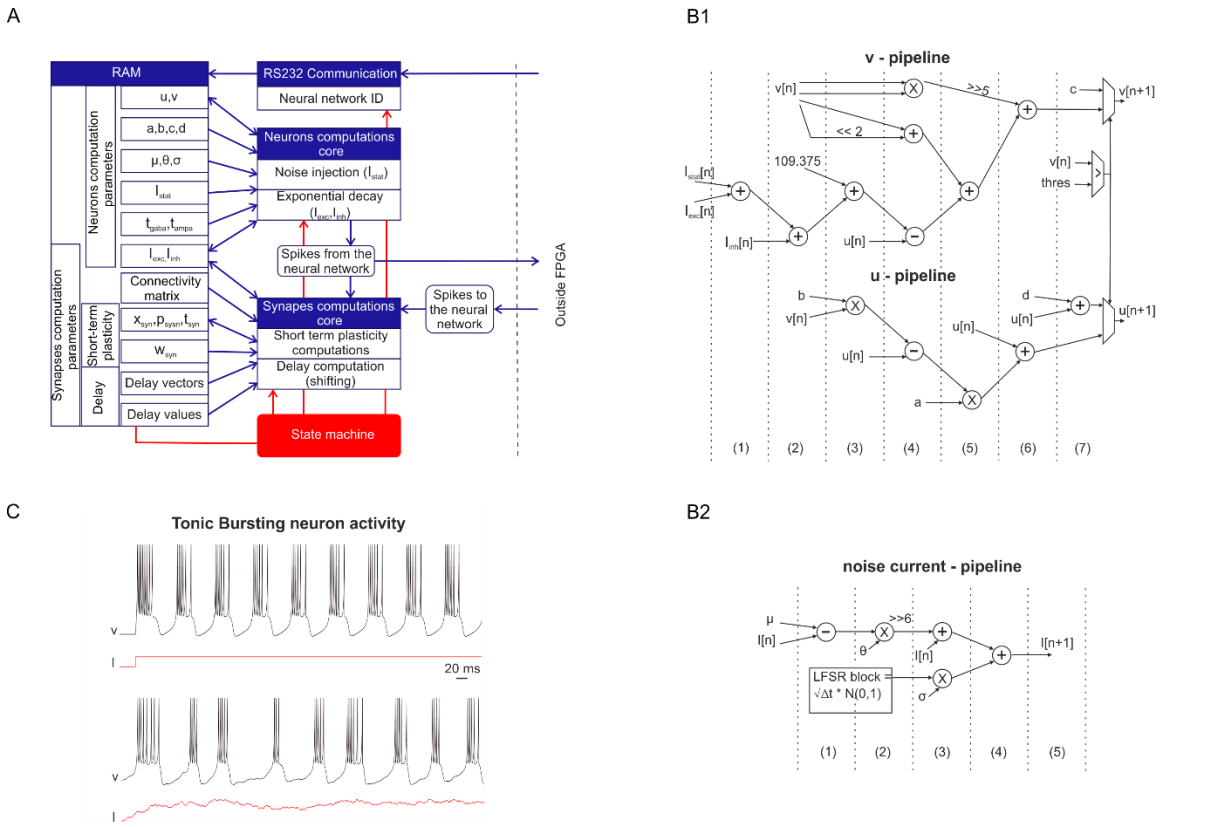


*Figure 2.10. Hardware system organization, pipeline implementation and synaptic noise results. A, Organization of the SNN system with two computation cores, the neuron and synapse. A state machine allows communication between the different blocks. The RAM stacks all the parameters and updates all values every 1 ms. RS232 communication allows communication with a computer to send the initial neural network topology. Spikes to the neural network block are for hybrid experiments where all detected spikes from the neuron culture are sent to the SNN via external synapses. B1, B2, Architecture of 'v', and 'w' and 'I' pipelines for digital implementation. The computation cycles are separated by dotted lines. Each of these dotted lines represents a rising clock edge on which the result of each operation is saved. For the sake of clarity, we have not shown the sequences of the flip-flops. 'u' and 'v' need 7 clock cycles (140 ns), and 'I' needs 5 clock cycles (100 ns). The synaptic noise current 'I' is modelled using an Ornstein-Uhlenbeck process, which makes the neuron implementation more biologically plausible, as shown in C. The parameter μ represents the equilibrium or mean value for the process. We set this value equal to 0 with a bias current value necessary for tonic bursting activity without noise. For the other parameters, σ represents the degree of volatility around the mean value caused by shocks, and ϑ represents the rate by which these shocks dissipate and the variable reverts towards the mean. The stationary variance depends on that parameter. Therefore, in our case, we can set the stationary (long-term) variance with σ and ϑ parameters (neuron bursting activity) of 35 and 1, respectively. C, SNN output of the tonic bursting neuron in which the parameters are set to obtain tonic bursting activity with and without synaptic noise. The synaptic noise allows for better biomimetic dynamics.*

### *Network configuration*

To add flexibility to our system, we added the ability to communicate with the FPGA via serial links to send the configuration, topology, and neural network options. Several options were possible depending on the desired application as follows: axonal delay, short-term plasticity, and synaptic noise. Then, we chose the family of neurons (excitatory, inhibitory), the percentage of connectivity between neurons, the inhibitory/excitatory ratio k, synaptic weight distributions, and the amplitude of the OU noise. From a library of configuration files, we could select the desired network for the given

application and particularly in terms of frequency of NB. Figure 2.21 (cf. Results, HBB) describes SNN library processing. Table 2.1 shows some metrics relative to the bursting features of the implemented artificial networks as well as the mean values of the excitatory and inhibitory weights.

| | # NB | NB/min | Mean exc | Mean inh | Add exc | Add inh |
|---|---|---|---|---|---|---|
| **SNN_1** | 39 | 1,95 | 0,99 | -2,02 | 0,00 | 0,00 |
| **SNN_2** | 55 | 2,75 | 1,00 | -2,02 | 0,01 | 0,00 |
| **SNN_3** | 73 | 3,65 | 1,02 | -2,02 | 0,03 | 0,00 |
| **SNN_4** | 90 | 4,50 | 1,03 | -2,02 | 0,04 | 0,00 |
| **SNN_5** | 111 | 5,55 | 1,04 | -2,02 | 0,05 | 0,00 |
| **SNN_6** | 128 | 6,40 | 1,01 | -1,22 | 0,02 | 0,80 |
| **SNN_7** | 136 | 6,80 | 1,00 | -1,02 | 0,01 | 1,00 |
| **SNN_8** | 159 | 7,95 | 1,01 | -1,03 | 0,02 | 0,99 |
| **SNN_9** | 164 | 8,20 | 1,02 | -1,22 | 0,03 | 0,80 |
| **SNN_10** | 186 | 9,30 | 1,02 | -1,04 | 0,03 | 0,98 |
| **SNN_11** | 208 | 10,40 | 1,08 | -2,02 | 0,09 | 0,00 |
| **SNN_12** | 227 | 11,35 | 1,03 | -1,05 | 0,04 | 0,97 |
| **SNN_13** | 239 | 11,95 | 1,08 | -1,92 | 0,09 | 0,10 |
| **SNN_14** | 265 | 13,25 | 1,06 | -1,22 | 0,07 | 0,80 |
| **SNN_15** | 295 | 14,75 | 1,07 | -1,37 | 0,08 | 0,65 |
| **SNN_16** | 303 | 15,15 | 1,08 | -1,52 | 0,09 | 0,50 |
| **SNN_17** | 329 | 16,45 | 1,07 | -1,22 | 0,08 | 0,80 |
| **SNN_18** | 384 | 19,20 | 1,08 | -1,22 | 0,09 | 0,80 |
| **SNN_19** | 420 | 21,00 | 1,09 | -1,22 | 0,10 | 0,80 |
| **SNN_20** | 597 | 29,85 | 1,12 | -1,14 | 0,13 | 0,88 |
| **SNN_21** | 743 | 37,15 | 1,15 | -1,22 | 0,16 | 0,80 |
| **SNN_22** | 842 | 42,10 | 1,16 | -1,18 | 0,17 | 0,84 |
| **SNN_23** | 968 | 48,40 | 1,18 | -1,20 | 0,19 | 0,82 |
| **SNN_24** | 1080 | 54,00 | 1,20 | -1,22 | 0,21 | 0,80 |
| **SNN_25** | 1303 | 65,15 | 1,24 | -1,26 | 0,25 | 0,76 |
| **SNN_26** | 1510 | 75,50 | 1,27 | -1,29 | 0,28 | 0,73 |
| **SNN_27** | 1882 | 94,10 | 1,34 | -1,36 | 0,35 | 0,66 |

*Table 2.1. Library of SNN, Related to Figure 4. SNN database was created to cover a wide range of NBRs from 1.95 NB/minute (SNN 1) to 94.1 NB/minute (SNN 27). To obtain such variability, we kept the same connectivity matrix with an average degree of 25% for all networks. The main parameters that we tuned to obtain such variability were the mean synaptic excitatory and inhibitory weights. Starting with SNN 1, we added a variable number to each synapse, maintaining separated excitatory (add exc) and inhibitory synapses (add inh). This SNN database can provide a wide range of activities and allows for a better choice of SNN for HBB experiments.*

The SNN library has been populated with network implementations sharing a fixed number of neurons (i.e. 100), the same topology (i.e. random connectivity) but with different synaptic weights (cf. Figure 2.11), necessary to reproduce different bursting behaviors.

Depending on the FPGA board, the maximum number of neurons varies. For instance, in a Spartan 6 FPGA board, we implemented 512 neurons, 66048 synapses with synaptic noise, axonal delay and synaptic plasticity. Table 2.2 describes the resources used. This biomimetic digital SNN worked in real-time, was tunable and reproduced complex biological neural networks due to the biophysically neuron model, synapses, plasticity, axonal delay and synaptic noise.

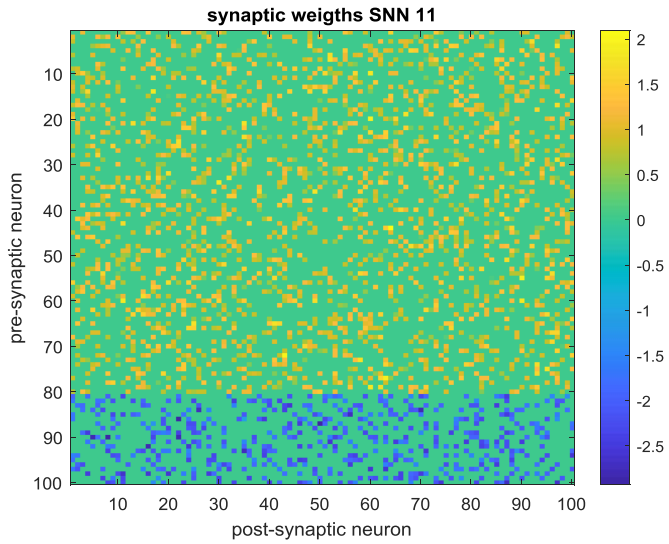


*Figure 2.11. SNN connectivity matrix, Related to Figure 4. The matrix represents the connectivity matrix of one of the 27 SNNs (SNN 11) belonging to the SNN library. Pre-synaptic neurons are on the y-axis and post-synaptic neurons are on the x-axis. Each element of the matrix represents the synaptic weight between the pre- and post-synaptic neuron. If the pre-synaptic neuron is excitatory (i.e. one of the first 80 neurons), the synaptic weight will be positive. Conversely, if the pre-synaptic neuron is inhibitory (i.e. one of the last 20 neurons), the synaptic weight will be negative. We set the outdegree (i.e., the number of post-synaptic neurons) to 25 for all neurons in the network, while the indegree (i.e., the number of pre-synaptic neurons) followed a normal distribution with a mean value of 25 and a standard deviation of 4.3 (Figure S6, R-Square=0.806).*

## *SNN implementation on FPGA*

### *Digital implementation of the Izhikevich model*

The mathematical equations must be modified to implement the IZH model in digital hardware. To make the IZH neural network more biorealistic, we split the current $I_{Izh}$ into the following currents: $I_{stat}$, $I_{exc}$, and $I_{inh}$. $I_{stat}$ is the biasing current, $I_{exc}$ is the positive contribution due to excitatory synapses and $I_{inh}$ is the negative contribution of inhibitory synapses.

We also used the methodology developed in (Cassidy and Andreou 2008) by multiplying the equation of the membrane voltage by 0.78125 such that all parameters are decomposable with powers of 2, which allows easier digital implementation.

$$\frac{dv}{dt} = \frac{1}{32}v^2 + 4v + 109.375 - u + I_{bias} + I_{exc} + I_{inh}$$
$$\frac{du}{dt} = a.(bv - u) \tag{6}$$

And $\frac{dv}{dt} = \frac{v[n+1] - v[n]}{\Delta t}$ knowing that the computation time of the IZH model is 1 ms (Δt = 1):

$$v[n+1] = \frac{1}{32}v[n]^2 + 5v[n] + 109.375 - u[n] + I_{bias}[n] + I_{exc}[n] + I_{inh}[n]$$
$$u[n+1] = u[n] + a.(b.v[n] - u[n]) \tag{7}$$

Using a calculation pipeline, we can compute different neurons in parallel. All model parameters are stored in RAM. Figure 2.10 B1 describes the calculation pipelines for *v* and *u*.

***Digital implementation of synapse and synaptic plasticity***

*Synapse model:* When $W_{syn}$ is positive, the synapse is excitatory, and when $W_{syn}$ is negative, the synapse is inhibitory. The current $I_{exc}$ is always positive, and the current $I_{inh}$ is always negative. However, these two synaptic currents obey the same law of exponential decay $\tau_{syn}$. $I_{syn}$, the synaptic current:

$$I_{syn}(t) = -\tau_{syn}.I'_{syn}(t) = -\tau_{syn}.\frac{I_{syn}(t+T) - I_{syn}(t)}{T} \tag{8}$$

$$I_{syn}(t+T) = \left(1 - \frac{T}{\tau_{syn}}\right).I_{syn}(t) \tag{9}$$

Where computation time T is 1 ms:

$$I_{syn}(t+1) = \left(1 - \frac{1}{\tau_{syn}}\right).I_{syn}(t) \tag{10}$$

In digital implementation:

$$I_{syn}[n+1] = I_{syn}[n] - \frac{1}{\tau_{syn}}.I_{syn}[n] \tag{11}$$

*The Short-term synaptic plasticity model* is defined by 3 parameters:

- a scalar factor $x_{syn}$, which indicates the state of the synapse (depression or facilitation) and computes the synaptic weight.
- a percentage *P*, which will be multiplied by the factor $x_{syn}$ after each emission of a pre-synaptic action potential. If this percentage is larger than 1, this synapse will describe a short-term facilitation. Otherwise, if this percentage is less than 1, this synapse will describe a short-term

depression. In facilitation (or depression), the value added to the stimulation current of a post-synaptic neuron will increase (or decrease) with each emission of action potential.

- a time constant $t_{syn}$ of exponential decay (or growth) in facilitation (or depression).

When a pre-synaptic spike occurs:

$$I_{syn}[n+1] = I_{syn}[n] - \frac{1}{\tau_{syn}} \cdot I_{syn}[n] + W_{syn}[n] \tag{12}$$

Where $W_{syn}$, the synaptic weight, is defined by:

$$W_s[n] = x_{syn}[n]\, W_{syn} \tag{13}$$

$$x_{syn}[n+1] = P\, x_{syn}[n] \tag{14}$$

Parameters $W_{syn}$, $x_{syn}$, $P$, $\tau_{syn}$ are stacked into RAM.

The digital implementation of the synaptic noise (cf. equation (4)) in the stimulation current of the neuron is given by:

$$I[n+1] = I[n] + \theta(\mu - I[n])\Delta t + \sigma \Delta W[n] \tag{15}$$

Where n is the iteration step, and $\Delta t = T/N$ is the time step after the partition of the interval $[0, T]$ into $N$ equal subintervals. Note that the random variables $\Delta W[n]$ are independent and identically distributed normal random variables with expected value zero and variance $\Delta t$, thus $\Delta W[n] \sim N(0, \Delta t) = \sqrt{\Delta t} * N(0,1)$.

Figure 2.10C represents the dynamic behavior of the neuron model in which the parameters are set for tonic bursting activity.

| | bit registers | | | LUTs | | | RAM blocks | | | multipliers | | |
|---|---|---|---|---|---|---|---|---|---|---|---|---|
| | numb. | Project | Device | numb. | Project | Device | numb. | Project | Device | numb. | Project | Device |
| Signal processing | 4753 | 31% | 3% | 6274 | 31% | 7% | 11 | 5% | 4% | 3 | 7% | 2% |
| SNN | 3433 | 23% | 2% | 5747 | 29% | 6% | 82 | 39% | 31% | 42 | 93% | 23% |
| Environment | 6993 | 46% | 4% | 7996 | 40% | 9% | 118 | 56% | 44% | 0 | 0% | 0% |
| Total | 15179 | 100% | 8% | 20017 | 100% | 22% | 211 | 100% | 79% | 45 | 100% | 25% |

*Table 2.2. Hardware resource usage for the different functions of the hardware board. The signal processing part includes filters, spike detection, and burst detection (for events from electrodes and from the SNN). The SNN is considered a part by itself, and the environment part includes the necessary engineering to interface the system to the real world. This part includes analogue front-end management, computer interface, VGA display management and SD-card storage management. Bit registers (referenced as flip-flops in digital computing) are used to synchronously store local values or module states. Look-Up tables (LUTs) are asynchronous devices used to implement arbitrary 6-input logic gates. Random Access Memory (RAM) blocks are mostly used to store indexed values (e.g., channel samples for filters, and waiting queues). Multipliers are hard-coded embedded multiplier circuits that are available to increase both performance and density since multiplications are resource-demanding functions in hardware. The high majority of RAM blocks are required by the environment for VGA display and SD-card data buffer. The SNN part uses RAM blocks extensively to address the individual parameters of neurons and synapses. The SNN also requires many hardware multipliers because of the original mathematical formalism. Resources for signal processing are more focused on bit registers and LUTs because of pipeline*

*structures that implement computations structures close to the device that stores data. The environmental cost in terms of resources is heavy, but this cost is constant and should not increase if implementing new signal processing features.*

## *Offline data analysis*

Offline data analysis was performed by custom scripts developed in MATLAB (MathWorks, Natick, MA, USA).

### *Preprocessing*

To characterize the activity level of BNNs, we used the percentage of active channels and the mean firing rate (MFR). To compute the former, we considered active electrodes only those presenting a firing rate higher than 0.01 spikes per second (spikes/s), while the latter was defined as the mean number of spikes per second, computed over the total recording time, of the active channels. The low threshold guaranteed excluding only those electrodes that were not covered by cells or with very few spikes, keeping all the others (Bisio et al. 2014). In stimulation phases, the activity of stimulated channels was deleted.

### *Cross-correlation*

To quantify the level of synchronization among multi-unit recordings, we applied correlation analysis (Chiappalone et al. 2007) to the spike trains. Cross-correlograms were built according to the method of the activity pairs described by (Eytan et al. 2004) as follows: given two trains (i.e., *X* and *Y*), we counted the number of events in the Y train within a time frame around the *X* event of ±T (T set at 500 ms), using bins of amplitude Δt (set at 1 ms). The CC function $C_{xy}(\tau)$ was obtained by a normalization procedure, according to the following formula (Pasquale et al. 2008):

$$C_{xy}(T) = \frac{1}{\sqrt{N_x N_y}} \sum_{t_i=\left(T-\frac{\Delta T}{2}\right)}^{\left(T+\frac{\Delta T}{2}\right)} X(t_s - t_i) \tag{16}$$

where $t_s$ indicates the timing of an event in the X train, $N_x$ and $N_y$ are the total number of events in the X and Y trains, respectively, and Δτ is the bin size. Equation (16) yields the symmetry between $C_{xy}(\tau)$ and $C_{yx}(\tau)$ (i.e., $C_{xy}(\tau)=C_{yx}(-\tau)$) (Eytan et al. 2004).

To evaluate the amount of correlation between two modules, we performed the computation between the collapsed spike trains for each module. A collapsed spike train is the result of a logic OR operation between the spike trains recorded on all the electrodes belonging to the same module. For control experiments and BB experiments, the modules were modules of the BNN. In the HBB protocol, we collapsed the activity of the entire SNN to a single spike train. We applied a locally weighted linear

regression to smooth the curve. The area of the CC was the integral of the curve in the range from -500 to 500 ms.

***Offline network burst detection***

The offline NBD was performed using a software implementation of the NBD algorithm running online on the neuromorphic device, called the "fixed window accumulator". Similar to the online version, the algorithm summed all the spikes fired from the neurons of the networks during a given time interval, and it detected a NB if this sum overcame a threshold. Each NB was highlighted by the generation of an event. The input parameters were the window time (i.e., time interval within which the spikes were summed), the threshold (i.e., the number of spikes to overcome to identify an NB event) and the source (i.e., the channels on which the analysis was performed).

Depending on the specific protocol we wanted to analyze, the source could be the whole BNN (in controls without lesions or pre-lesion spontaneous activity), a part of it (for example, to compute the NBR in only one module or to exclude stimulated electrodes), the SNN (for example, to characterize the SNN) or a hybrid network formed by both the SNN and whole BNN or part of it (in HBB). The offline version was also useful during the experimental protocols to set the best parameters (window time and threshold) to obtain a reliable NB detection and to choose the most suitable SNN, referring to NBR, for the HBB experiment.

***Probability single-module network burst***

To quantify the confinement of the electrophysiological activity in a single module, we used the single-module NB probability parameter. This parameter represented the probability that NBs were composed of spikes belonging to a single module (i.e., one of the modules of the BNN or the SNN). This parameter was computed by counting the number of spikes that belonged to each burst, followed by the percentage of spikes that belonged to each module. If this percentage was higher than 85%, we assumed that the burst was generated in a single module. Setting 85% as the threshold percentage allowed us to consider the possibility of having random spikes in the other module at the same time as the NB. To perform this analysis, we modified the NBD by adding start and stop thresholds. For each NB identified, the algorithm looked for an empty time window (i.e., a time window in which the number of spikes was equal or lower than the threshold) before and after the window in which a NB was detected. This was useful to identify the first and last spikes of that event as the first spike in the first window and the last spike in the last window belonging to the NB, respectively. We set the start and stop thresholds to zero and 5, respectively, for BNN and SNN (the SNN threshold was higher because of the presence of fast spiking neurons).

***Statistics***

Statistical tests were employed to assess significant differences among different experimental conditions. The normal distribution of experimental data was tested using the Shapiro-Wilk normality test. We performed one-way repeated measures ANOVA to compare data from the same group at different time points. When ANOVA gave a significant ($p < 0.05$) result, the post hoc Bonferroni test was employed to assess differences between all phases. When normality was rejected, we used Friedman's repeated measures ANOVA on the ranks test to compare data from the same group at different time points. To compare data from two different populations (Figure 2.13), we performed the Mann-Whitney test. Statistical analysis was carried out by using OriginPro (OriginLab Corporation, Northampton, MA, USA) and Sigma Stat (Systat Software Inc., San Jose, CA, USA).

## Results

### *Neuroprosthetic architecture*

To create bimodular *in vitro* systems, we developed PDMS masks with two connecting compartments that constrained the growth of neuronal cells in two precise areas over 60-electrode MEAs (cf. Figure 2.8). The obtained bimodular neuronal culture constitutes the biological neuronal network (BNN) of our system (Figure 2.12A). The signal from the BNN was amplified by a commercial system and acquired by a custom-developed FPGA-based neuromorphic board (cf. Figure 2.9) previously configured by a custom-made MATLAB code (MathWorks, Natick, MA, USA) running on a general purpose personal computer. The neuromorphic board triggered a commercial stimulator to close the loop with the BNN. The general protocol designed for this study involved three steps. First, spontaneous activity in both neuronal modules was recorded ('pre-lesion condition'). Then, laser ablation of the biological connections between the two modules was performed (cf. Methods), followed by recording of spontaneous activity in both modules ('post-lesion condition') to assess the viability of the networks. Finally, we tested our neuroprosthetic device using two experimental frameworks. In the first case, we applied a reconnection strategy using a bidirectional activity-dependent stimulation ('bidirectional bridging', BB), whereas in the second case, we interfaced a hardware-implemented biomimetic SNN with one of the two neuronal modules ('hybrid bidirectional bridging', HBB) to simulate a 'replacement' strategy that utilizes the bidirectional interaction between the biological system and its artificial counterpart (Figure 2.12B). The sequence of algorithms (e.g., spike detection, network burst detection) implemented on the board to realize both experimental approaches (BB or HBB) is schematically depicted in Figure 2.12C.

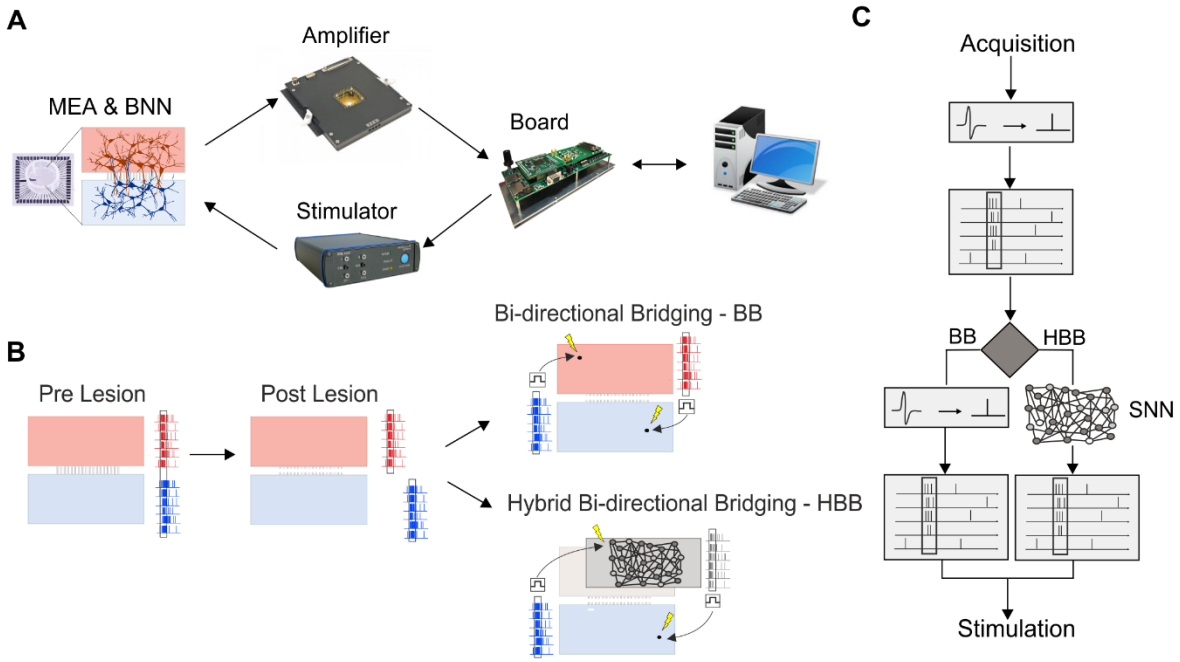


*Figure 2.12. Interfacing a biological neural network and neuromorphic neuroprosthesis. A, Schematic representation of the main elements of the setup: cartoon of an MEA coupled with a BNN; picture of the amplification system; picture of the custom FPGA board; picture of the stimulus generator. Out of the loop, we used a PC to configure the board. B, Schematic representation of the different phases of two experimental approaches which share a pre-lesion, a lesion (performed through laser ablation, not shown) and a post lesion phase. The final experimental phase can be either bidirectional bridging (BB) or hybrid bidirectional bridging (HBB). C, Schematic of real-time data processing performed by the board: the first step is spike detection followed by network burst (NB) detection monitoring module 1. After NB detection, delivering stimulation to module 2 of the BNN (BB approach) or to the SNN is possible. In the second modality, there is also NB detection of the SNN, which can result in stimulation delivered to the BNN (HBB approach).*

### *Control experiments*

#### *Bimodular*

To evaluate the stability and effect of the focal lesion on bimodular BNN activity, we first performed two sets of control experiments. In the first set defined as 'experiments with no lesion' (Figure 2.13 A1), we recorded 4 consecutive hours of spontaneous activity (S1-S4, n=9 cultures). In the second set defined as 'experiments with a lesion' (Figure 2.13 A2), we recorded one hour of spontaneous activity (S1), followed by laser ablation of the connections between the two modules, which usually took less than 20 minutes. Next, we recorded 3 hours of spontaneous activity post lesion (SPL1-SPL3) to quantify the effects of laser ablation (n=4 cultures). As depicted in the raster plot of one representative experiment (Figure 2.13 B1), bimodular neuronal networks exhibited spontaneous, synchronized, multi-unit activity composed of network-wide bursts (NBs) spreading over the two modules. Following laser ablation, the propagation between compartments was disrupted, as shown in Figure 2.13 B2.

With no lesion, the percentage of active channels with respect to the first hour of recording (S1) was higher than 98% and was maintained for the entire duration of the experiment (Figure 2.13 D1, light blue bars). The mean firing rate (MFR) was stable for all control experiments with no lesion (from S1 to S4, Figure 2.14 A). Alternatively, control experiments with lesions showed a reduced number of active channels (close to 73%) during the first hour after ablation (SPL1). During the following two hours (SPL2-SPL3), this value increased and reached 93% at the end of the recording (Figure 2.13 C1, dark grey bars). No significant differences were found. The MFR was quite stable for all control experiments with lesions except between S1 and SPL1 (Figure 2.15 A). The activity level with respect to the S1 phase, expressed by the MFR ratio with respect to S1, was stable during the control experiments without lesions (Figure 2.13 D2, light blue bars). The lesion produced a clear decrease in activity in most cultures, especially during the first two hours (SPL1-SPL2, Figure 2.13 D2). We found a significant difference between the two experimental sets during the first two hours after S1 but not during the last hour. This result suggests that two hours after a lesion, almost complete spontaneous recovery occurred in terms of the firing rate for the two neuronal modules.

To evaluate changes in the synchronicity between the two modules, we performed cross-correlation (CC) analysis between the collapsed spike trains of each module. The shape of the CC function was stable throughout the entire recordings in experiments without lesions, as reported in Figure 2.13 C1 for a representative experiment. After a lesion, the CC function collapsed to zero and did not recover during the experiment (Figure 2.13 C2: representative experiment). To quantify this difference, we integrated the CC function in a range of ±500 ms to obtain the CC area. We did not find any significant change in the CC area values for all experiments with no lesion (Figure 2.14 B). By contrast, the CC

area values showed a marked decrease following the lesion (SPL1). This decrease was due to the lack of anatomical connections between the compartments and did not recover by itself (Figure 2.15 B). Comparing the CC area ratio between later phases and S1 resulted in a significant difference between matching periods in 'lesion' and 'no lesion' experiments (Figure 2.13 E1). We also computed the correlation coefficient (i.e. Pearson Correlation, PC) among all the active channels both intra module and inter module (Figure 2.13 E2). The intra-module PC was constant across experimental phases for controls with no lesion (light blue bars). On the other hand, for controls with lesion (dark grey bars) there was a drop in the intra-module PC, related to the reduced firing rate following the lesion, but no statistical difference was found (Figure 2.13 E2, left panel). The inter-module CC was stable for controls with no lesion. On the other hand, following the lesion the inter-module PC collapsed and never recovered by itself (Figure 2.13 E2, right panel) as already demonstrated with the previous analysis.

The network bursting rate (NBR) was stable during all experiments with no lesions (Figure 2.14 C). For the experiments with lesions, this parameter was less stable but with no significant differences between phases (Figure 2.15 C). When comparing the two experimental protocols with the NBR ratio with respect to S1, we found significant differences during the first and the second hour post lesion (Figure 2.13 F1). The mean probability to have NBs composed of spikes belonging to a single module (i.e. Prob smNB, cf. Methods) was close to 0.2 in the experiments without lesions (Figure 2.14 D), meaning that the majority of NBs in an intact bimodular network involved both modules. Alternatively, following the lesion, the probability became close to 1 (Figure 2.15 D), meaning a total loss of functional communication between the two compartments. Using the Prob smNB ratio with respect to S1 (Figure 2.13 F2), we found significant differences between the two experimental groups during all phases post lesion (Mann-Whitney test; $p < 0.05$). Thus, for the no lesion experiment, the Prob smNB remained very similar to the initial values, while for the lesion experiments, it changed abruptly due to the lesion. This result further confirmed that the lesion was effective in functionally disconnecting the two modules.

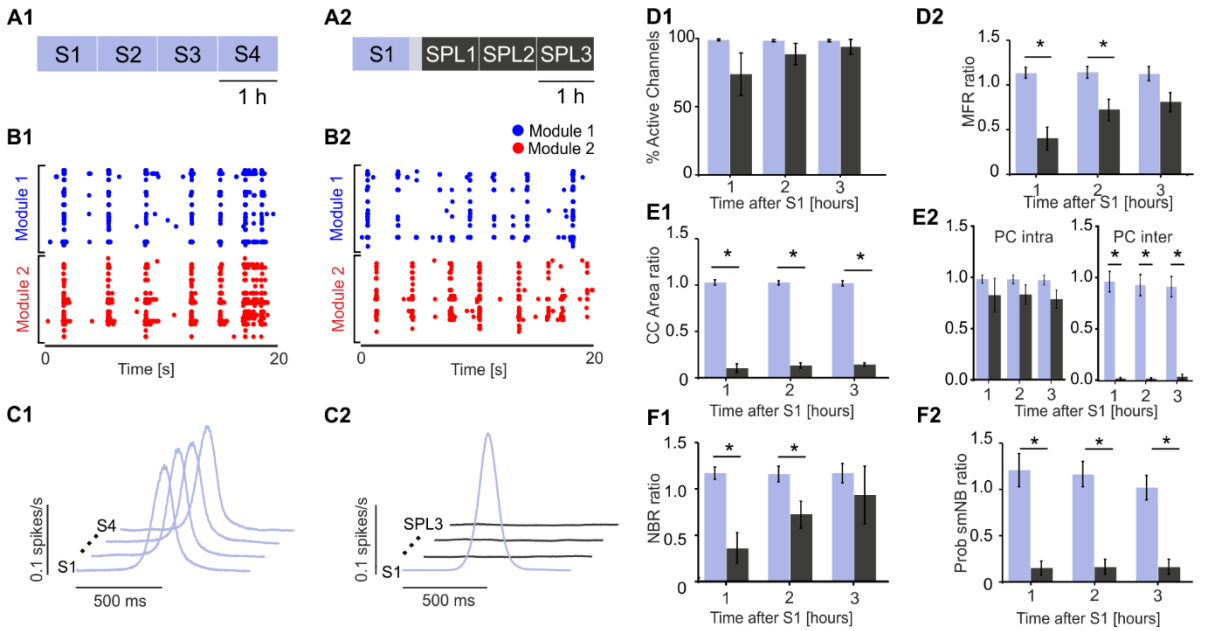


*Figure 2.13. A laser ablation-induced lesion can disconnect two neuronal modules. A1, Schematic of the first experimental protocol. Experiments with no lesion: we recorded four consecutive hours of spontaneous activity (S1-S4). A2, Schematic of the second experimental protocol. Experiments with lesion: we recorded one hour of spontaneous activity (S1) followed by laser ablation and three consecutive hours of spontaneous activity post lesion (SPL1-SPL3). The grey-shaded area indicates 20 minutes of no recording due to the execution of the lesion. B1, A 20 s raster plot of the network bursting activity of one representative experiment during the S1 phase. B2, a 20 s raster plot of the network bursting activity of one representative experiment during SPL3. C1, Cross-correlation (CC) function for one representative experiment during the S1-S4 phases. The CC profiles between the spike trains of each module (light blue) in the four phases of the experiment were high and stable (lines shifted for the sake of clarity). Time axis [-500, +500] ms. C2, CC profile between the spike trains of each module for one representative experiment with lesion. Before the lesion (light blue profile), CC was high; following the lesion (dark grey), CC collapsed to zero (lines shifted for the sake of clarity). Time axis [-500, +500] ms. D1 Percentage of active channels with respect to S1 for the experiments with no lesions (light blue columns, n=9) and with lesions (n=4, dark grey columns). No significant difference was found using the Mann-Whitney test (S2 VS SPL1 p = 0.2042; S3 VS SPL2: p=0.31608; S4 VS SPL3: p=0.70769). D2, Mean firing rate (MFR) ratio with respect to S1 for experiments without (light blue bars) and with lesions (dark grey bars). No significant difference was found during the last hour using the Mann-Whitney test (S2 vs SPL1: p = 0.0028; S3 vs SPL2: p = 0.01119; S4 vs SPL3: p = 0.10629). E1, Comparison of the CC area ratio with respect to S1 for the experiments without (light blue bars) and with lesions (dark grey bars) (Mann-Whitney test; S2 vs SPL1: p =0.0028; S3 vs SPL2: p = 0.0028; S4 vs SPL3: p = 0.0028). E2, On the left, comparison of the intra-module correlation coefficient (i.e., Pearson Correlation, PC) ratio with respect to S1 for the experiments without (light blue bars) and with lesions (dark grey bars). No significant difference was found using the Mann-Whitney test (S2 VS SPL1 p = 0.71049; S3 VS SPL2: p= 0.14825; S4 VS SPL3: p= 0.07552). On the right, the same comparison regarding inter-module PC that showed clear differences between experiments without and with lesion (Mann-Whitney test; S2 vs SPL1: p =0.0028; S3 vs SPL2: p = 0.0028; S4 vs SPL3: p = 0.0028). F1, Network burst rate (NBR) ratio with respect to S1 showing significant differences during the first and second hour after the lesion (Mann-Whitney test; S2 vs SPL1: p = 0.0028; S3 vs SPL2: p = 0.01119; S4 vs SPL3: p = 0.26014). F2, Probability of single-module NB (Prob smNB). The ratio with respect to S1 shows stability for experiments without (light blue bars) and with lesions (dark grey bars) (Mann-Whitney test; S2 vs SPL1: p = 0.0028; S3 vs SPL2: p = 0.0028; S4 vs SPL3: p = 0.0028).*

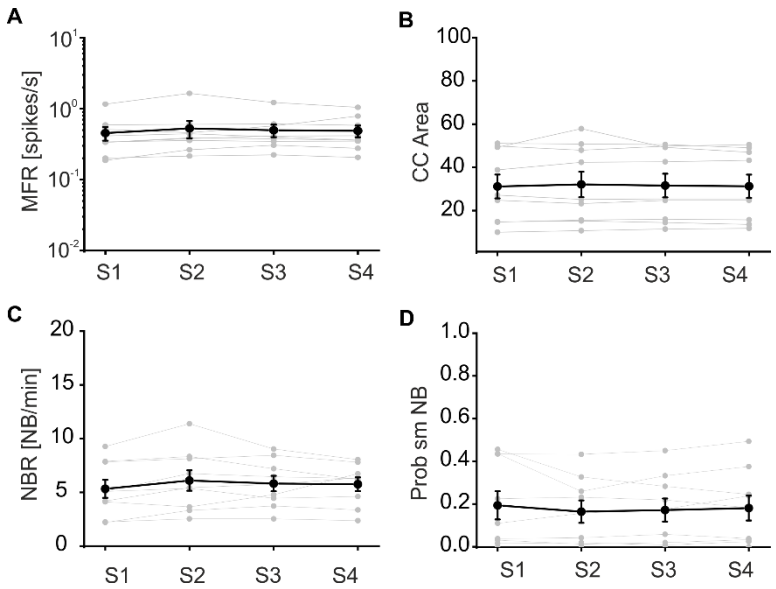


*Figure 2.14. Control no lesion. Mean firing rate (MFR) was stable for all control with no lesion experiments for all experimental phases (from S1 to S4). No significant difference was found (Friedman's repeated measures analysis of variance on ranks; n=9; p=0.04, DF=3, Chi-square= 8,333 but no significant difference between rank sums was found by the Tukey test). B, Cross-correlation (CC) area (obtained integrating the CC function of the collapsed spike trains from module 1 and 2 in a range of ±500 ms) was stable for all control with no lesion experiments for all experimental phases (from S1 to S4). No significant difference was found (Friedman's repeated measures analysis of variance on ranks; n=9; p=0.833, DF=3, Chi-square= 0.867). C, Network burst rate (NBR) was stable for all control with no lesion experiments for all experimental phases (from S1 to S4). No significant difference was found (one-way repeated measures analysis of variance. n=9; p=0.308, DF=3, F= 1.267). D, Probability of single-module network burst (Prob smNB) was stable for all control with no lesion experiments for all experimental phases (from S1 to S4). No significant difference was found (Friedman's repeated measures analysis of variance on ranks; n=9; p=0.789, DF=3, Chi-square= 1.050).*

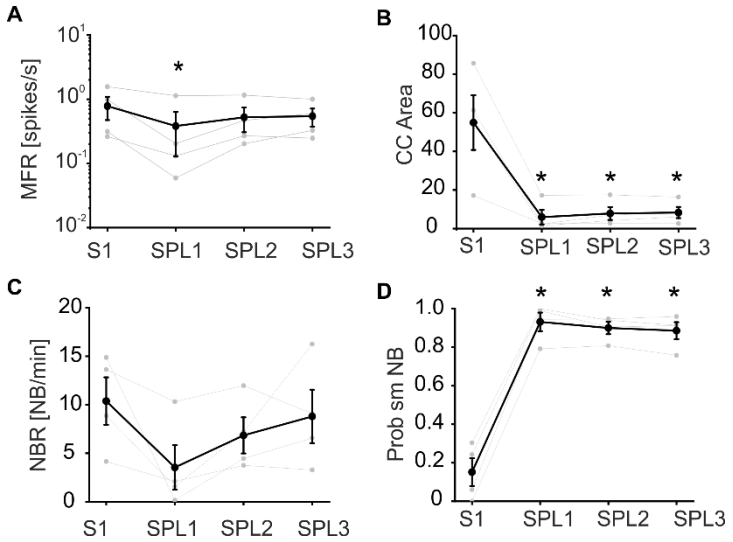


*Figure 2.15. Control with lesion, Related to Figure 2. A, Mean firing rate (MFR) was almost stable for all control with lesion experiments. The only significant difference was found between the first spontaneous phase (S1) before the lesion and the first spontaneous phase post lesion (SPL1). Starting from the second hour post lesion, no significant difference was found between SPL2 and S1 and SPL3 and S1 (one-way repeated measures analysis of variance. n=4; p=0.037, DF=3, F= 4,386; all pairwise multiple comparison procedures (Bonferroni t-test): S1 vs. SPL1: p=0.036; S1 vs. SPL2: p=0,282; S1 vs. SPL3: p=0.376; SPL3 vs. SPL1: p=1; SPL3 vs. SPL2: p=1; SPL2 vs. SPL1: p=1). B, Cross-correlation (CC) area (obtained integrating the CC function of the collapsed spike trains from modules 1 and 2 in a range of ± 500 ms) collapsed following laser ablation. We found significant differences*

*between all phases post lesion and the pre-lesion phase (one-way repeated measures analysis of variance. n=4; p<0.001, DF=3, F= 16,555; All Pairwise Multiple Comparison Procedures (Bonferroni t-test): S1 vs. SPL1: p=0.001; S1 vs. SPL2: p=0.002; S1 vs. SPL3: p=0.002; SPL3 vs. SPL1: p=1; SPL3 vs. SPL2: p=1; SPL2 vs. SPL1: p=1). C, Network burst rate (NBR) was stable for all control with lesion experiments (from S1 to SPL3). No significant difference was found (one-way repeated measures analysis of variance. n=4; p=0.142, DF=3, F= 2.331). d, Probability of single-module network burst (Prob smNB) before the lesion (S1) was on average close to 0.2, meaning that the majority of NBs involved both modules. Following the lesion, the probability increased to an average value higher than 0.85, meaning that the large majority of NBs involved only one module or the other. We found significant differences between SPL1 and S1 (one-way repeated measures analysis of variance. n=4; p<0.001, DF=3, F= 109.911; all pairwise multiple comparison procedures (Bonferroni t-test): SPL1 vs. S1: p<0.001; SPL1 vs. SPL3: p=1; SPL1 vs. SPL2: p=1; SPL2 vs. S1: p<0.001; SPL2 vs. SPL3: p=1; SPL3 vs. S1: p<0.001).*

***Multimodular***

In a similar set of control experiments, we used multi-modular cultures (instead of bimodular ones) to characterize the effect of the lesion. For these experiments, we did not used the neuromorphic device. We used a commercial system for both recording and stimulating cultures. The experimental dataset consisted of 8 modular networks (Figure 2.16 B) and the general protocol consisted of 5 consecutive phases:

i) Basal1: one-hour recording of spontaneous activity;

ii) Stim1: stimulation session I, which consists of serially stimulating at least two electrodes per module using a train of 50 positive then negative pulses at 0.2 Hz;

iii) Cut: laser ablation of inter-cluster neural connections, whose aim was to isolate a cluster which was physically and functionally connected to at least another one (Figure 2.16 C);

iv) Basal2: one-hour recording of spontaneous activity after performing the lesion;

v) Stim2: stimulation session II, from the same electrodes of phase ii.

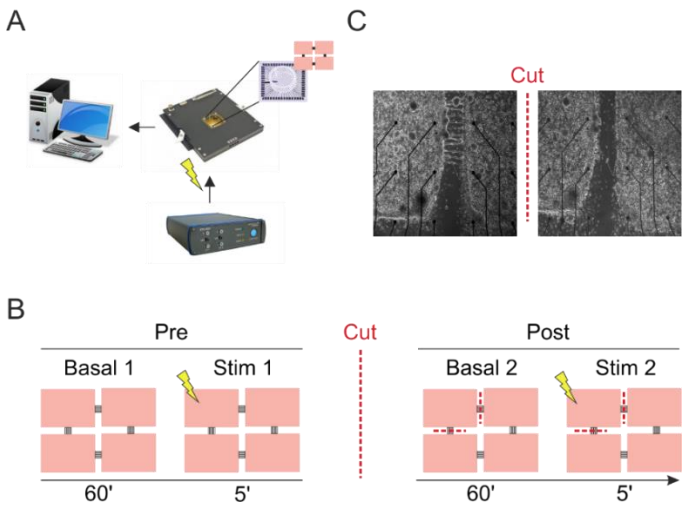


*Figure 2.16. Setup and protocol description. A) Schematic description of the setup. A personal computer equipped with MC-Card (Multichannel System, MCS) records the activity from the MEA 1060 Amplifier system. A*

*commercial stimulator (STG 4002, MCS) delivered open-loop regular stimulation to the MEA amplifier. B) Schematic of the experimental protocol, consisting of 60 minutes of basal (spontaneous) activity followed by 5 minutes of stimulation delivered to one electrode. Stimulation was delivered to different electrodes to test the propagation of the signal across modules. One of the clusters was then isolated by means of a laser cut. Following the laser ablation, the protocol was repeated as before cut. C) Optical micro-graphs depicting a corner of a modular culture before (left) and after (right) laser cut.*

Spiking activity of multi-modular networks appeared well synchronous for the entire duration of the experiment with no lesion condition, as it can be qualitatively appreciated by looking at the raster plot of Fig. 2.15 A. On the other hand, the laser dissection of a cluster induced a strong desynchronization of spiking activity between the isolated cluster and all the others (Figure 2.17 B).

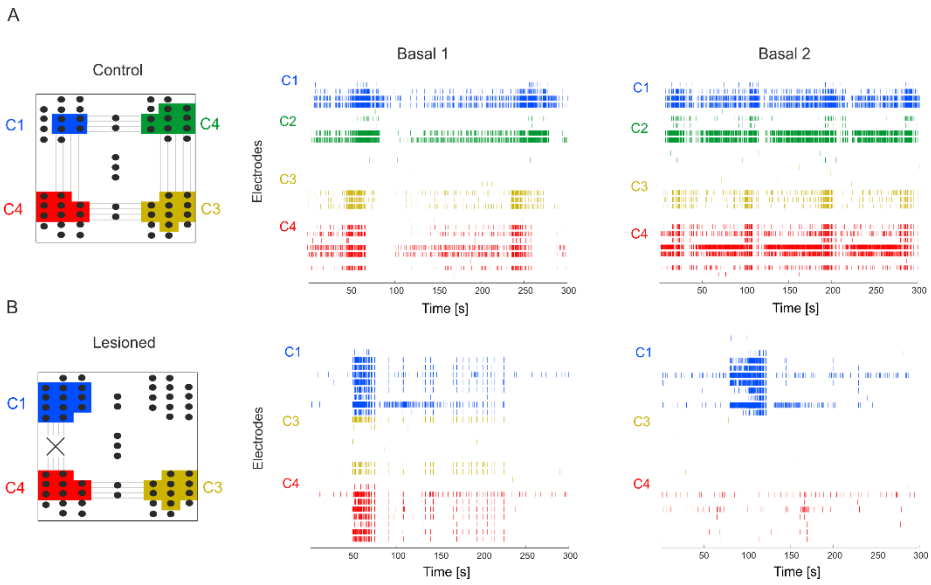


*Figure 2.17. Network activity in two representative experiments. A) Control experiment. On the left MEA modules are graphically depicted, black dots representing the channels, where the active ones have background colored according to the module they belong to. In the center, a raster plot of the activity recorded during the Basal 1 phase is colored according to modules as on the left. In the right a raster plot of the activity recorded during the Basal 2 phase is colored according to modules as on the left. B) Same as in A, for experiments with laser ablation (i.e. between Basal1 and Basal 2, a laser ablation – Cut phase - was performed).*

It is worth underlying that for this set of experiments, we recorded only one hour after the lesion and this can be the reason why we found a decrease in terms of some parameters.

Indeed, we observed a significant global decrease in the network mean firing rate, both inside the isolated cluster (Isolated, $p<0.05$), and in all the other clusters (Others, $p<0.001$) that were previously connected to the isolated one (Wilcoxon signed-rank test, Figure 2.18 A). No changes of firing rate were found in the control condition (Figure 2.18 A). Moreover, the analysis of the pairwise correlation indicated a stable level of synchronicity for the activity of the electrodes belonging to the same cluster (Intra, Figure 2.18 B, left), while a dramatic drop was observed between the electrodes of the isolated cluster and all the other ones (Inter, Figure 2.18 B, right).

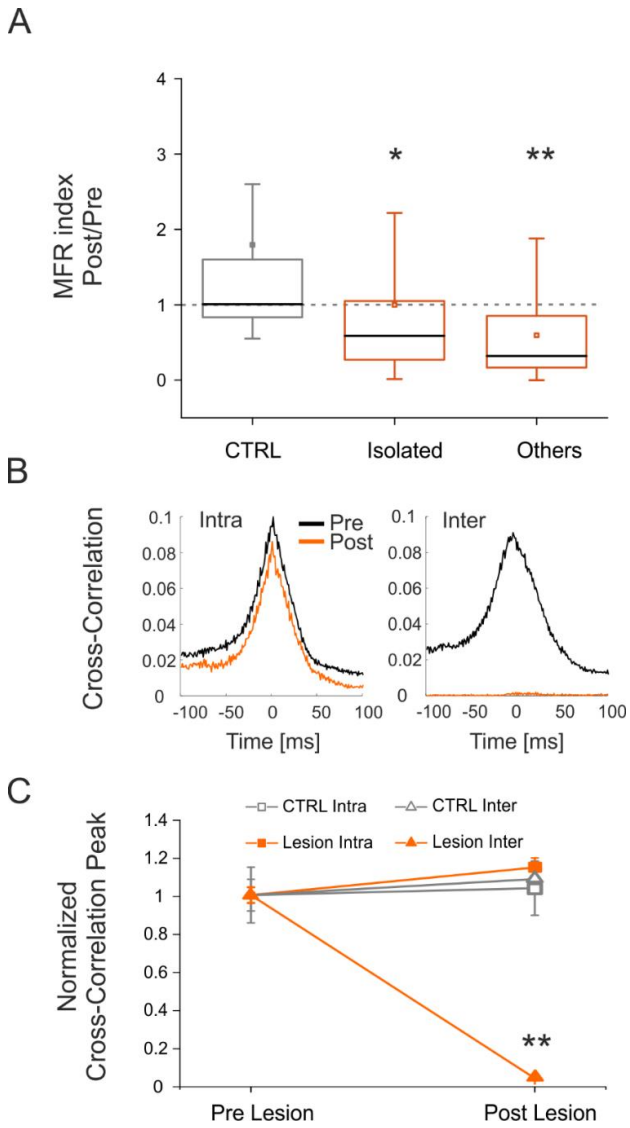


*Figure 2.18. Changes in spontaneous activity. A) MFR variation in control experiments (CTRL, no-lesion) and in modules belonging to experiments with laser ablation (Isolated and Others). B) Cross-Correlation pre and post lesion calculated in the same cluster (Intra) and among the isolated cluster electrodes and the other clusters (Inter) for the experiments with laser ablation. C) Normalized cross-correlations pre and post lesion both for the lesioned (Lesion) and control (CTRL) experiments. ** p<0.01, *p<0.05 Wilcoxon signed-rank test.*

Figure 2.18 C underlines this effect by showing the Cross-Correlation peaks normalized over the average value of correlation found before the laser dissection, calculated both in the same cluster (Intra) and among the isolated cluster electrodes and the other clusters (Inter). While correlation remained rather stable in the no-lesion and in the lesioned intra condition, it significantly dropped in the lesioned intra condition (p<0.001, Wilcoxon signed-rank test).

We also observed the effect of electrical stimulation in the different conditions. Before performing the lesion, electrical stimulation (Figure 2.19 A) was able to evoke activity both within the cluster hosting the stimulation channel and in the connected modules (Figure 2.19 B). After laser dissection,

the evoked activity remained confined within the isolated cluster without spreading towards the other ones (Figure 2.19 C).

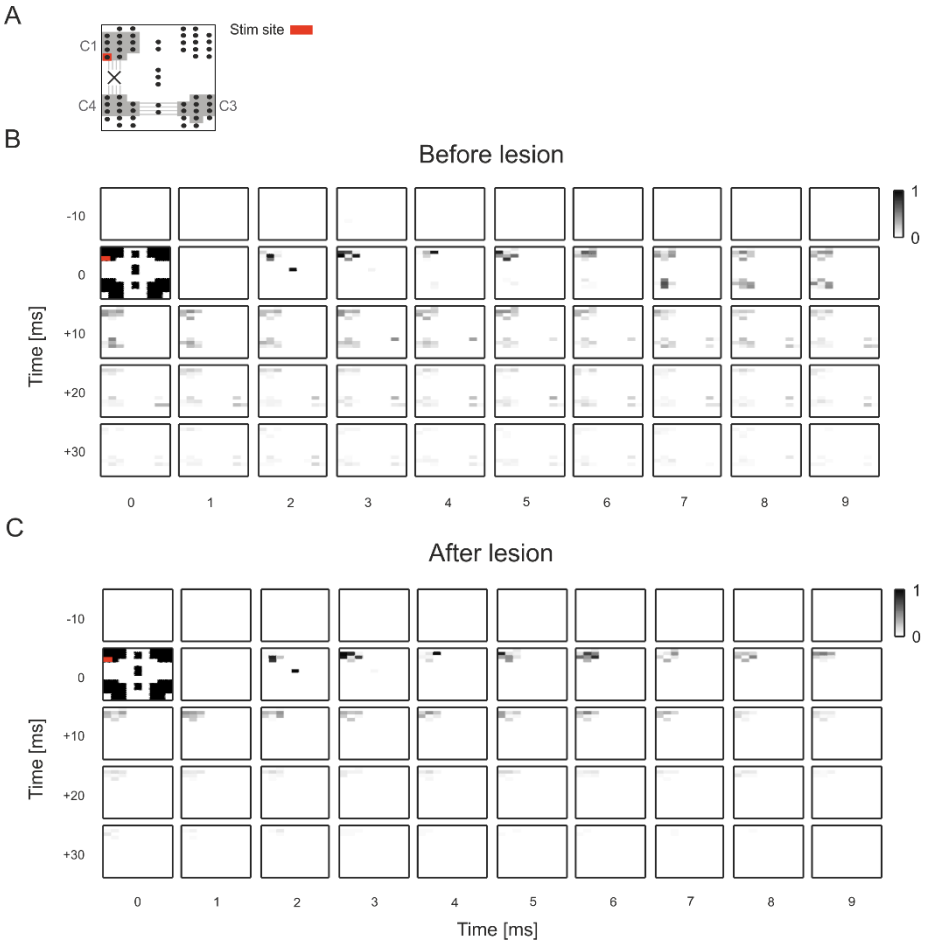


*Figure 2.19. Network response to stimulation. A) Graphical representation of the stimulation site over the MEA. Stimulation was a sequence of 50 stimuli delivered at 0.2Hz through an electrode in the top left module before lesion. B) Stimulation effects in the pre lesion condition. Each graph represents the 60-electrodes MEA response at different time points with respect to the stimulus: ranging from -10 ms before the stimulation to 30 ms after the stimulus onset. Each pixel represents, in grey level, the probability to detect a spike in 1 ms bin. Around the stimulus onset, the spike detection algorithm identifies artifacts on all electrodes that were then blanked to avoid false positive detections. Stimulation site is highlighted in red. C) Stimulation effects in the post lesion condition. Same as in A, but after lesion.*

Taken altogether, these results further confirmed that the lesion was effective in functionally disconnecting two or more modules and thus constitutes a starting point for a neuroprosthetic strategy as will be described in the following paragraphs.

### *Bidirectional Bridging (BB)*

The goal of this experiment was to restore communication between two neuronal assemblies after lesion-induced separation (only bimodular cultures were used here). To achieve this goal, we designed and implemented a stimulation reactive paradigm inspired by the 'activity-dependent stimulation' (ADS) described in (Guggenmos et al. 2013) in our neuromorphic board. In contrast to the control

experiments, the general protocol (Figure 2.20 A) included 20 minute recordings of spontaneous activity before the lesion (S1). Upon the lesion execution, we waited for two hours to reach stable activity in both modules, as shown by the results of control experiments (cf. Figure 2.13). Then, we recorded 20 minutes of spontaneous activity (SPL3). The raster plot of a representative experiment is reported in Figure 2.20 B. Before the lesion (S1), the bursting activity involved both modules (Figure 2.20 B1), whereas after the lesion (SPL3), the activity was characterized by single-module NBs (Figure 2.20 B2). To choose the best parameters (threshold and window time, see Methods) that allowed us to reliably detect NBs in both modules, we performed offline NB detection. After the FPGA update with these parameters, a 20-minute session of BB was conducted. The BB approach implemented a reactive paradigm: every time a NB was detected in one module, a stimulation pulse was delivered to an electrode in the other module (cf. Methods) in both directions. During the BB phase, the bursting activity involved both modules similar to the intact condition due to the bidirectional stimulation pulses (Figure 2.20 B3, blue and red lines represent electrical stimulation pulses delivered from module 1 to module 2 and vice versa). The last phase of the protocol involved 20 additional minutes of spontaneous activity (SPL4), which showed the same activity as SPL3 (Figure 2.20 B4). We did not observe significant changes in spiking activity (i.e., MFR) throughout the recordings (Figure 2.20 C).

Next, we evaluated the effect of this configuration in terms of CC (Figure 2.20 D1 and D2). During spontaneous activity before the lesion (S1), the CC peak was high and stable due to the functional and anatomical connections between the two modules, which was also reported for the control experiments. After the lesion (SPL3), there was a decrease in CC that was not expected to recover without external intervention, as we demonstrated before (see, Figure 2.13 D). The bidirectional stimulation at least partially recovered the CC area and consequently the communication between modules (Figure 2.20 D2), as demonstrated by statistical analysis. Regarding the number of NBs, we did not find any significant difference between the experimental phases (Figure 2.20 E1). However, the probability of isolated NBs was not uniform; it reached the maximum value after the lesion, as we previously observed in the control experiments with lesions (see, Figure 2.13 D2). During bidirectional stimulation, these values became closer to the spontaneous recording (Figure 2.20 E2), meaning that NBs mainly involved both modules. This finding further confirmed that the BB protocol could reconnect two disconnected modules though a real-time ADS acting in both directions (from module 1 to module 2 and from module 2 to module 1).

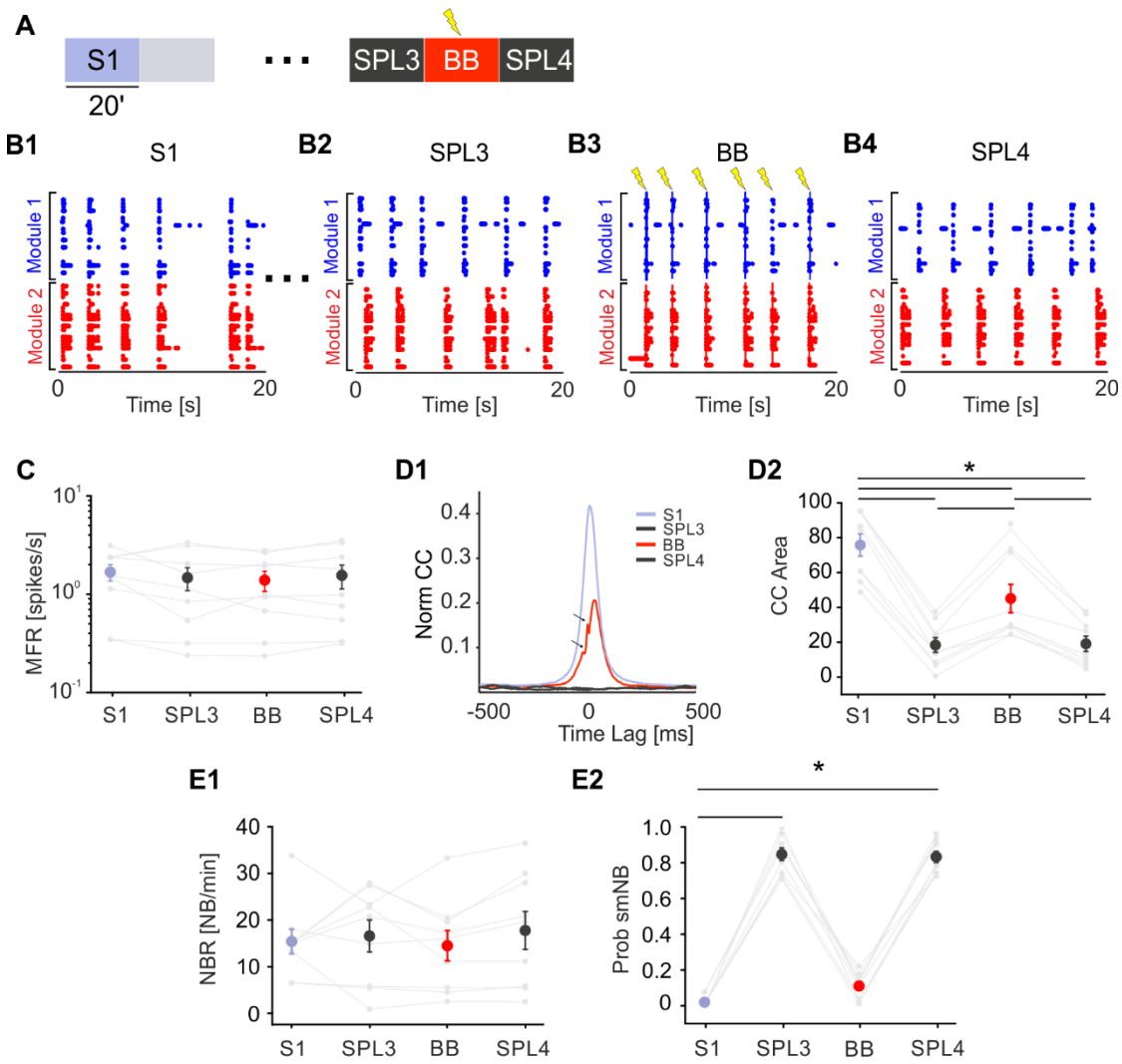


*Figure 2.20. Bidirectional bridging is effective in reconnecting functionally and anatomically disconnected neuronal modules. A, Schematic of the experimental protocol. We recorded 20 minutes of spontaneous activity (S1) followed by laser ablation. The grey-shaded area indicates 20 minutes of no recording during ablation. Dots represent two hours of no recording after the lesion to maintain a stable activity in both modules. Then, we recorded 20 minutes of SPL activity (SPL3) followed by 20 minutes of the bidirectional bridging (BB) protocol and another 20 minutes of spontaneous activity (SPL4). B1-4, The 20 s-long raster plots of representative experiments (respectively, from phases S1, SPL1, BB and SPL4). In B3, Blue and red lines represent electrical stimulation pulses delivered from module 1 to module 2 and vice versa, respectively. C, MFR during the 4 experimental phases was stable (colour code as in panel a: S1: light blue dot; SPL3, SPL4: dark grey dots; BB: red dot). No significant difference was found (one-way RM ANOVA, p=0.469, DF = 3, F = 0.872) D1, CC function during the 4 experimental phases. Small arrows indicate the blanking period of 8 ms following each stimulation. Colour code the same as that in panel a. Note that during BB, the cross-correlation function (red) recovers even if not completely with respect to the initial profile (light blue), while it stays at zero during the spontaneous activity phases post lesion (SPL3 and SPL4, dark grey profiles). D2, CC area was highly reduced during the post-lesion phases. The CC area partially recovered during the BB protocol and collapsed again when stimulation was switched off (one-way repeated measures analysis of variance; degrees of freedom=3; F=101,832. S1 vs SPL3 p=5.67E-13; S1 vs SPL4 p=7.54E-13; S1 vs BB p=1.60E-07; BB vs SPL3 p=1.77E-06; BB vs SPL4 p=2.81E-06; SPL4 vs SPL3 p=1). E1, NBR remained stable during the experiments. No significant difference was found (one-way repeated measures analysis of variance: p=0.501, DF=3; F=0.810). E2, Probability of the single-module NB (Prob smNB) was close to one after the lesion. During the BB protocol, the probability was similar to the pre-lesion condition. (Friedman's repeated measures analysis of variance; p<0.001, DF=3, Chi-square=24.3. SPL4 vs S1 and SPL3 vs S1: p<0.001).*

### *Hybrid bidirectional bridging (HBB)*

With an injury causing damage to an entire neuronal subnetwork, a reconnection strategy such as the BB illustrated above would not be feasible. For this reason, we developed a second reconnection strategy based on the use of a hardware SNN that can interact in real-time with its biological counterpart, HBB (see Figure 2.12). We created a set of SNNs (i.e., SNN library) by tuning the mean value of the synaptic weight distributions of our models to cover the variability of the BNNs (i.e., BNN library, Figure 2.21 A). The biomimetic SNN (see Figure 2.10), working in hardware real-time to allow bidirectional communication with living neurons, was modelled as a network of 100 Izhikevich (IZH) neurons (Izhikevich 2003), with 80 excitatory and 20 inhibitory neurons (cf. Methods), according to the biological composition of dissociated cultures (Hayashi et al. 2003, Bonifazi et al. 2005). Synaptic noise (Grassia et al. 2016), inhibitory and excitatory synapses (Izhikevich 2004), short-term plasticity (Izhikevich and Edelman 2008) and axonal delays were included in the model to recreate the network dynamics (cf. Methods and Figure 2.22 A1 and A2). Regarding the connectivity rules, we set the outdegree (i.e., the number of post-synaptic neurons) to 25 for all neurons in the network, while the indegree (i.e., the number of pre-synaptic neurons) followed a normal distribution with a mean value of 25 and a standard deviation of 4.3 (Figure 2.22, R-Square=0.806). The goal of creating an SNN library was to cover a wide range of NBRs because NB was chosen as the triggering event for our reconnection paradigm, as explained above. To this end, we tuned only the mean value of the normal distribution of synaptic weights (the standard deviation was kept constant at the value of 0.3). By increasing or decreasing the mean synaptic weights, we tuned the NBR. For excitatory synapses, the mean value ranged from 0.99 to 1.34 (Figure 2.21 C left), while that for inhibitory synapses ranged from -2.02 to -1.02 (Figure 2.21 C right and Table 2.1). As previously stated, our goal was to cover the NBR variability and not the MFR. The MFR variability in our BNN library was higher than that obtained with our SNN library (Figure 2.21 E and F1). Nevertheless, the BNN variability in terms of NBR was completely covered by our SNN library, which also contains networks with a much higher NBR than that in the BNN library (Figure 2.21 F2).

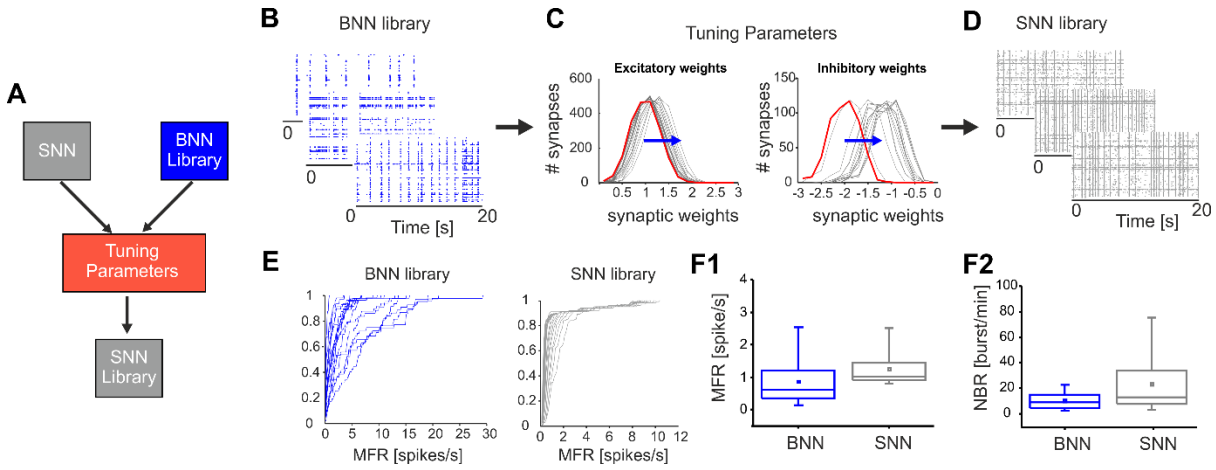


*Figure 2.21. Spiking neural network (SNN) design and characterization. A, Schematic of the procedure used to create a library of SNNs. Starting from the Izhikevich model implemented on the FPGA and a library of 34 BNNs with a large spectrum of activity, we tuned the mean value of the synaptic weight distribution to obtain and select from a collection of SNNs (SNN library, comprising 27 different configurations). B, Representative 20 s-long raster plots of different BNNs showing different NB rates. C, Left, distribution of excitatory synaptic weights from the 27 SNNs. In red, the slower SNN of the library (SNN 1). The blue arrow indicates the shift of the mean value (from 0.99 to 1.34) of the normal distribution with standard deviation = 0.3 to obtain increasing NBR values. Right, distribution of inhibitory synaptic weights from the 27 SNNs. In red, the slower SNN of the library (SNN 1). The blue arrow indicates the shift of the mean value (from -2.02 to -1.02) of the normal distribution with standard deviation = 0.3 to obtain increasing NBR values. D. Representative 20 s-long raster plots of different SNNs showing different NB rates. E, Left, cumulative MFR profile for the BNN library. Right, cumulative MFR profile for the SNN library. F1, Comparison between BNN and SNN libraries in terms of network MFR (i.e., the mean value of all active electrodes for BNN and neurons for SNN). F2, Comparison between BNN and SNN NBR, showing that the SNN library covers the BNN variability and contains networks with a higher NBR.*

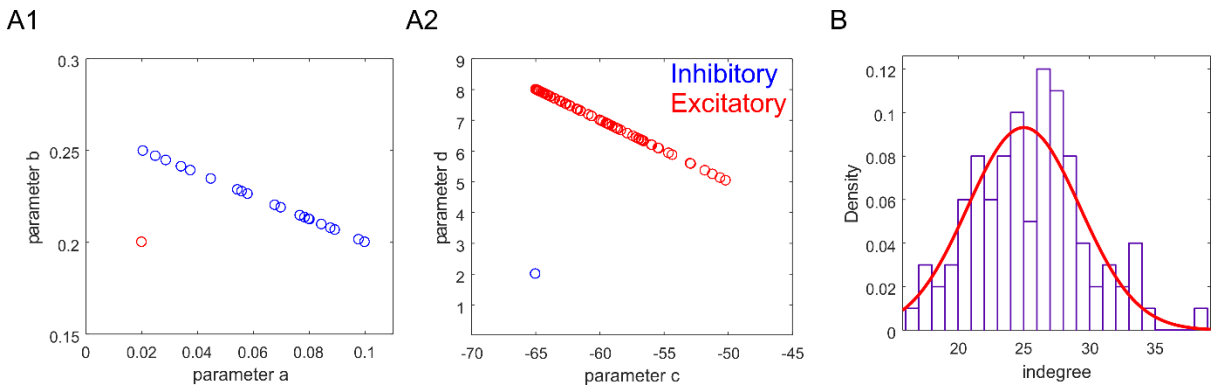


*Figure 2.22. SNN model parameters, Related to Figure 4. A1, Parameters 'a' and 'b' of the Izhikevich model (see Methods) for excitatory (red circle) and inhibitory (blue circles) neurons. All excitatory neurons have the same parameter a=0.02 and b=0.2. All inhibitory neurons have different parameters a (from 0.02 to 0.1) and b (from 0.2 to 0.25). A2, Parameters 'c' and 'd' of the Izhikevich model for excitatory (red circles) and inhibitory (blue circles) neurons. All inhibitory neurons have the same parameter c=-65 and d=2. All excitatory neurons have different parameters c (from -64.97 to -50.17) and d (from 5.04 to 7.99). B, Distribution of the indegree (i.e., the number of pre-synaptic neurons) with a Gaussian distribution superimposed (red curve). Mean value = 25, standard deviation = 4.3, R-Square = 0.806 (fit converged, Chi-square tolerance value of 1e-9 was reached).*

The general HBB protocol (Figure 2.23 A) is similar to the BB protocol. The HBB procedure included a 20 minute recording of spontaneous activity before the lesion. This recording was used to quantify

activity in terms of the NB rate of the network. This feature was used to choose one SNN from the SNN library that had an NB rate closer to its biological counterpart. We waited two hours after the lesion to allow activity in both modules to stabilize, as shown by the results of control experiments (e.g., Figure 2.13). Then, we recorded 20 minutes of spontaneous activity. After setting FPGA detection parameters, we performed a 20-minute HBB session (see, Figure 1B and C for the description of the HBB protocol). As anticipated, the HBB approach also implemented an ADS paradigm; every time a NB was detected on the 'surviving' module (i.e., when one of the two modules was completely damaged), a stimulation pulse was delivered to the SNN. The board implemented the corresponding paradigm in the opposite direction. Detection of NBs occurred in the SNN, while stimulation was delivered to the 'surviving' module, thus avoiding the imposition of any predefined unidirectional communication. Next, we recorded 20 additional minutes of spontaneous activity.

We did not observe significant changes in terms of spiking activity (i.e., MFR) throughout the recordings (Figure 2.23 C). Then, we evaluated the effect of this configuration in terms of CC (Figure 2.23 D1 and 2). During spontaneous activity before the lesion (S1), the CC peak was high and stable due to the functional and anatomical connections between the two modules, which was also reported for the control experiments. As expected, with no external intervention, CC decreased sharply after the lesion (SPL3), as we previously observed. One of the two modules was damaged, while the correlation was evaluated between the SNN and the surviving module during the HBB phase. The bidirectional stimulation created a relevant correlation area between SNN and the surviving module, as demonstrated by statistical analysis. Regarding the number of NBs, we did not find a significant difference between the S1 and HBB phases (Figure 2.23 E1). However, the probability of isolated NBs was not uniform; it reached the maximum value after the lesion, as we previously observed in the control experiments with lesions (see, Figure 2.20 E2). During the hybrid bidirectional stimulation, these values became closer to the spontaneous recording (Figure 2.23 E2), meaning that NBs mainly involved both modules. This finding further confirmed that the HBB protocol created a hybrid system with the surviving biological module though real-time ADS acting in both directions (from BNN to SNN and from SNN to the BNN).

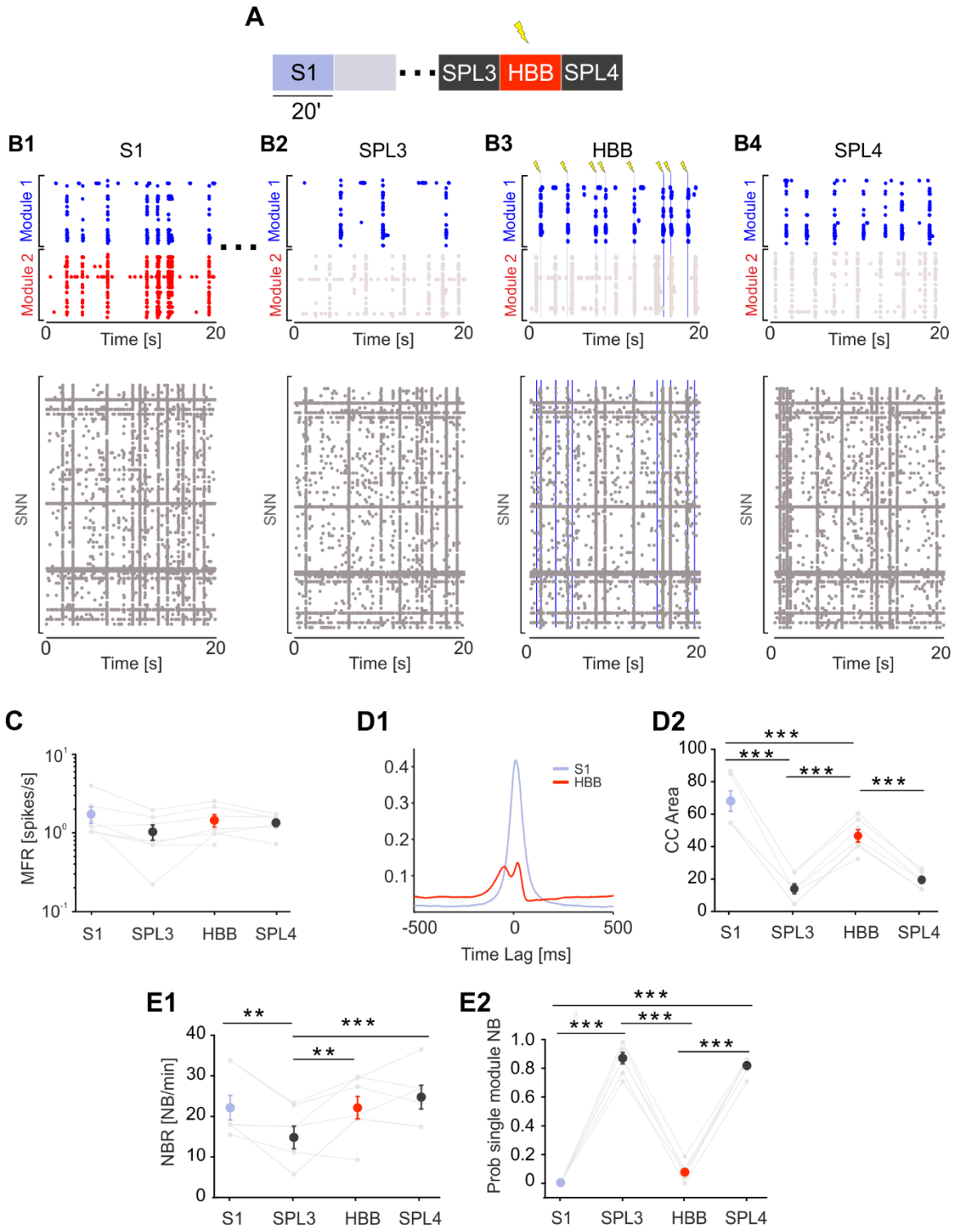


*Figure 2.23. The hybrid bidirectional bridging approach is effective when a neuronal assembly must be replaced. A, Schematic of the experimental protocols. We recorded 20 minutes of spontaneous activity (S1) followed by laser ablation. Grey-shaded area indicates 20 minutes of no recording during ablation. Dots represent two hours of no recording after the lesion to obtain stable activity in both modules and to test different stimulation channels. Then, we recorded 20 minutes of SPL activity (SPL3) followed by 20 minutes of a hybrid bidirectional bridging (HBB) protocol and another 20 minutes of spontaneous activity (SPL4). B1, Top, 20 s-long raster plot depicting the BNN bursting activity involving both modules before lesion. Bottom, activity of SNN uncorrelated with the BNN. The networks are not linked. B2, Top, 20 s-long raster plot after lesion showing uncorrelated bursting activity on BNN modules 1 and 2. Bottom, same as that in B1. B3, 20 s-long raster plot during HBB depicting two hybrid events. The first event on the left was an NB detected on module 1 of the BNN. The detection*

*resulted in a stimulation pulse delivered to 10 excitatory neurons of the SNN (blue line, bottom). An NB on the SNN was detected 18 ms after the stimulation and triggered the delivery of a stimulation pulse to module 1 of the BNN (grey line, top). B4, 20 s-long raster plot depicting the uncorrelated activity of BNN modules (top) and SNN network (bottom). C, MFR during the 4 experimental phases was stable (colour code as in panel a: S1: light blue dot; SPL3, SPL4: dark grey dots; HBB: red dot). No significant difference was found (one-way repeated measures analysis of variance. p<0.001, DF=3, F=3,16; Bonferroni test: all comparisons with p>0.05). D1, CC function during the 4 experimental phases. Colour code the same as that in panel A. Note that during BB, the cross-correlation function (red) recovers even if not completely with respect to the initial profile (light blue). D2, CC area was highly reduced during the post-lesion phases. The CC area partially recovered during the BB protocol and collapsed again when stimulation was switched off (one-way repeated measures analysis of variance. p<0.001, DF=3; F=70,448; S1 vs SPL3: p=5.80E-10; S1 vs SPL4 p=2.72E-09; S1 vs HBB: p=9.16E-04; HBB vs SPL3 p=1.16E-07; HBB vs SPL4 p=1.02E-06; SPL4 vs SPL3 p=0.73643). E1, NBR did not change during HBB with respect to the S1 phase (one-way repeated measures analysis of variance. p=0.005, DF=3; F=6,069; S1 vs SPL3 p=0.02482; S1 vs SPL4 p=1; S1 vs HBB p=1; HBB vs SPL3 p=0.01022; HBB vs SPL4 p=1; SPL4 vs SPL3 p=0.00674). E2, Probability of a single-module NB (Prob smNB) was close to one after the lesion. During the HBB protocol, the probability was similar to that in the pre-lesion condition (one-way repeated measures analysis of variance. p<0.001, DF=3; F=453,439; S1 vs SPL3 p=4.96E-13; S1 vs SPL4 p=1.03E-12; S1 vs HBB p=0.22606; HBB vs SPL3 p=1.94E-12; HBB vs SPL4 p=4.30E-12; SPL4 vs SPL3 p=1).*

## Discussion

We presented an innovative neuromorphic prosthesis based on a FPGA board and demonstrated two successful reconnection paradigms for a lesion interrupting the communication between two neuronal populations *in vitro*.

According to previous reports, *in vitro* systems constitute a successful experimental model of neuronal dynamics (Johnson et al. 2010, Javier et al. 2013), thus providing an excellent test bed for adaptive closed-loop neural interfaces (Potter 2010). Starting from our recently developed methodology (Kanner et al. 2015), we created custom bimodular cultures with the goal of reproducing two interacting neuronal populations, thus mimicking the intrinsic modularity of the brain (Bonifazi et al. 2013). Our bimodular cultures were highly temporally stable in terms of firing properties at the whole network level as the activity between the two populations remained highly correlated for the entire duration of the recording. A lesion produced via laser ablation was employed to physically cut the connections between the two modules. This methodology was proven to be safe because it produced localized damage by selectively ablating subcellular compartments without damaging adjacent structures (Difato et al. 2011, Habibey et al. 2015, Soloperto et al. 2016). We assume that such a focal damage, allowing to specifically cut few connections among those available in the network, together with possible intrinsic compensatory mechanisms of synaptic scaling (Turrigiano 2008, le Feber et al. 2017), were responsible of the spontaneous recovery of the firing rate on a timescale of two-three hours. This demonstrates the effectiveness of our technique in preserving the functionality of the two modules while decoupling their activity, as proven by the loss of correlation of bursting behavior.

Two different applications of our neuroprosthesis, BB and HBB, were tested. Our neuromorphic prosthesis, independently of the stimulation paradigm, works according to a closed-loop reactive policy as follows: each time a condition is met (i.e., an 'event' is detected), a stimulus is delivered. The hardware architecture was designed to be flexible enough to allow the implementation of different experimental paradigms and the definition of different triggering events. In our study, we chose 'NBs' as trigger events (see Methods). The choice to deliver a stimulation depending on a network-wide event has two main advantages as follows: first, NB frequency is low enough to avoid inducing plasticity phenomena by electrical stimulation in our cultures (Wagenaar et al. 2006), which could confound the final results and effectiveness of neuroprosthetic reconnection. The second point is anticipation of the following major issue that will emerge during *in vivo* recordings: monitoring single neurons presents problems at both theoretical (Guggenmos et al. 2013) and practical levels. Namely, how much information on complex functions can be obtained by single-neuron observation remains unclear (Luczak et al. 2015, Panzeri et al. 2017), while tracking the activity of the same neuron for extended periods of time is problematic (Kozai et al. 2015). Taking multiple input sources into account

was also used in the work of Berger (Berger et al. 2012), but they employed a neuroprosthetic strategy different from ours. In particular, these authors used a generalized linear model to predict the CA1 activity from spikes in CA3 of the hippocampal circuit. Our system is considered more flexible and adaptable to networks with different connectivity, not just feedforward similar to that in the hippocampus. Moreover, we were interested in mimicking the overall spiking activity of the network and not mapping an input-output transformation.

Another important novelty of our system regards directionality. To our best knowledge, this neuroprosthetic system is the first to implement a truly bidirectional interaction with a SNN through a hard real-time interface. We recorded activity from the first module (via multiple sources); when a criterion was met, the device stimulated the second module (this is how a 'typical' closed-loop in neuroscience works, for a review see (Greenwald et al. 2016)). The novelty is simultaneously monitoring multiple sources from another module and delivering the stimulation when the triggering event is detected. To date and as far as we are aware of, only Jung and colleagues (Jung et al. 2001) have performed a bidirectional interface to a neuromorphic device, but their models were not precise at the spike level (modelling neuron populations) and they used non configurable analogue electronics, which resulted in an experiment-specific setup. The other neuroprosthetic devices that have been proposed in the literature can implement a 'unidirectional' artificial link only from one area to another (or maybe the same) but not doubling it. Here, we are not imposing any preferred directionality to the communication; networks are self-organizing on the basis of their intrinsic natural relationship (we are not imposing who is driving whom). This approach has the main advantage of informing both brain regions (i.e., neuronal modules, in our case) that an event occurred in the other region, given that interaction in the brain is intrinsically bidirectional (Roelfsema and Holtmaat 2018). For example, in the sensorimotor system, sensory simulation can help motor recovery (Cuppone et al. 2018), and motor learning can enhance sensory functions (Ostry et al. 2010, Takeuchi and Izumi 2013). Applications of our neuroprosthetic systems to conditions where the sensorimotor interaction is impaired would allow restoration of both communication channels, suggesting improvements in current rehabilitation therapies. Moreover, although tested on a bimodular system, the neuromorphic FPGA board can be easily upgraded to play the bridging role on an arbitrary number (within reason) of different neuronal circuits. A recent work (Forró et al. 2018) developed directional networks of primary hippocampal neurons on MEA and compared the information flow of these networks with respect to bidirectional networks (similar to our bimodular preparations). They found that without physically imposing a unidirectional configuration, there is a continuous back and forth communication between nodes thus suggesting the importance of a bidirectional communication in a healthy network.

The second paradigm we tested was based on the use of a biomimetic SNN to 'substitute' a missing/damaged neuronal population. Currently, SNN applications span different fields, including computational neuroscience (Markram 2012, Melozzi et al. 2017), and very recently, they were used for sensory encoding in hand prosthesis for amputees (Osborn et al. 2018, Valle et al. 2018). SNNs can be simulated in software (Goodman and Brette 2009) and/or neuromorphic hardware (Thakur et al. 2018). As time and energy consumption are fundamental in neuroprosthetic applications for translational purposes, the use of hardware-based computing systems becomes mandatory.

In general, hybrid systems composed of *in vitro* BNNs coupled to SNNs are rare. In one approach, the SNN served as a self-organizing classifier of activity patterns exhibited by the BNN, with output of the SNN being subsequently used to control the behavior of a robot (Pizzi et al. 2009). Other studies focused on the unidirectional or bidirectional influence of the two networks, investigating the dynamics of the interaction between the BNN and SNN in which the SNN played a role of an artificial counterpart of its biological original (Bruzzone et al. 2015, Chou et al. 2015). However, closed-loop effects in those hybrid networks were not thoroughly determined. In one of these studies, only unidirectional connectivity was considered with input from the SNN to the BNN, which was also simulated beforehand (Bruzzone et al. 2015). In this study, we established hybrid communication in the case of an entire neuronal population that needed substitution.

A study by Chou *et al*. (Chou et al. 2015) implemented a bidirectional interface between an SNN and a retinal slice obtained from an adult rat and recorded by an MEA. This system is quite interesting, but there is a 1 s delay between the BNN and SNN interactions. Therefore, this delay is 3 orders of magnitude larger than that in our work, where the sampling of biological activity is never interrupted, and the step size of the SNN is 1 ms. The difference between the two systems is radical; bidirectional communication in real-time allows actual clinical application, whereas delays in the range of seconds prevent (or at least seriously reduce) the possibility of meaningful control of a biological system.

A recent study, inspired by a previous work (Hogri et al. 2015), implemented a hybrid interaction (Xu et al. 2018) between the cerebellum of a rat and an SNN implemented on FPGA. Their model involved 10k leaky integrate and fire (LIF) neurons and did not integrate other biomimetic behaviors, such as axonal delay, short-term plasticity and synaptic noise, unlike the IZH neurons implemented in our system. Both the hard real-time processing and simplified neuronal model (which allow mimicking the richness of the electrophysiological patterns *in vivo*) are mandatory for reproducing the biological dynamics of living neural networks and for performing useful real-time hybrid experiments.

A limitation of the present work is that we deliberately chose to downsample both the number of biological neurons recorded through a low density MEA and the number of artificial neurons

implemented on the FPGA. For the purpose of detecting network-wide activity, this oversimplification of biological complexity can be acceptable to test the functionality of the device and the feasibility of the approach, but if the goal is to functionally replace a biological network, a higher resolution would be preferable. It is worth underlying that this hardware implementation is not exploiting the full resources of the FPGA, thus in follow-up studies, also thanks to the flexibility of our system, we foresee to scale up the number of neurons and synapses and to upgrade the computational algorithms to deal with more complex experimental designs. From a technological point of view, the current state of the art makes possible the use of devices with a large number (thousands) of recording electrodes (Berdondini et al. 2009, Frey et al. 2009). Such an improvement would also allow to have more information about functional connectivity of the biological network (Pastore et al. 2018) and thus developing more realistic, in terms of topology, artificial models. In this work, we arbitrarily modeled the network connectivity with a random adjacency matrix since the use of MEAs with 60 electrodes made impossible to correctly identify the topological properties (e.g., hubs, recurring connections, modules, etc.) of the network under investigation.

In this work, we demonstrated the possibility to design a neuromorphic all-hardware prosthesis capable of artificially reconnect two disconnected neuronal networks or artificially replacing one entire neuronal sub-network. We are aware that the road is still long to target human applications. Despite this, we think that the extensive work performed represent an important milestone to start from. The next fundamental (and critical) step would be to test the neuromorphic prosthesis *in vivo*, for example on animal models affected by ischemic or traumatic lesions (Guggenmos et al. 2013). Even if the adaptation to the new experimental setups will require time, we believe these are necessary steps to further push the translational potential of our system, which will be able to create real innovation in the clinical therapeutics.

## Personal contribution

To achieve the results presented in this chapter we implemented a teamwork, including all the partners belonging to the BrainBow project. To better appreciate my contribution to the project, here I specify all the tasks that I performed.

I joined the BrainBow project at the time of the first release of the neuroprosthesis developed by our collaborators in Bordeaux (in particular Dr. Yannick Bornat and Dr. Timothée Levi). My first task was to test and validate the device and interface it with cell cultures (with both uniform and modular cultures) for electrophysiological experiments in vitro. To successfully test the device, I configured the electrophysiological setup, which included: the MEA commercial system, an electrical stimulator (to be triggered by the neuroprosthesis), a general purpose computer and the neuroprosthesis itself.

During testing and validation of a new device many practical issues can raise and therefore a tight collaboration with the developers in Bordeaux was needed. As a beta tester, I contributed to the development of a robust device that is still working with very rare issues. I implemented all the Matlab scripts, functions and classes to handle all the experimental phases on the fly. Regarding the offline signal processing, I designed all the methods to assess the performances of the system. I also implemented the scripts to send the parameters to the SNN on the FPGA with an intuitive approach in order to sweep parameters and obtain a library of SNNs. I designed and personally conducted the experimental sessions and I supervised a Master student involved in part of the experimental activities. I designed and performed the statistical analyses; I prepared most of the original figures and wrote almost entirely the main manuscript (which is the main reference of this chapter).

## Conclusions

Our neuromorphic prosthesis and the paradigms implemented herein represent the first example of a successful real-time next-generation neurobiohybrid system (Vassanelli and Mahmud 2016), implementing bidirectional reconnection between two neuronal networks with clear-cut potential for applications to brain injury (Broccard et al. 2017). The implemented SNN reproduces in real-time the biological neural network dynamics. The use of a fully integrated hardware computing system allowed hard real-time performances and low power consumption, which are crucial for translational purposes related to therapeutic applications in humans (Kipke et al. 2008, Wang et al. 2010).

## References


Abdulkader, S. N., A. Atia and M.-S. M. Mostafa (2015). "Brain computer interfacing: applications and challenges." Egypt. Inform. J. **16**(2): 213–230.

Ambroise, M., T. Levi, Y. Bornat and S. Saighi (2013). Biorealistic spiking neural network on FPGA. 2013 47th Annual Conference on Information Sciences and Systems (CISS), Baltimore, MD, USA, IEEE.

Aviv, M. S., M. Pesce, S. Tilve, E. Chieregatti, Z. Zalevsky and F. Difato (2013). "Motility flow and growth-cone navigation analysis during *in vitro* neuronal development by long-term bright-field imaging." J. Biomed. Opt. **18**(11): 111415.

Bassett, D. S. and E. T. Bullmore (2009). "Human brain networks in health and disease." Curr Opin Neurol **22**(4): 340-347.

Ben-Ari, Y. (2001). "Developing networks play a similar melody." Trends in neurosciences **24**(6): 353-360.

Ben-Ari, Y., R. Khazipov, X. Leinekugel, O. Caillard and J. Gaiarsa (1997). "GABAA, NMDA and AMPA receptors: a developmentally regulated 'ménage à trois'." Trends Neurosci. **20**(11): 523–529.

Berdondini, L., K. Imfeld, A. Maccione, M. Tedesco, S. Neukom, M. Koudelka-Hep and S. Martinoia (2009). "Active pixel sensor array for high spatio-temporal resolution electrophysiological recordings from single cell to large scale neuronal networks." Lab on a Chip **9**(18): 2644-2651.

Berger, T. W., D. Song, R. H. Chan, V. Z. Marmarelis, J. LaCoss, J. Wills, R. E. Hampson, S. A. Deadwyler and J. J. Granacki (2012). "A hippocampal cognitive prosthesis: multi-input, multi-output nonlinear modeling and VLSI implementation." IEEE Trans. Neural Syst. Rehabil. Eng. **20**(2): 198–211.

Biffi, E., G. Regalia, A. Menegon, G. Ferrigno and A. Pedrocchi (2013). "The influence of neuronal density and maturation on network activity of hippocampal cell cultures: a methodological study." PloS one **8**(12): e83899.

Bisio, M., A. Bosca, V. Pasquale, L. Berdondini and M. Chiappalone (2014). "Emergence of bursting activity in connected neuronal sub-populations." PLoS One **9**(9): e107400.

Blau, A., T. Neumann, C. Ziegler and F. Benfenati (2009). "Replica-moulded polydimethylsiloxane culture vessel lids attenuate osmotic drift in long-term cell cultures." J. Biosci. **34**(1): 59–69.

Bonifazi, P., F. Difato, P. Massobrio, G. L. Breschi, V. Pasquale, T. Levi, M. Goldin, Y. Bornat, M. Tedesco, M. Bisio, S. Kanner, R. Galron, J. Tessadori, S. Taverna and M. Chiappalone (2013). "In vitro large-scale experimental and theoretical studies for the realization of bi-directional brain-prostheses." Front Neural Circuits **7**: 40.

Bonifazi, P., F. Difato, P. Massobrio, G. L. Breschi, V. Pasquale, T. Levi, M. Goldin, Y. Bornat, M. Tedesco, M. Bisio, S. Kanner, R. Galron, J. Tessadori, S. Taverna and M. Chiappalone (2013). "*In vitro* large-scale experimental and theoretical studies for the realization of bi-directional brain-prostheses." Front. Neural Circuits **7**: 40.

Bonifazi, P., M. E. Ruaro and V. Torre (2005). "Statistical properties of information processing in neuronal networks." Eur. J. Neurosci. **22**(11): 2953–2964.

Bouton, C. E., A. Shaikhouni, N. V. Annetta, M. A. Bockbrader, D. A. Friedenberg, D. M. Nielson, G. Sharma, P. B. Sederberg, B. C. Glenn and W. J. Mysiw (2016). "Restoring cortical control of functional movement in a human with quadriplegia." Nature **533**(7602): 247.

Broccard, F. D., S. Joshi, J. Wang and G. Cauwenberghs (2017). "Neuromorphic neural interfaces: from neurophysiological inspiration to biohybrid coupling with nervous systems." J. Neural. Eng. **14**(4): 041002.

Bruzzone, A., V. Pasquale, P. Nowak, J. Tessadori, P. Massobrio and M. Chiappalone (2015). "Interfacing in silico and *in vitro* neuronal networks." Conf. Proc. IEEE Eng. Med. Biol. Soc. **2015**: 3391–3394.

Carrel, A. and M. T BURROWS (1910). "Cultivation of adult tissues and organs outside of the body."

Journal of the American medical association **55**(16): 1379-1381.
Cassidy, A. and A. G. Andreou (2008). Dynamical digital silicon neurons. Biomedical Circuits and Systems Conference, 2008. BioCAS 2008., Baltimore, MD, USA, IEEE.
Chiappalone, M., M. Bove, A. Vato, M. Tedesco and S. Martinoia (2006). "Dissociated cortical networks show spontaneously correlated activity patterns during in vitro development." Brain research **1093**(1): 41-53.
Chiappalone, M., A. Vato, L. Berdondini, M. Koudelka-Hep and S. Martinoia (2007). "Network dynamics and synchronous activity in cultured cortical neurons." Int. J. Neural Syst. **17**(2): 87–103.
Chou, Z., J. Lim, S. Brown, M. Keller, J. Bugbee, F. Broccard, M. L. Khraiche, G. A. Silva and G. Cauwenberghs (2015). "Bidirectional neural interface: closed-loop feedback control for hybrid neural systems." Conf. Proc. IEEE Eng. Med. Biol. Soc. **2015**: 3949–3952.
Colombi, I., S. Mahajani, M. Frega, L. Gasparini and M. Chiappalone (2013). "Effects of antiepileptic drugs on hippocampal neurons coupled to micro-electrode arrays." Front Neuroeng **6**: 10.
Colombi, I., F. Tinarelli, V. Pasquale, V. Tucci and M. Chiappalone (2016). "A simplified *in vitro* experimental model encompasses the essential features of sleep." Front. Neurosci. **10**: 315.
Cotterill, E., D. Hall, K. Wallace, W. R. Mundy, S. J. Eglen and T. J. Shafer (2016). "Characterization of early cortical neural network development in multiwell microelectrode array plates." Journal of biomolecular screening **21**(5): 510-519.
Cuppone, A. V., M. Semprini and J. Konczak (2018). "Consolidation of human somatosensory memory during motor learning." Behav. Brain Res. **347**: 184–192.
Cutts, C. S. and S. J. Eglen (2014). "Detecting pairwise correlations in spike trains: an objective comparison of methods and application to the study of retinal waves." Journal of Neuroscience **34**(43): 14288-14303.
Difato, F., M. Dal Maschio, E. Marconi, G. Ronzitti, A. Maccione, T. Fellin, L. Berdondini, E. Chieregatti, F. Benfenati and A. Blau (2011). "Combined optical tweezers and laser dissector for controlled ablation of functional connections in neural networks." J Biomed Opt **16**(5): 051306.
Difato, F., M. Dal Maschio, E. Marconi, G. Ronzitti, A. Maccione, T. Fellin, L. Berdondini, E. Chieregatti, F. Benfenati and A. Blau (2011). "Combined optical tweezers and laser dissector for controlled ablation of functional connections in neural networks." J. Biomed. Opt. **16**(5): 051306.
Difato, F., L. Schibalsky, F. Benfenati and A. Blau (2011). "Integration of optical manipulation and electrophysiological tools to modulate and record activity in neural networks." Int. J. Optomechatronics **5**(3): 191–216.
Eytan, D., A. Minerbi, N. Ziv and S. Marom (2004). "Dopamine-induced dispersion of correlations between action potentials in networks of cortical neurons." J. Neurophysiology **92**(3): 1817–1824.
Feigin, V. L., B. Norrving and G. A. Mensah (2017). "Global burden of stroke." Circ. Res. **120**(3): 439–448.
Flesher, S. N., J. L. Collinger, S. T. Foldes, J. M. Weiss, J. E. Downey, E. C. Tyler-Kabara, S. J. Bensmaia, A. B. Schwartz, M. L. Boninger and R. A. Gaunt (2016). "Intracortical microstimulation of human somatosensory cortex." Sci. Transl. Med. **8**(361): 361ra141.
Forro, C., G. Thompson-Steckel, S. Weaver, S. Weydert, S. Ihle, H. Dermutz, M. J. Aebersold, R. Pilz, L. Demko and J. Voros (2018). "Modular microstructure design to build neuronal networks of defined functional connectivity." Biosens Bioelectron **122**: 75-87.
Forró, C., G. Thompson-Steckel, S. Weaver, S. Weydert, S. Ihle, H. Dermutz, M. J. Aebersold, R. Pilz, L. Demkó and J. Vörös (2018). "Modular microstructure design to build neuronal networks of defined functional connectivity." Biosensors and Bioelectronics **122**: 75-87.
Fortunato, S. (2010). "Community detection in graphs." Physics reports **486**(3-5): 75-174.
Frega, M., V. Pasquale, M. Tedesco, M. Marcoli, A. Contestabile, M. Nanni, L. Bonzano, G. Maura and M. Chiappalone (2012). "Cortical cultures coupled to micro-electrode arrays: a novel approach to perform *in vitro* excitotoxicity testing." Neurotoxicol. Teratol. **34**(1): 116–127.
Frega, M., S. H. Van Gestel, K. Linda, J. Van der Raadt, J. Keller, J.-R. Van Rhijn, D. Schubert, C. A. Albers

and N. N. Kasri (2017). "Rapid neuronal differentiation of induced pluripotent stem cells for measuring network activity on micro-electrode arrays." JoVE (Journal of Visualized Experiments)(119): e54900.

Frey, U., U. Egert, F. Heer, S. Hafizovic and A. Hierlemann (2009). "Microelectronic system for high-resolution mapping of extracellular electric fields applied to brain slices." Biosensors and Bioelectronics **24**(7): 2191-2198.

Giard, D. J., S. A. Aaronson, G. J. Todaro, P. Arnstein, J. H. Kersey, H. Dosik and W. P. Parks (1973). "In vitro cultivation of human tumors: establishment of cell lines derived from a series of solid tumors." Journal of the National Cancer Institute **51**(5): 1417-1423.

Goodman, D. F. and R. Brette (2009). "The brian simulator." Front. Neurosci. **3**(2): 192–197.

Grassia, F., T. Kohno and T. Levi (2016). "Digital hardware implementation of a stochastic two-dimensional neuron model." J. Physiol. Paris **110**(4 Pt A): 409–416.

Greenwald, E., M. R. Masters and N. V. Thakor (2016). "Implantable neurotechnologies: bidirectional neural interfaces--applications and VLSI circuit implementations." Med. Biol. Eng. Comput. **54**(1): 1–17.

Guggenmos, D. J., M. Azin, S. Barbay, J. D. Mahnken, C. Dunham, P. Mohseni and R. J. Nudo (2013). "Restoration of function after brain damage using a neural prosthesis." Proc Natl Acad Sci U S A **110**(52): 21177-21182.

Habibey, R., A. Golabchi, S. Latifi, F. Difato and A. Blau (2015). "A microchannel device tailored to laser axotomy and long-term microelectrode array electrophysiology of functional regeneration." Lab Chip **15**(24): 4578-4590.

Harrison, R. G. (1912). "The cultivation of tissues in extraneous media as a method of morpho-genetic study." The Anatomical Record **6**(4): 181-193.

Harrison, R. R. (2003). A low-power integrated circuit for adaptive detection of action potentials in noisy signals. Proceedings of the 25th Annual International Conference of the IEEE Engineering in Medicine and Biology Society (IEEE Cat. No. 03CH37439), Cancun, Mexico, IEEE.

Hayashi, K., R. Kawai-Hirai, A. Harada and K. Takata (2003). "Inhibitory neurons from fetal rat cerebral cortex exert delayed axon formation and active migration *in vitro*." J. Cell Sci. **116**(21): 4419–4428.

Hogri, R., S. A. Bamford, A. H. Taub, A. Magal, P. Del Giudice and M. Mintz (2015). "A neuro-inspired model-based closed-loop neuroprosthesis for the substitution of a cerebellar learning function in anesthetized rats." Sci. Rep. **5**: 8451.

Ito, D., H. Tamate, M. Nagayama, T. Uchida, S. Kudoh and K. Gohara (2010). "Minimum neuron density for synchronized bursts in a rat cortical culture on multi-electrode arrays." Neuroscience **171**(1): 50-61.

Izhikevich, E. M. (2003). "Simple model of spiking neurons." IEEE Trans. Neural. Netw. **14**(6): 1569–1572.

Izhikevich, E. M. (2004). "Which model to use for cortical spiking neurons?" IEEE Trans. Neural. Netw. **15**(5): 1063–1070.

Izhikevich, E. M. and G. M. Edelman (2008). "Large-scale model of mammalian thalamocortical systems." Proc. Natl. Acad. Sci. U. S. A. **105**(9): 3593–3598.

Javier, G. O., J. Soriano, E. Alvarez-Lacalle, S. Teller and J. Casademunt (2013). "Noise focusing and the emergence of coherent activity in neuronal cultures." Nat. Phys. **9**(9): 582.

Johnson, H. A., A. Goel and D. V. Buonomano (2010). "Neural dynamics of *in vitro* cortical networks reflects experienced temporal patterns." Nature Neurosci. **13**(8): 917.

Jung, R., E. J. Brauer and J. J. Abbas (2001). "Real-time interaction between a neuromorphic electronic circuit and the spinal cord." IEEE Transactions on neural systems and rehabilitation engineering **9**(3): 319-326.

Kanner, S., M. Bisio, G. Cohen, M. Goldin, M. Tedesco, Y. Hanein, E. Ben-Jacob, A. Barzilai, M. Chiappalone and P. Bonifazi (2015). "Design, surface treatment, cellular plating, and culturing of modular neuronal networks composed of functionally inter-connected circuits." J. Vis.

Exp.(98): doi: 10.3791/52572.
Kipke, D. R., W. Shain, G. Buzsaki, E. Fetz, J. M. Henderson, J. F. Hetke and G. Schalk (2008). "Advanced neurotechnologies for chronic neural interfaces: new horizons and clinical opportunities." J. Neurosci. **28**(46): 11830–11838.
Kleim, J. A. and T. A. Jones (2008). "Principles of experience-dependent neural plasticity: implications for rehabilitation after brain damage." J Speech Lang Hear Res **51**(1): S225-239.
Klinshov, V. V., J.-n. Teramae, V. I. Nekorkin and T. Fukai (2014). "Dense neuron clustering explains connectivity statistics in cortical microcircuits." PloS one **9**(4): e94292.
Kohler, F., C. A. Gkogkidis, C. Bentler, X. Wang, M. Gierthmuehlen, J. Fischer, C. Stolle, L. M. Reindl, J. Rickert, T. Stieglitz, T. Ball and M. Schuettler (2017). "Closed-loop interaction with the cerebral cortex: a review of wireless implant technology." Brain Comput Interfaces **4**(3): 146–154.
Kozai, T. D., A. S. Jaquins-Gerstl, A. L. Vazquez, A. C. Michael and X. T. Cui (2015). "Brain tissue responses to neural implants impact signal sensitivity and intervention strategies." ACS Chem. Neurosci. **6**(1): 48–67.
le Feber, J., N. Erkamp, M. J. Van Putten and J. Hofmeijer (2017). "Loss and recovery of functional connectivity in cultured cortical networks exposed to hypoxia." Journal of neurophysiology **118**(1): 394-403.
Levy, O., N. E. Ziv and S. Marom (2012). "Enhancement of neural representation capacity by modular architecture in networks of cortical neurons." Eur J Neurosci **35**(11): 1753-1760.
Liu, X., E. Krawczyk, F. A. Suprynowicz, N. Palechor-Ceron, H. Yuan, A. Dakic, V. Simic, Y.-L. Zheng, P. Sripadhan and C. Chen (2017). "Conditional reprogramming and long-term expansion of normal and tumor cells from human biospecimens." Nature protocols **12**(2): 439.
Luczak, A., B. L. McNaughton and K. D. Harris (2015). "Packet-based communication in the cortex." Nat. Rev. Neurosci. **16**(12): 745–755.
Maas, A. I. R., D. K. Menon, P. D. Adelson, N. Andelic, M. J. Bell, A. Belli, P. Bragge, A. Brazinova, A. Buki, R. M. Chesnut, G. Citerio, M. Coburn, D. J. Cooper, A. T. Crowder, E. Czeiter, M. Czosnyka, R. Diaz-Arrastia, J. P. Dreier, A. C. Duhaime, A. Ercole, T. A. van Essen, V. L. Feigin, G. Gao, J. Giacino, L. E. Gonzalez-Lara, R. L. Gruen, D. Gupta, J. A. Hartings, S. Hill, J. Y. Jiang, N. Ketharanathan, E. J. O. Kompanje, L. Lanyon, S. Laureys, F. Lecky, H. Levin, H. F. Lingsma, M. Maegele, M. Majdan, G. Manley, J. Marsteller, L. Mascia, C. McFadyen, S. Mondello, V. Newcombe, A. Palotie, P. M. Parizel, W. Peul, J. Piercy, S. Polinder, L. Puybasset, T. E. Rasmussen, R. Rossaint, P. Smielewski, J. Soderberg, S. J. Stanworth, M. B. Stein, N. von Steinbuchel, W. Stewart, E. W. Steyerberg, N. Stocchetti, A. Synnot, B. Te Ao, O. Tenovuo, A. Theadom, D. Tibboel, W. Videtta, K. K. W. Wang, W. H. Williams, L. Wilson, K. Yaffe, T. P. In and Investigators (2017). "Traumatic brain injury: integrated approaches to improve prevention, clinical care, and research." Lancet Neurol. **16**(12): 987–1048.
Markram, H. (2012). "The human brain project." Sci. Am. **306**(6): 50–55.
Mata, A., A. J. Fleischman and S. Roy (2005). "Characterization of polydimethylsiloxane (PDMS) properties for biomedical micro/nanosystems." Biomed. Microdevices **7**(4): 281–293.
Melozzi, F., M. M. Woodman, V. K. Jirsa and C. Bernard (2017). "The virtual mouse brain: a computational neuroinformatics platform to study whole mouse brain dynamics." eNeuro **4**(3): doi: 10.1523/ENEURO.0111–1517.2017.
Meunier, D., R. Lambiotte, A. Fornito, K. D. Ersche and E. T. Bullmore (2009). "Hierarchical modularity in human brain functional networks." Front Neuroinform **3**: 37.
Nakai, J. and Y. Kawasaki (1959). "Studies on the mechanism determining the course of nerve fibers in tissue culture." Zeitschrift für Zellforschung und mikroskopische Anatomie **51**(1): 108-122.
Nudo, R. J. (1999). "Recovery after damage to motor cortical areas." Curr Opin Neurobiol **9**(6): 740-747.
Okujeni, S., S. Kandler and U. Egert (2017). "Mesoscale architecture shapes initiation and richness of spontaneous network activity." Journal of Neuroscience **37**(14): 3972-3987.
Osborn, L. E., A. Dragomir, J. L. Betthauser, C. L. Hunt, H. H. Nguyen, R. R. Kaliki and N. V. Thakor (2018).

"Prosthesis with neuromorphic multilayered e-dermis perceives touch and pain." Sci. Robot. **20**(9): eaat3818.

Ostry, D. J., M. Darainy, A. A. Mattar, J. Wong and P. L. Gribble (2010). "Somatosensory plasticity and motor learning." J. Neurosci. **30**(15): 5384–5393.

Panzeri, S., C. D. Harvey, E. Piasini, P. E. Latham and T. Fellin (2017). "Cracking the Neural Code for Sensory Perception by Combining Statistics, Intervention, and Behavior." Neuron **93**(3): 491-507.

Pasquale, V., P. Massobrio, L. L. Bologna, M. Chiappalone and S. Martinoia (2008). "Self-organization and neuronal avalanches in networks of dissociated cortical neurons." Neuroscience **153**(4): 1354-1369.

Pastore, V. P., P. Massobrio, A. Godjoski and S. Martinoia (2018). "Identification of excitatory-inhibitory links and network topology in large-scale neuronal assemblies from multi-electrode recordings." PLoS computational biology **14**(8): e1006381.

Pesquet, J.-C., H. Krim and H. Carfantan (1996). "Time-invariant orthonormal wavelet representations." IEEE Trans. Signal Process. **44**(8): 1964–1970.

Peterson, E. R. and M. R. Murray (1955). "Myelin sheath formation in cultures of avian spinal ganglia." American Journal of Anatomy **96**(3): 319-355.

Pirog, A., Y. Bornat, R. Perrier, M. Raoux, M. Jaffredo, A. Quotb, J. Lang, N. Lewis and S. Renaud (2018). "Multimed: an integrated, multi-application platform for the real-time recording and sub-millisecond processing of biosignals." Sensors (Basel) **18**(7): 2099.

Pizzi, R. M., D. Rossetti, G. Cino, D. Marino, A. L. Vescovi and W. Baer (2009). "A cultured human neural network operates a robotic actuator." Biosystems **95**(2): 137–144.

Potter, S. M. (2010). "Closing the loop between neurons and neurotechnology." Front. Neurosci. **4**: 15.

Potter, S. M. and T. B. DeMarse (2001). "A new approach to neural cell culture for long-term studies." J Neurosci Methods **110**(1-2): 17-24.

Quotb, A., Y. Bornat, M. Raoux, J. Lang and S. Renaud (2012). NeuroBetaMed: A re-configurable wavelet-based event detection circuit for in vitro biological signals. IEEE International Symposium on Circuits and Systems (ISCAS). Seoul, South Korea, IEEE**:** 1532 - 1535.

Roelfsema, P. R. and A. Holtmaat (2018). "Control of synaptic plasticity in deep cortical networks." Nat. Rev. Neurosci. **19**(3): 166–180.

Rosin, B., M. Slovik, R. Mitelman, M. Rivlin-Etzion, S. N. Haber, Z. Israel, E. Vaadia and H. Bergman (2011). "Closed-loop deep brain stimulation is superior in ameliorating parkinsonism." Neuron **72**(2): 370-384.

Rudolph, M. and A. Destexhe (2005). "An extended analytic expression for the membrane potential distribution of conductance-based synaptic noise." Neural Comput. **17**(11): 2301–2315.

Shein-Idelson, M., E. Ben-Jacob and Y. Hanein (2011). "Engineered neuronal circuits: a new platform for studying the role of modular topology." Front Neuroeng **4**: 10.

Soloperto, A., M. Bisio, G. Palazzolo, M. Chiappalone, P. Bonifazi and F. Difato (2016). "Modulation of neural network activity through single cell ablation: an in vitro model of minimally invasive neurosurgery." Molecules **21**(8): 1018.

Takeuchi, N. and S. Izumi (2013). "Rehabilitation with poststroke motor recovery: a review with a focus on neural plasticity." Stroke Res. Treat. **2013**: 128641.

Taylor, A. M. and N. L. Jeon (2010). "Micro-scale and microfluidic devices for neurobiology." Curr. Opin. Neurobiol. **20**(5): 640–647.

Tessadori, J., M. Bisio, S. Martinoia and M. Chiappalone (2012). "Modular neuronal assemblies embodied in a closed-loop environment: toward future integration of brains and machines." Front Neural Circuits **6**: 99.

Thakur, C. S. T., J. Molin, G. Cauwenberghs, G. Indiveri, K. Kumar, N. Qiao, J. Schemmel, R. M. Wang, E. Chicca and J. Olson Hasler (2018). "Large-scale neuromorphic spiking array processors: A quest to mimic the brain." Frontiers in neuroscience **12**: 891.

Tuckwell, H. C., F. Y. Wan and J.-P. Rospars (2002). "A spatial stochastic neuronal model with Ornstein–

Uhlenbeck input current." Biol. Cybern. **86**(2): 137–145.
Turrigiano, G. G. (2008). "The self-tuning neuron: synaptic scaling of excitatory synapses." Cell **135**(3): 422-435.
Valle, G., A. Mazzoni, F. Iberite, E. D'Anna, I. Strauss, G. Granata, M. Controzzi, F. Clemente, G. Rognini, C. Cipriani, T. Stieglitz, F. M. Petrini, P. M. Rossini and S. Micera (2018). "Biomimetic intraneural sensory feedback enhances sensation naturalness, tactile sensitivity, and manual dexterity in a bidirectional prosthesis." Neuron **100**(1): 37–45.
Van Pelt, J., M. Corner, P. Wolters, W. Rutten and G. Ramakers (2004). "Longterm stability and developmental changes in spontaneous network burst firing patterns in dissociated rat cerebral cortex cell cultures on multielectrode arrays." Neuroscience letters **361**(1-3): 86-89.
Vassanelli, S. and M. Mahmud (2016). "Trends and challenges in neuroengineering: toward "intelligent" Neuroprostheses through brain-"brain inspired systems" communication." Front Neurosci. **10**: 438.
Vassanelli, S. and M. Mahmud (2016). "Trends and Challenges in Neuroengineering: Toward "Intelligent" Neuroprostheses through Brain-"Brain Inspired Systems" Communication." Front Neurosci **10**: 438.
Wagenaar, D. A., J. Pine and S. M. Potter (2004). "Effective parameters for stimulation of dissociated cultures using multi-electrode arrays." J. Neurosci. Methods **138**(1-2): 27–37.
Wagenaar, D. A., J. Pine and S. M. Potter (2006). "An extremely rich repertoire of bursting patterns during the development of cortical cultures." BMC neuroscience **7**(1): 11.
Wagenaar, D. A., J. Pine and S. M. Potter (2006). "Searching for plasticity in dissociated cortical cultures on multi-electrode arrays." J. Negat. Results Biomed **5**: 16.
Wang, W., J. L. Collinger, M. A. Perez, E. C. Tyler-Kabara, L. G. Cohen, N. Birbaumer, S. W. Brose, A. B. Schwartz, M. L. Boninger and D. J. Weber (2010). "Neural interface technology for rehabilitation: exploiting and promoting neuroplasticity." Phys. Med. Rehabil. Clin. N. Am. **21**(1): 157–178.
Weibel, D. B., W. R. Diluzio and G. M. Whitesides (2007). "Microfabrication meets microbiology." Nat. Rev. Microbiol. **5**(3): 209–218.
Whitesides, G. M., E. Ostuni, S. Takayama, X. Jiang and D. E. Ingber (2001). "Soft lithography in biology and biochemistry." Annu. Rev. Biomed. Eng. **3**: 335–373.
Xu, T., N. Xiao, X. Zhai, C. P. Kwan and C. Tin (2018). "Real-time cerebellar neuroprosthetic system based on a spiking neural network model of motor learning." J. Neural. Eng. **15**(1): 016021.
Yamamoto, H., S. Moriya, K. Ide, T. Hayakawa, H. Akima, S. Sato, S. Kubota, T. Tanii, M. Niwano, S. Teller, J. Soriano and A. Hirano-Iwata (2018). "Impact of modular organization on dynamical richness in cortical networks." Sci Adv **4**(11): eaau4914.
Zamora-López, G., Y. Chen, G. Deco, M. L. Kringelbach and C. Zhou (2016). "Functional complexity emerging from anatomical constraints in the brain: the significance of network modularity and rich-clubs." Scientific reports **6**: 38424.
Zhang, S.-C., M. Wernig, I. D. Duncan, O. Brüstle and J. A. Thomson (2001). "In vitro differentiation of transplantable neural precursors from human embryonic stem cells." Nature biotechnology **19**(12): 1129.

# Chapter 3: Rectify: *ex vivo* neuroprosthesis

## Overview

In this chapter, I will describe the development of a Simulink (Mathworks) model for real-time activity dependent stimulation of mouse brain slices (recorded through MEA) in order to suppress ictal-like events. The advantage of using *ex vivo* electrophysiological techniques consists in preserving, at least in part, the original architecture and connectivity of the brain regions of interest (ROI).This work was part of the Marie Skłodowska Curie project Re.B.Us (Rewiring Brain Units) granted to Dr G. Panuccio (https://www.rebus-project.eu/). One of the project's aims was to suppress ictal-like activity of brain slices with specific patterns of electrical stimulation (cf. Chapter 1, Rectify). For that purpose, I developed a closed-loop system, implemented in Simulink, which functionally reconnects two disconnected brain areas in order to prevent or reduce ictal-like discharges.

## Introduction

Epilepsy is a common neurologic disease, affecting 1,2% of the US population (Zack and Kobau 2017). In the majority of patients, epilepsy can be controlled with anti-epileptic drugs, but approximately one third have drug-resistant disease (Salanova et al. 2015). One option consists in the resective surgery; this procedure can be particularly useful if the seizure focus is well localized in a part of a brain that can be removed with minor side-effects. Another option uses electrical stimulation. This procedure is a promising approach if multiple seizure foci are present, the focus cannot be easily localized or when removing brain tissue is not possible due to the localization. It is worth noticing that brain stimulation can be applied either within or outside the seizure focus.

Non-focal stimulation assumes that stimulation applied to a critical location can suppress seizures in a wide brain region (Chiang et al. 2013) (possible targets studied are: the thalamus (Hamani et al. 2008), cerebellum (Davis 2000), sub-thalamic nucleus (Lado et al. 2003) and others).

Focal stimulation assumes that the electrical stimuli can suppress seizures originating at that location (Wyckhuys et al. 2007).

Besides the location, the stimulation frequency, current amplitude and pulse-width can be also crucial. Both low (<10 Hz) and high (>50 Hz) regular, open-loop stimulation has been shown to generate a reduction of seizure frequency. Low frequency regular stimulation (below 10Hz) has been shown to generate a reduction of seizure frequency *in-vitro* (Jerger and Schiff 1995, D'Arcangelo et al. 2005) and *in vivo* (Weiss et al. 1995, Wozny et al. 2017). High frequency stimulation is mainly used in DBS where it was proven in different studies to reduce the likelihood of ictal discharges (Chang 2018) by means of a desynchronization of the background activity. The main drawback of high frequency stimulation

is the amount of stimuli and thus the electric charge delivered to the patient that can have negative side effects. In a recent study on non-human primates (Wozny et al. 2017), low frequency stimulation was studied. In this study, the authors identified the combination of 2 Hz hippocampal stimulation, with a pulse width of 150 µs and 4mA amplitude as the one that maximally suppressed local hippocampal activity. After a series of chronic experiments, they pointed out that low-frequency hippocampal stimulation:

- diminish when delivered continuously but are maintained when stimulation is cycled on and off,
- depends on circadian rhythms,
- do not necessarily confer seizure protective effects.

They concluded that high frequency stimulation have a suppressive effect in acute and is capable of aborting seizure activity while low-frequency stimulation can be useful to reduce the likelihood of those events. Therefore, they suggested a possible synergistic stimulation fashion in which low-frequency can be chronically delivered decreasing the likelihood of seizure occurrence whereas targeted HFS may terminate any epileptiform activity (Wozny et al. 2017). This kind of stimulation paradigm is somehow implemented in the NeuroPace RNS system (Hartshorn and Jobst 2018, Sisterson et al. 2019), and in the Medtronic Activa PC+S and Activa RC+S, where a stimulation train is delivered in response (responsive stimulation) to an epileptic seizure detected in real-time through an ECoG array (cf. Chapter 1). Taken altogether, these observations point out that there is a need to find a way to reduce the likelihood and possibly abolish epileptic seizures, which implies the restoration of the healthy circuit.

Regarding *ex vivo* studies, changing the ionic composition of the artificial cerebrospinal fluid (ACSF) can acutely induce seizure-like activity in brain slices. More than thirty years ago, Rutecki and co-workers (Rutecki et al. 1987) demonstrated that continuous perfusion of brain slices with the convulsant drug 4-aminopyridine (4AP), a $K^+$ channel blocker, enhances both excitatory and inhibitory neurotransmission. This was crucial to allow the study of acute ictogenesis while keeping overall synaptic activity intact (Rutecki et al. 1987). The mouse hippocampus-entorhinal cortex (EC) slice is a functional model of epileptiform-like activity, induced by 4-AP and generated in the EC. The hippocampus and the EC (brain structures located in the medial temporal lobe) play a special role in the development of seizures, especially in the case of temporal lobe epilepsy. In a series of works, the group of Dr Avoli discovered that in combined mouse enthorinal cortex (EC)-hippocampus slices, superfused with 4AP or $Mg^{2+}$ -free medium, the CA3-driven interictal activity inhibits the EC propensity to generate ictal discharges (Barbarosie and Avoli 1997, Barbarosie et al. 2002). Moreover, they discovered that when this inhibitory control is removed by cutting the Schaffer collaterals (which

represent the main output pathway for CA3 pyramidal cells), electrical stimuli delivered in the subiculum at frequencies similar to those of CA3-driven interictal discharges are capable of depressing EC ictogenesis (D'Arcangelo et al. 2005). The same authors tested different, repetitive subicular stimulation protocols in a range between 0.2 to 10 Hz and they identified 1Hz as the best frequency to reduce the intensity and likelihood of ictal events (D'Arcangelo et al. 2005).

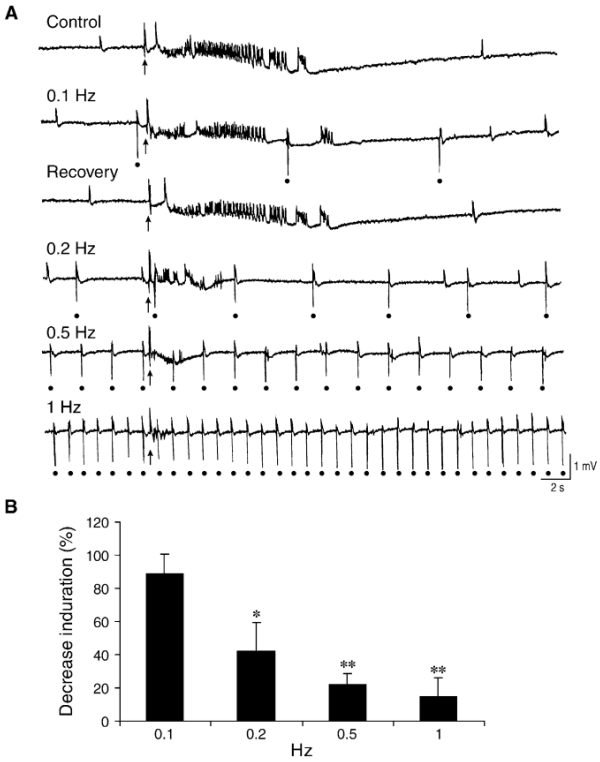


*Figure 3.1: Repetitive subicular stimulation reduces ictal-like discharges generated, during 4AP application, by EC networks in response to local single-shock stimulation of the deep layers at 0.01 Hz. (A) Field potential activity recorded from the EC middle layers under control conditions and during repetitive stimuli delivered in subiculum at frequencies ranging from 0.1 to 1 Hz. Stimuli delivered in the EC and subiculum are identified by arrows and filled circles, respectively. (B) Normalized reduction of the duration of the epileptiform responses induced by EC stimulation in 8 slices that were studied during different subicular stimulation protocols. from (D'Arcangelo et al. 2005)*

In this context, the idea behind the Re.B.Us (Rewiring Brain Units) project was to forward the CA3 interictal activity (after cutting the Shaffer collaterals) to the cortex. In order to do this, we designed a model within the Simulink Desktop Real-Time (The Mathworks) environment, capable of recording the activity, process the incoming signals and deliver stimulation in real-time to the Subiculum area.

## Materials and Methods

### *Dissection procedure*

Adult (4-6-week-old) male CD1 mice were perfused intracardially with ice-cold (0-2 °C) ACSF under deep isoflurane anesthesia and then decapitated. The brain was quickly removed (within 60 seconds, Figure 3.2) and placed in a small bowl containing equilibrated ice-cold (0-2 °C) cutting ACSF; the ACSF was continuously bubbled with a gas mixture (5% $CO_2$ and 95% $O_2$) to set it at pH 7.35-7.40. The brain was allowed to chill for 90-120 seconds (Figure 3.2 right panel). The cerebellum was removed, and a straight cut was made along the coronal plane to remove the frontal third of the brain. The isolated tissue block was glued with cyanoacrylate to the specimen disc of the vibratome (VT1000S, Leica, Germany) with the entorhinal cortex facing the blade and immediately placed in the slicing chamber containing carbogenated (5% $CO_2$ and 95% $O_2$) cold (0-2 °C) cutting ACSF (Figure 3.2 D). Hippocampus-EC slices (400 µm thick) were cut in the horizontal plane. Tissue sections were discarded until the hippocampus was clearly visible (usually ~900 µm). The two hemispheres were separated using a scalpel blade. The brain slices were gently transferred to a beaker using an inverted Pasteur pipette and rinsed twice with standard ACSF solution. The slices were then transferred to a commercial holding chamber (KF Technologies) containing carbogenated ACSF solution and incubated for approximately 20 minutes at 32 °C and then for at least 1 hour at room temperature (Figure 3.2 F).

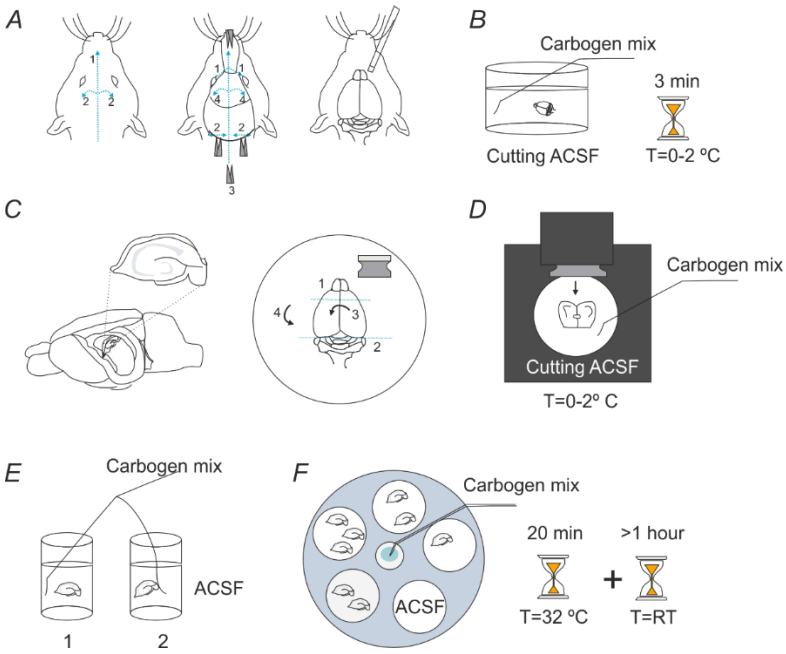


*Figure 3.2: Schematic representation of the brain slice preparation. A) Once the head is cut, the scalp is removed using scissors (left panel, 1-2). Using the scissors, two mediolateral cuts are made above the eyes (middle panel, 1); subsequently, two more cuts are made at the base of the head (middle panel, 2). Then, by a postero-anterior cut in the midline of the skull, two skull flaps are formed (middle panel 3). The brain is exposed using scissors, and a small spatula is used to gently extract it from the skull (left panel). C) The brain is immersed in ice-cold*

*ACSF for at least 2-3 min. C) The brain is placed in a cold Petri dish, and the cerebellum and one third of the frontal brain (along the coronal plane) are removed. D) The isolated tissue block is glued with cyanoacrylate to the specimen disc of the vibratome (VT1000S, Leica, Germany) with the entorhinal cortex facing the blade. E) The brain slices are gently transferred to a beaker using an inverted Pasteur pipette and rinsed twice with standard ACSF solution. F) The slices are then transferred to a commercial holding chamber (KF Technologies) containing carbogenated ACSF solution and incubated for approximately 20 min at 32 °C and then for at least 1 hour at room temperature. From (Colombi 2019)*

### *Custom chamber and perfusion control system for brain slices*

To keep the brain slices active for the MEA recording, we used a customized recording chamber inspired by the design of the patch-clamp recording chamber; this provides stable and reliable laminar flow (Figure 3.3). The use of this chamber allows the use of brain slices with a thickness up to 400 µm, making it possible to achieve a fair trade-off between tissue viability and intrinsic connectivity. The use of recording chambers with relatively small volume (~1.5 mL) and a high perfusion rate (~ 2 mL/min) allows adequate exchange of the perfusion medium. The customized chamber can be obtained from commercial sources (e.g., Crisel Instruments) at an affordable price or produced in-house using 3D printing technology.

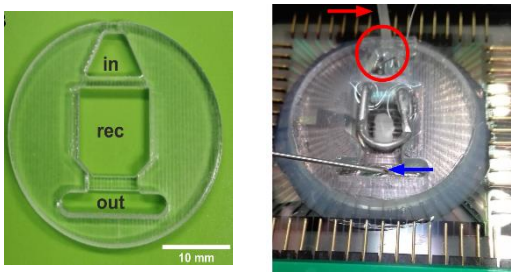


*Figure 3.3 Left, custom recording chamber. in: inlet reservoir to accommodate the heating cannula and the reference electrode; out: outlet reservoir to accommodate the suction needle; rec: recording chamber. Right, final assembly of the recording chamber mounted on the MEA chip (60MEA500/30iR-Ti-w/o, Multichannel Systems). A brain slice rests on the bottom and is held in place by the anchor. The red arrow indicates the PTFE tubing covering the heating cannula; the red circle indicates the reference electrode, a saturated KCl pellet submerged in ACSF in the inlet reservoir. The blue arrow indicates the suction needle in the outlet reservoir From (Colombi 2019).*

## Results

The setup depicted in (Figure 3.4) is made of:

- a 60-electrodes MEA (Multichannel Systems, MCS, Reutlingen, Germany). Planar microelectrodes are arranged in an 8×8 layout, excluding corners and one reference electrode, for a total of 59 TiN/SiN planar round recording electrodes (30 µm diameter; 200 µm center-to-center inter electrode distance);
- a MEA1060 amplifier (Multichannel Systems, MCS, Reutlingen, Germany);
- a custom made breakout box that makes possible the connection between the MEA amplifier, the MCRack commercial acquisition software (MCS) and the NI PCI-6255 acquisition card (National Instruments) accessible from Simulink.

- a commercial stimulator (STG4002, Multichannel system) is triggered by the Simulink model, if all the criteria are met. The pulse-width, the amplitude and the number of stimuli delivered for each TTL pulse were set before starting the experiment by means of the commercial software associated with the stimulator.

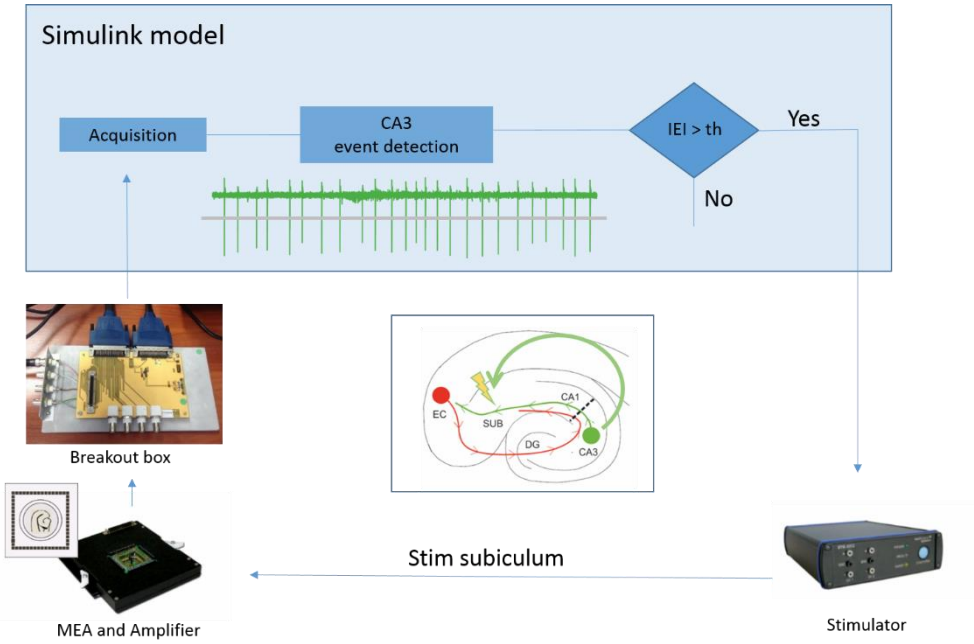


*Figure 3.4. Setup for closed-loop experiment. Data is first acquired and amplified through the commercial MEA system. The signal goes to Simulink thanks to a custom-made breakout box and a National Instrument card. Once in Simulink, signal from a CA3 electrode passes a threshold condition. If the Inter Event Interval (IEI) is higher than a threshold (th) a TTL pulse is delivered to a commercial stimulator that closes the loop by stimulating an electrode in the Subiculum area.*

Building a real-time system can be tough when using a procedural or object-oriented programming language (like C and C++). Implementing such systems by means of a graphical programming environment (like Simulink or LabView) can speed up the process. Simulink® Desktop Real-Time™ provides a real-time kernel for executing Simulink models on a Windows® or Mac laptop or desktop. Using a model-based design tool like this allows the user to focus on the algorithm and therefore reduces the development time (which is crucial especially in a lab environment where testing different prototypes is mandatory).

The Simulink model (reported in Figure 3.5) has different building blocks:

- **Analog input**. We recorded activity from 3 electrodes at a sampling rate of 1 kHz. The electrodes were usually choose from CA3 (the trigger channel), from EC (Entorhinal cortex) and from PC (Perirhinal cortex). All 60 electrodes could be contemporary recorded through the commercial McRack software (Multichannel Systems) to have a complete picture of the *ex vivo* tissue (an additional element, the Y-Box from Multichannel Systems is required in this

case). We decided to limit the number of electrodes recorded by Simulink in order to reduce the computational effort made by the general-purpose PC used to run the software and equipped with the National Instruments acquisition card.

- **Event detection subsystem**. Before starting the stimulation phase, we set a threshold on the trigger electrode (from CA3) to detect inter-ictal events which triggered an electrode stimulation back to the Subiculum area.
- **Time since last event subsystem**. A digital clock runs at the same sampling rate of the entire system (1 kHz). Every time an event is detected (i.e. threshold crossed) by the previous subsystem, a triggered subsystem (Figure 3.6) allows the digital clock to be reset to zero, thus implementing a time to last event counter.
- **A memory block**. This is necessary to get the value at the previous time step. If this block was not included, in case of detection, the time since last event would be always zero (as described in the previous block). Including it in the model allows to get the value of the clock one sample before the new detection (i.e. the real time since last detected event).
- **The enabling condition**. To deliver a stimulation the time since last event must be greater than the threshold. We usually set the enabling condition to 0.25s (i.e. 250ms of minimum distance between two consecutives stimuli) to avoid high-frequency stimulations.
- **The stimulation subsystem**. This is an enabled and triggered subsystem. When the enabling condition is true, it enables this subsystem but the output of the subsystem is true only when an event is detected (trigger event) and the enabling condition is true.
- **The digital output**. This block is triggered by the previous subsystem and delivers a TTL pulse, which triggers a commercial stimulator (STG4002, Multichannel system) that closes the loop.

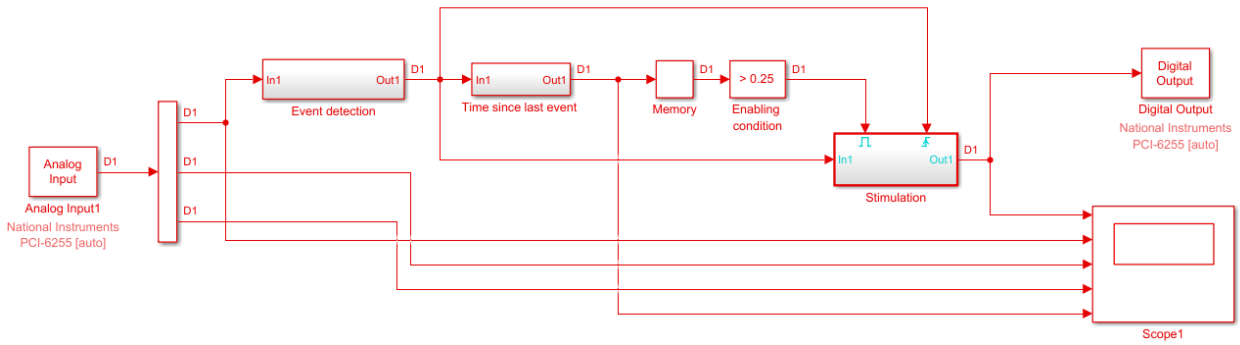


*Figure 3.5: Schematic of the Simulink Desktop Real model for real-time activity dependent stimulation. The sustem also includes a Scope block to monitor the activity in real time.*

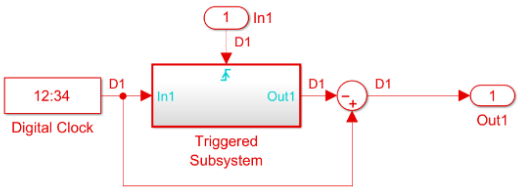


*Figure 3.6. Schematic of the "Time since last event" subsystem within of the main model. Each time a trigger event arrives (i.e. an interictal event is detected) the output starts counting from zero.*

So far, we performed only few successful tests. In the preliminary experiment that we present here, we used a brain slice depicted in Figure 3.7. We recorded 30' of spontaneous activity and recorded 8 ictal-like discharges. After a series of tests, we found the best parameters for the stimulation by visual inspection. The parameters that we choose were: biphasic pulse (100 µs per phase), bipolar (positive electrode 32, negative electrode 42) with an amplitude of 250 µA. Electrode 12 was connected to ground because of noise, electrode 15 was the ground electrode.

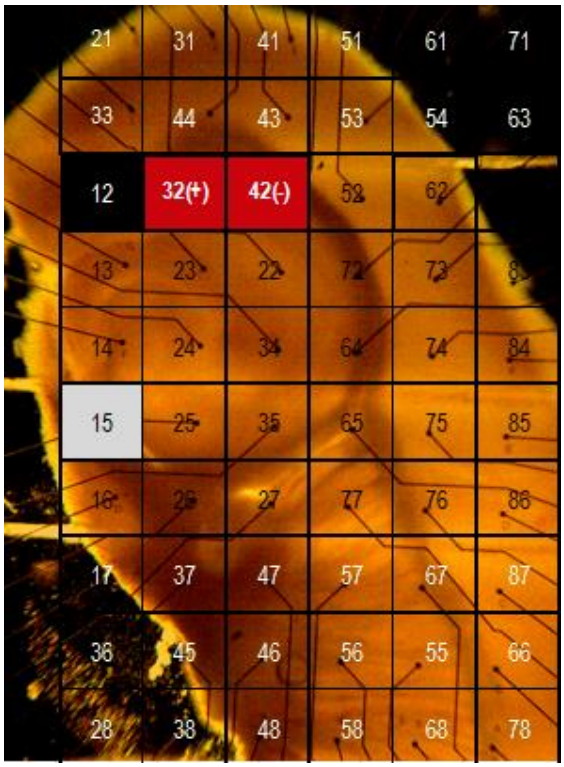


*Figure 3.7: Picture of the brain slice recorded during a preliminary experiment with the MCS electrode nomenclature superimposed.*

A screenshot from the scope block that we used to monitor the model performance shows the stimulation triggers (i.e. the digital output on the Simulink model that generates a TTL pulse on the National Instrument acquisition card and thus triggers the stimulator), the traces of 3 recorded channels (from CA3, EC and PC) and the time since last event.

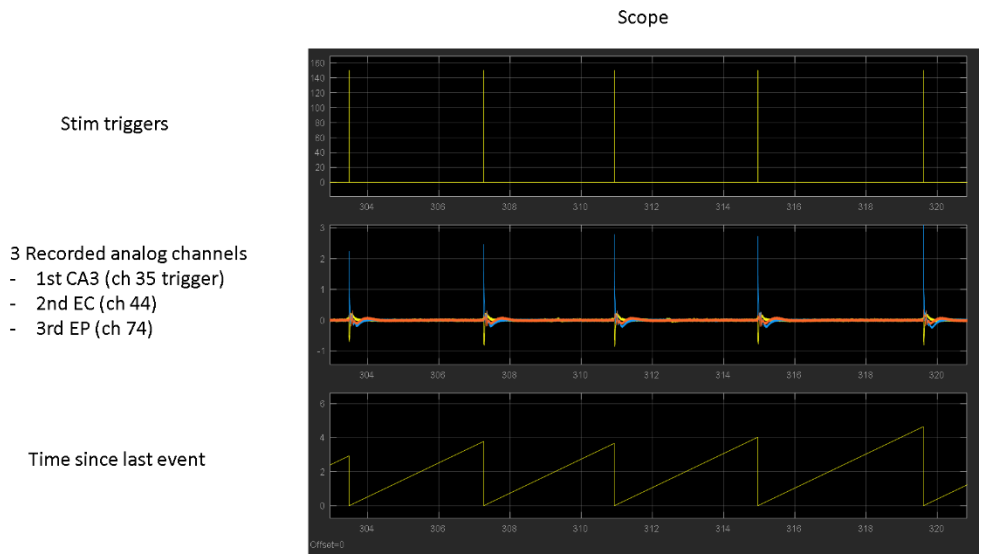


*Figure 3.8. Screenshot of the scope during a stimulation protocol. The first (top) panel represents the stimulation triggers (i.e. detected interictal CA3 activity). The amplitude is arbitrary set to 150 (but it is a binary type, true or false). The second panel (in the middle) represents the raw data acquired from 3 electrodes placed respectively in CA3, Entorhinal cortex and Perirhinal cortex. The third panel (bottom) represents the time since last detected event.*

From the preliminary results obtained so far, there was a promising reduction of the ictal discharge but we would need to perform additional and systematic experiments to prove the efficacy of this protocol. In (Figure 3.9), we show different zooms of the same recording to better appreciate how the inter-ictal activity detected in CA3 resulted in a stimulation of the subiculum, causing a reduction of the ictal discharge in EC and PC.

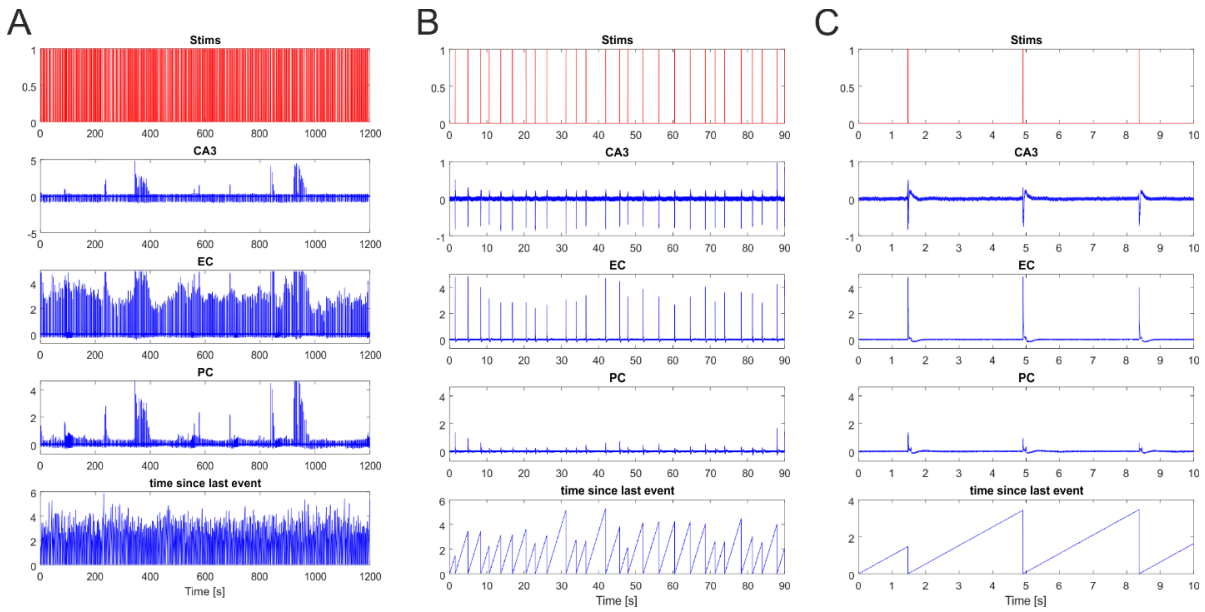


*Figure 3.9: 20 minutes of CA3 to Subiculum stimulation. First row (top) represents the detected events which correspond to the delivered stimuli. The following 3 rows represent the CA3, EC and PC traces. The last row represents the time since last detected event. B, a zoom of the first panel in the range 0-90 s; C a zoom of the first panel in the range 0-10 s.*

A different overview of two attempts to generate an ictal discharge (Figure 3.10).

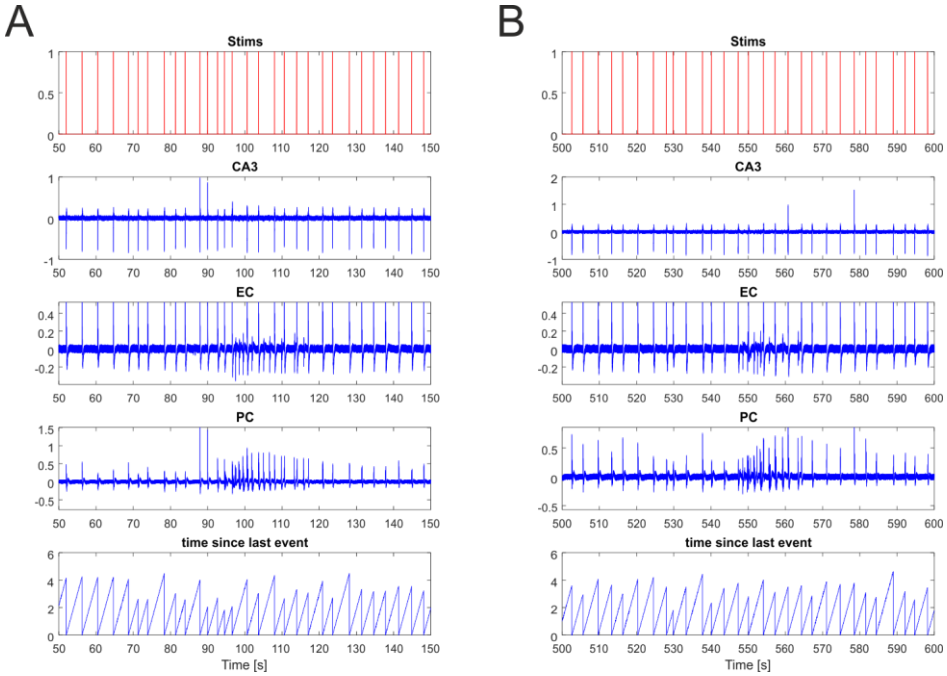


*Figure 3.10: Two ictal attempts during stimulation. A, ictal attempt between 90 and 120 seconds; B, ictal attempt between 550 and 570 seconds.*

A representative comparison between an ictal discharge during the spontaneous phase (Figure 3.11 panel A) and during stimulation (Figure 3.11 panel B).

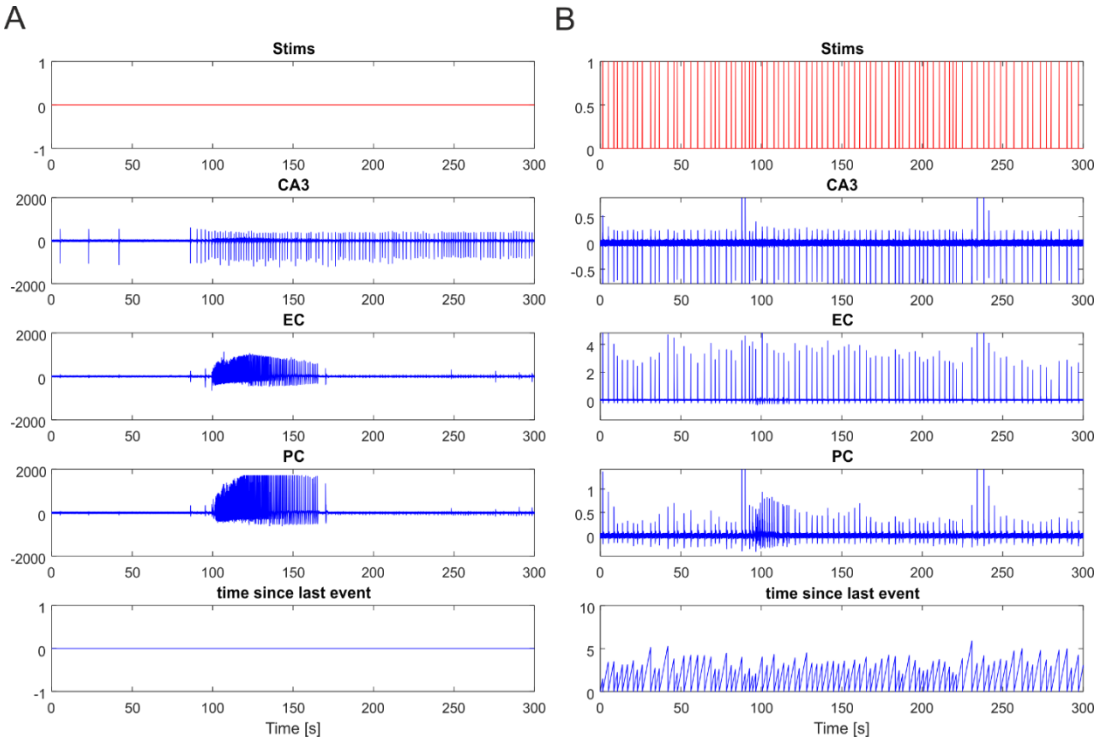


*Figure 3.11: Comparison between spontaneous and stimulated. A, 5 minutes of spontaneous activity with a clear ictal event that lasted almost one minute. The first and the last subplot are empty because we were not stimulating the brain slice (they are present just to allow an easier comparison with the stimulation phase). B, 5*

*minutes of activity during stimulation. There is a clear attempt to generate an ictal discharge but reduced in time and amplitude with respect to the control. Y axes during spontaneous and stimulation are different because of the different scaling made by the MCRack commercial system (during spontaneous) and the National Instrument acquisition card (during stimulation).*

As anticipated, these represent preliminary and qualitative results that need further investigations and analysis to understand the real value of this stimulation protocol. It is worth noting that open-loop stimulation was proved to be useful in reducing ictal-events (D'Arcangelo et al. 2005) and thus dedicated experiments comparing open-loop and closed-loop experiments should be implemented extensively. Nevertheless, the Simulink model was proved functional and can be a good starting point for different experimental protocols and can provide a personalized stimulation targeted to the actual state of the brain.

Various different scientific hypothesis can be tested with a similar Simulink model. For instance, a question could be: *what is the optimal delay between the detection and the stimulation?* This should match the delay of the interictal propagation from CA3 to EC through the Shaffer's collaterals. Modifying the described model would be trivial: it would require the drag and drop of a "delay" Simulink block that waits a certain amount of time before delivering the TTL pulse.

Assuming that the forward of CA3 interictal activity is a good model of the Shaffer's collateral and thus is able to suppress ictal event in a consistent way, we can ask: *Can we mimic a non-functional CA3 activity that is not able to suppress ictal events?* To answer this question, I implemented a modified version of the original Simulink model to mimic the failure of the CA3 to EC propagation. To reach this goal, I added a counter (activated every time a new stimulation would be delivered) that counts just "0" and "1". Every time the counter outputs a "1", the stimulation is effectively delivered, reaching a failure rate of 50% (Figure 3.12). This would serve as a testbed to understand how many pulses one would need to have an effective reduction of epileptic discharges. Counting up to "3" and delivering the stimulation only when "3" is the output of the counter would result in a 75% failure rate (i.e. it delivers 1 stimulation out of 4 CA3 events, when the counter starts at 0).

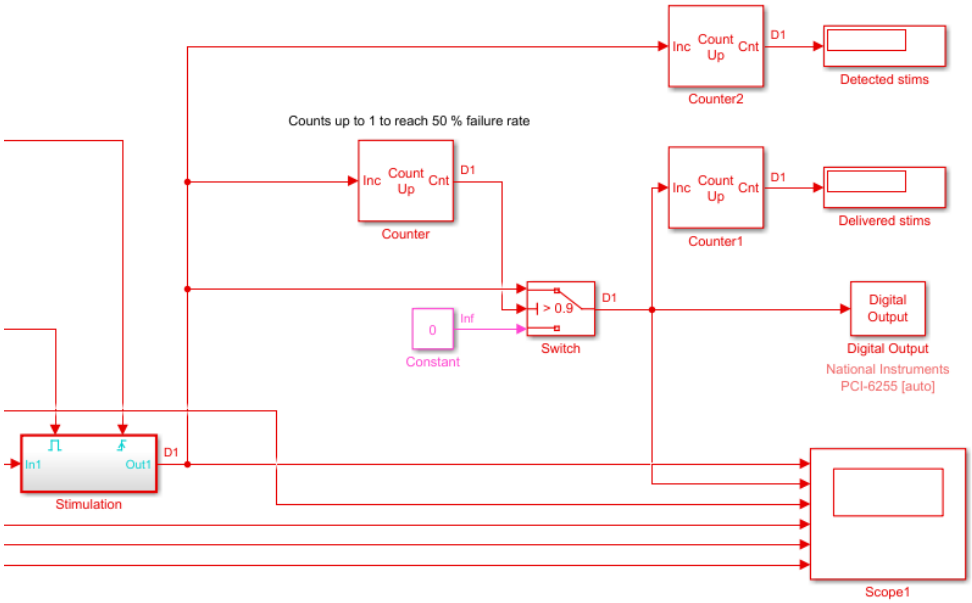


*Figure 3.12: modified model to mimic a failure in the process of forwarding the CA3 events. A counter reduces the amount of stimuli effectively delivered to back to the brain slice.*

Such hypothesis was tested thanks to the implemented model of failure as depicted in the following figure. 20 minutes of stimulation with a 75% failure rate (or, equivalently 25% efficacy of CA3 forward) were tested. As can be seen from the first subplot of all the panels, the number of detected events is four times the number of delivered stimuli. The CA3 trace clearly shows that 3 out of four interictal events were not forwarded in EC and PC thus confirming that the model was running as expected. With this simple improvement to the original Simulink model, one can test several scientific question in a rapid and functional way.

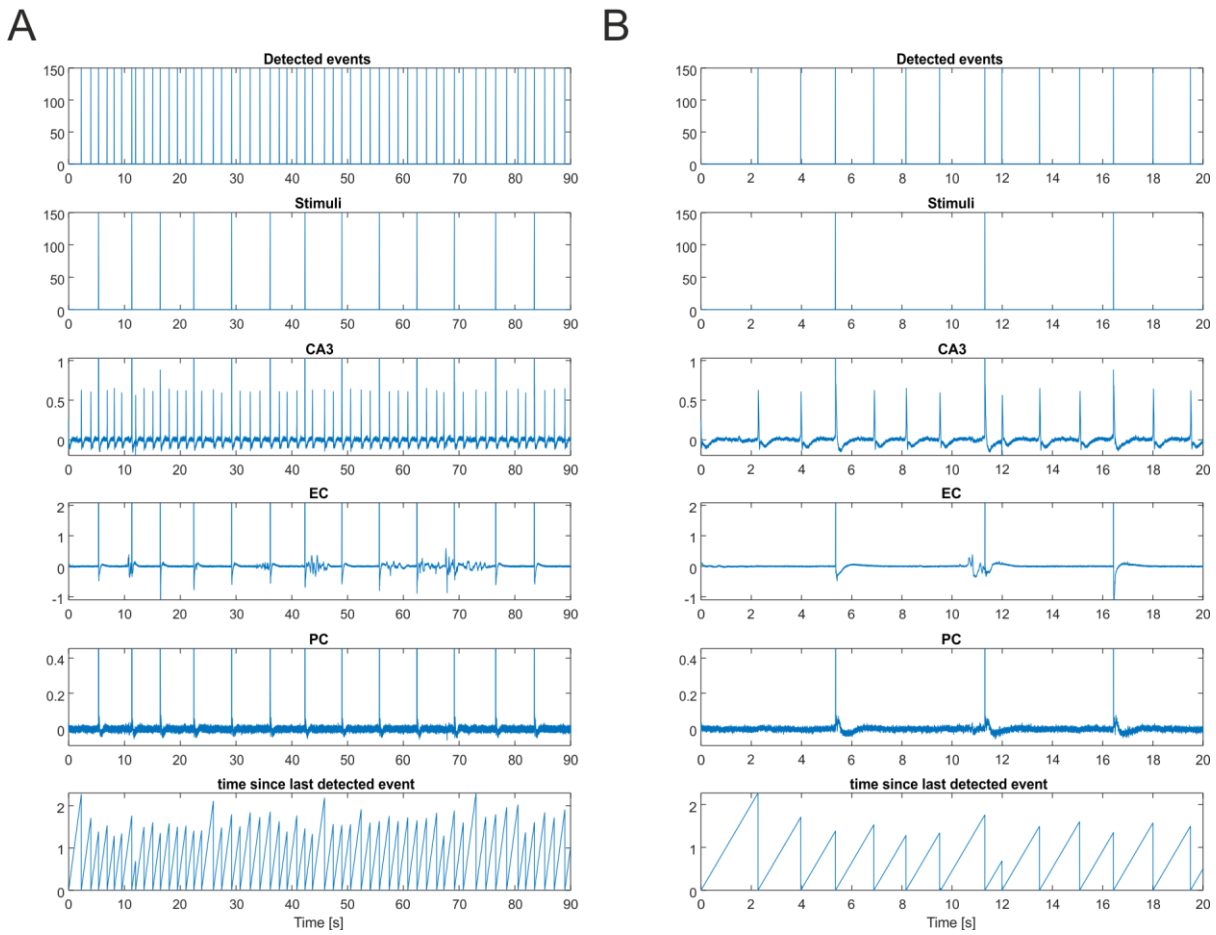


*Figure 3.13: A, 90 seconds of recording with 75% failure rate. First row represents the detected events (y-value is arbitrary equal to 150 but it is a binary value 0 or 1). The second row represents the delivered stimuli (25% of the detected ones, again they are arbitrary values). The other 3 rows represent the CA3, EC and PC traces. The last row represents the time since last detected event. B, a zoom of the first panel in the range 0-20 s.*

Implementing advanced closed-loop strategies is also possible; for instance, adding a feedback, that monitors the actual ictal discharge and decides whether to increment the stimulation frequency. This improved version would be implementable in a reasonable amount of time given the rapid-prototyping environment.

## Conclusion

Despite its simplicity, this Simulink model provides a user-friendly solution to perform basic closed-loop experiments. The model-based design approach implemented here, allows non-experts to perform activity dependent stimulation in a reliable way, without spending too many resources on the optimization of the computational speed with a procedural or object-oriented programming language (like C or C++). This rapid-prototyping approach can serve as a starting point towards the validation of innovative neuroprosthetic approaches. Moreover, once the algorithm is ready, it is possible to deploy it to an embedded system (like RaspberryPi, Arduino etc) or to a field-programmable gate array (FPGA) or system on a chip (SoC). In conclusion, using such development environment can be the right choice

to test the embedded devices that can constitute the first step towards the development of implantable devices. Indeed, this project was useful to learn how to code in this environment, Simulink (which is more commonly used in mechanical engineering and in control systems) and allowed me to use it also for *in vivo* applications (cf. Chapter 4).

## References


Barbarosie, M. and M. Avoli (1997). "CA3-driven hippocampal-entorhinal loop controls rather than sustains in vitro limbic seizures." Journal of Neuroscience **17**(23): 9308-9314.

Barbarosie, M., J. Louvel, M. D'Antuono, I. Kurcewicz and M. Avoli (2002). "Masking synchronous GABA-mediated potentials controls limbic seizures." Epilepsia **43**(12): 1469-1479.

Chang, B. S. (2018). "Deep Brain Stimulation Works for Drug-Resistant Epilepsy, But How?" Epilepsy currents **18**(6): 378-379.

Chiang, C.-C., C.-C. K. Lin, M.-S. Ju and D. M. Durand (2013). "High frequency stimulation can suppress globally seizures induced by 4-AP in the rat hippocampus: An acute in vivo study." Brain stimulation **6**(2): 180-189.

Colombi, I. (2019). In vitro neuronal cultures on MEA: an engineering approach to study physiological and pathological brain networks. PhD, Università degli Studi di Genova.

D'Arcangelo, G., G. Panuccio, V. Tancredi and M. Avoli (2005). "Repetitive low-frequency stimulation reduces epileptiform synchronization in limbic neuronal networks." Neurobiology of disease **19**(1-2): 119-128.

Davis, R. (2000). "Cerebellar stimulation for cerebral palsy spasticity, function, and seizures." Archives of medical research **31**(3): 290-299.

Hamani, C., M. Hodaie, J. Chiang, M. del Campo, D. M. Andrade, D. Sherman, M. Mirski, L. E. Mello and A. M. Lozano (2008). "Deep brain stimulation of the anterior nucleus of the thalamus: effects of electrical stimulation on pilocarpine-induced seizures and status epilepticus." Epilepsy research **78**(2-3): 117-123.

Hartshorn, A. and B. Jobst (2018). "Responsive brain stimulation in epilepsy." Therapeutic advances in chronic disease **9**(7): 135-142.

Jerger, K. and S. J. Schiff (1995). "Periodic pacing an in vitro epileptic focus." Journal of Neurophysiology **73**(2): 876-879.

Lado, F. A., L. Velíšek and S. L. Moshé (2003). "The effect of electrical stimulation of the subthalamic nucleus on seizures is frequency dependent." Epilepsia **44**(2): 157-164.

Rutecki, P. A., F. J. Lebeda and D. Johnston (1987). "4-Aminopyridine produces epileptiform activity in hippocampus and enhances synaptic excitation and inhibition." Journal of neurophysiology **57**(6): 1911-1924.

Salanova, V., T. Witt, R. Worth, T. R. Henry, R. E. Gross, J. M. Nazzaro, D. Labar, M. R. Sperling, A. Sharan and E. Sandok (2015). "Long-term efficacy and safety of thalamic stimulation for drug-resistant partial epilepsy." Neurology **84**(10): 1017-1025.

Sisterson, N. D., T. A. Wozny, V. Kokkinos, A. Constantino and R. M. Richardson (2019). "Closed-loop brain stimulation for drug-resistant epilepsy: Towards an evidence-based approach to personalized medicine." Neurotherapeutics **16**(1): 119-127.

Weiss, S., X.-L. Li, J. B. Rosen, H. Li, T. Heynen and R. M. Post (1995). "Quenching: inhibition of development and expression of amygdala kindled seizures with low frequency stimulation." Neuroreport **6**(16): 2171-2176.

Wozny, T. A., W. J. Lipski, A. Alhourani, E. D. Kondylis, A. Antony and R. M. Richardson (2017). "Effects of hippocampal low-frequency stimulation in idiopathic non-human primate epilepsy assessed via a remote-sensing-enabled neurostimulator." Experimental neurology **294**: 68-77.

Wyckhuys, T., T. De Smedt, P. Claeys, R. Raedt, L. Waterschoot, K. Vonck, C. V. d. Broecke, C. Mabilde, L. Leybaert and W. Wadman (2007). "High frequency deep brain stimulation in the hippocampus modifies seizure characteristics in kindled rats." Epilepsia **48**(8): 1543-1550.

Zack, M. M. and R. Kobau (2017). "National and state estimates of the numbers of adults and children with active epilepsy—United States, 2015." MMWR. Morbidity and mortality weekly report **66**(31): 821.

# Chapter 4: Retrain: *in vivo* neuroprosthesis

## Overview

In this chapter, I will describe some of the results of the MAECI project, a bilateral project between IIT and Kansas University Medical Center (KUMED). The aim of the project was to study the effect of intracortical microstimulation (ICMS) when applied in open and closed-loop in a model of brain injury (e.g. stroke and traumatic brain injury). Recording and stimulating *in vivo* is obviously different from working on cell cultures or brain slices over MEAs. but some of the concepts and tools used in the previous projects were useful here. Being closer to a real-word scenario adds complexity to these recordings (e.g. artifacts caused by movement, chewing and whisking) which must be taken in consideration when developing closed-loop algorithms.

One of our collaborators from KUMED, Dr. Guggenmos, recently published a work (Guggenmos et al. 2013) investigating the feasibility of ICMS in promoting rehabilitation after brain injury. In that work, they performed a traumatic brain injury to the caudal forelimb area (CFA) which shares many properties with primary motor cortex (M1) of primates. As previously reported by the same authors, a controlled cortical impact centered on the CFA of rat motor cortex caused forelimb deficits in the limb contralateral to the injury (Nishibe et al. 2010). The substantial output that M1 provides to the spinal cord and thus the limb has been thought to play a central role in the deficit. However, M1 is strongly connected with the primary somatosensory cortex (S1), as can be seen in Figure 4.1 (panel A). M1 gets critical information about the position of the limb in space thanks to the long-range corticocortical fibers. Starting from these observation, the authors tested the hypothesis that functional recovery can be facilitated by an artificial bridging between premotor cortex (PM) and S1 (as depicted in Figure 4.1, panel B).

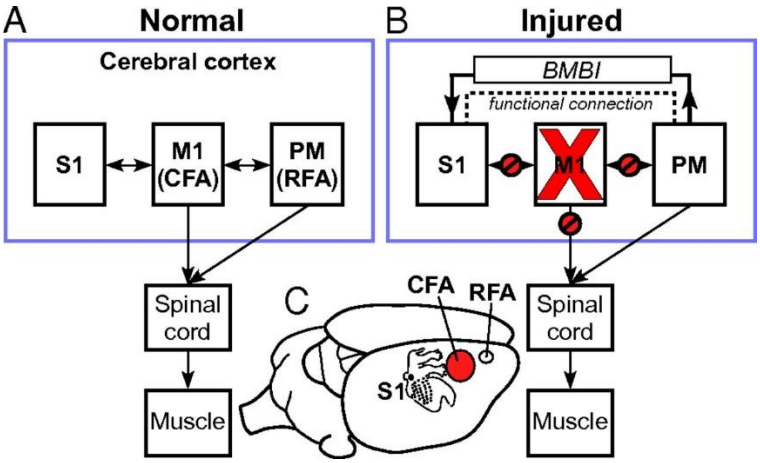


*Figure 4.1: Theoretical model of neuroprosthetic treatment approach after brain injury. (A) Normal connectivity of M1, S1, and PM. Both M1 (CFA in rat) and PM (RFA in rat) send substantial outputs to the spinal cord via the corticospinal tract. Also, extensive reciprocal connections exist between M1 and PM, as well as between M1 and*

*S1. (B) Effects of focal M1 injury on brain connectivity and the hypothetical effect of a BMBI to restore somatosensory-motor communication. An injury to M1, as might occur in stroke or brain trauma, results in a focal area of necrosis, as well as loss of M1 outputs to the spinal cord. Corticocortical communication between M1 and S1 (and between M1 and PM) is also disrupted, further contributing to functional impairment. Because the uninjured PM also contains corticospinal neurons, it might have the ability to serve in a vicarious role. The dotted line indicates the supposed enhanced functional connection between PM and S1 after treatment with a BMBI. (C) Location of target areas in rat cerebral cortex. A topographic map of the somatosensory representation in S1 is superimposed on the cortex. from (Guggenmos et al. 2013)*

The rostral forelimb area (RFA) is a premotor area and the large majority of its output fibers project to motor area. Few, long range corticocortical connection with S1 are also present but weak compared with M1's connections with S1 (Dancause et al. 2005). Therefore, performing an activity dependent stimulation based on spikes detected in PM and stimulation delivered in S1, after a damage in M1, could facilitate the rehabilitation process. To test this hypothesis, the authors developed a microdevice, able to detect spikes and deliver stimulation with a fixed delay (as depicted in the figure below); this protocol was named BMBI which stands for Brain Machine Brain Interface, a different name for activity dependent stimulation (ADS).

The microdevice delivered ADS 24 h per day up to 28 days post-injury. Behavioral recovery in ADS rats was compared with recovery in rats with open-loop stimulation (OLS), in which S1 stimulation was uncorrelated with spikes in PM, and with control rats that had no microdevice implanted.

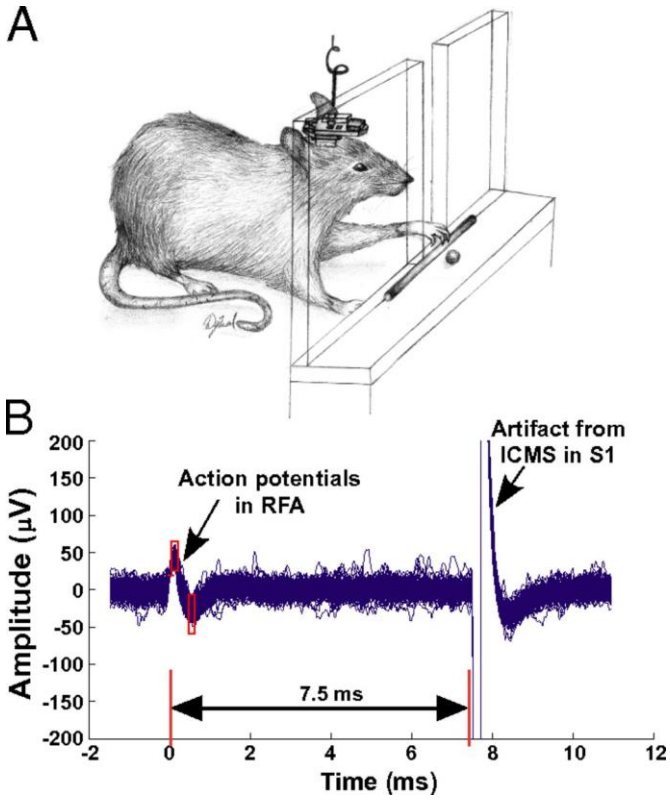


*Figure 4.2: Stimulation protocol. After injury to the CFA, a recording microelectrode was placed in the RFA, whereas a stimulating microelectrode was placed in the distal forelimb field of S1. A BMBI discriminated action potentials in the RFA, and after a 7.5-ms delay, it delivered a low-level electrical current pulse to S1. (A) Sketch*

*of a rat retrieving a food pellet with a BMBI attached to the skull. (B) Sample traces of recordings from the RFA showing action potentials and stimulus artifacts from an ICMS current delivered to S1. Time-amplitude window discriminators are indicated by red boxes. A total of 100 superimposed traces are shown. From (Guggenmos et al. 2013)*

The main result of this work was related to a behavioral assessment of the skilled reaching task. Rats were pre-trained to achieve a minimum criterion score of >70% successful pellet retrievals. After the lesion, rats were tested on the task on post-lesion days 3, 5, 8, 14, 21, and 28. During each post lesion assessment session, rats were tested under two conditions: first with the stimulation OFF and then with the stimulation function turned ON. Rats in each of the three groups demonstrated a severe deficit on the skilled reaching task in the first few days after the injury (Figure 4.3) with no significant differences between groups. By post-lesion day 8, rats in the ADS group showed a statistically significant behavioral improvement in reaching success compared with rats in the other groups in the ON condition. It is worth noting that by post-lesion day 21, no statistical difference was found between OLS and ADS even though the reaching success was overall higher in ADS.

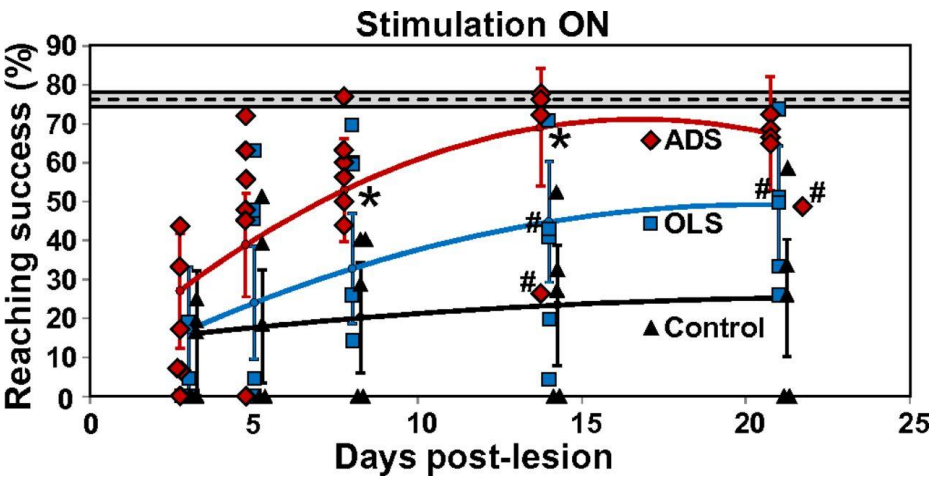


*Figure 4.3: Performance of rats on a skilled reaching task after injury to M1 (ON condition). The dotted line indicates the average pre-lesion performance of all animals in the study. The bounded area indicates the 95% confidence interval. Regression lines are based on an linear mixed model (McCulloch and Searle 2001). Error bars represent 95% confidence intervals. *P < 0.05 (pairwise difference between the ADS and OLS groups). Only one rat in the ADS group had a microdevice that was functional by post-lesion day 28; thus, figures are presented through post-lesion day 21 Diamonds, squares, and triangles represent individual animal data points. #, microdevice not functional. From (Guggenmos et al. 2013)*

In this proof-of-principle study, it was demonstrated that an activity dependent stimulation could enhance functional connectivity between distant cortical locations and generate rapid improvement in motor function after cortical injury in M1. This kind of approach can pave the way for future implantable systems aimed at rehabilitating in case of severe stroke or traumatic brain injury.

One of the main problems related to the device used for that work is that it is expensive and non-flexible. If one want to change the detection algorithm, for instance, it would imply the design of a new device with all the related problems. This technology drastically limits the number of people that

can modify the device and thus slows down the development of innovative neuroprosthetic devices. Devices based on field programmable gate array (FPGA) have a much higher flexibility and thus allow high-performance and flexibility in a single device. In this chapter, I describe the implementation of a window-discriminator spike detection algorithm. Large part of this chapter, is part of the following publication:

- Murphy M*, Buccelli S*, Bornat Y, Bundy D, Nudo R, Guggenmos D, Chiappalone M. Improving an open-source commercial system to reliably perform activity-dependent simulation. Journal of Neural Engineering (2019).- Doi: https://doi.org/10.1088/1741-2552/ab3319

## Introduction

As anticipated in the previous paragraph, recent preclinical work has investigated the feasibility and efficacy of intracortical microstimulation (ICMS) coupled to neural activity to promote rehabilitation after brain injury (Azin et al. 2011, Azin et al. 2011, Guggenmos et al. 2013). In brain-injured rats, constraining the timing of ICMS to within a few milliseconds of a detected extracellular action potential recorded in a second area improves motor skill beyond that achieved by randomly timed stimuli (Guggenmos et al. 2013). This ICMS paradigm, known as activity-dependent stimulation (ADS), has also been used in healthy macaques to pair sites within motor cortex and alter evoked EMG output (Jackson et al. 2006). The efficacy of these protocols relies both upon the accuracy of the spike detector and upon the reliability of subsequent low-latency (<10 ms) delivery of ICMS. Furthermore, because the invoked strengthening of connections between sites is thought to be generated by a Hebbian mechanism, low jitter in the delivery of stimuli (<1 ms) is critical; for example, the difference in timing between invoking maximal potentiation and maximal depression of synaptic efficacy in hippocampal cultures is <5 ms (Bi and Poo 1998). Depending upon the distance, type, and number of synapses that are putatively involved between the targets of ADS, it is also possible that the <10 ms latency constraint may be restricted to as low as <3-4 ms.

Historically, spike detection has been performed by applying a monopolar voltage threshold to the amplified and filtered neurophysiological signal, counting each rising edge of the resultant logical signal as the onset of a spike (Cheney and Fetz 1985). However, spike detection done in this way tends to conflate signals generated by movement and chewing with spikes from neural units when used in awake animal experiments, due to the similar frequency characteristics and larger amplitude of the former. For ADS, which relies upon the specific pairing of neurophysiological activity between two sites, non-specific stimulation due to biological noise sources would be obviously problematic.

Although many algorithms that are superior to monopolar voltage thresholds now exist and are easily implemented in various software packages for spike detection and sorting, the latency required in

communicating with a host device can be prohibitive for ADS. Previously, ADS had been implemented in lightweight telemetric devices using an application-specific integrated circuit (Azin et al. 2011, Azin et al. 2011). However, for a long-term neurophysiological data acquisition solution, a more flexible architecture that can simultaneously acquire signals from hundreds of channels would be desirable. In addition, due to the timing constraints mentioned previously (<10 ms latency between detection and stimulation; <1 ms jitter in stimulus delivery), software solutions that involve a USB chain cannot be used. Therefore, the most tenable solutions need to be implemented algorithmically in hardware, such as through a field programmable gate array (FPGA), a PCIe card interfaced through an ethernet connection, or some other comparable digital signal processing unit.

Recently, the commercial availability of high-gain, high-resolution custom amplifier integrated circuits (Harrison and Charles 2003, Harrison 2007), which interface to a host device through a serial parallel interface (SPI) has made it possible to construct relatively inexpensive neurophysiological acquisition systems that scale to high numbers of recording channels. These systems, such as the acquisition system provided by Intan or the Open-Ephys acquisition board (Siegle et al. 2017), use an FPGA to run the SPI that controls the amplifier chip while maintaining a buffer for USB communication with a host computer. Several proposed spike detection and spike sorting techniques take advantage of the FPGA, an integrated circuit that the end-user can reconfigure (Biffi et al. 2010, Gibson et al. 2013, Park et al. 2017, Vallicelli et al. 2017). Implementing the detection and sorting circuit on an FPGA allows the use of neurophysiological spiking as a reliable control signal in real-time, with low-latency; however, most implementations require custom integration with respect to the design of the full data acquisition circuit, which typically varies from laboratory to laboratory.

Here, we implemented a spike detection state machine designed to provide multiple threshold windows, reducing the likelihood of activity from sources other than spiking neural units on a single channel leading to the delivery of stimulation. The algorithm reduces the erroneous detection of spikes during biological noise in awake animals using an intuitive algorithm that requires minimal computational power. The implementation is conveniently designed to work as a modification to the existing open-source code provided by Intan for use in conjunction with their low-cost commercial platform for neurophysiological data acquisition and stimulus delivery. Importantly, the system allows the application of ADS with a fixed minimum latency <1 ms and has the potential to scale to a high number of channels in future design iterations.

## Methods

### *Hardware architecture*

The hardware architecture of the acquisition system and spike detector consists of three core components (Figure 4.4):

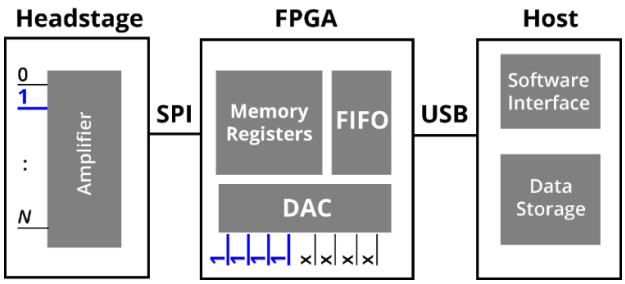


*Figure 4.4: Overview of system architecture and implementation. An amplifier chip is interfaced to the field-programmable gate array (FPGA), via a serial-parallel interface (SPI). N electrode channels are routed to a high-gain amplifier. On board the FPGA, amplifier data from the FIFO buffer are piped to the host device via a USB interface. The digitized signals from any selected combination of amplifier channels (blue) can also be routed to up to 8 digital-to-analog converter (DAC) channels, where threshold comparator logic can be applied with sub-millisecond latency. In this example, 4 threshold windows are applied to the filtered data stream from amplifier channel 1.*

1. Headstage: an amplifier circuit connected to a microelectrode array with an arbitrary number *N* of physical microelectrode leads placed near the neural substrate of interest;
2. FPGA: an interface that allows the amplifier circuit to multiplex both the incoming microelectrode signals and any outgoing stimulation commands to the appropriate microelectrodes;
3. Host: a general-purpose computer that provides an interface to the system, allowing the user to select the desired microelectrode channels and how a closed-loop stimulation scheme will be implemented.

This implementation used a commercially available integrated circuit and pre-assembled headstage (RHS2116; Intan Technologies, Los Angeles, CA, USA) to connect to the microelectrodes. To interface with this circuit, we used the Intan Stimulation/Recording Controller, which consists of an FPGA evaluation board (XEM6010-LX45; Opal Kelly Inc., Portland, OR, USA), equipped with a Xilinx Spartan 6 FPGA (XC6SLX45-2; Xilinx Inc., San Jose, CA, USA), a 128-Mbyte SDRAM chip, a 100-MHz clock source, I/O connectors, and a USB 2.0 interface chip capable of streaming data to a host computer at rates

exceeding 20 Mbyte/s. A desktop personal computer (Z230; Hewlett-Packard, Palo Alto, CA, USA) running Windows 7 (Microsoft, Redmond, WA, USA) was used to control the USB chain.

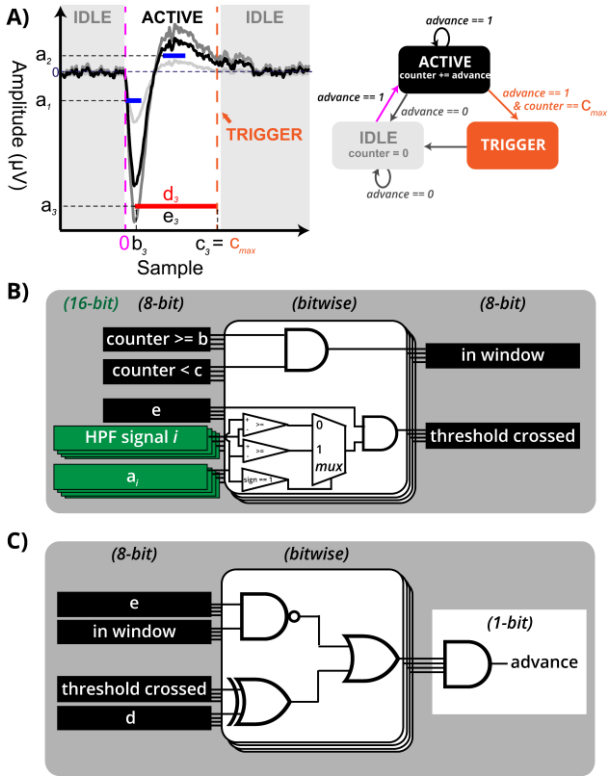


*Figure 4.5: Spike detection state machine implementation. A) Left: Example of a spike that would be included (black) and waveforms that would be rejected (grey) by the three state machine levels depicted ($L_1$, $L_2$, and $L_3$, denoted by corresponding thresholds $a_1$, $a_2$, and $a_3$). The dark-grey waveform exceeds the red exclusion threshold ($a_3$), while the light-grey waveform does not meet the second blue inclusion threshold ($a_2$). The black spike is included because the absolute value of its negative component does not exceed the absolute value set by $a_3$, while the absolute value of its positive component exceeds the level set by the second blue inclusion level $a_2$. The parameters (a-e) are defined by the user during acquisition and are illustrated for the red exclusion level shown. Right: state flow diagram for the spike detection state machine. By default, the detector is in the idle state (grey), but transitions to active (black) as soon as the data stream fulfils the parameters for the earliest window (magenta). If the waveform meets all criteria specified by the defined levels, the state switches to trigger (orange), then automatically reverts to idle. B) Threshold logic in the DAC module. For each of the 8 DAC channels, the corresponding parameters determine if the machine is within the start and stop points of the window, relative to when the counter started, as well as whether it crossed the threshold (depending on threshold polarity). C) Active and idle counter incrementing logic. If the data stream meets criteria of each enabled level that applies to the current counter value, the counter is advanced by 1.*

Intan provides a hardware design that embeds the open-source USB/FPGA interface developed by Opal Kelly. This design makes it possible to read and modify registers of the RHS2116 from a host computer. It consists of verilog Hardware Description Language (HDL) code written for the XEM6010-LX45 evaluation board. This code is synthesized using the free Xilinx ISE WebPack software. The resulting bitfile is locally stored on the board in a dedicated Flash memory and can be updated through the USB interface. It is loaded on the Spartan-6 FPGA at each power-up, allowing the FPGA to interpret commands and parameters issued by the user from the USB chain.

At its core, the USB/FPGA design provided by Intan is a state machine that controls SPI buses on up to eight peripheral RHS2116 amplifier circuits. The interface also contains a module that implements a short-latency threshold comparator on up to eight channels of digitized amplifier data streams routed to 16-bit digital-to-analog converters (DAC; AD5662; Analog Devices, Norwood, MA, USA) mounted on the evaluation board. The comparator logic state is routed to a TTL output wire that corresponds to the DAC channel number. The DAC module also implements a single-pole high-pass filter (HPF) on the selected amplifier data stream.

A second module, also included in the existing Intan USB/FPGA interface, contains a state machine that controls the delivery of ICMS to a selected amplifier channel. The module can be configured through the GUI to deliver stimuli on the rising or falling edge of a TTL input signal. Thus, by physically connecting pairs of TTL inputs and outputs, "closed-loop" stimulation based on the detection of threshold-crossing events (in this case, extracellular action potentials, or spikes) is already possible using the USB/FPGA interface as provided by the vendor.

The main contribution described herein is the addition of a state machine for spike detection that offers improved artifact rejection, while taking advantage of the short-latency comparator in the DAC module of the existing USB/FPGA interface. Importantly, we sought to make as few changes as possible to the existing toolkit provided and validated by the commercial vendor, in the hopes that any changes we introduced could be more easily integrated to existing workflows. Overall, the changes amount to an increase of 408 flip flops compared to the originally synthesized architecture, well within the bounds of the available resources on the XEM6010-LX45.

### *Software interface*

Software was modified from the original open-source C/C++ code provided by Intan Technologies for use with the RHS2116 amplifier IC, retaining many similarities with the original. The software implements a GUI, which provides a front-end to the USB/FPGA interface. Modifications described in the present study were added using Qt (version 5.8). Applications were compiled for Windows 32- and 64-bit operating systems using compilers for Microsoft Visual Studio 2015. This modified GUI includes a tab that allows configuration of the DAC (Figure 4.5 A, left panel) and the popup window for visualizing spikes is altered to accommodate online specification of each of the four parameters for each DAC channel used in the state machine detector, as described in Figure 4.5 A.

### *Spike detection state machine*

The core of the spike detection state machine is a simple logic cycle that runs in the main module of the USB/FPGA interface (Figure 4.5 A, right). The state machine allows up to 8 threshold levels (Li, where i is an integer from 1 to 8) with the following user-defined parameters (Figure 4.5 A, left):

- **Threshold,** $a_i$, refers to the voltage value (µV) that the signal must pass through to count as a crossing. If the threshold is negative, then a crossing occurs when the signal value is less-than or equal-to the threshold value (Figure 4.5 B, multiplex logic). If the threshold is positive, then a crossing occurs when the signal is greater-than or equal-to the threshold value. This number is an unsigned 16-bit integer, which is limited between -5,000 µV and +5,000 µV, based on the dynamic range and scaling of the amplifier and DAC.
- **Start,** $b_i$, refers to the (inclusive) onset sample of the window $L_i$. If the state machine counter is less than this value, the threshold conditions for the specified window will not be considered in the state machine logic. The state machine switches from idle to active (as defined below) once the filtered amplifier data stream routed to DAC channel *i* meets the criteria for $L_i$, if $b_i$ = 0.
- **Stop,** $c_i$, refers to the (exclusive) end sample of the window $L_i$. If the state machine counter is equal or higher than this value, the threshold conditions for the specified window will not be considered in the state machine logic. The maximum stop value, $c_{max}$, defines the total duration of the spike detection state machine.
- **Type,** $d_i$, refers to the amplitude bounding for window $L_i$. It depends upon the polarity of the threshold. A value of zero corresponds to an "include" type window, which means that the signal must be less than a negative threshold or greater than a positive threshold while the state machine counter is within the range defined by the start and stop samples (Figure 4.5 C). A value of one corresponds to an "exclude" type window, which enforces the opposite conditions (signal must be greater than a negative threshold or less than a positive threshold).
- **Enable,** $e_i$, refers to whether window $L_i$ is involved in the decision circuit for the state machine. The state machine can run with as few as 1 and as many as 8 windows enabled.

In the specific example of Figure 2A, we have defined three levels (e.g. L1, L2, and L3), where a1 and a2 are the blue 'inclusion' thresholds (d1 = d2 = 0) and a3 is the red exclusion threshold (d3 = 1). Therefore, the dark-grey spike, which crosses threshold a3, is excluded, but the black spike is not. Likewise, the light-grey spike, which does not cross the a2 blue 'inclusion' threshold is also excluded. In total, the state machine runs for cmax samples, starting whenever the state is 'idle' and the filtered signal is less than a1.

The state machine increments a counter on the rising edge of the sample clock depending upon its current state, which is always in one of these three conditions:

- idle, when one or more of the level criteria is not met or no DAC channel is enabled (Figure 4.5 A, grey);
- active, when the criteria for each enabled DAC with a start value less than or equal to the current sample index and a stop value greater than the current sample index channel is true (Figure 4.5 A, black); or,
- trigger, when the counter equals the largest enabled DAC window stop value (Figure 4.5 A, orange).

The counter increments only when the state machine is in the active state, and resets to zero any time it enters the idle state (Figure 4.5 A; right). If the state machine reaches the trigger state, it returns to the idle state on the ensuing sample clock cycle. Each state of the machine is reported by the high state on a unique pair of TTL output and input wires (cf. Appendix).

### *Surgical implant and recording for in vivo testing*

All protocols for animal use were approved by the Kansas University Medical Center Institutional Animal Care and Use Committee in compliance with the Guide for the Care and Use of Laboratory Animals (Eighth Edition, The National Academies Press, 2011). Briefly adult male Long Evans rats were anesthetized using a combination of ketamine and xylazine as described previously (Nishibe et al. 2010). A laminectomy was performed to minimize edema during the procedure. Five 00-80 stainless steel skull screws were fixed around the perimeter of the skull to improve attachment of the dental acrylic cap. Using stereotaxic coordinates, a craniectomy was made over sensorimotor cortex of the left hemisphere. Microwire arrays were positioned to span the rostral forelimb area (RFA), caudal forelimb area (CFA), and forelimb sensory cortex (S1), which was confirmed by a brief ICMS mapping procedure before insertion to a depth of approximately 1500 µm. An external silver wire on each array was tied to the same skull screw placed in the interparietal bone, which acted as a common ground. In the rat used for session A (recording sessions described below), the microwire array was a custom in-house design consisting of 32 channels of 33 µm diameter polyimide-coated tungsten wire (California Fine Wire Co., Grover Beach, CA), which were distributed throughout RFA, CFA, and S1 in a non-uniform grid pattern. The rat used for sessions B and C was implanted with a commercial microwire array (MicroProbes for Life Science, Gaithersburg, MD) consisting of 16 channels of nickel-chromium alloy 50 µm diameter wires arranged in a 4x4 grid with 250 µm site spacing implanted in S1. Qualitatively, spiking activity from both datasets was similar, but session A contained a few channels with large, stereotyped spikes, while spikes tended to be smaller in amplitude for sessions B

and C. Prior to each recording, the rat was placed under anaesthesia via isofluorane induction, and subsequently one channel located within RFA was used for recording, while a single S1 channel was used in any stimulation sessions Electrode impedances ranged from 750 – 1,500 kΩ at recording sites. Recordings were made in 3- to 5-minute blocks during and after recovery from anaesthesia.

Recordings were made during three separate sessions. Recording sessions were assigned the codes 'A,' 'B,' and 'C.' The main features and how these data were used within the current work are summarized in Table 4.1. Session A was taken from a first rat, three days after implantation, and contains a single epoch in which no stimulation was performed,

which was used for subsequent offline characterizations due to the presence of large, stereotypical spike waveforms and low noise floor (RMS 18.6 µV, rectified median 11.3 µV). Sessions B and C were taken from a second rat approximately three months after the implantation. Session B tested the latency between spike detection using the state machine and onset of stimulation. Session C tested the online performance of the spike detection state machine using ad hoc parameters selected while the experiment was ongoing (e.g. to mimic a typical use case). Specific parameters for each recording session are reported in detail in

| *Name* | *Stim?* | *Feature* | *Use* |
|---|---|---|---|
| *A* | No | Large stereotypical spikes; low noise | Offline performance |
| *B* | Yes | Stimulus artifacts | Test latency of stimulation |
| *C* | No | Typical use case; synchronized video | Online performance |

*Table 4.1: Summary of recording data sets taken from rats. Recordings were taken from awake, ambulatory rats implanted in RFA and S1. Columns describe whether stimulation was used, the main feature that distinguishes that recording dataset from the others, and the reason the recording was used in this study.*

Table 4.2; sub-indices indicate identical recording data that was re-run offline using a simulated test bench to characterize performance. To identify chewing periods (which bias performance toward false positive spike detection due to the presence of high-amplitude biological noise), a simultaneous video stream was synchronized with the neurophysiological data from session C through co-registration of a flashing LED that was tied to a digital input on the acquisition board.

| Date | ID | Duration | Start | Stop | Threshold | Type | Vid | Stim | Simulated |
|---|---|---|---|---|---|---|---|---|---|
| **2018-04-27** | A0 | 304.2 sec | 0 | 1 | -70 µV | Include | No | No | Yes |
| **2018-04-27** | A1 | 304.2 sec | 0<br>0<br>1<br>8 | 1<br>5<br>2<br>15 | -70 µV<br>-200 µV<br>-90 µV<br>-50 µV | Include<br>Exclude<br>Include<br>Exclude | No | No | Yes |
| **2019-01-31** | B0 | 181.1 sec | 0<br>1<br>5<br>5 | 1<br>7<br>8<br>9 | -46 µV<br>-66 µV<br>-13 µV<br>39 µV | Include<br>Exclude<br>Exclude<br>Exclude | No | Yes | No |
| **2019-02-01** | C0 | 162.3 sec | 0<br>1<br>4<br>3 | 1<br>6<br>11<br>15 | -40 µV<br>-149 µV<br>-25 µV<br>13 µV | Include<br>Exclude<br>Exclude<br>Exclude | Yes | No | No |
| **2019-02-01** | C1 | 162.3 sec | 0<br>4<br>6<br>7<br>13<br>18<br>19<br>22 | 3<br>24<br>7<br>8<br>15<br>21<br>24<br>24 | -25 µV<br>-110 µV<br>-40 µV<br>-30 µV<br>-45 µV<br>-5 µV<br>60 µV<br>15 µV | Exclude<br>Exclude<br>Include<br>Include<br>Exclude<br>Exclude<br>Exclude<br>Include | Yes | No | Yes |
| **2019-02-01** | C2 | 162.3 sec | 0 | 1 | -40 µV | Include | Yes | No | Yes |
| **2019-02-01** | C3 | 162.3 sec | 0 | 1 | -100 µV | Include | Yes | No | Yes – Ground Truth Synthesized |
| **2019-02-01** | C4 | 162.3 sec | 0<br>1 | 12<br>10 | -70 µV<br>-600 µV | Include<br>Exclude | Yes | No | Yes – Ground Truth Synthesized |

*Table 4.2: Parameters used during in vivo recordings. Three recordings ('A', 'B', and 'C') were taken during separate recording sessions from channels within RFA. Each column details parameters used online or during simulations. For recordings using the spike detection state machine, sub-rows within the 'Start,' 'Stop,' 'Threshold,' and 'Type' columns correspond to parameters given for each DAC channel. Recording A was used for simulated performance due to the low noise floor and large, stereotypical spike waveforms. Recording B was used to evaluate the latency from spike detection to stimulation. Recording C was used to evaluate performance in a "typical use" scenario, where online parameters were set quickly by the operator (C0) and compared to both a more stringent parameterization (C1) as well as a monopolar threshold simulation (C2). In addition, recording C contains asynchronized video record, that allowed the verification of manually identified epochs of biological artifact, such as chewing, so that qualitative performance of the different spike detector parameterizations could be assessed. Two additional recordings (C3 and C4) were artificially generated by superimposing large spike waveforms onto an amplifier channel that did not generate much spiking activity. These recordings were used to allow for a known ground truth regarding spike times (Figure. 4.9).*

### *Offline performance testing*

Performance of the spike detection state machine was evaluated by comparing offline detection of spikes from the *in vivo* data from session A, either using a monopolar threshold detector or the state machine detector. To ensure that the analyses accurately captured online performance, we first validated the fidelity of the reconstructed recorded signals by ensuring that the DAC amplifier data stream and digital logic state streams recorded *in vivo* during session C matched those generated by the offline DAC filter and state machine simulation. Simulations were performed using test benches compiled in verilog, MATLAB (R2017a+), and Simulink (R2018b), as described in the Appendix. The test benches are included in the online code repository along with the modified software and hardware code. Once we verified that there was no difference in the simulated digital logic state signals and the recorded ones, we used the DAC amplifier data stream recorded from session A to simulate the spikes detected using both a single-threshold detector (A0) as well as all events that entered the active and trigger states using the state machine detector (A1). For the monopolar threshold detector, spikes were only counted on the logical rising edge of the threshold crossing. Selection of a monopolar threshold was fixed at 40 µV, which was initially determined online by visual inspection of the spike scope to set a level that appeared qualitatively to reject noise while accepting most multi-unit spiking.

To characterize the ability of the spike detection state machine to reject artifact while still detecting viable spikes we calculated accuracy, defined as the ratio of the sum of correctly classified spikes (true positives; TP) and correctly classified artifacts (true negatives; TN) to the total number of spikes and artifacts detected. To determine whether spikes or artifacts detected during a simulation were correctly classified, a set of target classifications for spike and artifact waveforms were obtained offline using manual sorting to group similar waveforms. This consisted of a cluster cutting technique in which the spikes and artifactual waveforms were assigned iteratively through the manual selection of waveforms from the candidate set of waveforms detected as either spikes or artifacts by the detector, similar to the technique described in (Harris et al. 2000). While this method of classifying multi-unit spike waveforms has limitations depending on the amplitude of units under consideration (Harris et al. 2000), the purpose was to illustrate the ability of the spike detection state machine to reject artifactual waveforms, a situation for which an experienced operator is well-suited.

To verify our results on a dataset in which the ground truth spike times are already known, we synthesized an additional set of recordings (C3, in which a threshold detector was applied, and C4, in which the state machine detector was applied; parameters in Table 4.2). In these simulations, known spike waveforms were added to a non-spiking recording channel at 1,500 uniformly sampled random samples throughout the duration of the sample record. It should be noted that in these simulations,

identical recordings can yield slightly different numbers of total detected spike and artifact waveforms depending on which spike detection procedure was simulated even if the initial inclusion threshold is the same. This because the state machine has a minimum duration that requires multiple samples in order to detect the spike, probabilistically there are more opportunities to identify candidate spike and artifact waveforms when using a single-threshold detector, potentially leading to a slightly higher number of total event classifications when using the monopolar threshold detector.

After either sorting the detected spike and artifact waveforms to obtain the target classifications or using the a priori known ground truth spike times as targets, performance was obtained using confusion matrices to compare the detected outputs (e.g. spikes or artifacts) against the target outputs (e.g. spike or artifact classifications of the detected outputs using offline sorting). Sensitivity (or true positive rate; TPR) was estimated as the ratio of correctly classified spikes to the sum of correctly classified spikes (true positives; TP) and outputs given as artifacts that were determined to be spikes by offline sorting (false negatives; FN). True negative rate (TNR) was estimated as the ratio of correctly classified artifacts (true negatives; TN) to the sum of correctly classified artifacts and outputs given as spikes that were determined to be artifacts by offline sorting (false positives; FP). Precision (positive predictive value) was estimated as the ratio of true positives to the sum of true positives and false positives. The false discovery rate (FDR) was estimated as the ratio of false positives to the sum of true positives and false positives. The false negative rate (FNR) was estimated as the ratio of false negatives to the sum of true positives and false negatives. These last two metrics (FDR and FNR) were of special interest, as we aimed to reduce FDR while maintaining a low FNR.

## Results

### *Ability to detect waveforms of interest*

An important feature of the spike detector state machine is the ability to identify relatively low-amplitude spikes during epochs that contain periods of relatively high-amplitude biological artifact. Biological noise, such as arises from mechanical vibration and EMG that occur during chewing and whisking, leads to large-amplitude, high-frequency (>300 Hz) deflections in the signals observed on electrodes embedded within cortex. To illustrate this, we isolated a short exemplar epoch from recording session C in which the presence of chewing was verified by synchronizing the electrophysiological data stream with video of the rat moving freely in the recording chamber. While these epochs of activity are likely generated by biological sources, they may still be undesirable during motor recordings designed to study neurophysiological spiking of units related to other motor behavior (i.e. forelimb movement during pellet retrievals). Unfortunately, the simple threshold detector produces many false-positive spike detections during such epochs (Figure 4.6 A, red highlighting). By contrast, the state machine detector is still able to correctly detect spikes (Figure 4.6 B, blue highlighting) during the noisy periods without mistakenly triggering from the same waveforms that are problematic for the threshold detector (Figure 4.6 B, green highlighting).

Even within a single recording session and on a single recording amplifier channel, it was possible to distinguish between substantially different spike waveforms by customizing the parameters sent to the spike detection state machine online. Parameters that were selected online (recording C0, table S1) captured the smaller multi-unit activity (Figure 4.6 C), whereas offline adjustment of parameters led to the ability to isolate waveforms from the larger of the two units (Figure 4.6 D). Importantly, the ability to set the level parameters in real-time, thanks to the modified GUI (Figure 4.6), improved ease-of-use compared to existing systems, in which a “training” recording must first be obtained and analysed offline before allowing parameters to be set (Azin et al. 2011, Azin et al. 2011, Guggenmos et al. 2013).

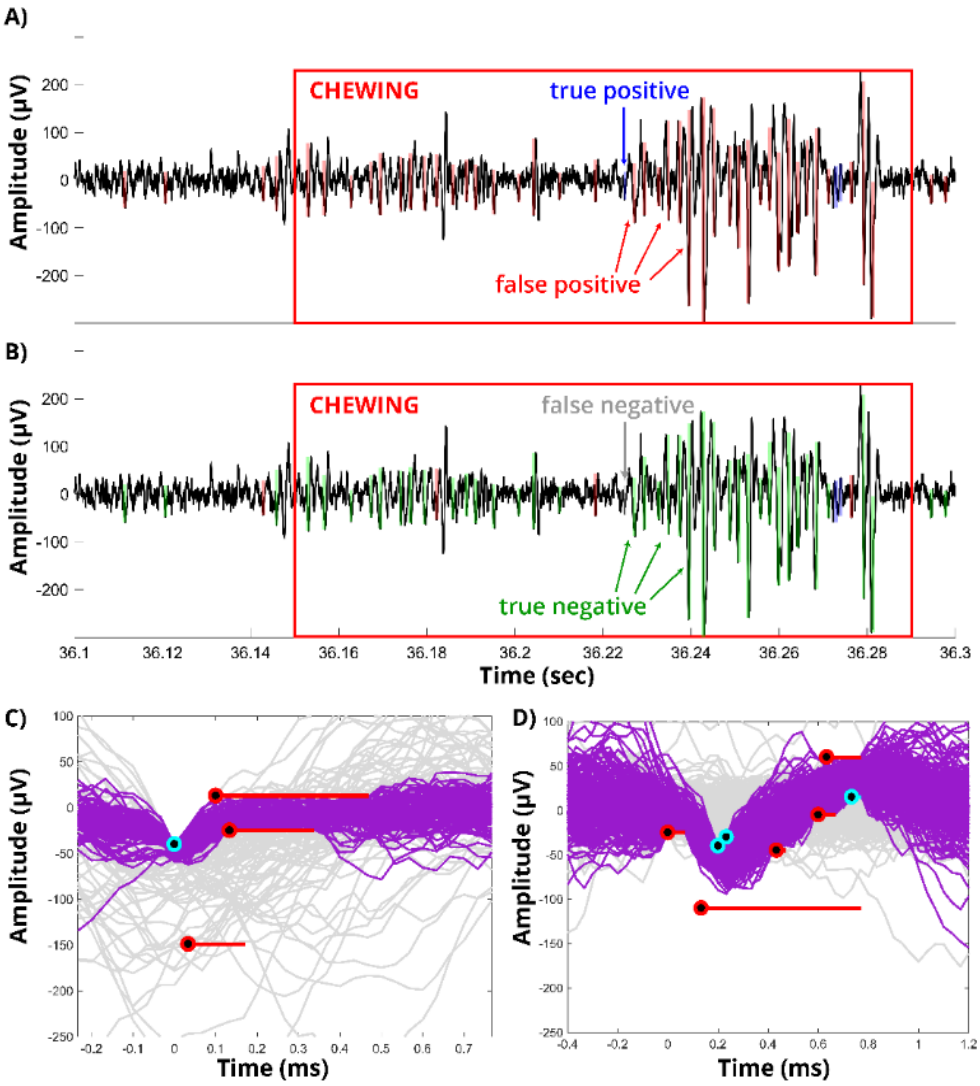


*Figure 4.6: Qualitative performance of the implemented spike detection. A) 200ms of high-pass filtered data from session C during single-threshold (-40µV; simulation C2) spike detection. Red box represents a 130ms epoch of chewing. Red highlighting (false positive) indicates spikes that were wrongly detected. Blue highlighting (true positive) shows spikes that were correctly identified. B) Same data as in panel A with superimposed detections from the state machine spike detector. Green highlighting (true negative) indicates artifacts that were correctly rejected by the state machine. Grey highlighting (false negative) indicates a case of true spike not detected by the state machine. C) Random sub-sampling of 250 detected (magenta) and 250 rejected (grey) waveforms using the spike detection state machine in real-time (recording C0), using the digital outputs from the online state machine. Flat lines represent threshold levels. Black spots represent inclusive samples that must meet the threshold criteria, while ends of lines are open to represent the non-inclusive threshold criterion. Cyan thresholds must be exceeded, whereas red thresholds must not be exceeded. D) An offline reconstruction (recording C1) was used to simulate the state machine using different window parameters. This random sub-sampling of 250*

*detected and 250 rejected waveforms indicates how the parameters could be set differently to isolate spikes from a different unit. Note that increasing the duration of the state machine also increases the total time to detection.*

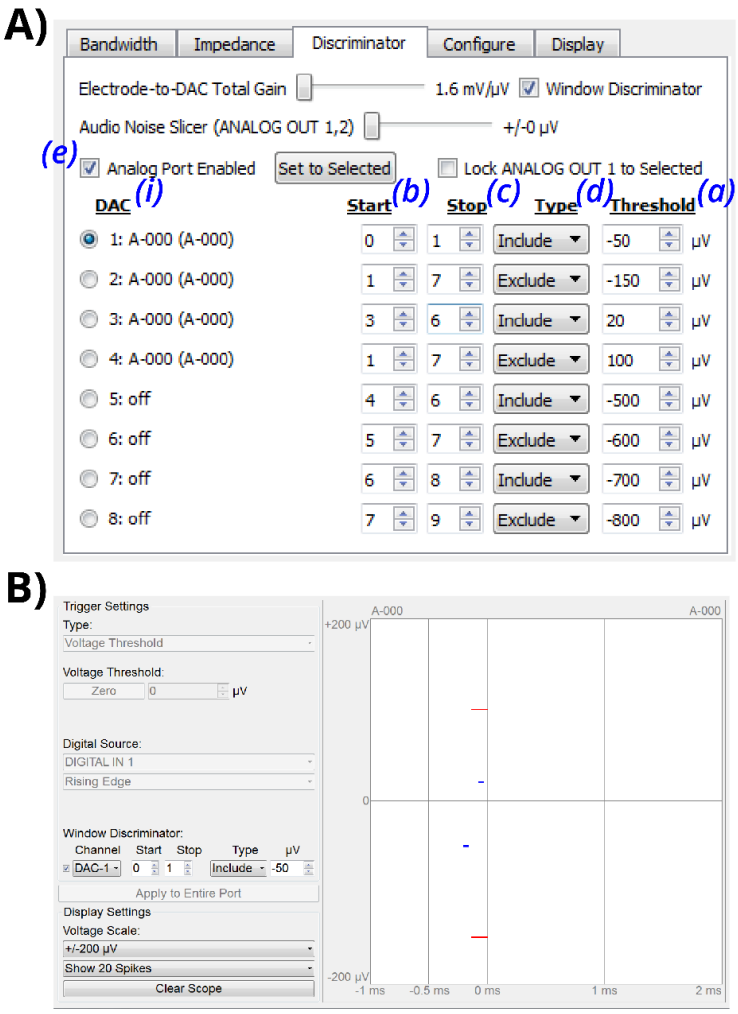


*Figure 4.7: Modifications to the graphical user interface (GUI). A) The original DAC tab was modified to create a new Discriminator tab. Parameters for the currently-selected DAC channel (i) are set using the spin box for start (b) and stop (c) samples, dropdown box that sets the type (d) as either "Include" or "Exclude," threshold (a) spin box, and check box to enable (e) the current DAC channel. Other elements, such as the button to "Set to Selected," are used in the same way as the previous interface (e.g. to route the selected amplifier channel to the highlighted DAC channel as indicated by the radio buttons on the left). B) (Left) The spike scope was modified as well, to accommodate the additional parameters described in A. (Right) Each enabled DAC channel has a corresponding window that is either blue ("Include") or red ("Exclude"). Window amplitude for the current channel can be set by clicking within the white window, which places the level for the currently selected DAC channel at the mouse cursor's current amplitude within the spike plot on the right.*

### *Performance in awake ambulatory rats*

To quantify the online performance of the state machine we performed manual offline sorting of spike and artifact waveforms (from session C). We considered the offline sorting as ground truth, which allowed us to compute confusion matrices comparing the online classification (e.g. spike or artifact) to the offline sorted classification for the same waveform for each monopolar threshold crossing (Figure 4.8). The number of spikes correctly detected by the online spike detector state machine was

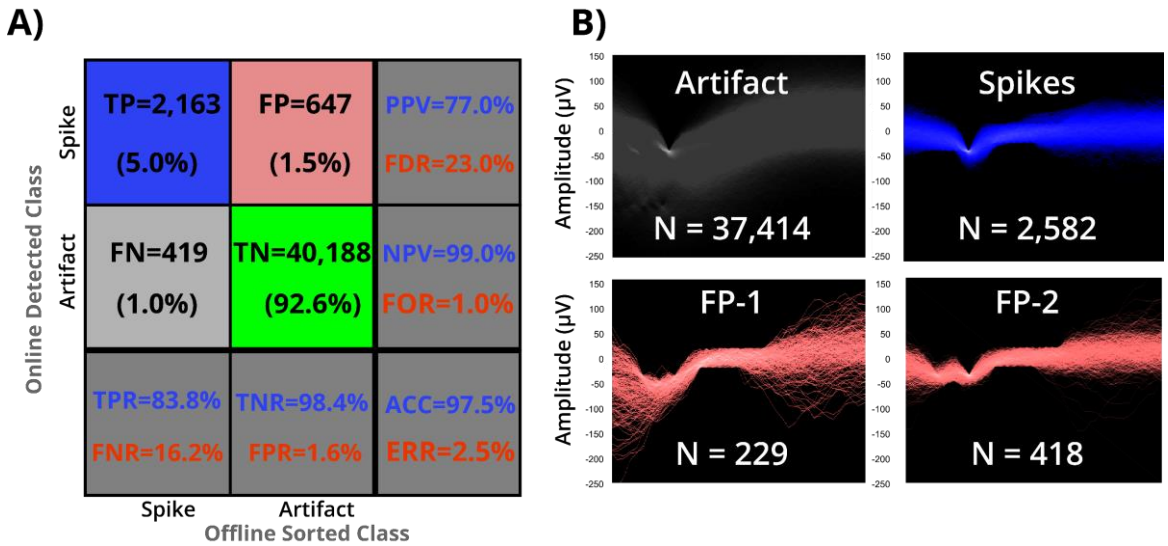


*Figure 4.8: Typical performance compared to offline sorted spikes. A) Confusion matrix for comparison of online spike detection state machine performance after manual offline sorting of spike and artifact waveforms (recording C0). The blue box contains the number of true positive spikes and the percentage of the overall detected events that fit this category. The salmon box contains the number of false positive spikes detected by the algorithm, as determined by manual sorting. The grey box indicates the number of rejected spikes (which entered but did not complete the state machine) that were scored offline as spikes. The green box represents waveforms that were rejected by the state machine and were also classified manually offline as artifact. The top row on the far-right column show the positive predictive value (PPR) in blue and false discovery rate (FDR) in red. The second row on the far-right column shows the negative predictive value (NPV) in blue, and the false omission rate (FOR) in red. The first column on the bottom of the matrix show the sensitivity (or true positive rate, TPR) in blue and the false negative rate (FNR) in red. The second column on the bottom of the matrix shows the true negative rate (TNR) in blue and the false positive rate (FPR) in red. The box in the bottom right of the plot shows the overall accuracy (ACC) in blue and its complement (the error percentage, ERR) in red. B) Offline sorting used for comparison. Lighter regions indicate a higher density of waveforms passing through those voltage values. Spikes were manually sorted using cluster cutting to separate units into characteristic waveforms. Magenta outline indicates spike profile used for offline sorting in panel A. Bottom two panels (FP-1 and FP-2) are characteristic waveform types that sometimes passed the state machine conditions, contributing to the number of false positives.*

2,163 out of 2,582 (meaning a sensitivity, or true positive rate, of 83.8%). The number of true negative (i.e. artifacts not detected as spikes) was 40,188 out of 40,835 (meaning a specificity, or true negative rate, of 98.4%). The number of artifacts incorrectly classified as spikes was 647, resulting in a 23% false discovery rate (FDR) for the online spike detector state machine. Artifacts that led to false-positives contained qualitative similarities with the spikes of interest, which may account for this value (Fig. 4.8 B, FP-1 and FP-2). Overall, the online accuracy of the spike detector state machine was 97.5% (Fig. 4.8

A; recording C0), which is inflated by a high number of true negative samples due to the relatively large number of artifacts passed by the monopolar threshold. In practice, this could be mitigated using a monopolar threshold set to a much higher value; however, while increasing the threshold could reduce the number of artifacts falsely detected as spikes, it would also reduce the number of true positive spikes and is therefore not a feasible solution. Indeed, even the synthetic insertion of large-amplitude (-150µV peak) spikes at known times to a non-spiking channel results in an FDR of 90.5% for a monopolar threshold of -100 µV, while the state machine detector yielded an FDR of 29.3% and overall accuracy of 72.2% (Fig. 4.9).

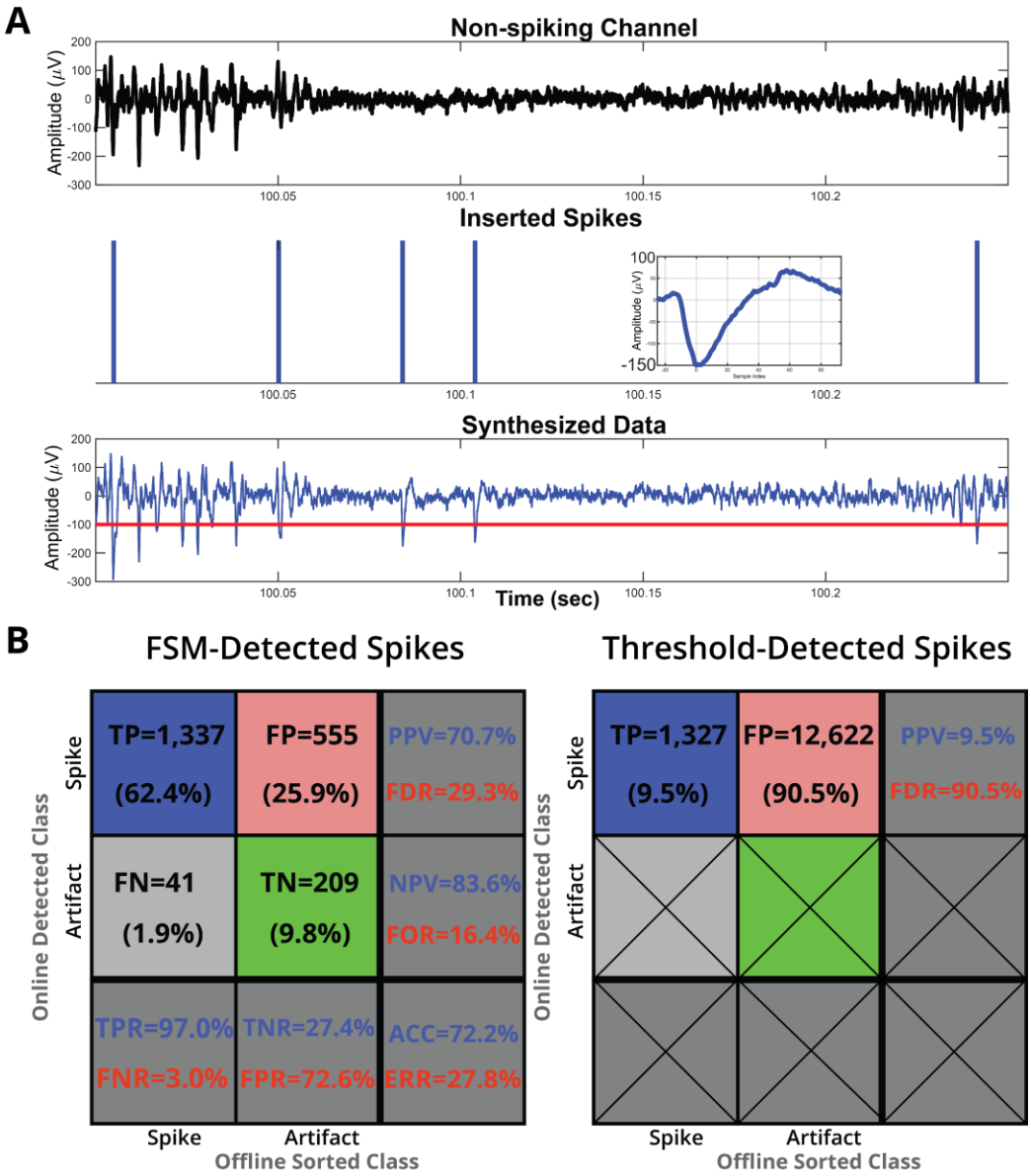


*Figure 4.9: Performance on simulation using non-spiking channel with known spike profiles inserted. A) Overview demonstrating original data (top), spike waveforms (inset) and blue bars indicating times of negative peak onset to superimpose (middle), and generated waveform with known spike times (bottom). Red line on the bottom panel denotes the threshold (-100μV) used in panel B (for the threshold-detected spikes, right panel). In total, 1,500 known spike waveforms were added to the synthetic dataset. B) Confusion matrix for performance of both the state machine detector (left) and standard threshold detector (right). The state machine detector is much more robust in picking out the spike waveform from noise. Parameters for both detectors are listed in table S1; although the initial inclusion threshold for the state machine detector is lower (-70μV), it still has a much lower false discovery rate (FDR; 29.3% vs 90.5%). The threshold detector was only allowed to detect spikes on the rising edge of a signal, but still identified many more candidate waveforms despite sharing the same initial inclusion threshold, since the state machine detector is longer (12 samples to completion). Note that the threshold detector only detects spikes (it cannot classify waveforms).*

Using a channel selected for its low noise floor and large-amplitude spike waveforms recorded *in vivo* (session A), we computed the same performance measures used in the previous case (Figure 4.10 A). Performance overall was comparable (97.1% accuracy) due to the large number of correctly rejected waveforms. However, careful parameter selection also yielded an improved FDR (6.9%) and FNR (2.8%) for the state machine spike detector under these ideal conditions. We compared the best-case performance of our state machine detector to a monopolar threshold detector. Using identical recordings, there is a dramatic improvement in the FDR when using the state machine detector (189 artifacts characterized as spikes, of a total 2,075 spikes detected online, Figure 4.10 B) compared to the monopolar threshold detector (2,770 artifacts characterized as spikes, of a total 7,075 detected spikes, Figure 4.10 B). This improvement results from the rejection of artifactual waveforms, such as occur during epochs of biological noise (cf. chewing, Figures 4.6 A, 4.6 B).

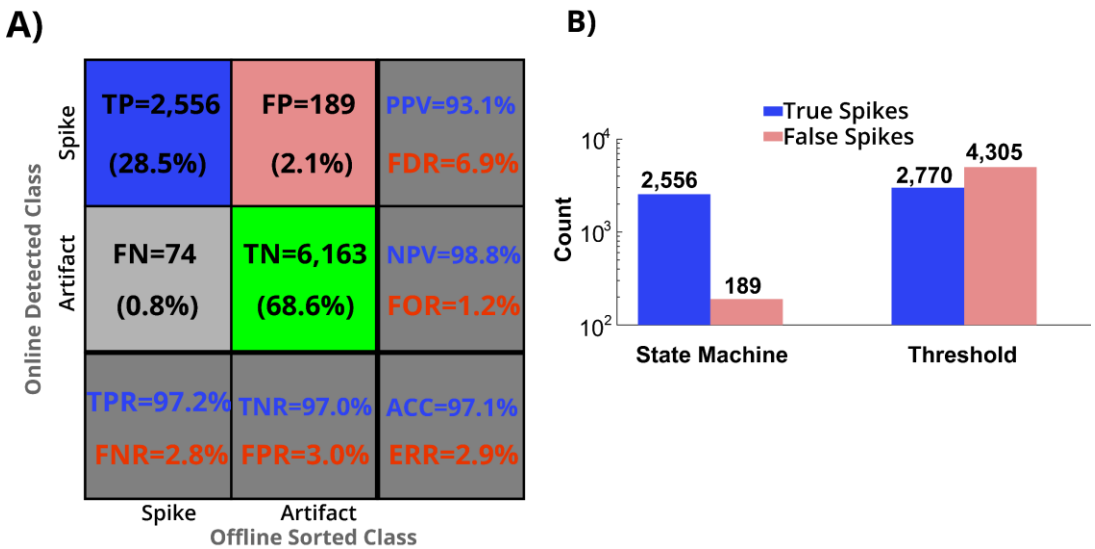


*Figure 4.10: Ideal performance compared to offline sorted spikes and monopolar threshold detection. A) Simulated performance using an ideal in vivo recording with large spikes (recording A1). Although the simulated performance is applied to a channel with high-amplitude spike waveforms, the overall accuracy effectively remains consistent. This is due to the relatively large proportion of waveforms that are correctly rejected (middle box). B) Manual offline sorting performed for recording A1 (presented in panel A), as well as a comparison to performance of true (blue) to false (salmon) discoveries for the state machine detector and a simple threshold detector for the same dataset (recording A0).*

### *Mean latency from spike peak to stimulus delivery*

The total latency for an activity-dependent stimulus can be considered as the sum of the algorithmic latency (to reliably detect an event) and the computational latency (due to the system). Algorithmic latency, in this case, depends on the maximum number of samples needed to detect a spike. In this work, spikes were detected using state machines that varied between 300µs (session B; 9 samples at 30 kHz sample frequency) and 800µs (session C; 24 samples at 30 kHz sample frequency). Therefore,

the exact algorithmic latency is specific to the parameterization of the user-defined threshold levels. Our work did not alter the computational latency between the event detection and the delivery of the stimulus. During session B, the Intan Stimulation/Recording Controller stimulation sequencer module delay was set to zero milliseconds, allowing us to estimate the computational latency as the minimum latency between the rising edge of the virtual TTL input corresponding to the trigger state of the spike detection state machine and the onset of stimulus artifact. The computational latency obtained in this way was 167µs (5 samples at 30 kHz sample frequency; Figure 4.11). Therefore, the total latency of the system during spike detection was reliably less than 1 ms, mainly due to the algorithmic latency, and indicates that the detector is responsive on a timescale that is both fast and reliable enough to be used for performing ADS.

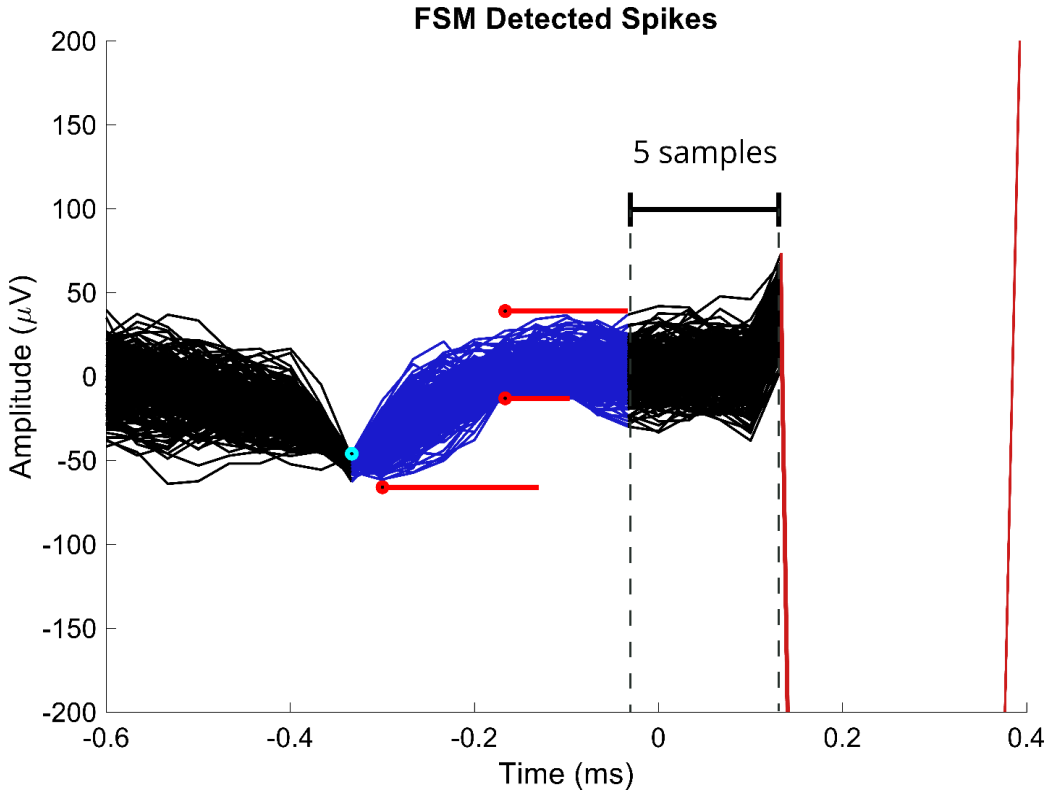


*Figure 4.11: Random sub-sampling of 250 triggered stimuli from recording B0. The Intan RHS Stimulation/Controller system has a built-in stimulation sequencer state machine, which limits the minimum latency from detection to stimulation to 5-samples, or 167 µs when sampling at 30 kHz. The trigger spikes used for stimulation are highlighted in blue. Red indicates the stimulus artifact (60 µV biphasic pulse, 100µs per phase), and rebound from amplifier saturation.*

## Discussion

We developed a modified version of an open-source commercial system to implement closed-loop stimulation with sub-millisecond latency. The main improvement is the implementation of a spike detection state machine with an interface that allows the application of eight reconfigurable

thresholds to any combination of different or identical amplifier channels. The implemented state machine slightly reduces sensitivity (i.e. true positive rate, Figure 4.8 A), but drastically improves specificity (i.e. reduced FDR; Figures 4.10 A, 4.10 B), which may be critical in designing closed-loop electrical stimulation paradigms in the central nervous system *in vivo*. This improvement in selectivity is particularly important when the stimulation paradigm must be implemented during ongoing natural behavior, such as chewing or whisking (Figure 4.6).

Although the focus of this study was on applying the improved detector for use in ADS, we envision that this type of low-latency, highly-selective discriminator could be useful in a range of closed-loop applications. For example, feedback needs not be delivered in the form of stimulation pulses but could instead be incorporated as a part of the experimental design itself, such as the delivery of a reward contingent upon the discrimination of a unique spike waveform (Koralek et al. 2012). However, the context of developing closed-loop neuroprostheses for applications such as neurorehabilitation provides important constraints. For example, a critical aspect of the ADS paradigm is the timing of stimuli based on the detection of a stereotyped waveform that represents a small group of cells near the recording microelectrode (Guggenmos et al. 2013). Therefore, it is desirable to minimize the FDR while maintaining a detection algorithm that can be implemented with low latency and customizable sensitivity to maximize the chances of invoking Hebbian mechanisms of plasticity between cells at the detection site and those at the stimulation electrode (Bi and Poo 1998). It is possible that such a stimulation regime could be augmented by incorporating multiple stimulation sites at offset latencies from a single trigger source; this is also possible using the system presented in this study. Similarly, although not tested here, the modifications presented can apply simultaneous thresholds to several spatially distributed sites simultaneously. This provides a practical way to mitigate the large, non-neural sources of noise that result from a failure in the common-mode rejection, which are typically present on multiple channels simultaneously. Future versions of the discriminator presented here that scale to an arbitrarily large number of thresholds could then be useful in sorting using tetrodes or other high-density arrays.

With the rising interest in applications of closed-loop technologies for stimulation of the central nervous system (Levi et al. 2018), a number of methods for implementing closed-loop stimulation have been made openly available. These include software packages, such as Falcon (Ciliberti and Kloosterman 2017), the Open Ephys GUI (Siegle et al. 2017), and NeuroRighter (Newman et al. 2012); however, software implementations of online spike detection and triggered stimulation typically suffer from the latencies imposed when performing serial communication with the host computer. One exception is the Real-Time eXperiment Interface (RTXI, (Patel et al. 2017)); however, because the

system is designed to operate using a National Instruments Data Acquisition card (NI-DAQ), it may be difficult to scale to a very high channel architecture. On the other hand, the ADC of the RHS2116 is scalable, and because digitization occurs very close to the source (on the headstage), yields improved noise characteristics.

Hardware implementations, such as the synthesized bitfile that can be readily uploaded to effectively transform an FPGA into a commercial neurophysiological acquisition system, are not as widely distributed. Because hardware implementations typically have very specific design constraints and are optimized to meet those constraints, it is impractical to develop and distribute open-source hardware for closed-loop neuroprosthetics. Just as the RTXI system is not readily compatible with the Intan amplifier chips, hardware implementations (Buccelli et al. 2019) are designed to interface with *in vitro* microelectrode arrays that interface to an FPGA with different input and output pin configurations, making it difficult to provide a ubiquitous hardware bitfile for every experimental setup. Alternatively, moving from a hardware implementation in an FPGA to a custom application specific IC (and subsequent commercialization) becomes more practical for individual applications.

To minimize changes to the existing open-source software provided by Intan, the spike detection state machine was implemented in the DAC module. This imposes the limitation that only one spike detection state machine can run at a time. At a maximum, up to eight different amplifier channels could be polled for synchronous or near-synchronous events, or eight threshold criteria could be applied to the waveform of a single amplifier channel. Making substantial modifications to the existing FPGA might allow scaling of a spike detection state machine module to any arbitrary number of thresholds on different channels. A natural extension of this work would be to scale up the number of trigger sources for multi-stream ADS, particularly as FPGA evaluation boards with increased on-board resources become available. Generalizing the state machine to a higher number of independent channels by running it as a module that is independent of the DAC, automating the process of setting threshold levels (e.g. using spike “templates”), and integrating independent state machines to allow concurrent detection of events in multiple frequency ranges are currently being investigated to improve their application in closed-loop neuroprosthetic interfaces. Automating the process of setting threshold levels, especially as channel counts scale up, will be important, as the improved rejection may also reduce sensitivity, depending upon the ad hoc parameters set by the operator. Algorithmically, the state machine is fundamentally similar to the one implemented in (Azin et al. 2011); however, the state machine described here allows more flexibility in the parameterization of

each threshold level by allowing the end-user to set each of the four parameters while the application is running.

We have provided modifications to an existing interface for conducting electrophysiological experiments using closed-loop stimulation. These improvements allow spike detection to be performed with a higher selectivity at the expense of a reduced sensitivity. This trade-off is dependent upon the ad hoc selection of parameters, which can be adjusted by the experimenter in real-time. The architecture in which this improved spike detection state machine is implemented has the possibility to scale to a very high number of channels in the future, improving current and future functionality. Our contribution to the original design improves the accessibility of investigating of closed-loop stimulation paradigms, which may be necessary for effective, therapeutic neuroprosthetic systems.

## References


Azin, M., D. J. Guggenmos, S. Barbay, R. J. Nudo and P. Mohseni (2011). "A battery-powered activity-dependent intracortical microstimulation IC for brain-machine-brain interface." IEEE Journal of Solid-State Circuits **46**(4): 731-745.

Azin, M., D. J. Guggenmos, S. Barbay, R. J. Nudo and P. Mohseni (2011). "A miniaturized system for spike-triggered intracortical microstimulation in an ambulatory rat." IEEE Transactions on Biomedical Engineering **58**(9): 2589-2597.

Bi, G. and M. Poo (1998). "Synaptic modifications in cultured hippocampal neurons: dependence on spike timing, synaptic strength, and postsynaptic cell type." The Journal of Neuroscience **18**(24): 10464-10472.

Biffi, E., D. Ghezzi, A. Pedrocchi and G. Ferrigno (2010). "Development and Validation of a Spike Detection and Classification Algorithm Aimed at Implementation on Hardware Devices." Computational Intelligence and Neuroscience **2010**: 15.

Buccelli, S., Y. Bornat, I. Colombi, M. Ambroise, L. Martines, V. Pasquale, M. Bisio, J. Tessadori, P. Nowak and F. Grassia (2019). "A neuromorphic prosthesis to restore communication in neuronal networks." iScience **19**: 402-414.

Cheney, P. D. and E. E. Fetz (1985). "Comparable patterns of muscle facilitation evoked by individual corticomotoneuronal (CM) cells and by single intracortical microstimuli in primates: evidence for functional groups of CM cells." Journal of Neurophysiology **53**(3): 786-804.

Ciliberti, D. and F. Kloosterman (2017). "Falcon: a highly flexible open-source software for closed-loop neuroscience." Journal of Neural Engineering **14**(4): 045004.

Dancause, N., S. Barbay, S. B. Frost, E. J. Plautz, D. Chen, E. V. Zoubina, A. M. Stowe and R. J. Nudo (2005). "Extensive cortical rewiring after brain injury." Journal of Neuroscience **25**(44): 10167-10179.

Gibson, S., J. W. Judy and D. Markovic (2013). "An FPGA-based platform for accelerated offline spike sorting." Journal of Neuroscience Methods **215**(1): 1-11.

Guggenmos, D. J., M. Azin, S. Barbay, J. D. Mahnken, C. Dunham, P. Mohseni and R. J. Nudo (2013). "Restoration of function after brain damage using a neural prosthesis." Proc Natl Acad Sci U S A **110**(52): 21177-21182.

Guggenmos, D. J., M. Azin, S. Barbay, J. D. Mahnken, C. Dunham, P. Mohseni and R. J. Nudo (2013). "Restoration of function after brain damage using a neural prosthesis." Proceedings of the National Academy of Sciences of the united States of America **110**(52): 21177-21182.

Harris, K. D., D. A. Henze, J. Csicsvari, H. Hirase and G. Buzsáki (2000). "Accuracy of tetrode spike separation as determined by simultaneous intracellular and extracellular measurements." Journal of Neurophysiology **84**(1): 401-414.

Harrison, R. R. (2007). A Versatile Integrated Circuit for the Acquisition of Biopotentials. IEEE Custom Integrated Circuits Conference. San Jose, CA, IEEE**:** 115-122.

Harrison, R. R. and C. Charles (2003). "A low-power low-noise CMOS amplifier for neural recording applications." IEEE Journal of Solid-State Circuits **38**(6): 958-965.

Jackson, A., J. Mavoori and E. E. Fetz (2006). "Long-term motor cortex plasticity induced by an electronic neural implant." Nature **444**(7115): 56-60.

Koralek, A. C., X. Jin, J. D. Long Ii, R. M. Costa and J. M. Carmena (2012). "Corticostriatal plasticity is necessary for learning intentional neuroprosthetic skills." Nature **483**(7389): 331-335.

Levi, T., P. Bonifazi, P. Massobrio and M. Chiappalone (2018). "Editorial: Closed-Loop Systems for Next-Generation Neuroprostheses." Frontiers in Neuroscience **12**(26).

McCulloch, C. and S. Searle (2001). "Generalized Linear and Mixed Models.,(Wiley: New York.)."

Newman, J. P., R. Zeller-Townson, M.-F. Fong, S. Arcot Desai, R. E. Gross and S. M. Potter (2012). "Closed-Loop, Multichannel Experimentation Using the Open-Source NeuroRighter Electrophysiology Platform." Frontiers in Neural Circuits **6**: 98.

Nishibe, M., S. Barbay, D. Guggenmos and R. J. Nudo (2010). "Reorganization of motor cortex after controlled cortical impact in rats and implications for functional recovery." Journal of Neurotrama **27**(12): 2221-2232.

Park, J., G. Kim and S. Jung (2017). "A 128-Channel FPGA-Based Real-Time Spike-Sorting Bidirectional Closed-Loop Neural Interface System." IEEE Transactions on Neural Systems and Rehabilitation Engineering **25**(12): 2227-2238.

Patel, Y. A., A. George, A. D. Dorval, J. A. White, D. J. Christini and R. J. Butera (2017). "Hard real-time closed-loop electrophysiology with the Real-Time eXperiment Interface (RTXI)." PLoS Computational Biology **13**(5): e1005430.

Siegle, J. H., A. C. López, Y. A. Patel, K. Abramov, S. Ohayon and J. Voigts (2017). "Open Ephys: an open-source, plugin-based platform for multichannel electrophysiology." Journal of Neural Engineering **14**(4): 045003.

Vallicelli, E. A., M. De Matteis, A. Baschirotto, M. Rescati, M. Reato, M. Maschietto, S. Vassanelli, D. Guarrera, G. Collazuol and R. Zeiter (2017). Neural spikes digital detector/sorting on FPGA. IEEE Biomedical Circuits and Systems Conference. Turin, Italy, IEEE**:** 1-4.

# Chapter 5: Perspective on humans

The first step towards a successful delivery of brain stimulation in humans is to compare the resting state brain activity in physiological pathological conditions. Several studies are looking for biomarkers in neurological (Wang et al. 2010) and psychiatric (Drysdale et al. 2017) disorders by recording the brain activity through fMRI, EEG and MEG. Resting state functional connectivity is one of the most studied conditions in humans and can give an overview of the brain organization at the macro and meso-scale. Recent advancements in computational methods for source reconstruction starting from EEG and MEG recordings allow to study even deep brain regions starting from non-invasive techniques (Liu et al. 2018). One of the most elegant ways of studying brain networks implies the use of graph theory (Bullmore and Sporns 2009) where each node represents a brain area and each link represents a relationship between brain areas (e.g. correlation, anatomical connection etc.). The classical separation between functional (i.e. statistical association) and effective (i.e. causal interaction from statistical association) connectivity is going to be surpassed by a unified framework (Reid et al. 2019). Indeed, none of the existing methods can be considered superior (in all conditions) to all the others in assessing a connectivity between brain areas and therefore all the methods can be informative in different scenarios; for a complete review, see (Reid et al. 2019). In this context, studying the dynamical changes of functional connectivity after a stroke can help to understand the cortical reorganization that takes place during the first months after stroke onset (Wang et al. 2010). Understanding the critical issues related to this process can be crucial for the design of a personalized treatment based on non-invasive brain stimulation. To this end, in our lab we recently started to study the resting state connectivity of the human brain by using high-density EEG in healthy subjects (actiCHamp 128 ch, Brain Products, Germany), sampled at 1kHz. Using such a high density setup allowed us to reconstruct the sources by means of the exact low-resolution brain electromagnetic tomography, eLORETA, algorithm (Pascual-Marqui et al. 2011). Per each subject, we map the sources onto the 384 regions of interest (ROIs) of the AICHA (Atlas of Intrinsic Connectivity of Homotopic Areas) atlas (Joliot et al. 2015). AICHA includes 192 homotopic region pairs (122 gyral, 50 sulcal, and 20 gray nuclei) and is well suited for intrinsic/effective connectivity analyses. Once we have these time-series we can start applying spectral analysis, correlation measures and graph theory to understand the brain organization at different levels of complexity.

To study the importance of different frequencies, we are using the generalized Morse wavelets superfamily (Lilly and Olhede 2008, Lilly and Olhede 2012) because of the best time-frequency tradeoff (thanks to the minimum Heisenberg area) of these wavelets with a particular choice of its parameters. The convolution of the 384 time-series with the Morse wavelet with central frequencies ranging from

$2^{0.5}$ to $2^6$ Hz in quarter steps (f = $2^{(0.5:0.25:6)}$ Hz) allows a fine analysis in the time/frequency domain. The following figure shows a Morse Wavelet with a central frequency of 8Hz (Figure 5.1, Panel A).

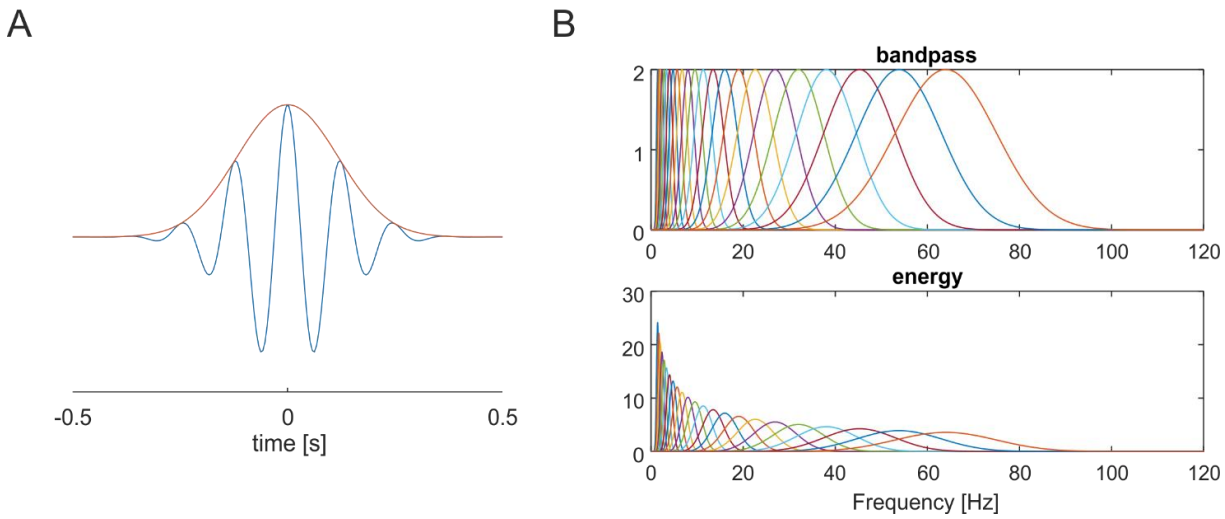


*Figure 5.1: A, real part of a Morse Wavelet with a central frequency of 8Hz (blue line) with the envelope superimposed (red line). B, different Gaussian shapes in the frequency domain (FFT of the wavelets in the time domain) for the 23 central frequencies, ranging from $2^{0.5}$ to $2^6$ Hz. Top, bandpass normalization (meaning that all the frequencies have the same peak value equal to 2 and therefore can be compared). Bottom, energy normalization (meaning that the time-domain energy value is 1 for all frequencies).*

One of the aspects to be considered, when using Generalized Morse Wavelet, regards the normalization factor for each scale (i.e. frequency) as depicted in Figure 5.1, Panel B. A bandpass normalization (i.e. L1 normalization) is the best solution when it is necessary to compare different frequencies in terms of amplitude since the amplitude is not scaled for different frequencies. Energy normalization, on the other hand, preserves energy in the time domain and scales the amplitude depending on the frequency (Figure 5.1, Panel B, bottom). All of these technical considerations are crucial when dealing with similar data analysis and can have a critical impact on the final result.

If, on the other hand, we want a broad picture of the activity that is present at different locations in the brain, with no particular focus on specific frequency bands, we can run analysis on the wideband signals.

Single-subject resting-state functional connectivity can be defined as the Pearson's correlation coefficient ($r$) between the time series of each ROIs (note that many other measures have pros and cons when compared to the Pearson coefficient). An adjacency matrix from a representative healthy subject is reported below.

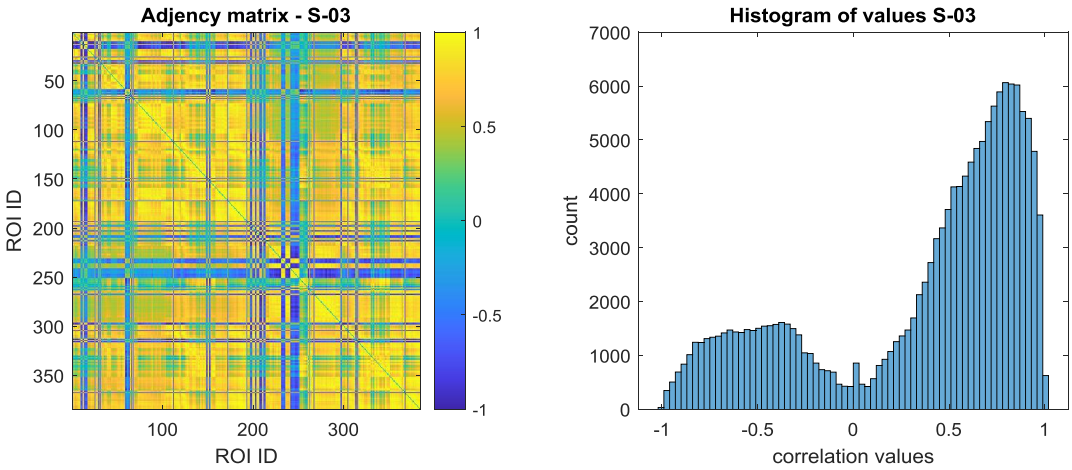


*Figure 5.2: Left, representative adjacency matrix, subject 03. Each position represents one of the 384 ROIs on the AICHA atlas. Right, histogram of the values of the adjacency matrix on the left.*

Starting from this representation, one can apply several different algorithms to find communities of different sizes, representing a coherent activity in different regions of interest. This can be crucial to find a different organization following an injury or in case of neurological pathologies. For instance, the application of the Louvain community detection algorithm (with symmetric treatment of negative weights) resulted in three communities in this case (parameter gamma = 1), separated by red lines, as depicted in the following figure.

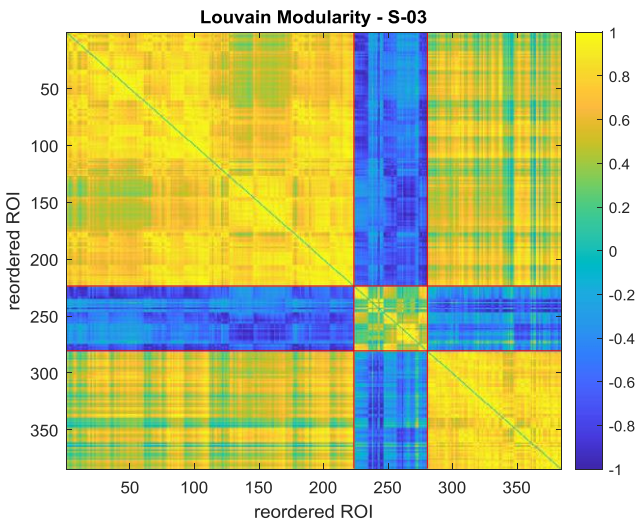


*Figure 5.3: reordered adjacency matrix (same as in Figure 5.2) with 3 clearly separated clusters (separated by red lines) found by Louvain Modularity algorithm.*

The modularity algorithm is by nature biased towards the assortative community structure, as the goal is to maximize the connectivity within each community while minimizing the connectivity between communities. Other algorithms, like the core-periphery algorithm divide the network in a core group and a periphery group, in a way that maximizes the weight of within core-group edges and minimizes the weight of within periphery-group edges as depicted in the following figure.

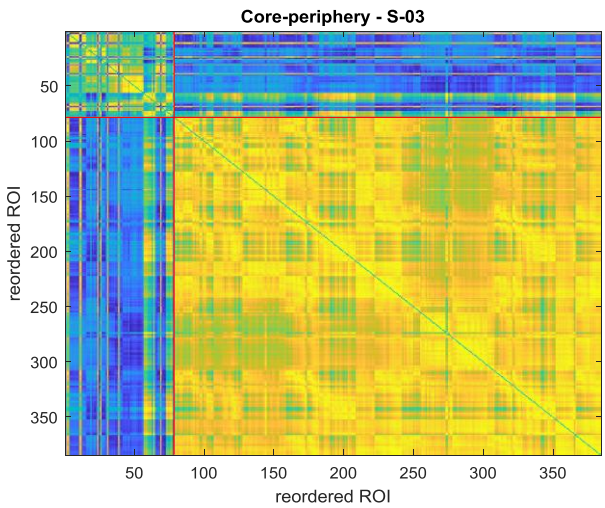


*Figure 5.4: reordered adjacency matrix (same as in Figure 5.2) with 2 clearly separated clusters (separated by red lines) found by Core-Periphery algorithm. The core is the largest cluster (staring at the 80$^{th}$ reordered ROI), the periphery is the smallest cluster, the one with the lower within cluster weight.*

A possible way to overcome these biases is to use the weighted stochastic block model (WSBM). WSBM is as an unsupervised learning algorithm for the identification of networks communities that group together network nodes that have similar group-level connectivity pattern (Aicher et al. 2014). The WSBM can work without the need of thresholding the adjacency matrix which might have a negative impact onto the identification of the real structure of the connectivity (Aicher et al. 2014). The main drawback is the fact that the user must set the number of clusters. In the following figure, we set k = 5 (as reported in literature).

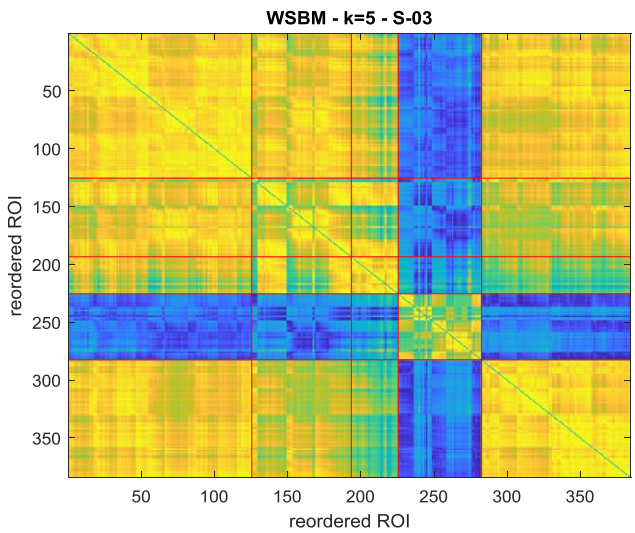


*Figure 5.5: reordered adjacency matrix (same as in Figure 5.2) with 5 clusters (separated by red lines) found by WSBM algorithm.*

It is worth underlying that the choice of the number of communities can dramatically change the results. We are now working towards the definition of a reliable way of selecting the best *k* based on

different metrics such as the Normalized Variation of Information (NVI) (Meilă 2007) and the Adjusted Rand Index (Hubert and Arabie 1985).

It is crucial to say that these methods were not built to run online; they usually need large amounts of data, many iterations and therefore are computationally expansive. Nevertheless, these studies can help to highlight a critical network or a critical aspect of the connectivity that can be studied in detail. Several metrics such as the Small World Propensity (Muldoon et al. 2016) will be used to find a biomarker in terms of graph properties. Once we found a solid metric, we can work towards the implementation of a strategy to counterbalance that pathologic behavior. One of the available options is to stimulate the brain by means of a non-invasive technique (for a complete list refer to Chapter 1). Transcranial alternate current stimulation (tACS) is one of the most promising, non-invasive techniques, especially when a specific rhythm (which can be found by means of the wavelet analysis described before) shows a deficiency with respect to the healthy cohort. The main drawback related to tACS regards the huge stimulation artifacts recorded through the EEG electrodes. This issue reduces our understanding of the real effect of tACS on the brain. To overcome this issue, we recently investigated the possibility to reduce the stimulation artifact and we compared the efficacy of different algorithms in both real and synthetic data (Barban et al. 2019). We found that independent component analysis (ICA) was the best performing artifact removal algorithm but still lot needs to be done in this direction to extract meaningful data while stimulation is delivered. Other non-invasive stimulation options, like tDCS and TMS must be considered depending on the insight we will get from the current and future experiments.

## References


Aicher, C., A. Z. Jacobs and A. Clauset (2014). "Learning latent block structure in weighted networks." Journal of Complex Networks **3**(2): 221-248.

Barban, F., S. Buccelli, D. Mantini, M. Chiappalone and M. Semprini (2019). Removal of tACS artefact: a simulation study for algorithm comparison. 2019 9th International IEEE/EMBS Conference on Neural Engineering (NER), IEEE.

Bullmore, E. and O. Sporns (2009). "Complex brain networks: graph theoretical analysis of structural and functional systems." Nature reviews neuroscience **10**(3): 186.

Drysdale, A. T., L. Grosenick, J. Downar, K. Dunlop, F. Mansouri, Y. Meng, R. N. Fetcho, B. Zebley, D. J. Oathes and A. Etkin (2017). "Resting-state connectivity biomarkers define neurophysiological subtypes of depression." Nature medicine **23**(1): 28.

Hubert, L. and P. Arabie (1985). "Comparing partitions." Journal of classification **2**(1): 193-218.

Joliot, M., G. Jobard, M. Naveau, N. Delcroix, L. Petit, L. Zago, F. Crivello, E. Mellet, B. Mazoyer and N. Tzourio-Mazoyer (2015). "AICHA: An atlas of intrinsic connectivity of homotopic areas." Journal of neuroscience methods **254**: 46-59.

Lilly, J. M. and S. C. Olhede (2008). "Higher-order properties of analytic wavelets." IEEE Transactions on Signal Processing **57**(1): 146-160.

Lilly, J. M. and S. C. Olhede (2012). "Generalized Morse wavelets as a superfamily of analytic wavelets." IEEE Transactions on Signal Processing **60**(11): 6036-6041.

Liu, Q., M. Ganzetti, N. Wenderoth and D. Mantini (2018). "Detecting large-scale brain networks using EEG: impact of electrode density, head modeling and source localization." Frontiers in neuroinformatics **12**: 4.

Meilă, M. (2007). "Comparing clusterings—an information based distance." Journal of multivariate analysis **98**(5): 873-895.

Muldoon, S. F., E. W. Bridgeford and D. S. Bassett (2016). "Small-world propensity and weighted brain networks." Scientific reports **6**: 22057.

Pascual-Marqui, R. D., D. Lehmann, M. Koukkou, K. Kochi, P. Anderer, B. Saletu, H. Tanaka, K. Hirata, E. R. John and L. Prichep (2011). "Assessing interactions in the brain with exact low-resolution electromagnetic tomography." Philosophical Transactions of the Royal Society A: Mathematical, Physical and Engineering Sciences **369**(1952): 3768-3784.

Reid, A. T., D. B. Headley, R. D. Mill, R. Sanchez-Romero, L. Q. Uddin, D. Marinazzo, D. J. Lurie, P. A. Valdés-Sosa, S. J. Hanson and B. B. Biswal (2019). "Advancing functional connectivity research from association to causation." Nat Neurosci **22**: 1751-1760.

Wang, L., C. Yu, H. Chen, W. Qin, Y. He, F. Fan, Y. Zhang, M. Wang, K. Li and Y. Zang (2010). "Dynamic functional reorganization of the motor execution network after stroke." Brain **133**(4): 1224-1238.

# Conclusions

Taken altogether, the results described in this thesis, show the importance of the three steps needed to understand and interact with the nervous system: reading, processing and writing the neural code. These three steps are the building block of all the projects described above that covered the three "R" of neurotechnologies: rectify, replace and retrain. Depending on the scientific question, these three steps can be implemented on different models with different techniques, as described in (Chapter 1). The closed-loop, or activity dependent stimulation, paradigm is the most promising approach for innovative neurotechnologies to date.

In this work, I showed various projects with a clear scale up of closed-loop applications from *in vitro* to *ex vivo* and *in vivo* models. The first project was based on modular cell cultures plated over Micro Electrode Arrays (MEAs). Correlation analysis showed a strong connection between modules (integration) which is crucial for the information flow. Resection of the anatomical connections between modules (by means of a custom-made laser setup) caused a permanent drop of the information flow between modules that resembles and exaggerates what happen after a focal brain lesion. The main advantage related to the use of cell cultures is that you can record and control the entire network with a fine detail when compared with an *in vivo* study. One of the main limitations of cell cultures studies is that you only have an electrophysiological measure and not a behavioral outcome. Nevertheless, it is a convenient testbed for innovative stimulation paradigms like the ones described in (Chapter 2). In that chapter, I described the use of a Field Programmable Gate Array (FPGA) to perform two different approaches following the lesion. The first approach was the Bidirectional Bridging, which consists in a real-time monitoring of the network activity on the first module and whenever a network burst was detected, the system delivered an electrical stimulation to the second module. In parallel, monitoring the activity from the second module we delivered a stimulation to the first one. This real bidirectional approach has the main advantage of not imposing any unidirectional communication but depends on the activity still present after lesion. As a proof of principle, in case of disruption of an entire module, I implemented the so called hybrid bidirectional bridging (HBB). Here, the term hybrid is due to the spiking neural network that we implemented on the FPGA to resemble the activity of the damaged module. In this set of experiments, the interaction is between the biological module survived after lesion and the artificial network (a mathematical model) implemented on the so-called neuroprosthesis. Once more, the main advantage of using simplified models like these lies in the freedom of testing ambitious solutions in a controlled environment.

Increasing the complexity, for the second project (Chapter 3) I used *ex vivo* brain slices, recorded through MEAs. In this case, the neuronal circuits in the region of interest are almost intact and this allows the study of stimulation protocols in a more complex scenario. The goal was to reduce the occurrence of epileptic-like seizure by means of activity dependent stimulation recording in the hippocampal area CA3 and stimulating the subiculum. For that project, I realized the computational architecture to deliver electrical stimulation at the right time. The use of the graphical environment for rapid prototyping (Simulink, Mathworks) allowed the implementation of a reliable detection and stimulation protocol in a rapid way. The first experiments where successful in assessing the feasibility of these protocols and can be a promising starting point for the future.

One step forward towards the application of activity dependent stimulation on behaving animals was the topic of the third project (Chapter 4). There we implemented a reliable spike-detection algorithm on a low-cost commercial, fully open source setup for recording and stimulating on up to 128 channels. The spike detection implemented on the FPGA is more robust in rejecting stimulation and movement artifact thanks to multiple thresholds that can be adjusted to fit the desired spike shape. We released the code in a fully open source way (both the software for the graphical interface and the code for the FPGA implementation). The open source release, in this case, opens new avenues for the development of high-performance algorithms and fits the aim of the open science movement. Next steps, along the same line, will include the implementation of different spike detection algorithms to be tested on all the 128 channels or even local field potential (LFP) analysis in real time. The multi-frequency analysis in real time, including both spikes and LFP is going to be crucial in the near future to better understand and interact with the brain.

A similar approach can be carried out on humans with obvious limitations. The first clinical trials of intracortical activity dependent stimulation on humans are starting now in US. In five years from now, I expect the widespread diffusion of radically innovative techniques like endovascular recordings, Neural dust and Neural lace (see Radically innovative techniques) that will allow an unprecedented detail of human brain recordings. The closed-loop approaches described in this thesis can serve as a starting point towards the development of innovative neuroprosthesis both for classical, as well as for innovative neurotechnologies. Nevertheless, non-invasive stimulation techniques are a much easier and safer option nowadays and I believe that an integration of multi-frequency analysis, together with concepts like modularity and graph theory (Chapter 5) will be part of a unique framework aimed at ameliorating the quality of life in various neurological conditions.

# List of related publications

**Journal papers:**

- Buccelli S, Bornat Y, Colombi I, Ambroise M, Martines L, Pasquale V, Bisio M, Tessadori J, Nowak P, Grassia F, Averna A, Tedesco M, Bonifazi P, Difato F, Massobrio P, Levi T, Chiappalone M. A neuroprosthetic system to restore neuronal communication in modular networks. iScience (2019). Vol 19, P402-414. Doi: https://doi.org/10.1016/j.isci.2019.07.046
- Murphy M*, Buccelli S*, Bornat Y, Bundy D, Nudo R, Guggenmos D, Chiappalone M. Improving an open-source commercial system to reliably perform activity-dependent simulation. Journal of Neural Engineering (2019).- Doi: https://doi.org/10.1088/1741-2552/ab3319
- Ambroise M, Buccelli S, Grassia F, Pirog A, Bornat Y, Chiappalone M and Levi T. Biomimetic neural network for modifying biological dynamics during hybrid experiments. Artificial Life and Robotics (2017) 22: 398. https://doi.org/10.1007/s10015-017-0366-1
- Panuccio G, Semprini M, Natale L, Buccelli S, Colombi I, Chiappalone M. Progress in Neuroengineering for brain repair: New challenges and open issues. Brain and Neuroscience Advances (2018). Volume 2: 1–11 DOI: 10.1177/2398212818776475.
- Iandolo R, Semprini M, Buccelli S, Barban F, Zhao M, Samogin J, Bonassi G, Avanzino L, Mantini D, Chiappalone M. Small-World Propensity Reveals the Frequency Specificity of Resting State Networks. IEEE Open Journal of Engineering in Medicine and Biology (2020). doi: 10.1109/OJEMB.2020.296532

**Book chapters:**

- Bisio M, Pimashkin A, Buccelli S, Tessadori J, Semprini M, Levi T, Colombi I, Gladkov A, Mukhina I, Averna A, Kazantsev V, Pasquale V, Chiappalone M. Closed-Loop Systems and In Vitro Neuronal Cultures: Overview and Applications. In In Vitro Neuronal Networks (pp. 351-387). Springer, Cham.

**Peer-reviewed conference proceedings:**

- Averna A, Caré M, Buccelli S, Semprini M, Difato F and Chiappalone M. A multimodular system to study the impact of a focal lesion in neuronal cell cultures. Lecture Notes in Computer Science (2019), 11705, pp. 5--19, 2019. Doi: https://doi.org/10.1007/978-3-030-28042-0_1
- Barban F, Buccelli S, Mantini D, Chiappalone M, Semprini M. Removal of tACS Artefact: A Simulation Study for Algorithm Comparison. 9th International IEEE EMBS Conference on Neural Engineering, March 2019, San Francisco, USA

- Iandolo R, Chiappalone M, Samogin, Barban F, Buccelli S, Taberna G, Semprini M, Mantini D. A pipeline integrating high-density EEG analysis and graph theory: a feasibility study on resting state functional connectivity. 9th International IEEE EMBS Conference on Neural Engineering, March 2019, San Francisco, USA
- Buccelli S; Tessadori J; Colombi I;Martines L; Bisio M; Averna A; Semprini M; Pasquale V; Chiappalone M. Closed-loop electrophysiology: Past, present and future perspectives and applications, 2018 IEEE International Symposium on Circuits and Systems (ISCAS), Florence, Italy, 2018, pp. 1-5. doi: 10.1109/ISCAS.2018.8351890
- Ito D, Tessadori J, Buccelli S, Chiappalone M. Changes in network activity in a neuro-robotic environment. Joint Conference of the European Medical and Biological Engineering Conference (EMBEC) and the Nordic-Baltic Conference on Biomedical Engineering and Medical Physics (NBC), Tampere, Finland, June 2017

**Awards:**

- Best paper award. Ambroise M, Buccelli S, Grassia F, Pirog A, Bornat Y, Chiappalone M and Levi T. Biomimetic neural network for modifying biological dynamics during hybrid experiments. 22th International Symposium on Artificial Life and Robotics. Beppu, Japan, 2017

**Oral presentations**

- Invited Talk at Mathworks headquarters during the “Development Knowledge Form (DKF)” seminar series, May 31st 2019

# Appendix

## Chapter 4 Appendix

### Verilog testbench

This is the main testbench, developed within the same environment used to program the FPGA. It accurately simulates all registers and wires used in the *in vivo* FPGA implementation. This was particularly useful to reduce the need to synthesize the entire FPGA configuration every time changes occurred.

The core of the original Verilog code is the "main.v" module implementing a state machine that cycles through a pattern of 140 repeating states (managing all the communication from the RHS2116 to the USB and vice versa).

We implemented a testbench "main_mod_tb.v" that acts as the RHS2116 chip streaming data to the "main_reduced.v" module (a reduced version of the huge "main.v" module). This reduced module contains only 7 states, that are enough to communicate to the module "DAC_modified.v". The "DAC_modified.v" module is a modified version of the original "DAC_output_scalable_HPF.v" module that filters the data and compares each sample with a user-defined threshold (for the single threshold spike detection). In addition to the original function of that module, our modified version checks whether the current counter of the spike detection state machine falls within the user-defined window limits for that specific module.

The testbench performs the following steps:

1. reads a binary file (16-bit words) encoding the amplifier data of a previous recording (or synthetic data);
2. Cycles through a reduced number of repeating states (with respect to the original 140 states);
3. During one of these states, it sends data to the module deals with filtering and comparing with voltage and window thresholds;
4. Writes a binary file (16-bit words) encoding the filtered data;
5. Writes a binary file (32-bit words) encoding the spike detection state machine counter (FSM_counter);

One can easily modify the testbench to write additional files for debug purposes or can simply inspect the output of the simulator (ISim in our case) during development. Once saved, the binary files can be inspected and compared with the real results with a different software package, such as MATLAB (see available code).

### *Simulink testbench*

To provide a graphical depiction of the verilog implementation, a Simulink version of the spike detection state machine was first developed. The model-based design can help in understanding the algorithm implementation on the FPGA. We implemented the state machine and not the filtering that is implemented on the FPGA, therefore the input for this testbench is the already high-pass filtered data. The high-pass filter is a single-pole, 300-Hz state filter, as contained in "HPF.m"

Detailed description:

1. Data is loaded from the workspace in double precision (even though it's uint16 precision multiplied by the ADC step size of 0.195µV/bit within the RHS2116 chip);
2. Each sample clock the model checks a series of parameters (the same used in the FPGA implementation) including voltage and window thresholds;
3. Spike detection results are saved for each simulation and allow comparison with actual FPGA recordings or running completely new offline tests;

All intermediate values can be easily accessed and viewed during or after simulation making it a perfect tool to design and test different algorithms.

### *MATLAB testbench*

The last testbench is implemented in MATLAB. It is faster than the other testbenches and can be used after a first spontaneous recording and before the activity-dependent stimulation session to choose the best parameters for a reliable spike detection. For example, an initial recording is made, with an ad hoc parameterization set by the operator. Subsequently, the data (likely only a few minutes long in order for there to be enough spikes) is simulated using the MATLAB testbench to evaluate how the spiking would look for a given set of threshold and sample start and stop values for each DAC to which a state machine level has been applied.

### *Validation*

For each test bench, we compared the simulated result from running the testbench to those obtained when running the model online using identical parameters. First, we measured the difference between the filtered DAC waveform and the simulated filter applied to the raw data. The maximum sample-wise error was always within a tolerance of 1-bit (the least significant bit), which was considered sufficiently accurate for using the testbenches to generate any subsequent comparisons. Next, the algorithmic implementation of the testbench was compared to verify that the output state ('Idle,' 'Active,' or 'Trigger') was identical between the output of the testbench and the online

recording with identical parameters. Once this validation was performed, we considered the results of simulations using the testbench effectively equivalent to those obtained online, and therefore suitable for making comparisons of different algorithms on the same test data.

### *Code Availability*

Code is freely available at https://github.com/m053m716/Intan-DAC-State-Machine-Detector. The modified source code to run the graphical user interface, as well as the new main.bit file and associated executable and dll files are located in the same repository. It should be noted that this implementation uses Digital-Input and Digital-Output Channels 13, 14, and 15 to track the state machine detector trigger, complete, and idle states respectively.

# Acknowledgements

First, I want to thank my advisor Michela. Without her patience, knowledge and kindness it would have been impossible to arrive here. After a Master, an internship and a PhD under her supervision I learned a lot in many fields not limited to my work. I have no doubt I was very lucky in meeting her many years ago and I hope we can continue working together in the future.

The first project Michela assigned me was probably the most important during the first years of work with her. The international nature of that project allowed me to meet other scientist in Europe. In particular Yannick Bornat and Timothée Levi from IMS in Bordeaux. During my PhD, I spent three months in Bordeaux under the supervision of Yannick, and I learned a lot from him during my first experience abroad. It was a pleasure working with them and I had the chance to meet many nice people with different but interesting experiences.

On a different project, I had the chance to spend a couple of weeks in Kansas City. It was a great time, where I met the group of Prof. Nudo, an amazing team of scientists and friends. I cannot list all of them but special thanks goes to Max for his help and tough work. I hope I can continue working with that amazing group of people in the future.

I want to thank IIT and in particular NBT people for the support during the first years of work. Now I moved to the Rehab Technologies department here in IIT and I have to thank this group of people for their support and kindness. My lab mates (both former and actual) deserve special thanks for their contribution and help. Special thanks also to the external reviewers of this thesis: Prof. Renaud and Prof. Vassanelli for their useful feedbacks and comments.

Finally, I want to express gratitude to my family and friends for their love and support.

P.S. Ila, as you know, I would probably need a dedicated paragraph for you… ☺